IOP Publishing Reports on Progress in Physics
Rep. Prog. Phys. **77** (2014) 126401 (60pp) doi:10.1088/0034-4885/77/12/126401

Review Article

Light-induced gauge fields for ultracold atoms

N Goldman[1], G Juzeliūnas[2], P Öhberg[3] and I B Spielman[4]

[1] College de France, 11 place Marcelin Berthelot & Laboratoire Kastler Brossel, CNRS, UPMC, ENS, 24 rue Lhomond, 75005 Paris, France
[2] Institute of Theoretical Physics and Astronomy, Vilnius University, A Goštauto 12, LT-01108 Vilnius, Lithuania
[3] SUPA, Institute of Photonics and Quantum Sciences, Heriot-Watt University, Edinburgh EH14 4AS, UK
[4] Joint Quantum Institute, National Institute of Standards and Technology, and University of Maryland, Gaithersburg, MD 20899, USA

E-mail: ngoldman@ulb.ac.be, gediminas.juzeliunas@tfai.vu.lt, p.ohberg@hw.ac.uk and ian.spielman@nist.gov

Received 3 September 2013, revised 30 May 2014
Accepted for publication 2 July 2014
Published 24 November 2014

Invited by Gordon Baym

Abstract

Gauge fields are central in our modern understanding of physics at all scales. At the highest energy scales known, the microscopic universe is governed by particles interacting with each other through the exchange of gauge bosons. At the largest length scales, our Universe is ruled by gravity, whose gauge structure suggests the existence of a particle—the graviton—that mediates the gravitational force. At the mesoscopic scale, solid-state systems are subjected to gauge fields of different nature: materials can be immersed in external electromagnetic fields, but they can also feature emerging gauge fields in their low-energy description.

In this review, we focus on another kind of gauge field: those *engineered* in systems of ultracold neutral atoms. In these setups, atoms are suitably coupled to laser fields that generate effective gauge potentials in their description. Neutral atoms 'feeling' laser-induced gauge potentials can potentially mimic the behavior of an electron gas subjected to a magnetic field, but also, the interaction of elementary particles with non-Abelian gauge fields. Here, we review different realized and proposed techniques for creating gauge potentials—both Abelian and non-Abelian—in atomic systems and discuss their implication in the context of quantum simulation. While most of these setups concern the realization of background and classical gauge potentials, we conclude with more exotic proposals where these synthetic fields might be made dynamical, in view of simulating interacting gauge theories with cold atoms.

Keywords: ultracold atoms, gauge potentials, light–matter interaction

(Some figures may appear in colour only in the online journal)

Contents

1. Introduction 3
2. Non-inertial frame 4
2.1. Rotation 4
2.2. Shaking 6
3. Geometric gauge potentials 7
3.1. Formulation 7
3.2. Adiabatic approximation 8
3.3. Artificial magnetic and electric fields: Abelian and non-Abelian cases 8
3.4. Geometric gauge potentials and rotation 9
4. Light–matter interaction 10
4.1. Light–matter coupling 10
4.2. Rotating wave approximation 11
4.3. Effective atomic ground-state Hamiltonian 12
4.3.1. General. 12
4.3.2. No fine structure. 12
4.3.3. Including fine structure. 13
4.3.4. Complete electronic ground state. 13
4.4. Bichromatic light field 14
4.4.1. General analysis. 14
4.4.2. Two Raman beams. 15
5. Schemes for creating Abelian gauge potentials 15
5.1. The Λ setup 16
5.2. Spins in effective Zeeman fields 17
5.2.1. General treatment. 17
5.2.2. A pair of Raman beams. 18
5.2.3. Optical flux lattices. 18
5.3. Dressed states: explicit picture 19
5.3.1. The two-level system. 19
5.3.2. Synthetic gauge fields. 21
5.3.3. Limitations. 21
5.3.4. Three-level system. 22
5.4. Experimental implementation 23
5.4.1. The effective vector potential. 23
5.4.2. Creating artificial electric fields. 23
5.4.3. Inclusion of a magnetic field. 23
6. Non-Abelian gauge potentials and SOC 24
6.1. The tripod scheme 25
6.2. SOC for ultracold atoms 25
6.3. Experimental realization of SOC 27
7. The effects of collisions in the presence of SOC 27
7.1. The weakly interacting Bose gas with SOC 28
7.1.1. The homogeneous interacting system with Rashba SOC. 29
7.1.2. The trapped interacting system with Rashba SOC. 29
7.2. Interacting Fermi gases with SOC 29
8. Gauge potentials in optical lattices: Engineering the Peierls phases 32
8.1. Introduction: optical lattices 32
8.2. Gauge structures on the lattice 33
8.2.1. The Abelian case. 33
8.2.2. The non-Abelian case. 34
8.2.3. Genuine non-Abelian structures and the Wilson loop. 35
8.3. The lattice Hamiltonians: a few models 36
8.3.1. A uniform magnetic flux through the lattice: the Hofstadter model. 36
8.3.2. Local magnetic flux: the Haldane model. 36
8.3.3. SOC on the lattice: the Kane–Mele and the spin-dependent Hofstadter models. 37
8.3.4. The square lattice subjected to a non-Abelian gauge potential. 38
8.4. Experimental realizations using optical lattices 38
8.4.1. Laser-assisted-tuneling using different internal states. 38
8.4.2. Laser-assisted-tuneling using shaking methods. 38
8.4.3. Laser-assisted tunneling methods: the main ingredients. 39
8.4.4. Flux configurations on the square lattice. 40
8.4.5. Flux configurations on the hexagonal lattice. 40
8.4.6. Matrix link variables: non-Abelian gauge potentials. 41
8.5. Other relevant schemes 41
8.5.1. Shaking the lattice. 41
8.5.2. Using RF fields. 42
8.5.3. On a chip. 43
8.5.4. Immersion into a rotating BEC. 43
8.5.5. Quasi-2D gauge structures using 1D optical lattices. 43
9. Probing the effects of synthetic gauge potentials: a quantum simulation perspective 44
9.1. Probing quantum Hall physics in synthetic magnetic fields: from atomic Landau levels to strongly correlated states 45
9.2. Identifying topological order 45
9.2.1. Atomic Chern insulators: measuring the Chern number and topological edge states. 46
9.2.2. Simulating Z_2 topological insulators and axion electrodynamics. 48
9.2.3. Majorana fermions in atomic topological superconductors. 49
10. Interacting gauge theories and dynamical gauge fields 49
10.1. Density-dependent gauge potentials 49
10.2. Simulating quantum gauge theories 51
11. Conclusions 52
Acknowledgments 53
References 53

1. Introduction

The laboratory realization of ultracold neutral atomic gases such as Bose–Einstein condensates (BECs) [1, 2] and degenerate Fermi gases [3]—quantum gases—delivered remarkably versatile experimental systems that can realize physical effects with analogs throughout physics. The coherence properties of BECs allow them to address concepts from optics and nonlinear optics: classical and quantum atom optics [4, 5]. Quantum gases have shed light on many effects predicted in the context of traditional condensed matter systems such as the bosonic superfluid to Mott transition in optical lattices [6–8], and the Bardeen–Cooper–Schrieffer crossover in degenerate Fermi gases [9–13]. Even phenomena commonplace in high-energy physics can occur in ultracold settings, where Higgs modes have been observed [14, 15], unconventional 'color' superfluidity [16] is possible, and where confinement mechanisms [17–19] and axion electrodynamics [20] have been predicted.

Atomic quantum gases are charge neutral, and therefore, they are not affected by external electromagnetic fields the way electrons are. However, atom–light coupling allows for the creation of versatile gauge potentials that effectively emerge in the atoms dynamics, allowing experimental access to a panoply of new phenomena at the quantum level. Using this technology, atoms can be subjected to static Abelian gauge fields, offering a framework where synthetic electric and magnetic fields can be experimentally tuned with lasers (see the first experimental works at NIST [21–23]). These setups can also be extended to generate versatile non-Abelian gauge potentials [24]. These static non-Abelian gauge fields could be tailored so as to reproduce the effects of Rashba-type spin–orbit couplings (SOCs), but also, to mimic a variety of properties encountered in the context of high-energy physics. The first experimental steps towards the realization of a two-dimensional (2D) spin–orbit-coupled atomic gas have been reported in [25–32], where the SOC acts along a single spatial dimension. Mimicking magnetic and spin–orbit effects in cold atom laboratories enables the assembly of quantum simulators of new kinds of exotic quantum matter [33–35]. Indeed, cold atomic gases are ideally suited for quantum simulation, as numerous physical parameters governing the systems dynamics are experimentally tunable: particle density, confining potentials, effective dimensionality [36], and even the collisional properties [37] can be easily controlled in the same laboratory. Taken together, this greatly enlarges the range of systems that can realize Richard Feynman's vision [38] for constructing physical quantum emulators of systems or situations that are computationally or analytically intractable.

Gauge theories, with their associated gauge potentials, are central in our understanding of the interactions between elementary particles. Electromagnetism is the simplest example, where the scalar and vector potentials together describe the coupling between charged matter and electromagnetic fields. In the standard model, interactions are mediated by more complex gauge fields which often are of a non-Abelian character. Also, the idea of *emergent* gauge fields, where the low energy sector of a more complicated system is described by an effective gauge theory, is not new. Mead and Truhlar [39] and Berry [41] noted that the adiabatic motion of quantum particles with internal structure can be described in terms of an effective 'geometric' gauge potential. This property was first studied in molecular physics, where the Jahn–Teller effect revealed the geometric phases and corresponding vector potentials [39, 41–44].

The adiabatic and Born–Oppenheimer approximations are closely linked to geometric gauge fields in atomic systems. These geometric vector potentials appear when each atom's external motion is described separately from its internal dynamics, yet the Hamiltonian governing the internal dynamics parametrically depends on the atomic position (for example, via the light–matter interaction). In this context, the possibility of emergent vector potentials was first noted by Taichenachev *et al* [45], Dum and Olshanii [46], as well as by Visser and Nienhuis [47]. References [48–52] proposed setups for systematically engineering vector potentials which provide a non-zero artificial (synthetic) magnetic field for quantum degenerate gases. These synthetic magnetic fields were recently experimentally realized [21, 22], whereas the effect of geometric scalar potentials in optical lattices was experimentally observed a decade earlier [53]. When the local atomic internal states 'dressed' by the laser fields have degeneracies, effective non-Abelian gauge potentials can be formed [54–56], often manifesting as a SOC would in material systems. These artificial SOCs lead to the spin Hall effect in atomic systems [50, 57], as recently demonstrated experimentally [58]. Artificial gauge fields are therefore a highly versatile tool for creating exotic condensed matter analogs in atomic gases [25–32].

These approaches can be extended in a powerful way by adding optical lattice potentials [33–35, 59, 179], where the link to quantum simulation of condensed matter phenomena is particularly evident. Here, the artificial magnetic field can be understood as resulting from a laser induced tunneling between the lattice sites [179] or lattice shaking [59, 100, 101]. Numerous theoretical proposals for simulating condensed matter models and realizing strongly correlated systems have been put forth, and recently, artificial gauge potentials corresponding to staggered [61–63] and uniform [64, 65] magnetic fluxes have been produced in optical lattices.

All of these schemes create *static* gauge fields, in the sense that they are described by additional terms in the atomic Hamiltonian (although the gauge fields can still have an externally imposed time dependence, leading to effective electric fields [23]). Dynamical gauge fields (which are described by their own Hamiltonian and are not just imposed) are important in many areas of physics, from particle physics where the gauge fields are the fundamental force carriers (e.g., [66]), to many-body condensed matter physics where they appear in effective field theories [67]. As such, a number of proposals exist for creating dynamic gauge fields with ultracold atoms [17, 18, 68–72], but to date their complexity has stymied experimental realization.

By emulating a fully dynamical field theory, which includes gauge fields, it is certainly tempting to envisage a quantum simulator that can address open questions from the

Standard Model [68]. Mapping out the complete quantum chromodynamics (QCD) phase diagram is a formidable task. It is also an NP hard problem, and therefore highly intractable using classical computation. A special purpose quantum computer able to emulate the corresponding machinery from the Standard Model would significantly contribute to our understanding of the fundamental forces and processes in Nature.

Although the fundamental nature of being able to create gauge fields for charge neutral ultracold quantum gases, with clear links to particle physics and the forces of Nature, is a compelling argument for pursuing such an endeavor, there are also other, more practical, motivations to create these gauge fields. Magnetic fields and SOC, in particular, appear to provide a route towards the preparation of topological states of matter [73, 74], with some quite remarkable properties and promises for future applications [75]. Ultracold gases subject to artificial gauge fields provide an alternative route for reaching such exotic states of matter, with some added benefits from their unique probes and unprecedented flexibility in controlling many experimental parameters in these systems [33, 34]. Topology is the branch of mathematics that deals with properties of geometric objects that do not change under smooth deformations [76]. The great interest in topological states of matter relies on the fact that such states are robust against external perturbations (e.g. finite temperature, noise, or in general experimental imperfections). There are many intriguing phenomena associated with topological matter. The most striking is the existence of metallic edge states in a material that is insulating in the bulk [73, 74]. In the integer quantum Hall effect (IQHE) [77, 78], these edge modes carry precisely one quantum of conductance, which leads to the quantization of the Hall conductivity. Due to the bulk-edge correspondence [78], much of the properties and information of topological systems can be extracted from the edge states. Depending on the details of the particular physical setup (e.g. the lattice geometry, the interactions, the number of magnetic flux per particle, the presence of SOC), these edge modes may turn out to have very exotic properties [60, 73, 75, 79]. For instance, some topological edge states do not satisfy the traditional statistics of fermions or bosons. These enigmatic *anyons* [73, 75], have not been identified in Nature, but are expected to live as excitations in quantum Hall liquids [75] and topological superfluids [73]. The unusual braiding properties associated with the so-called non-Abelian anyons [75], together with their robustness against imperfections and noise, makes topological matter a promising candidate for building an error-free quantum computer [75], which has all the potential to revolutionize modern technology. Generating and probing anyonic excitations in cold-atom setups, using artificial gauge fields, is certainly one of the most important goals in the field. One of the challenges and open questions would be how to develop schemes which allow for the creation and stability of such states, e.g. against various decay and heating processes that are generally present in experiments, and by doing so manipulate anyonic excitations in a well-controlled environment.

In this review, we summarize different techniques for creating artificial gauge potentials in cold-atom systems (both implemented and proposed), pedagogically describing the main physical mechanisms behind each. We then illustrate the gauge potential's role in a number of applications and highlight the connections between these engineered gauge potentials and other branches of physics. Since the publication of a shorter Review of Modern Physics Colloquium on artificial gauge fields for ultracold atoms [80], there has been a great deal of theoretical and experimental activities in the area, which are reflected in the present review.

The manuscript is organized as follows. In section 2.1, we review the initial technique where rotating gases experienced effective uniform magnetic fields. In sections 3 we present a general framework for light-induced gauge potentials. In section 4 we study the basic interaction between laser fields and atoms, providing guidelines for designing realistic artificial gauge potentials in alkali systems. We then show in section 5 how light–matter interactions can optically induce Abelian gauge potentials for ultracold atoms. Section 6 considers the schemes for generating non-Abelian gauge potentials and SOC for ultracold atoms. In section 7, we study how collisions are altered by the light–matter coupling, illustrating their role first for ground-state BECs, and for the pairing mechanisms in interacting Fermi gases. Section 8 adds optical lattices, and describe how synthetic magnetic fluxes and SOCs can be engineered in a lattice environment. Then, in section 9, we discuss several quantum simulators based on the gauge potential concept, and comment on experimental techniques for detecting the gauge field's effects. In section 10, we then briefly discuss the concept of interacting gauge theories with their unconventional current nonlinearities, and also recent proposals for emulating fully dynamical gauge fields in optical lattices. We conclude by a summary of the current techniques available for creating artificial gauge potentials and indicate potential applications of these ideas.

2. Non-inertial frame

Artificial gauge fields result from spatially and/or temporally inhomogeneous Hamiltonians. In this section we consider two situations where one can eliminate the time dependence of a trapping potential by going to a non-inertial frame of reference.

2.1. Rotation

Both conceptually, and experimentally, the most simple example of an artificial gauge field appears in a spatially rotating frame [60, 81]. This exploits the familiar equivalence between the Coriolis force in a rotating system and the Lorentz force acting on a charged particle in a uniform magnetic field.

Let us consider in detail the quantum dynamics of an electrically neutral atom in a trap rotating with an angular frequency $\Omega_{\rm rot}$ around the $\boldsymbol{e}_z$ axis, as depicted in figure 1. Recalling that a spatial rotation by an angle $\theta = \Omega_{\rm rot} t$ around the rotation vector $\boldsymbol{\Omega}_{\rm rot} = \Omega_{\rm rot}\boldsymbol{e}_z$ is described by the transformation $R_z(t) = \exp(-\mathrm{i}t\boldsymbol{\Omega}_{\rm rot}\cdot\boldsymbol{L}/\hbar)$ involving an orbital angular momentum operator $\boldsymbol{L} = \boldsymbol{r}\times\boldsymbol{p}$, the atomic Hamiltonian is

$$H(t) = \frac{\boldsymbol{p}^2}{2m} + V\left(\boldsymbol{r}'\right), \quad \boldsymbol{r}' = R_z(t)\boldsymbol{r}R_z^{\dagger}(t), \tag{1}$$

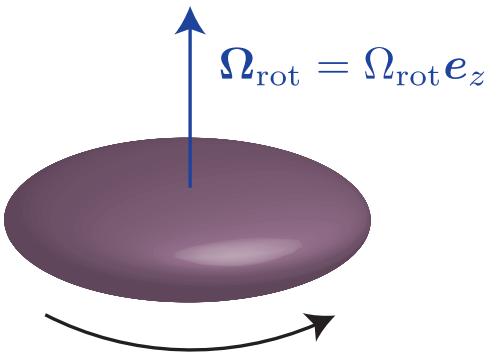

Figure 1. The atomic cloud rotating with an angular frequency $\Omega_{\rm rot}$ around the e_z axis.

where $\boldsymbol{r} = x\boldsymbol{e}_x + y\boldsymbol{e}_y + z\boldsymbol{e}_z$, and $\boldsymbol{p} = p_x\boldsymbol{e}_x + p_y\boldsymbol{e}_y + p_z\boldsymbol{e}_z$ are respectively the position and momentum vectors in the inertial frame of reference, and $\boldsymbol{r}' = x'\boldsymbol{e}_x + y'\boldsymbol{e}_y + z\boldsymbol{e}_z$ is the position vector in the rotating frame, with $x' = x\cos\theta + y\sin\theta$ and $y' = -x\sin\theta + y\cos\theta$. The usual canonical commutation relations between the Cartesian components of the position and momentum vectors $[r_l, p_j] = \mathrm{i}\hbar\delta_{l,j}$ allows us to represent the momentum vector $\boldsymbol{p} = -\mathrm{i}\hbar(\boldsymbol{e}_x\partial_x + \boldsymbol{e}_y\partial_y + \boldsymbol{e}_z\partial_z) \equiv -\mathrm{i}\hbar\boldsymbol{\nabla}$ for problems explicitly expressed in the coordinate representation. Thus any time dependence of the trapping potential $V(\boldsymbol{r}')$ emerges exclusively through the temporal dependence of the rotating vector $\boldsymbol{r}'$.

Because the magnitude of the momentum is unchanged by rotations, $R_z(t)\boldsymbol{p}^2R_z^\dagger(t) = \boldsymbol{p}^2$, the Hamiltonian $H(t)$ is related to its time-independent counterpart via the unitary transformation $R_z(t)$

$$H(t) = R_z(t)\left[\frac{\boldsymbol{p}^2}{2m} + V(\boldsymbol{r})\right]R_z^\dagger(t).$$

The time-dependent Schrödinger equation (TDSE) $\mathrm{i}\hbar\partial_t|\psi\rangle = H(t)|\psi\rangle$ governs the system's dynamics. Inserting the transformed wavefunction $|\psi\rangle = R_z(t)|\psi'\rangle$ into the TDSE yields a rotating frame TDSE

$$\mathrm{i}\hbar\partial_t|\psi'\rangle = H'|\psi'\rangle,$$

with the time-independent Hamiltonian

$$H' = \boldsymbol{p}^2/2m + V(\boldsymbol{r}) - \boldsymbol{\Omega}_{\rm rot}\cdot\boldsymbol{L}, \tag{2}$$

where the term $\boldsymbol{\Omega}_{\rm rot}\cdot\boldsymbol{L} = \mathrm{i}\hbar R_z^\dagger\partial_t R_z$ results from the temporal dependence of $R_z(t)$. Using $\boldsymbol{\Omega}_{\rm rot}\cdot\boldsymbol{L} = (\boldsymbol{\Omega}_{\rm rot}\times\boldsymbol{r})\cdot\boldsymbol{p}$, the Hamiltonian H' can be represented as

$$H' = \frac{(\boldsymbol{p}-\boldsymbol{\mathcal{A}})^2}{2m} + V(\boldsymbol{r}) + W_{\rm rot}(\boldsymbol{r}). \tag{3}$$

The emerging symmetric-gauge vector potential

$$\boldsymbol{\mathcal{A}} = m\boldsymbol{\Omega}_{\rm rot}\times\boldsymbol{r} = m\Omega_{\rm rot}\left(x\boldsymbol{e}_y - y\boldsymbol{e}_x\right),$$

describes the cyclotron motion of the atom in the $\boldsymbol{e}_x - \boldsymbol{e}_y$ plane. An additional anti-trapping (centrifugal) potential

$$W_{\rm rot}(\boldsymbol{r}) = -\frac{\boldsymbol{\mathcal{A}}^2}{2m} = -\frac{1}{2}m\Omega_{\rm rot}^2\left(x^2+y^2\right),$$

repels the atom away from the rotation axis $\boldsymbol{e}_z$. The Hamiltonian (3) has the same form as that for a particle with a unit charge moving in a uniform magnetic field [82] $\boldsymbol{\mathcal{B}} = \boldsymbol{\nabla}\times\boldsymbol{\mathcal{A}} = 2m\Omega_{\rm rot}\boldsymbol{e}_z$. The above analysis does not involve any assumption concerning a specific form of the trapping potential $V(\boldsymbol{r})$. Thus the creation of an artificial magnetic flux via rotation can be applied not only to the usual trapping potentials [83–85] and also to other structures, such as rotating optical lattices [86, 87] or superfluid atom circuits with a rotating weak link [88]. The centrifugal potential can compensate for harmonic trapping potentials

$$V(\boldsymbol{r}) = \tfrac{1}{2}m\left(\omega_x^2x^2 + \omega_y^2y^2\right),$$

when the rotation frequency approaches the trap frequencies $\Omega_{\rm rot}\to\omega_x$ and $\Omega_{\rm rot}\to\omega_y$. In this limit, the problem reduces to that of an unconfined free particle in the constant magnetic field $\boldsymbol{B} = 2m\Omega\boldsymbol{e}_z$. Interestingly, the associated cyclotron frequency $\Omega_{\rm c} = B_{\rm rot}/m = 2\Omega_{\rm rot}$ is twice the rotation frequency.

Having seen how the single-particle Hamiltonian transforms into the rotating frame, we now turn to the question of interactions. For now, consider an arbitrary pairwise interaction $V(|\boldsymbol{r}_1 - \boldsymbol{r}_2|)$ which is a function only of the separation between particles. Under the transformation to the rotating frame the potential

$$R_z(t)V(|\boldsymbol{r}_1 - \boldsymbol{r}_2|)R_z^\dagger(t) = V(|\boldsymbol{r}_1 - \boldsymbol{r}_2|)$$

is unchanged. This follows from the identities $R_z(t)\boldsymbol{r}^2R_z^\dagger(t) = \boldsymbol{r}^2$, and $R_z(t)\boldsymbol{r}_1\cdot\boldsymbol{r}_2R_z^\dagger(t) = \boldsymbol{r}_1\cdot\boldsymbol{r}_2$ which simply state that relative geometry is not changed by rotations. The potential $V(|\boldsymbol{r}_1 - \boldsymbol{r}_2|)$ remains the same, but the two body problem does change due to the emerging vector and centrifugal potentials.

Ultracold atoms have been rotated to large angular frequency with spectacular success (see figure 2(*a*)) by several groups, lead by pioneering experiments at JILA [83], ENS [84], and MIT [85] in conventional harmonic traps. These experiments addressed several important technical questions: (1) how to start an ultracold atomic gas rotating, (2) how to keep it rotating, and (3) how to detect rotation.

Questions (1) and (2) are related. As is evident in equation (3), the desired rotating frame Hamiltonian should have no remnant time dependence. The trapping potential must be asymmetric in the $\boldsymbol{e}_x$–$\boldsymbol{e}_y$ plane in order to induce rotation into an initially non-rotating system. Generally this is achieved either by rotating an initially deformed harmonic trap, or by stirring with focused 'tweezer' lasers. (The initial JILA experiment used an ingenious technique involving transitions between internal atomic states [83], but adopted the deformed trap method to great success as described below.) For experiments featuring the most rapid rotation—equivalently the largest effective magnetic fields—the trap potential is generally returned to near-perfect axial symmetry. Any non-rotating component of the potential (in the lab frame) transforms to an unwanted rotating contribution (in the rotating frame) that can frictionally heat, or slow rapidly rotating clouds (the edges of which can easily exceed the critical velocity for superfluid flow in the lab frame). With sufficient

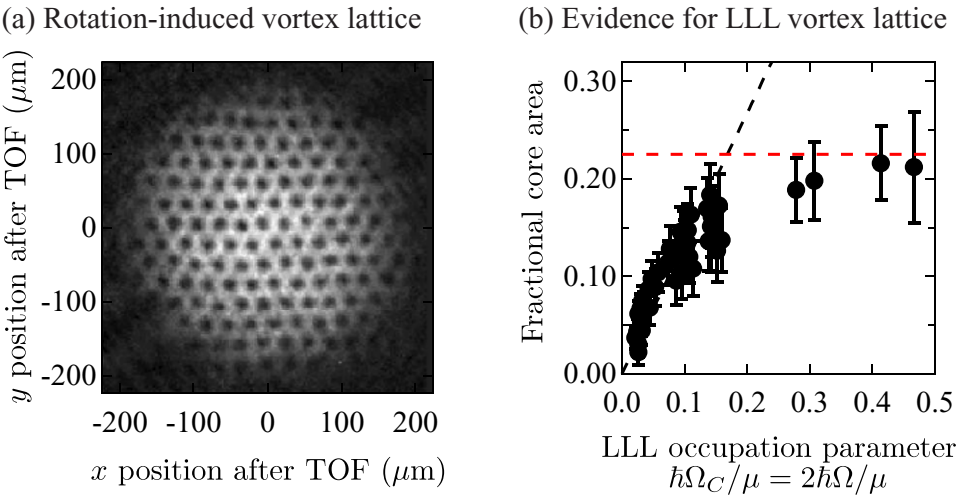

Figure 2. Rapidly rotating BECs. (*a*) Representative image of a symmetrically trapped rapidly rotating BEC, with $\Omega/\omega_{x,y} \approx 0.95$, showing a well ordered vortex lattice. (*b*) Rotating systems entering the LLL. For slowly rotating systems, vortices occupy only a small fraction of the system (black dashed line), whereas in the LLL the vortex density is constant (red-dashed line). As the chemical potential falls below the effective cyclotron frequency, the BEC can be well described by a wavefunction projected into the LLL. Figures are included by permission of Eric Cornell, and first appeared in [89] and [90].

effort, it is possible to achieve nearly perfect axial symmetry, and in the later JILA experiments, there was no discernible decrease in angular frequency for the lifetime of their atomic ensembles [89, 90].

For superfluid Bose gases, there are three primary techniques for detecting rotation. Firstly, the presence of vortices in a BEC directly indicates the existence of an effective magnetic field, or rotation. These vortices result in a change in the atomic density over a small region, with a length scale set by the condensate's healing length $\xi = (\hbar^2/2m\mu)^{1/2}$, where μ is the chemical potential. Typically ξ is between 0.3 μm and 1 μm: below the usual imaging resolution. As a result, vortices have not been measured directly in the trap, and are revealed by removing the confining potential and allowing the BEC and vortices to expand before imaging. Secondly, the evolution of collective modes directly reveals rotation [91, 92]. Lastly, rotation can be inferred by observing the weakening of the trap from the centripetal anti-confinement [90].

In spite of the success creating large vortex lattices, rotating systems have not entered the strongly correlated regime where the filling factor $\nu \lesssim 10$ [60]. This results from a technical limitation: at some point it becomes difficult to increase the angular momentum per particle and remain in equilibrium. The most rapidly rotating BEC just barely entered the lowest Landau level (LLL) regime, where the vast majority of the particles reside in the LLL (unlike electron systems, this can occur at quite large ν). A BEC will enter the LLL when the occupation parameter $\hbar\Omega_c/\mu$ becomes large; the onset of this crossover was observed by the JILA group (see figure 2(*b*)) using a series of ingenious evaporation tricks to increase the mean angular momentum per particle. A secondary technical challenge for studying strongly correlated systems is to confine the atoms into 2D planes. The confinement along $\boldsymbol{e}_z$ should be large compared to the radial trapping. This is generally achieved using one-dimensional (1D) optical lattices, but technically it is difficult to create lattices with the required axial symmetry for rapid rotation experiments.

Most experiments with rotating systems worked with large atomic gases in a single trapping potential, however, a recent experiment created an optical lattice with ~10 atoms per site, where each lattice site was separately rotated [93] (as opposed to rotating the optical lattice in its entirety [86, 87]). In this regime, very rapid rotation is possible owing to the very strong confinement in individual lattice sites, and the authors argue they have entered the few-atom strongly correlated regime.

2.2. Shaking

Besides rotation, shaking optical lattices is another widely used experimental technique [63, 94–99], which can trigger non-trivial topological effects and gauge structures in a rather direct manner [100–104]. Driven-induced gauge fields, using modulated cold-atom systems, is deeply related to the concept of 'Floquet topological states' [105–107] and strain-induced magnetic fields [108], which are currently explored in solid-state laboratories. In particular, a shaken atomic system can be tailored so as to reproduce the dynamics of electronic systems subjected to circularly polarized light (see below and Reference [102]); such an observation is instructive since light-driven electronic systems were predicted to produce Floquet topological states in materials such as graphene [106, 107, 109].

To give a general description of the phenomenon, let us consider atoms in an arbitrary trapping potential (e.g. a periodic optical lattice or a harmonic potential), which is affected by shaking. The Hamiltonian $H(t)$ then has the form of equation (1), in which the trapping potential $V(\boldsymbol{r}')$ depends on the position vector $\boldsymbol{r}' \equiv \boldsymbol{r}'(t)$ defined by

$$\boldsymbol{r}'(t) = \boldsymbol{r} - \boldsymbol{r}_0(t) = R_{\boldsymbol{r}_0}(t)\boldsymbol{r}R^{\dagger}_{\boldsymbol{r}_0}(t), \quad \text{with}$$
$$R_{\boldsymbol{r}_0}(t) = \exp\left[-\mathrm{i}\boldsymbol{p}\cdot\boldsymbol{r}_0(t)/\hbar\right]. \tag{4}$$

Namely, $\boldsymbol{r}'(t)$ contains a time-dependent shift $\boldsymbol{r}_0(t)$ with respect to the inertial frame vector $\boldsymbol{r}$, which depends on the shaking protocol [99].

In contrast to the case of rotation, the orientation of the coordinate system is not altered. Only the origin $\boldsymbol{r}_0(t)$ changes in time. If the motion was chosen to be linear in time, $\boldsymbol{r}_0(t) = \boldsymbol{v}_0 t$, the transformation would imply a simple transition to another inertial frame. Here, we are interested in another scenario, where the trapping potential is modulated in a periodic manner, $\boldsymbol{r}_0(t+T) = \boldsymbol{r}_0(t)$, with $T = 2\pi/\omega$ being the period of the shaking. For instance, considering a single harmonic, the linear and circular driving are respectively described by

$$\boldsymbol{r}_0(t) = \kappa \boldsymbol{e}_x \sin(\omega t) \quad \text{and}$$
$$\boldsymbol{r}_0(t) = \kappa \boldsymbol{e}_x \sin(\omega t) - \kappa \boldsymbol{e}_y \cos(\omega t), \tag{5}$$

where κ denotes the driving amplitude.

The transformation to the non-inertial frame does not alter the momentum, $R_{r_0}(t)\boldsymbol{p}R^{\dagger}_{r_0}(t) = \boldsymbol{p}$, so that the transformed Hamiltonian reads

$$H' = R^{\dagger}_{r_0}(t)H(t)R_{r_0}(t) - \mathrm{i}\hbar R^{\dagger}_{r_0}(t)\partial_t R_{r_0}(t)$$
$$= \boldsymbol{p}^2/2m + V(\boldsymbol{r}) - \boldsymbol{p}\cdot\dot{\boldsymbol{r}}_0(t), \tag{6}$$
$$= \frac{(\boldsymbol{p}-\boldsymbol{\mathcal{A}})^2}{2m} + V(\boldsymbol{r}), \quad \text{with} \quad \boldsymbol{\mathcal{A}} = m\dot{\boldsymbol{r}}_0(t), \tag{7}$$

where the vector potential $\boldsymbol{\mathcal{A}} \equiv \boldsymbol{\mathcal{A}}(t)$ represents the momentum of a particle moving with the frame velocity $\dot{\boldsymbol{r}}_0(t)$. In the last relation (7), we have neglected the uniform term $-\boldsymbol{\mathcal{A}}^2/2m$, which can be eliminated by including a position-independent phase factor to the atomic wave function.

The time-dependent vector potential yields a spatially uniform force $\boldsymbol{\mathcal{F}} = -\dot{\boldsymbol{\mathcal{A}}}(t) = -m\ddot{\boldsymbol{r}}_0(t)$ acting on atoms due to acceleration of the non-inertial frame. In contrast to the transformation to a rotating frame considered in the previous section 2.1, the vector potential $\boldsymbol{\mathcal{A}}(t)$ does not have any spatial dependence, but instead, it is time-dependent [99]. Note also that the vector potential $\boldsymbol{\mathcal{A}}(t)$ associated with a linear (resp. circular) harmonic shaking given by equation (5) is equivalent to the one emerging for a charged particle in a linear (respectively, circular) polarized electric field [109–111]. As mentioned above, this analogy with electronic systems emphasizes the possibility to generate driven-induced (Floquet) topological phases [107] with shaken optical lattices [100–104]. The effective gauge structures and topological phases emanating from lattice modulations will be further addressed in section 8.5.1.

3. Geometric gauge potentials

3.1. Formulation

Geometric gauge potentials arise throughout physics [24, 39, 41–44, 112–117]. One place they can emerge in cold-atom systems is when the atomic center of mass motion is coupled to its internal ('spin') degrees of freedom [46–53, 55, 118–121]. To understand these gauge fields, we begin with the full (and in general time-dependent) atomic Hamiltonian

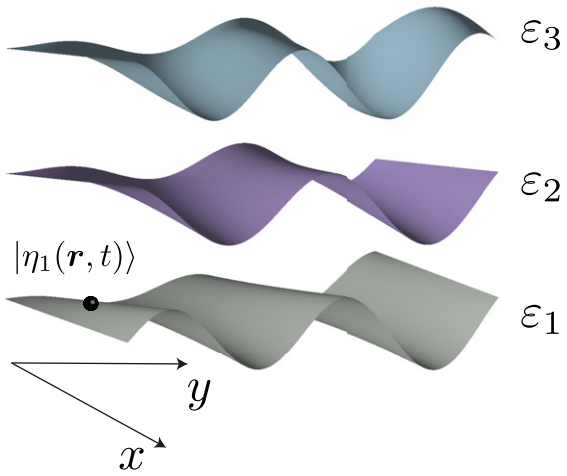

Figure 3. Illustration of the position-dependence of the eigenenergies $\varepsilon_m \equiv \varepsilon_m(\boldsymbol{r},t)$ of the atomic dressed states $|\eta_m\rangle \equiv |\eta_m(\boldsymbol{r},t)\rangle$.

$$\hat{\tilde{H}} \equiv \hat{\tilde{H}}(\boldsymbol{r},t) = \left(\frac{\boldsymbol{p}^2}{2m} + V\right)\hat{1} + \hat{M}, \tag{8}$$

where $V \equiv V(\boldsymbol{r},t)$ is the state-independent trapping potential, $\boldsymbol{r}$ and $\boldsymbol{p}$ are the atomic center of mass coordinate and momentum, and $\hat{1}$ is the unit operator acting on the internal atomic degrees of freedom. The operator $\hat{M} \equiv \hat{M}(\boldsymbol{r},t)$ includes the Hamiltonian for the atomic internal motion, as well as the atom–light coupling term. As a result, $\hat{M}$ explicitly depends on $\boldsymbol{r}$, and in general time. Hats over operators (like $\hat{M}$ and $\hat{1}$) signify that they act on the internal atomic degrees of freedom; center of mass operators such as $\boldsymbol{r}$ and $\boldsymbol{p}$, will be hatless. In this section, we adopt the coordinate representation for the center of mass motion, so $\boldsymbol{r}$ simply denotes the atomic position, and $\boldsymbol{p} = -\mathrm{i}\hbar\boldsymbol{\nabla}$ is the associated momentum operator. In subsequent sections, we will turn to the momentum representation to view the gauge potentials from another angle [51].

The operator $\hat{M}(\boldsymbol{r},t)$ can be cast in terms of the atomic bare internal states $|m\rangle$

$$\hat{M}(\boldsymbol{r},t) = \sum_{n,m=1}^{N} |n\rangle M_{nm}(\boldsymbol{r},t)\langle m|, \tag{9}$$

so the position and time dependence of $\hat{M}(\boldsymbol{r},t)$ comes exclusively from the matrix elements $M_{nm}(\boldsymbol{r},t)$. Here N is the number of atomic internal states involved.

The diagonalization of the operator $\hat{M}(\boldsymbol{r},t)$ provides a set of eigenstates $|\eta_m\rangle \equiv |\eta_m(\boldsymbol{r},t)\rangle$ $(m = 1, 2, \ldots N)$, known as the atomic dressed states, with eigenenergies $\varepsilon_m \equiv \varepsilon_m(\boldsymbol{r},t)$ that depend on the atomic position $\boldsymbol{r}$, as depicted in figure 3. Any atomic state-vector can be expanded in this position-dependent basis

$$|\tilde{\psi}\rangle = \sum_{m=1}^{N} \psi_m(\boldsymbol{r},t)\,|\eta_m(\boldsymbol{r},t)\rangle, \tag{10}$$

where $\psi_m(\boldsymbol{r},t) \equiv \psi_m$ is a wave-function for the center of mass motion of the atom in the mth internal dressed state.

The atomic bare and dressed basis states are connected via a position-dependent unitary transformation $|\eta_m(\boldsymbol{r},t)\rangle = \hat{R}|m\rangle$ which makes the operator $\hat{M}(\boldsymbol{r},t)$ diagonal:

$$\hat{R}^{\dagger}\hat{M}\,(\boldsymbol{r},t)\,\hat{R} = \hat{\varepsilon}, \quad \text{with} \quad \hat{\varepsilon} = \sum_{m=1}^{N} |m\rangle\,\varepsilon_m\,(\boldsymbol{r},t)\,\langle m|\,. \tag{11}$$

Replacing the original state vector $|\tilde{\psi}\rangle$, in equation (10), by the transformed one

$$|\psi\rangle = \hat{R}^{\dagger}|\tilde{\psi}\rangle = \sum_{n=1}^{N} \psi_n\,(\boldsymbol{r},t)\,|n\rangle\,, \tag{12}$$

the Hamiltonian governing the transformed TDSE $\mathrm{i}\hbar\partial_t|\tilde{\psi}\rangle = \hat{H}(\boldsymbol{r},t)|\tilde{\psi}\rangle$ reads $\hat{H} = \hat{R}^{\dagger}\tilde{\hat{H}}(\boldsymbol{r},t)\hat{R} - \mathrm{i}\hbar\hat{R}^{\dagger}\partial_t\hat{R}$, giving

$$\hat{H} = \frac{\left(\boldsymbol{p} - \hat{\boldsymbol{\mathcal{A}}}\right)^2}{2m} + V + \hat{\varepsilon} + \hat{\Phi}. \tag{13}$$

The vector operator

$$\hat{\boldsymbol{\mathcal{A}}} = \mathrm{i}\hbar\hat{R}^{\dagger}\nabla\hat{R} = \sum_{n,m=1}^{N} |n\rangle\,\boldsymbol{\mathcal{A}}_{nm}\,\langle m|\,, \quad \boldsymbol{\mathcal{A}}_{nm} = \mathrm{i}\hbar\,\langle\eta_n|\,\nabla\,|\eta_m\rangle \tag{14}$$

emerges due to the spatial dependence of the atomic dressed states, whereas the additional scalar operator

$$\hat{\Phi} = -\mathrm{i}\hbar\hat{R}^{\dagger}\partial_t\hat{R} = \sum_{n,m=1}^{N} |n\rangle\,\Phi_{nm}\,\langle m|\,,$$
$$\Phi_{nm} = -\mathrm{i}\hbar\,\langle\eta_n|\,\partial_t\,|\eta_m\rangle \tag{15}$$

arises because of their temporal dependence. For the sake of simplicity, we have omitted the unit operator $\hat{1}$ multiplying the momentum operator $\boldsymbol{p}$ and the state-independent potential V in the transformed Hamiltonian $\hat{H}$, equation (13).

3.2. Adiabatic approximation

If a subset containing $q \leqslant N$ dressed states is well separated in energy from the remaining ones, it is appropriate to make an adiabatic (Born–Oppenheimer) approximation by projecting the system's dynamics onto the truncated space of the internal states, using the operator $\hat{P}^{(q)} = \sum_{m=1}^{q}|m\rangle\langle m|$. The Hamiltonian $\hat{H}^{(q)} = \hat{P}^{(q)}\hat{H}\hat{P}^{(q)}$ describing such a reduced dynamics reads

$$\hat{H}^{(q)} = \frac{\left(\boldsymbol{p} - \hat{\boldsymbol{\mathcal{A}}}^{(q)}\right)^2}{2m} + \hat{V}_{\mathrm{tot}}^{(q)},$$
$$\hat{V}_{\mathrm{tot}}^{(q)} = V + \hat{\varepsilon}^{(q)} + \hat{\Phi}^{(q)} + \hat{W}^{(q)}, \tag{16}$$

where $\hat{\varepsilon}^{(q)}$, $\hat{\boldsymbol{\mathcal{A}}}^{(q)}$ and $\hat{\Phi}^{(q)}$ are the projections onto the reduced subspace of the corresponding operators featured in the full Hamiltonian $\hat{H}$, equation (13). Here we have omitted the projector $\hat{P}^{(q)}$ multiplying $\boldsymbol{p}$ and the state-independent potential V.

An extra operator

$$\hat{W}^{(q)} = \frac{1}{2m}\hat{P}^{(q)}\hat{\boldsymbol{\mathcal{A}}}\left(\hat{1} - \hat{P}_q\right)\hat{\boldsymbol{\mathcal{A}}}\hat{P}^{(q)} \tag{17}$$

with the matrix elements

$$W_{nm} = \frac{1}{2m}\sum_{l=q+1}^{N} \boldsymbol{\mathcal{A}}_{nl}\cdot\boldsymbol{\mathcal{A}}_{lm}, \quad n\,,m = 1,\,\ldots\,,q \tag{18}$$

results from projecting $\hat{\boldsymbol{\mathcal{A}}}^2$ onto the selected subspace of the internal dressed states. The potential $\hat{W}^{(q)}$ can be interpreted as a kinetic energy of the atomic micro-trembling due to off-resonance non-adiabatic transitions to the omitted dressed states with $m > q$ [122, 123].

In this way, the geometric vector potential $\hat{\boldsymbol{\mathcal{A}}}^{(q)}$ and scalar potential $\hat{W}^{(q)}$ emerge from the atomic dressed states' spatial dependence. The potential $\hat{\Phi}^{(q)}$ on the other hand, stems from their time dependence. The latter $\hat{\Phi}^{(q)}$ describes the population transfer between the atomic levels due to the temporal dependence of the external fields [54, 124, 125].

When the truncated space includes a single dressed state ($q = 1$) well separated from the others, as is the case in figure 3, the vector and scalar potentials reduce to the ordinary commuting vector and scalar fields,

$$\hat{\boldsymbol{\mathcal{A}}}^{(q)} \to \boldsymbol{\mathcal{A}} = \mathrm{i}\hbar\,\langle\eta_1|\,\nabla\,|\eta_1\rangle \quad \text{and}$$
$$\hat{V}_{\mathrm{tot}}^{(q)} \to V_{\mathrm{tot}} = \frac{1}{2m}\sum_{l=2}^{N}\boldsymbol{\mathcal{A}}_{nl}\cdot\boldsymbol{\mathcal{A}}_{lm}. \tag{19}$$

In this case, the resulting artificial electric and magnetic fields are the standard $\boldsymbol{\mathcal{E}} = -\boldsymbol{\nabla}V_{\mathrm{tot}} - \partial_t\boldsymbol{\mathcal{A}}$ and $\boldsymbol{\mathcal{B}} = \boldsymbol{\nabla}\times\boldsymbol{\mathcal{A}}$. However, for $q > 1$ the more general relations discussed in the following are required.

3.3. Artificial magnetic and electric fields: Abelian and non-Abelian cases

The vector and scalar potentials $\hat{\boldsymbol{\mathcal{A}}}^{(q)}$ and $\hat{W}^{(q)}$ featured in the projected Hamiltonian $\hat{H}^{(q)}$, equation (16), can be related to the operator generalizations of conventional magnetic and electric fields. The situation is more complicated than for classical electromagnetism, because the scalar potential and the Cartesian components of the vector potential are now operators which do not necessarily commute.

To elucidate the problem, we turn to the Heisenberg equations of motion governing the projected dynamics. The velocity operator defined via the Heisenberg equation is

$$\hat{\boldsymbol{v}} = -\frac{\mathrm{i}}{\hbar}[\boldsymbol{r},\hat{H}^{(q)}] = \frac{1}{m}(\boldsymbol{p} - \hat{\boldsymbol{\mathcal{A}}}^{(q)}). \tag{20}$$

The acceleration is defined via the Heisenberg equation for the velocity operator $\dot{\hat{\boldsymbol{v}}} = \partial_t\hat{\boldsymbol{v}} - \mathrm{i}[\hat{\boldsymbol{v}},\hat{H}^{(q)}]/\hbar$. Since the only explicit time dependence of $\hat{\boldsymbol{v}}$ resides in $\hat{\boldsymbol{\mathcal{A}}}^{(q)}$, then $\partial_t\hat{\boldsymbol{v}} = \partial_t\hat{\boldsymbol{\mathcal{A}}}^{(q)}/m$, giving

$$\dot{\hat{\boldsymbol{v}}} = -\frac{1}{m}\partial_t\hat{\boldsymbol{\mathcal{A}}}^{(q)} - \frac{\mathrm{i}m}{2\hbar}[\hat{\boldsymbol{v}},\hat{v}^2] - \frac{\mathrm{i}}{\hbar}[\hat{\boldsymbol{v}},\hat{V}_{\mathrm{tot}}^{(q)}]. \tag{21}$$

This equivalently gives the Cartesian components of the acceleration

$$\dot{\hat{v}}_k = -\frac{1}{m}\partial_t \hat{\mathcal{A}}_k^{(q)} - \frac{\mathrm{i}m}{2\hbar}(\hat{v}_l[\hat{v}_k, \hat{v}_l] + [\hat{v}_k, \hat{v}_l]\hat{v}_l) - \frac{\mathrm{i}}{\hbar}[\hat{v}_k, \hat{V}_{\mathrm{tot}}^{(q)}], \tag{22}$$

where a summation over the repeated Cartesian indices is again implied. Expressing the velocity commutators $m^2[\hat{v}_k, \hat{v}_l] = \mathrm{i}\hbar\hat{\mathcal{F}}_{kl}$ in terms of the antisymmetric tensor

$$\hat{\mathcal{F}}_{kl} = \partial_k \hat{\mathcal{A}}_l^{(q)} - \partial_l \hat{\mathcal{A}}_k^{(q)} - \frac{\mathrm{i}}{\hbar}[\hat{\mathcal{A}}_k^{(q)}, \hat{\mathcal{A}}_l^{(q)}], \tag{23}$$

one arrives at the equation of motion

$$m\dot{\hat{v}} = \tfrac{1}{2}(\hat{v} \times \hat{\boldsymbol{\mathcal{B}}}^{(q)} - \hat{\boldsymbol{\mathcal{B}}}^{(q)} \times \hat{v}) + \hat{\boldsymbol{\mathcal{E}}}^{(q)}. \tag{24}$$

The vector operator

$$\hat{\boldsymbol{\mathcal{B}}}^{(q)} = \nabla \times \hat{\boldsymbol{\mathcal{A}}}^{(q)} - \frac{\mathrm{i}}{\hbar}\hat{\boldsymbol{\mathcal{A}}}^{(q)} \times \hat{\boldsymbol{\mathcal{A}}}^{(q)} \tag{25}$$

with components $\hat{\mathcal{B}}_j^{(q)} = \frac{1}{2}\epsilon_{jkl}\hat{\mathcal{F}}_{kl}$ is the artificial magnetic field (Berry curvature) providing the Lorentz force. Using equation (14) for $\boldsymbol{\mathcal{A}}_{nm}$ together with the completeness relation, the matrix elements of the curvature can be represented as a sum over the eliminated states

$$\boldsymbol{\mathcal{B}}_{nm} = -\frac{\mathrm{i}}{\hbar}\sum_{l=q+1}^{N} \boldsymbol{\mathcal{A}}_{nl} \times \boldsymbol{\mathcal{A}}_{lm}, \quad n, m = 1, \ldots, q. \tag{26}$$

Hence, the Berry curvature is non-zero only for the reduced atomic dynamics ($q < N$) when some of the atomic states are eliminated. The same applies to the geometric scalar potential W_{nm} given by equation (18).

Additionally the atom is affected by an effective electric field

$$\hat{\boldsymbol{\mathcal{E}}}^{(q)} = -\partial_t \hat{\boldsymbol{\mathcal{A}}}^{(q)} - \nabla \hat{V}_{\mathrm{tot}} + \frac{\mathrm{i}}{\hbar}[\hat{\boldsymbol{\mathcal{A}}}^{(q)}, \hat{V}_{\mathrm{tot}}^{(q)}] \tag{27}$$

that contains a commutator $[\hat{\boldsymbol{\mathcal{A}}}^{(q)}, \hat{V}_{\mathrm{tot}}^{(q)}]$ together with the usual gradient $\nabla\hat{V}_{\mathrm{tot}}^{(q)}$ and induced $\partial_t\hat{\boldsymbol{\mathcal{A}}}^{(q)}$ contributions.

When all the Cartesian components of $\hat{\boldsymbol{\mathcal{A}}}^{(q)}$ commute with each other, the vector potential is said to be Abelian (this is always the case when $q = 1$). Otherwise, when some components do not commute, $[\hat{\mathcal{A}}_j^{(q)}, \hat{\mathcal{A}}_l^{(q)}] \neq 0$ for some j and l, we will state that the system exhibits a non-Abelian gauge potential $\hat{\boldsymbol{\mathcal{A}}}^{(q)}$[5].

For Abelian vector potentials, we recover $\boldsymbol{\mathcal{B}}^{(q)} = \nabla \times \boldsymbol{\mathcal{A}}^{(q)}$ and $\boldsymbol{\mathcal{E}}^{(q)} = -\partial_t\boldsymbol{\mathcal{A}}^{(q)} - \nabla V_{\mathrm{tot}}^{(q)}$. An Abelian geometric vector potential $\hat{\boldsymbol{\mathcal{A}}}^{(q)}$ has already been engineered for ultracold atoms in the cases $q = 1$ [21–23] and $q = 2$ [25–32, 127]. For a single adiabatic state ($q = 1$) the spatial dependence of $\hat{\boldsymbol{\mathcal{A}}}^{(q)}$ yield an artificial magnetic field [21, 22] and its temporal dependence generate an effective electric field [23]. We shall return to the latter issue in the section 5.4.2 on experimentally creating the artificial electric field.

[5] We note that genuine non-Abelian properties are captured by the non-Abelian character of the field strength [42], $[\hat{\mathcal{F}}_{kl}(\boldsymbol{r}), \hat{\mathcal{F}}_{k'l'}(\boldsymbol{r}')] \neq 0$, or by the non-commutativity of successive loop operations, see e.g. [126]. However, in this review, a vector potential satisfying the criterion $[A_j, A_k] \neq 0$ will generally be referred to as a 'non-Abelian gauge potential'. This issue will be further addressed in section 8.2.3.

3.4. Geometric gauge potentials and rotation

Now we turn to an interplay between geometric gauge potentials and rotation, motivated by a possibility for simultaneously generating an Abelian vector potential (via rotation) and a light-induced non-Abelian geometric vector potential (equivalent to SOC). Here we outline a general framework for adding an Abelian gauge potential via rotation to a non-Abelian geometric gauge potential [128–134]. This scenario has several associated subtle issues: (1) In proper rotation experiments, the whole Hamiltonian should be static in the rotating frame. In this context, both the center of mass and coupling terms should be rotating, implying that the whole laser system should rotate. (2) Generally, techniques for creating artificial gauge fields involve Raman-resonant transitions, and in such cases the 'orientation' of Zeeman terms results from a relative phase (for the $\boldsymbol{e}_x$ and $\boldsymbol{e}_y$ components) and detuning from resonance (for the $\boldsymbol{e}_z$ component), not geometry. The following discussion focuses on the broad picture and will not treat these points.

Let us suppose that the system is described by the Hamiltonian (8), in which both the center of mass and internal contributions rotate with the frequency Ω_{rot} around $\boldsymbol{e}_z$. Both the state-independent and state-dependent potentials are assumed to be time-independent in the rotating frame of reference, so that in the lab frame the time dependence of $V(\boldsymbol{r}, t) = V(\boldsymbol{r}')$ and $\hat{M}(\boldsymbol{r}, t) = \hat{M}(\boldsymbol{r}')$ come exclusively from the rotating radius vector $\boldsymbol{r}' \equiv \boldsymbol{r}'(\boldsymbol{r}, t)$. This means the trapping potential as well as all the lasers producing the atom–light coupling $\hat{M}$ should rotate with the same frequency Ω_{rot} around the rotation vector $\boldsymbol{\Omega}_{\mathrm{rot}}$. Reference [130] includes a comparison with an experimentally more feasible situation where the center of mass degrees of freedom are set into rotation, but the lasers (and hence internal degrees of freedom) are not.

Note that realizing the rotating laser configuration is a challenging task, but this geometry can be realized by extending techniques for creating dynamical [135] and rotating [87] optical lattices. Figure 4 depicts the required experimental geometry. This setup uses a pair of scanning galvanometer-based mirrors that direct the Raman lasers to intersect at the depicted cloud of atoms with wave-vectors $\boldsymbol{k}_1$ and $\boldsymbol{k}_2$, with difference $\delta\boldsymbol{k} = \boldsymbol{k}_1 - \boldsymbol{k}_2$ that rotates sinusoidally in the $\boldsymbol{e}_x - \boldsymbol{e}_y$ plane.

Assuming that the internal degrees of freedom are characterized by the total angular momentum $\hat{\boldsymbol{F}}$, the transformation to the rotating frame of the original Hamiltonian $\hat{\tilde{H}}$ (equation (8)) is described by the unitary operator $\hat{R}_z^{\mathrm{full}}(t) \equiv \exp[-\mathrm{i}t\boldsymbol{\Omega}_{\mathrm{rot}} \cdot (\boldsymbol{L} + \hat{\boldsymbol{F}})/\hbar]$ involving the sum of the center of mass angular momentum $\boldsymbol{L} = \boldsymbol{r} \times \boldsymbol{p}$ and the internal angular momentum $\hat{\boldsymbol{F}}$. Transforming to the rotating frame the full atomic state-vector $|\tilde{\psi}\rangle = \hat{R}_z^{\mathrm{full}}(t)|\tilde{\psi}'\rangle$, one arrives at a TDSE for $|\tilde{\psi}'\rangle$ described by the Hamiltonian $\hat{\tilde{H}}'$. The latter is connected to the laboratory frame Hamiltonian $\hat{\tilde{H}}$ as $\hat{\tilde{H}}' = \hat{\tilde{H}} - \boldsymbol{\Omega}_{\mathrm{rot}} \cdot (\boldsymbol{L} + \hat{\mathbf{F}})$ and hence

$$\hat{\tilde{H}}' = \left[\frac{(\boldsymbol{p} - \boldsymbol{\mathcal{A}}_{\mathrm{rot}})^2}{2m} + V(\boldsymbol{r}) + W_{\mathrm{rot}}(\boldsymbol{r})\right]\hat{I} + \hat{M}(\boldsymbol{r}) - \boldsymbol{\Omega}_{\mathrm{rot}} \cdot \hat{\boldsymbol{F}}, \tag{28}$$

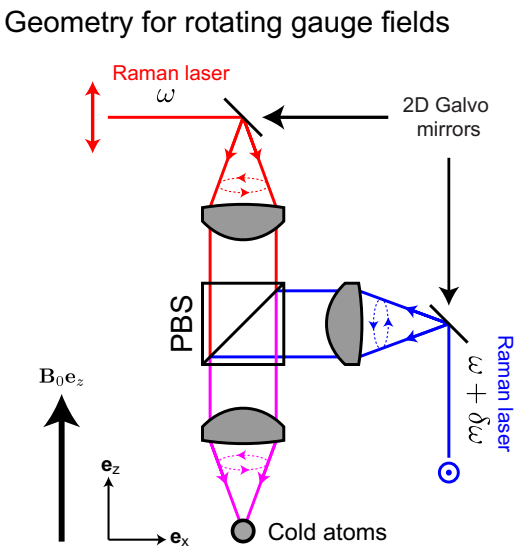

Figure 4. Laser geometry for creating rotating artificial gauge fields. 'NIST-style' artificial gauge fields [21, 22] and SOC [25] can be induced in the rotating frame using a pair of 2D galvanometer-based scanning mirrors ('galvo's') that steer the Raman beams on circular trajectories in an otherwise circularly symmetric confining potential. In this example the lasers are combined on a polarizing beam splitter (PBS), producing the polarizations required to drive Raman transitions. Because of the rotating orientation of the lasers' polarization vectors, there are in principle additional polarization present in this diagram, however, these lead only to changes in the overall scalar potential. This contribution can be tuned to zero by suitable choice of wavelength.

where the rotation vector potential $\boldsymbol{\mathcal{A}}_{\rm rot} = m\boldsymbol{\Omega}_{\rm rot} \times \boldsymbol{r}$ and the antitrapping (centrifugal) potential $W_{\rm rot} = -\mathcal{A}_{\rm rot}^2/2m$ are as in equation (3). The additional term $-\boldsymbol{\Omega}_{\rm rot} \cdot \hat{\boldsymbol{F}}$ is analogous to the Hamiltonian describing the atomic internal spin in a magnetic field proportional to the rotation vector $\boldsymbol{\Omega}_{\rm rot}$. This is not surprising, because the rotation manifests itself like the magnetic field not only for the center of mass motion, but also for the internal dynamics of the atom. Consequently the operator $-\boldsymbol{\Omega}_{\rm rot} \cdot \hat{\boldsymbol{F}}$ introduces a $\hbar\Omega_{\rm rot}$ shift of the atomic spin states. For typical rotation experiments, the shift $\hbar\Omega_{\rm rot} \lesssim h \times 100\,{\rm Hz}$ is small compared to the other frequencies characterizing the atomic internal dynamics.

The state-dependent operator $\hat{M}(\boldsymbol{r}) - \boldsymbol{\Omega}_{\rm rot} \cdot \hat{\boldsymbol{F}}$ featured in $\hat{\tilde{H}}'$ has a set of time-independent eigenstates $|\eta_m\rangle \equiv |\eta_m(\boldsymbol{r})\rangle$ with eigenenergies $\varepsilon_m \equiv \varepsilon_m(\boldsymbol{r})$. Subsequently, like in the section 3.1, the (rotating frame) atomic state-vector $|\tilde{\psi}'\rangle$ is transformed to $|\tilde{\psi}'\rangle = \hat{R}^\dagger|\psi'\rangle$ by means of the unitary transformation $\hat{R} \equiv \hat{R}(\boldsymbol{r}, t) = \sum_{m=1}^{N} |\eta_m(\boldsymbol{r})\rangle\langle m|$ converting the atomic bare states into the dressed ones. The transformed Hamiltonian $\hat{H}' = \hat{R}^\dagger \hat{\tilde{H}}'(\boldsymbol{r}, t)\hat{R} - {\rm i}\hbar\hat{R}^\dagger\partial_t\hat{R}$ has the same form as equation (13) with the geometric vector potential $\hat{\boldsymbol{\mathcal{A}}}$ replaced by $\hat{\boldsymbol{\mathcal{A}}} + \boldsymbol{\mathcal{A}}_{\rm rot}$ and the centrifugal potential $W_{\rm rot}$ added:

$$\hat{H}' = \frac{\left(\boldsymbol{p} - \boldsymbol{\mathcal{A}}_{\rm rot} - \hat{\boldsymbol{\mathcal{A}}}\right)^2}{2m} + V + W_{\rm rot} + \hat{\varepsilon}, \qquad (29)$$

where we put $\Phi = 0$ because the dressed states are time-independent in the rotating frame.

The adiabatic approximation outlined in section 3.2 gives the effective Hamiltonian for the atomic dynamics in the reduced internal space

$$\hat{H}'^{(q)} = \frac{\left(\boldsymbol{p} - \boldsymbol{\mathcal{A}}_{\rm rot} - \hat{\boldsymbol{\mathcal{A}}}^{(q)}\right)^2}{2m} + \hat{V}_{\rm tot}^{(q)},$$
$$\hat{V}_{\rm tot}^{(q)} = V + W_{\rm rot} + \hat{\varepsilon}^{(q)} + \hat{W}^{(q)}, \qquad (30)$$

where the geometric scalar potential $\hat{W}^{(q)}$ is as in equations (17)–(18). Thus, rotation adds an Abelian potential $\boldsymbol{\mathcal{A}}_{\rm rot}$ to the geometric vector potential $\hat{\boldsymbol{\mathcal{A}}}^{(q)}$, and also introduces the centrifugal potential $W_{\rm rot} = -\mathcal{A}_{\rm rot}^2/2m$.

4. Light–matter interaction

In this section, we study the basic interaction between laser-light and atoms, before explicitly analyzing light-induced gauge potentials. Specifically, we consider the far off-resonant coupling [136–139] between an alkali atom in its electronic ground state manifold and an oscillatory optical field, providing guidelines for designing realistic artificial gauge fields in alkali systems. The same basic line of reasoning is generally valid in other atomic systems, but the ground and excited states will of course differ, and specific conclusions may not cross over [140].

4.1. Light–matter coupling

We focus on the largest light–matter coupling term—the electric dipole (see [141], for example)—that links electronic motion to the optical electric field $\boldsymbol{E}(t)$ with vector components E_j ($j = 1, 2, 3$) and frequency ω

$$\hat{H}_{\rm dip} = \hat{\boldsymbol{d}} \cdot \boldsymbol{E}(t) = \hat{d}_j E_j \cos(\phi_j - \omega t), \qquad (31)$$

where the summation over repeated Cartesian indices is assumed. Here, $\hat{\boldsymbol{d}} = -e\sum_\alpha \hat{\boldsymbol{r}}_\alpha$ is the electric dipole operator, e is the electron's charge, and $\hat{\boldsymbol{r}}_\alpha$ is the position of the α'th electron within the atom. We will study the impact of this coupling term on the atomic ground state manifold to second order in perturbation theory, in a step-by-step manner including different effects in order of decreasing importance.

We analyze the lowest energy electric dipole transition in an alkali atom, between the ground (n)S electron orbital and the excited (n)P orbital with excitation energy E_e, as pictured in figure 5. The atom is then described by the Hamiltonian

$$\hat{H}_{\rm at} = E_e\hat{P}_e + \frac{A_{\rm FS}}{\hbar^2}\hat{\boldsymbol{L}} \cdot \hat{\boldsymbol{S}}, \qquad (32)$$

where $A_{\rm FS}$ is the fine-structure coupling constant; $\hat{P}_{g,e}$ are the projectors onto the space of ground or excited states; and $\hat{\boldsymbol{L}}$ and $\hat{\boldsymbol{S}}$ are the total electronic orbital angular momentum and the spin, respectively. (The electronic orbital momentum $\hat{\boldsymbol{L}}$ should not be confused with the orbital momentum of the atomic center of mass motion $\boldsymbol{L}$ appearing in the analysis of the rotating systems in the sections 2.1 and 3.4.)

The orbital angular momentum $\hat{\boldsymbol{L}}$ has eigenstates $\{|l = 0, m_L = 0\rangle,\ |l = 1, m_L = 0, \pm 1\rangle\}$, with eigenvalues $\hbar^2 l(l+1)$ and $\hbar m_L$ for $\hat{\boldsymbol{L}}^2$ and $\hat{L}_z$, respectively; the electron spin $\hat{\boldsymbol{S}}$ along the quantization axis $\boldsymbol{e}_z$ has the eigenstates

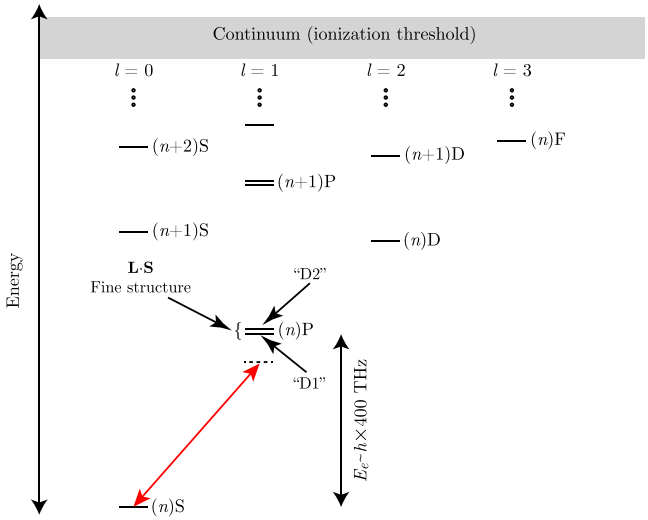

Figure 5. Typical alkali atom level structure. This figure illustrates the typical level structure of the alkali atoms with the primary nS to nP transition (with their typical $\approx h \times 400$ THz transition energies, and labeled by the archaic D1 and D2 designations for the two fine-structure resolved group of states) required for the discussed herein. This transition is driven by the far-detuned coupling laser indicated in red. Also pictured is the much smaller $\Delta_{\rm FS}$ fine-structure splitting (ranging from $\approx$10 GHz in ^{6}Li to $\approx$17 THz in ^{133}Cs) that enables state-dependent 'vector' light shift.

$\{|s = 1/2, m_S = \pm 1/2\rangle\}$. In a similar manner, the atomic nuclear spin $\hat{\boldsymbol{I}}$ provides the eigenstates $\{|i, m_I = -i, \cdots, i\rangle\}$. Because the electronic degree of freedom [(n) or $(n+1)$] is uniquely defined by the total electronic angular momentum quantum number, the operator $\hat{P}_g = \hat{1} - \hat{L}^2/2\hbar^2$ projects onto the space of ground electronic states [(n)S, with $l = 0$] and $\hat{P}_e = \hat{L}^2/2\hbar^2$ projects onto the set of electronic excited states [(n)P, with $l = 1$], as long as only these two sets of states are involved.

In the alkali atoms, there are three excited-state energy scales: the ground-excited splitting E_e, the fine structure splitting $\Delta_{\rm FS}$ (with eigenstates of the combined angular momentum $\hat{\boldsymbol{J}} = \hat{\boldsymbol{L}} + \hat{\boldsymbol{S}}$), and the typical scale of hyperfine splittings $\Delta_{\rm HFS}$ (with eigenstates of the total angular momentum $\hat{\boldsymbol{F}} = \hat{\boldsymbol{L}} + \hat{\boldsymbol{S}} + \hat{\boldsymbol{I}}$). In any given alkali atom, these are ordered $E_e \gg \Delta_{\rm FS} \gg \Delta_{\rm HFS}$. In an experiment, the detuning from the excited states is generally large compared to $\Delta_{\rm HFS}$. Consequently, to analyze the effect of far off-resonant light fields on ground state atoms, it suffices to include just the electronic excited level structure as corrected by the $\hat{\boldsymbol{L}} \cdot \hat{\boldsymbol{S}}$ fine-structure term. The hyperfine structure of the excited level enables further transitions, but these can only be resolved when the lasers are tuned so near to the atomic resonance that the rate of spontaneous emission prohibits any practical use for engineering artificial gauge fields, or quantum simulation in general.

4.2. Rotating wave approximation

We focus on optical fields not too far from resonance, $|E_e - \hbar\omega| \ll E_e$. In that case it is convenient to transform the atomic excited state vectors $|e\rangle$ into the rotating frame $|e'\rangle = \exp(i\omega t)|e\rangle$ via the unitary transformation

$$\hat{U}_{\rm rot}(t) = \exp(-i\omega t\,\hat{P}_e) \equiv \hat{P}_g + \hat{P}_e \exp(-i\omega t), \tag{33}$$

where the transformed state vector is $|\psi'\rangle = \hat{U}^\dagger_{\rm rot}(t)|\psi\rangle$, and the projection operators $\hat{P}_g$ and $\hat{P}_e$ are as defined above. In this temporally rotating frame, the dipole Hamiltonian (equation (31)) is

$$\hat{H}_{\rm dip'} = \hat{U}^\dagger_{\rm rot}(t)\hat{H}_{\rm dip}\hat{U}_{\rm rot}(t) \approx \frac{1}{2}\left[\tilde{E}^*_j \hat{P}_g \hat{d}_j \hat{P}_e + \tilde{E}_j \hat{P}_e \hat{d}_j \hat{P}_g\right], \tag{34}$$

where we introduced the complex electric field $\tilde{E}_j = E_j \exp(i\phi_j)$ and applied the rotating wave approximation (RWA) by removing the terms oscillating at the frequencies ω and 2ω in the second relation of equation (34). In the rotating frame and after the RWA, the full atomic and coupling Hamiltonian is

$$\hat{H}_{\rm full} = \hat{H}_{\rm at'} + \hat{H}_{\rm dip'}, \tag{35}$$

where the rotating frame atomic Hamiltonian $\hat{H}_{\rm at'} = \hat{H}_{\rm at} - \hbar\omega\hat{P}_e$ acquires an extra term $-\hbar\omega\hat{P}_e \equiv -i\hbar\hat{U}^\dagger_{\rm rot}(t)[\partial_t \hat{U}_{\rm rot}(t)]$ from the the unitary transformation's temporal dependence. Hence, the excited state energy E_e is supplanted by the detuning $\Delta_e = E_e - \hbar\omega$ in the transformed Hamiltonian

$$\hat{H}_{\rm at'} = \Delta_e \hat{P}_e + \frac{A_{\rm FS}}{\hbar^2}\hat{\boldsymbol{L}} \cdot \hat{\boldsymbol{S}} \equiv \Delta_e \hat{P}_e + \frac{A_{\rm FS}}{2\hbar^2}\left(\hat{J}^2 - \hat{L}^2 - \hat{S}^2\right). \tag{36}$$

4.3. Effective atomic ground-state Hamiltonian

4.3.1. General. Within the ground state manifold (adiabatically eliminating the excited states), the effect of the RWA electric dipole term $\hat{H}_{\rm dip'}$ is described to second-order by the effective atomic Hamiltonian

$$\hat{H}_{\rm eff} = -\hat{P}_g \hat{H}_{\rm dip'} \hat{H}^{-1}_{\rm at'} \hat{H}_{\rm dip'} \hat{P}_g, \tag{37}$$

which can be represented as

$$\hat{H}_{\rm eff} = -\tfrac{1}{4}\tilde{E}^*_i \hat{D}_{i,j} \tilde{E}_j. \tag{38}$$

Here we have introduced the rank-2 Cartesian tensor operator

$$\hat{D}_{i,j} = \hat{P}_g \hat{d}_i \hat{P}_e \hat{H}^{-1}_{\rm at'} \hat{P}_e \hat{d}_j \hat{P}_g \equiv \hat{P}_g \hat{d}_i \hat{H}^{-1}_{\rm at'} \hat{d}_j \hat{P}_g \tag{39}$$

acting on the ground state manifold. In the second relation of equation (39) we have omitted the excited state projectors $\hat{P}_e$, because the atomic ground states do not have a permanent electric dipole moment: $\hat{P}_g \hat{d}_j \hat{P}_g = 0$.

Operators of this form can be expressed as the sum

$$\hat{D}_{i,j} = \hat{D}^{(0)}_{i,j} + \hat{D}^{(1)}_{i,j} + \hat{D}^{(2)}_{i,j} \tag{40}$$

of irreducible tensor operators of rank-0 (transforms as a scalar under rotation)

$$\hat{D}^{(0)}_{i,j} = \tfrac{1}{3}\delta_{i,j}{\rm Tr}\hat{D} \equiv \tfrac{1}{3}\hat{D}_{l,l}\delta_{i,j}, \tag{41}$$

rank-1 (transforms as a vector under rotation)

$$\hat{D}^{(1)}_{i,j} = \tfrac{1}{2}\left(\hat{D}_{i,j} - \hat{D}_{j,i}\right) \equiv \tfrac{1}{2}\epsilon_{i,j,k}\epsilon_{i',j',k}\hat{D}_{i',j'}, \tag{42}$$

and rank-2

$$\hat{D}^{(2)}_{i,j} = \tfrac{1}{2}\left(\hat{D}_{i,j} + \hat{D}_{j,i}\right) - \tfrac{1}{3}\hat{D}^{(0)}_{i,j}, \tag{43}$$

where the summation over the repeated Cartesian indices is again implied. This separation allows one to classify the light–matter interaction in a powerful way.

4.3.2. No fine structure. Let us begin by considering the simple case when $A_{\rm FS} = 0$, implying that the excited states are degenerate, and allowing us to completely neglect electronic and nuclear spin. In this case, we replace the atomic Hamiltonian $\hat{H}_{\rm at'}$ with $\Delta_e \hat{P}_e$, and the tensor $\hat{D}_{i,j}$ in equation (39) takes the particularly simple form

$$\hat{D}_{i,j} = \Delta_e^{-1}\hat{P}_g \hat{d}_i \hat{d}_j \hat{P}_g. \tag{44}$$

In the present case, let us study how equation (44) transforms under rotations as effected by the unitary operator $\hat{R}(\boldsymbol{\theta}) = \exp(-\mathrm{i}\hat{\boldsymbol{L}}\cdot\boldsymbol{\theta}/\hbar)$. Because the ground S state has $l = 0$, it is clear that $\hat{L}_{x,y,z}\hat{P}_g = 0$, therefore

$$\hat{R}(\boldsymbol{\theta})\hat{D}_{i,j}\hat{R}^{\dagger}(\boldsymbol{\theta}) = \hat{D}_{i,j}. \tag{45}$$

Thus $\hat{D}_{i,j}$ transforms like a scalar under rotation and must be proportional to the unit tensor. Consequently only the zero-rank contribution $\hat{D}^{(0)}_{i,j}$ is non-zero

$$\hat{D}^{(0)}_{i,j} = \hat{P}_g \frac{\hat{d}_l \hat{d}_l}{3\Delta_e}\delta_{ij}\hat{P}_g = -4u_s\delta_{ij}\hat{P}_g, \tag{46}$$

where u_s is proportional to the atoms' ac polarizability (without including the fine-structure corrections)

$$u_s = -\frac{\left|\langle l=0|\,|\boldsymbol{d}||l'=1\rangle\right|^2}{12\,(E_e-\hbar\omega)}. \tag{47}$$

Here $|\,\langle l=0|\,|\boldsymbol{d}||l'=1\rangle|^2 \equiv \sum_{m'_L=0,\pm1}|\,\langle l=0, m_L=0|\,\boldsymbol{d}\times|l'=1, m'_L\rangle|^2 \approx 4e^2a_0^2$ is the commonly used reduced matrix element and a_0 is the Bohr radius (the reduced matrix element is a single number, even though the conventional notation makes it look like it should have three vector components).

Equations (38) and (46) yield the *scalar light shift*

$$\hat{H}^{(0)}_{\rm eff} = u_s|\tilde{\boldsymbol{E}}|^2\hat{P}_g, \tag{48}$$

Alternatively $\hat{H}^{(0)}_{\rm eff}$ can be expressed as

$$\hat{H}^{(0)}_{\rm eff} = -\frac{3\pi\hbar^3c^2I}{2E_e^3}\frac{\hbar\Gamma_{1\to0}}{\Delta_e}, \tag{49}$$

where we defined the intensity $I = \epsilon_0 c|\tilde{\boldsymbol{E}}|^2/2$, used the speed of light c, the transition's natural linewidth $\Gamma_{1\to0}$, the electric constant ϵ_0, and the expression

$$\hbar\Gamma_{l'\to l} = \frac{E_e^3}{3\pi\epsilon_0\hbar^3c^3}\frac{2l+1}{2l'+1}\left|\langle l|\,|\boldsymbol{d}||l'\rangle\right|^2 \tag{50}$$

for the linewidth [142]. This result is valid whenever it is safe to ignore the excited state fine structure; a good zero-order approximation when the $\Delta_e = E_e - \hbar\omega$ detuning from the optical transition is much larger than $\Delta_{\rm FS}$. This result reminds us of several important facts: the scalar light shift is a potential that is independent of optical polarization, scales like $1/\Delta_e$, and for red-detuned beams ($\Delta_e > 0$) is attractive.

4.3.3. Including fine structure. Let us now turn to the effects of the fine structure by recalling that the excited eigenstates $|j, m_J\rangle$ of the Hamiltonian $\hat{H}_{\rm at'}$ equation (36) corresponding to $l = 1$ are characterized by the quantum numbers j and m_J of the combined angular momentum $\hat{\boldsymbol{J}} = \hat{\boldsymbol{L}} + \hat{\boldsymbol{S}}$, with $j = 1/2$ and $j = 3/2$. Specifically we have $\hat{H}_{\rm at'}|j, m_J\rangle = \Delta_j|j, m_J\rangle$, where $\Delta_{1/2} = \Delta_e - A_{\rm FS}$ and $\Delta_{3/2} = \Delta_e + A_{\rm FS}/2$ are the detunings for the corresponding fine structure transitions.

Next we shall determine the tensor $\hat{D}_{i,j} = \hat{P}_g\hat{d}_i\hat{H}^{-1}_{\rm at'}\hat{d}_j\hat{P}_g$ describing the light-induced coupling between the atomic ground states, without explicitly involving the excited fine-structure states $|j, m_J\rangle$. For this we use equation (36) for $\hat{H}_{\rm at'}$ and write down a Dyson-type equation for the inverse atomic Hamiltonian $\hat{H}^{-1}_{\rm at'}$ projected onto the excited-state manifold,

$$\hat{H}^{-1}_{\rm at'} = \frac{1}{\Delta_e}\hat{P}_e - \frac{\alpha}{\Delta_e}\hat{\boldsymbol{L}}\cdot\hat{\boldsymbol{\sigma}}\hat{H}^{-1}_{\rm at'}, \tag{51}$$

with $\alpha = A_{\rm FS}/2\hbar\Delta_e$ and $\hat{\boldsymbol{S}} = \hbar\hat{\boldsymbol{\sigma}}/2$.

Calling on the commutation relations $[\hat{L}_i, \hat{d}_j] = \mathrm{i}\hbar\epsilon_{ijk}\hat{d}_k$ [82] together with $\hat{\boldsymbol{L}}\hat{P}_g = 0$, we replace $\hat{P}_g\hat{d}_i\hat{\boldsymbol{L}}\cdot\hat{\boldsymbol{\sigma}}$ with the commutator $-\hat{P}_g[\hat{\boldsymbol{L}}\cdot\hat{\boldsymbol{\sigma}}, \hat{d}_i] = \mathrm{i}\hbar\epsilon_{i\ell m}\hat{P}_g\hat{d}_m\hat{\sigma}_l$. Using the relation $\hat{P}_g\hat{d}_i\hat{d}_j\hat{P}_g = |\langle\|\boldsymbol{d}\|\rangle|^2\hat{P}_g\delta_{ij}/3$, equations (39) and (51) yield

$$\hat{D}_{ij} = \frac{|\langle\|\boldsymbol{d}\|\rangle|^2}{3\Delta_e}\delta_{ij}\hat{P}_g - \mathrm{i}\alpha\hbar\epsilon_{i\ell m}\hat{\sigma}_\ell\hat{D}_{mj}, \tag{52}$$

where the reduced matrix element $|\langle\|\boldsymbol{d}\|\rangle|^2 \equiv |\,\langle l=0||\boldsymbol{d}||\,l'=1\rangle|^2$ has already been featured in the previous subsection. As equation (52) contains operators that act only within the electronic ground state, we may now omit the projectors $\hat{P}_g$. Furthermore, since the only operators acting in the electronic ground state are the Pauli matrices, $\hat{D}_{ij}$ must take the form

$$\hat{D}_{ij} = D^{(0)}\delta_{ij} + \mathrm{i}D^{(1)}\epsilon_{ijk}\sigma_k, \tag{53}$$

where we also used the fact that $\hat{D}_{ij}$ can be decomposed into a scalar and vector component (no rank-2 component is possible with Pauli matrices alone).

Replacing the proposed solution (53), permuting one Levi–Civita symbol and exploiting the identity $\hat{\sigma}_i\hat{\sigma}_j = \delta_{ij} + \mathrm{i}\epsilon_{ijk}\sigma_k$, equation (52) gives

$$\left(D^{(0)} - 2\alpha\hbar D^{(1)}\right)\delta_{ij} + \mathrm{i}\epsilon_{ijk}\left(D^{(1)} - \alpha\hbar D^{(0)} - \alpha\hbar D^{(1)}\right)\hat{\sigma}_k = \frac{|\langle\|\boldsymbol{d}\|\rangle|^2}{3\Delta_e}\delta_{ij}.$$

The resulting pair of linear equations has solutions

$$D^{(0)} = \frac{1}{3}\left(\frac{2}{\hbar\alpha+1} - \frac{1}{2\hbar\alpha-1}\right)\frac{|\langle\|\boldsymbol{d}\|\rangle|^2}{3\Delta_e} \quad \text{and}$$

$$D^{(1)} = \frac{\alpha\hbar}{1-\hbar\alpha}D^{(0)}.$$

In the initial notation with $\hbar\alpha = A_{\rm FS}/2\Delta_e$ and $\Delta_e = E_e - \hbar\omega$, we associate the denominators appearing in the scalar coefficient $D^{(0)}$ with the detuning from the excited-state fine-structure split levels $E_{\rm D1} = E_e - A_{\rm FS}$ and $E_{\rm D2} = E_e + A_{\rm FS}/2$, giving

$$D^{(0)} = \frac{|\langle\|\boldsymbol{d}\|\rangle|^2}{9}\left(\frac{2}{E_{D2}-\hbar\omega} + \frac{1}{E_{D1}-\hbar\omega}\right).$$

Additionally introducing an average $\bar{E} = (2E_{D1} + E_{D2})/3$ and the fine-structure splitting $\Delta_{FS} = 3A_{FS}/2$, the complete tensor operator takes the form

$$\hat{D}_{ij} = D^{(0)}\left[\delta_{ij} + \mathrm{i}\epsilon_{ijk}\frac{2}{3\hbar}\frac{\Delta_{FS}}{\bar{E}-\hbar\omega}\hat{J}_k\right], \tag{54}$$

where we used $\hat{J}_i = \hat{S}_i$ as is suitable in the $l = 0$ electronic ground state. This leads to the light shift

$$\begin{aligned}\hat{H}_{\mathrm{eff}} &= -\frac{1}{4}\tilde{E}_i^*\hat{D}_{i,j}\tilde{E}_j \\ &= \left[u_s\left(\tilde{\boldsymbol{E}}^*\cdot\tilde{\boldsymbol{E}}\right) + \frac{\mathrm{i}u_v\left(\tilde{\boldsymbol{E}}^*\times\tilde{\boldsymbol{E}}\right)}{\hbar}\cdot\hat{\boldsymbol{J}}\right]\hat{P}_g\end{aligned} \tag{55}$$

in terms of the scalar and vector polarizabilities

$$\begin{aligned}u_s &= -\frac{|\langle\|\boldsymbol{d}\|\rangle|^2}{36}\left(\frac{2}{E_{D2}-\hbar\omega}+\frac{1}{E_{D1}-\hbar\omega}\right), \\ \text{and}\quad u_v &= \frac{2u_s\Delta_{FS}}{3\left(\bar{E}-\hbar\omega\right)}.\end{aligned} \tag{56}$$

When $E_{D2} = E_{D1}$, we recover our previous result, equations (47)–(48).

As an illustration, consider an atom illuminated with circularly σ^+ (along $\boldsymbol{e}_z$) polarized light, $\tilde{\boldsymbol{E}} = -|\tilde{\boldsymbol{E}}|^2(\boldsymbol{e}_x + \mathrm{i}\boldsymbol{e}_y)/\sqrt{2}$. For this field $\tilde{\boldsymbol{E}}^*\times\tilde{\boldsymbol{E}} = -\mathrm{i}|\tilde{\boldsymbol{E}}|^2\boldsymbol{e}_z$, so the vector light shift is described by the operator $\hat{J}_z$ acting on the ground state manifold. Consequently $\hat{H}^{(1)}_{\mathrm{eff}}$ provides opposite light shifts for the spin-up and spin-down atomic ground states.

4.3.4. Complete electronic ground state. In the presence of an external magnetic field, an alkali atom in its electronic ground state manifold is described by the Hamiltonian

$$\hat{H}_B = A_{\mathrm{hf}}\hat{\boldsymbol{I}}\cdot\hat{\boldsymbol{J}} + \frac{\mu_B}{\hbar}\boldsymbol{B}\cdot\left(g_J\hat{\boldsymbol{J}} + g_I\hat{\boldsymbol{I}}\right), \tag{57}$$

where μ_B is the Bohr magneton (henceforth the projector $\hat{P}_g$ is kept implicit in the ground state operators). The first term in equation (57) takes into account the coupling between the electron and nuclear spins of the atom, and is described by the magnetic dipole hyperfine coefficient A_{hf}. The second (Zeeman) term includes separate contributions from the electronic spin $\hat{\boldsymbol{J}} = \hat{\boldsymbol{L}} + \hat{\boldsymbol{S}}$ and the nuclear angular momentum $\hat{\boldsymbol{I}}$, along with their respective Landé factors g_J and g_I. For the alkali atoms $|g_I/g_J| \simeq 0.0005$, so we will safely neglect the nuclear contribution $\mu_B g_I \boldsymbol{B}\cdot\hat{\boldsymbol{I}}/\hbar$ to the Zeeman term.

The previous subsection showed that laser fields induce the scalar and vector light shifts featured in the effective ground-state Hamiltonian $\hat{H}_{\mathrm{eff}}$, equation (55). The two terms can be independently controlled by choosing the laser frequency ω and polarization. Evidently, the vector light shift is a contribution to the total Hamiltonian acting like an effective magnetic field [119, 136, 138, 143, 144]

$$\boldsymbol{B}_{\mathrm{eff}} = \frac{\mathrm{i}u_v(\tilde{\boldsymbol{E}}^*\times\tilde{\boldsymbol{E}})}{\mu_B g_J} \tag{58}$$

that affects $\hat{\boldsymbol{J}}$ but not the nuclear spin $\hat{\boldsymbol{I}}$. Thus the complete effective Hamiltonian for the ground state atoms affected by the magnetic field and light reads

$$\hat{H}_{B\&E} = u_s(\tilde{\boldsymbol{E}}^*\cdot\tilde{\boldsymbol{E}}) + \frac{\mu_B g_J}{\hbar}(\boldsymbol{B}+\boldsymbol{B}_{\mathrm{eff}})\cdot\hat{\boldsymbol{J}} + A_{\mathrm{hf}}\hat{\boldsymbol{I}}\cdot\hat{\boldsymbol{J}}, \tag{59}$$

where $\boldsymbol{B}_{\mathrm{eff}}$ acts as a true magnetic field and adds vectorially with $\boldsymbol{B}$. Instead of using the full Breit–Rabi equation [145, 146] for the Zeeman energies, we assume that the Zeeman shifts are small in comparison with the hyperfine splitting corresponding to the linear, or anomalous, Zeeman regime. In this case, the effective Hamiltonian for a single manifold of total angular momentum $\hat{\boldsymbol{F}} = \hat{\boldsymbol{J}} + \hat{\boldsymbol{I}}$ states is obtained by replacing $g_J\hat{\boldsymbol{J}} \to g_F\hat{\boldsymbol{F}}$ in the magnetic field interaction term [146], giving

$$\hat{H}^{(f)}_{B\&E} = u_s(\tilde{\boldsymbol{E}}^*\cdot\tilde{\boldsymbol{E}}) + \frac{\mu_B g_F}{\hbar}(\boldsymbol{B}+\boldsymbol{B}_{\mathrm{eff}})\cdot\hat{\mathbf{F}}, \tag{60}$$

where we have introduced the hyperfine Landé g-factor

$$g_F = g_J\frac{f(f+1)-i(i+1)+j(j+1)}{2f(f+1)}$$

and omitted the last term $A_{\mathrm{hf}}\hat{\boldsymbol{I}}\cdot\hat{\boldsymbol{J}} = A_{\mathrm{hf}}(\hat{\boldsymbol{F}}^2-\hat{\boldsymbol{J}}^2-\hat{\boldsymbol{I}}^2)/2$ which is constant for the single hyperfine manifold with fixed f. For example, in ^{87}Rb's for which $i = 3/2$ and $j = 1/2$ in the electronic ground state, the lowest energy hyperfine manifold with $f = 1$ corresponds to $g_F = -g_J/4 \approx -1/2$.

In this way, at second order of perturbation the light shift contains the term $u_s(\tilde{\boldsymbol{E}}^*\cdot\tilde{\boldsymbol{E}})$ described as a rank-0 (scalar) tensor operator resulting directly from the electric dipole transition, as well as the term $\mu_B g_F \boldsymbol{B}_{\mathrm{eff}}\cdot\hat{\boldsymbol{F}}/\hbar$ described by the rank-1 (vector) tensor operator emerging from adding excited state fine structure. Since the latter operator is linear with respect to the total momentum $\hat{\boldsymbol{F}}$, it can induce only transitions which change m_F by ± 1.

Adding effects due to the excited state hyperfine coupling leads to an additional rank-2 tensor contribution to the light-induced coupling within the atomic ground-state manifold. Because the scale of this term is set by the MHz to GHz scale excited-state hyperfine couplings, the smallness makes these light shifts unsuitable for most equilibrium-system applications in quantum gases.

4.4. Bichromatic light field

4.4.1. General analysis. We now turn to a situation frequently encountered in the current experiments on artificial gauge potentials [21–23] where an ensemble of ultracold atoms is subjected to a magnetic field $\boldsymbol{B} = B_0\boldsymbol{e}_z$ and is simultaneously illuminated by possibly several laser beams with two frequencies ω and $\omega + \delta\omega$. The frequency separation $\delta\omega = g_F\mu_B B_0/\hbar + \delta$ differs by a small detuning δ (with $|\delta/\delta\omega| \ll 1$) from the linear Zeeman shift between m_F states. The effective magnetic field induced by the complex electric field $\boldsymbol{E} = \boldsymbol{E}_{\omega_-}\exp(-\mathrm{i}\omega t) + \boldsymbol{E}_{\omega_+}\exp[-\mathrm{i}(\omega+\delta\omega)t]$ can be cast into its frequency components using equation (58)

$$\boldsymbol{B}_{\mathrm{eff}} = \boldsymbol{B}_{\mathrm{eff}\,0} + \boldsymbol{B}_{\mathrm{eff}\,-}\mathrm{e}^{-\mathrm{i}\delta\omega t} + \boldsymbol{B}_{\mathrm{eff}\,+}\mathrm{e}^{\mathrm{i}\delta\omega t}, \tag{61}$$

where

$$\boldsymbol{B}_{\mathrm{eff}\,0} = \frac{\mathrm{i}u_v}{\mu_{\mathrm{B}} g_J}\left(\boldsymbol{E}^*_{\omega_-}\times\boldsymbol{E}_{\omega_-} + \boldsymbol{E}^*_{\omega_+}\times\boldsymbol{E}_{\omega_+}\right),$$
$$\boldsymbol{B}_{\mathrm{eff}\,\mp} = \frac{\mathrm{i}u_v}{\mu_{\mathrm{B}} g_J}\boldsymbol{E}^*_{\omega_\mp}\times\boldsymbol{E}_{\omega_\pm} \qquad (62)$$

are the corresponding amplitudes. The first term $\boldsymbol{B}_{\mathrm{eff}\,0}$ adds to the static bias field $B_0\boldsymbol{e}_z$, and the remaining time-dependent terms $\boldsymbol{B}_{\mathrm{eff}\,\pm}\mathrm{e}^{\pm\mathrm{i}\delta\omega t}$ can drive transitions between different m_F levels.

The real magnetic field is assumed to be much greater than the effective one $B_0 \gg |\boldsymbol{B}_{\mathrm{eff}}|$, and the frequency difference $\delta\omega$ is taken to be large compared to the kinetic energy scales. In this case, the time-dependence of the Hamiltonian $\hat{H}^{(f)}_{B\&E}$ in equation (60) can be eliminated via the unitary transformation $\hat{S} = \exp(-\mathrm{i}\delta\omega t\,\hat{F}_z)$ and the subsequent application of the RWA by removing the terms oscillating at the frequencies $\delta\omega$ and $2\delta\omega$ in the transformed Hamiltonian $\hat{S}^\dagger\hat{H}^{(f)}_{B\&E}\hat{S} - \mathrm{i}\hbar S^\dagger\partial_t S$. The transformation does not alter $\hat{F}_z$, whereas the raising and lowering operators $\hat{F}_\pm = \hat{F}_x \pm \mathrm{i}\hat{F}_y$ change to $\hat{F}_\pm\exp(\pm\mathrm{i}\delta\omega t)$.

The resulting Hamiltonian can be represented as

$$\hat{H}_{\mathrm{RWA}} = V(\boldsymbol{r})\hat{1} + \hat{M}(\boldsymbol{r}). \qquad (63)$$

The state-independent (scalar) potential is given by

$$V(\boldsymbol{r}) = u_s\left(\boldsymbol{E}^*_{\omega_-}\cdot\boldsymbol{E}_{\omega_-} + \boldsymbol{E}^*_{\omega_+}\cdot\boldsymbol{E}_{\omega_+}\right) \qquad (64)$$

and

$$\hat{M}(\boldsymbol{r}) = \boldsymbol{\Omega}\cdot\hat{\boldsymbol{F}} = \Omega_z\hat{F}_z + \Omega_-\hat{F}_+ + \Omega_+\hat{F}_-, \qquad (65)$$

where

$$\Omega_z = \delta + \frac{\mu_{\mathrm{B}} g_F}{\hbar}\boldsymbol{B}_{\mathrm{eff}\,0}\cdot\boldsymbol{e}_z \qquad (66)$$

and

$$\Omega_\pm \equiv \frac{\Omega_x \pm \mathrm{i}\Omega_y}{2} = \frac{\mu_{\mathrm{B}} g_F}{2\hbar}\left[\boldsymbol{B}_{\mathrm{eff}\,\pm}\cdot\left(\boldsymbol{e}_x \pm \mathrm{i}\boldsymbol{e}_y\right)\right] \qquad (67)$$

are the circular components of the RWA effective Zeeman magnetic field $\boldsymbol{\Omega}$. The latter Zeeman field is explicitly

$$\boldsymbol{\Omega} = \left[\delta + \mathrm{i}\frac{u_v g_F}{\hbar g_J}\left(\boldsymbol{E}^*_{\omega_-}\times\boldsymbol{E}_{\omega_-} + \boldsymbol{E}^*_{\omega_+}\times\boldsymbol{E}_{\omega_+}\right)\cdot\boldsymbol{e}_z\right]\boldsymbol{e}_z$$
$$- \frac{u_v g_F}{\hbar g_J}\mathrm{Im}\left[\left(\boldsymbol{E}^*_{\omega_-}\times\boldsymbol{E}_{\omega_+}\right)\cdot\left(\boldsymbol{e}_x - \mathrm{i}\boldsymbol{e}_y\right)\right]\boldsymbol{e}_x \qquad (68)$$
$$- \frac{u_v g_F}{\hbar g_J}\mathrm{Re}\left[\left(\boldsymbol{E}^*_{\omega_-}\times\boldsymbol{E}_{\omega_+}\right)\cdot\left(\boldsymbol{e}_x - \mathrm{i}\boldsymbol{e}_y\right)\right]\boldsymbol{e}_y.$$

The form of the effective coupling operator $\hat{M}(\boldsymbol{r})$ shows that, while it is related to the initial vector light shifts, the RWA effective Zeeman magnetic field $\boldsymbol{\Omega}$ is composed of both static and resonant couplings in a way that goes beyond the restrictive $\boldsymbol{B}_{\mathrm{eff}} \propto \mathrm{i}\boldsymbol{E}^*\times\boldsymbol{E}$ form.

In this way, the operator $\hat{F}_z$ featured in the vector coupling $\hat{M}(\boldsymbol{r})$, equation (65), induces the opposites light shifts for the spin-up and spin-down atomic ground states, whereas the operators $\hat{F}_\pm$ describe the Raman transitions which change m_F by ±1. If the detuning from atomic resonance Δ_e is large compared to the excited state fine structure splitting Δ_{FS}, the magnitude of this vector coupling proportional to u_v drops off as $\Delta_{\mathrm{FS}}/\Delta_e^2$, not like the scalar shift $V(\boldsymbol{r})$ which drops off as $1/\Delta_e$. Since the amount of the off-resonant light scattering is also proportional to $1/\Delta_e^2$, the balance between the off-resonant scattering and the vector coupling is bounded, and cannot be improved by large detuning. While this is a modest problem for rubidium (15 nm fine structure splitting), it turns to be a serious obstacle for atoms with smaller fine structure splitting such as potassium (≈4 nm) and lithium (≈0.02 nm).

4.4.2. Two Raman beams. Within this formalism, let us consider a straightforward example of two counter propagating Raman beams depicted in figure 6. Such a setup is often used in current experiments on synthetic gauge fields [21, 62, 147] and SOC [26, 32] for ultracold atoms. In this case

$$\boldsymbol{E}_{\omega_-} = E\mathrm{e}^{\mathrm{i}k_R x}\boldsymbol{e}_y \quad\text{and}\quad \boldsymbol{E}_{\omega_+} = E\mathrm{e}^{-\mathrm{i}k_R x}\boldsymbol{e}_z \qquad (69)$$

describe the electric field of two lasers counterpropagating along $\boldsymbol{e}_x$ with equal intensities, crossed linear polarization and wave-number $k_R = 2\pi/\lambda$, giving $\boldsymbol{B}_{\mathrm{eff}\,0} = 0$ and $\boldsymbol{B}_{\mathrm{eff}\,\pm} = \mp\frac{\mathrm{i}u_v E^2}{\mu_{\mathrm{B}} g_J}\mathrm{e}^{\pm\mathrm{i}2k_R x}\boldsymbol{e}_x$. Consequently $\Omega_z = \delta$ and

$$2\Omega_\pm = \Omega_x \pm \mathrm{i}\Omega_y = \Omega_R\mathrm{e}^{\pm\mathrm{i}(2k_R x - \pi/2)}, \qquad (70)$$

where $\Omega_R = (g_F/g_J)u_v E^2/\hbar$ is the Rabi frequency of the Raman coupling. The resulting effective Zeeman field $\boldsymbol{\Omega}$ entering the vector light shift is

$$\boldsymbol{\Omega} = \delta\boldsymbol{e}_z + \Omega_R\left[\sin(2k_R x)\,\boldsymbol{e}_x - \cos(2k_R x)\,\boldsymbol{e}_y\right]. \qquad (71)$$

Together, $V(\boldsymbol{r}) = 2u_s E^2$ and $\boldsymbol{\Omega}(\boldsymbol{r})$ describe a constant scalar light shift along with a spatially rotating Zeeman field.

It is evident from equations (58) and (67) that for this spatially rotating Zeeman field to be non-zero, the effective Zeeman field $\boldsymbol{B}_{\mathrm{eff}}$ must not be parallel to the quantizing axis defined by the applied magnetic field $\boldsymbol{B} = B_0\boldsymbol{e}_z$. In the present case, this implies that the counter propagating beams cannot be aligned along $\boldsymbol{e}_z$. Physically, any projection of $\boldsymbol{B}_{\mathrm{eff}}$ along $\boldsymbol{e}_z$ yields a spin-dependent optical lattice [138, 139, 148] rather than a spatially rotating Zeeman field. But since the Raman beams have different frequencies, the spin-dependent lattice is moving fast and vanishes after performing the RWA.

Note also that in order to produce the vector light shifts like the one given by equation (71), there is no need for the two Raman beams to counter-propagate. When the beams intersect with opening angle α, the momentum exchange is changed from $2k_R$ to $2k_L = 2k_R\cos[(\pi-\alpha)/2]$. Since this altered wave-vector simply changes the energy and length scales of the problem, we shall concentrate on the counter propagating setup, equations (69). To obtain an exact correspondence with the notations used in most of the experimental papers on the artificial gauge fields [21–23, 62, 147, 149] and the SOC [25–28, 32], one needs to interchange the $\boldsymbol{e}_z$ and $\boldsymbol{e}_y$ axes in our analysis.

It is instructive to note that the z component of the effective Zeeman field $\boldsymbol{\Omega}$, equation (71), does not depend on the intensity of the Raman beams. The situation is not universal. For example, consider a pair of Raman laser beams with complex electric fields

$$\boldsymbol{E}_{\omega_-} = E_-\mathrm{e}^{\mathrm{i}k_R z}\left(\boldsymbol{e}_x - \mathrm{i}\boldsymbol{e}_y\right)/\sqrt{2}, \quad\text{and}\quad \boldsymbol{E}_{\omega_+} = E_+\mathrm{e}^{\mathrm{i}k_R x}\boldsymbol{e}_z, \qquad (72)$$

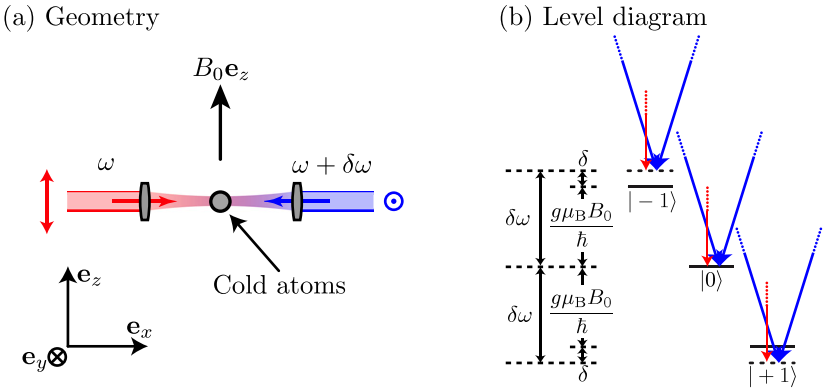

Figure 6. Typical two beam experimental geometry. (*a*) Laser geometry for creating Abelian artificial gauge fields showing two counter propagating linearly polarized beams in the e_x-e_y plane with frequency ω and $\omega + \Delta$. (*b*) Physical level diagram for three-level total angular momentum $f = 1$ case, as is applicable for the common alkali atoms ^{7}Li, ^{23}Na, ^{39}K, ^{41}K, and ^{87}Rb (all of which have $g_F = -g_J/4 \approx -1/2$). The generally small quadratic Zeeman effect that makes the $|-1\rangle$-$|0\rangle$ energy difference different from the $|0\rangle$-$|+1\rangle$ splitting is not included in this diagram.

intersecting with angle $\alpha = \pi/2$, and where the ω_- beam is circularly polarized [52]. In this case $\boldsymbol{E}^*_{\omega_-} \times \boldsymbol{E}_{\omega_-} = -\mathrm{i}|E_-|^2 \boldsymbol{e}_z$, $\boldsymbol{E}^*_{\omega_+} \times \boldsymbol{E}_{\omega_+} = 0$, and $\boldsymbol{E}^*_{\omega_-} \times \boldsymbol{E}_{\omega_+} = \mathrm{i}E^*_- E_+ (\boldsymbol{e}_x + \mathrm{i}\boldsymbol{e}_y)/\sqrt{2}$ giving

$$\hbar\Omega_z = \hbar\delta + \left(u_v \frac{g_F}{g_J}\right)|E_-|^2\,,$$

$$\hbar\Omega_\pm = -\left(u_v \frac{g_F}{g_J}\right)\frac{E_- E_+}{\sqrt{2}} \mathrm{e}^{\pm \mathrm{i}k_R(z-x)}, \tag{73}$$

so Ω_z becomes intensity-dependent, providing an extra control of the light-induced gauge potential.

Finally, more sophisticated spatial dependence of the Zeeman field $\boldsymbol{\Omega}$ can be created using additional Raman beams with specially chosen polarizations, for example leading to optical flux lattices [144, 150], to be considered in the section 5.2.3.

5. Schemes for creating Abelian gauge potentials

In this section, we describe how the atom–light coupling can be exploited to generate Abelian gauge potentials in cold-atom systems. We present useful schemes based on the adiabatic motion of atomic dressed states, and we eventually describe the specific experimental setup used at NIST to generate synthetic gauge fields.

5.1. The Λ setup

Let us begin our analysis of Abelian gauge potentials with the illustrative case of atoms characterized by the Λ type level structure, where the laser beams couple two atomic internal states $|1\rangle$ and $|2\rangle$ with a third one $|0\rangle$, see figures 7. The atom–light coupling operator $\hat{M}$ featured in the full atomic Hamiltonian (8) has then the following form:

$$\hat{M}(\boldsymbol{r}) = \hbar\delta\,(|2\rangle\langle 2| - |1\rangle\langle 1|) + \hbar\Delta|2\rangle\langle 2| + \hbar(\Omega_1|0\rangle\langle 1| + \Omega_2|0\rangle\langle 2| + \mathrm{H.c.})/2, \tag{74}$$

where the frequencies δ and Δ characterize the detuning between the atomic states. The Rabi frequencies $\Omega_1 \equiv \Omega_1(\boldsymbol{r})$ and $\Omega_2 \equiv \Omega_2(\boldsymbol{r})$ are generally complex and position-dependent.

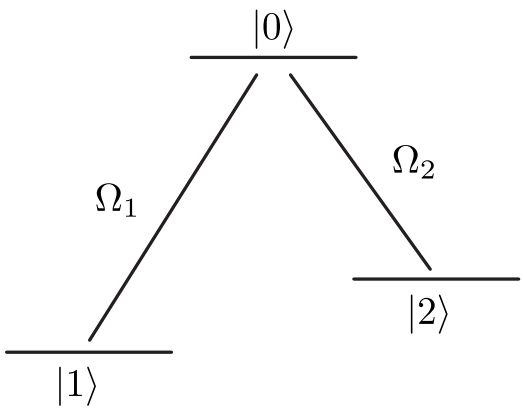

Figure 7. The Λ scheme of the atom–light coupling in which the laser beams induce atomic transitions $|1\rangle \to |0\rangle$ and $|2\rangle \to |0\rangle$ characterized by the Rabi frequencies Ω_1 and Ω_2.

In the context of the light-induced gauge potential for ultracold atoms, the Λ scheme was first explored in the late 90's [46, 47, 53]. Subsequently it was shown that the scheme can yield a non-zero artificial magnetic field (inducing the Lorentz force for electrically neutral atoms) using non-trivial arrangements of laser fields [48–50, 52, 120, 123, 151–154] or position-dependent detuning [22, 51]. In most of these treatments the state $|0\rangle$ is assumed to be the atomic excited state coupled resonantly to the ground states $|1\rangle$ and $|2\rangle$ by laser beams, as shown in figure 7. The involvement of the excited states is inevitably associated with a substantial dissipation due to the spontaneous emission.

To avoid such losses, one can choose $|0\rangle$ to be an atomic ground state coupled to the other two ground states $|1\rangle$ and $|2\rangle$ via the Raman transitions [51, 154]. In that case Ω_1 and Ω_2 featured in the coupling operator (74) represent the Raman Rabi frequencies. This forms a Ladder scheme which is equivalent to the Λ scheme. In particular, if $\Omega_1 = \Omega_2^* = \Omega_+\sqrt{2}$ and $\Delta = 0$, the Hamiltonian (74) reduces to the Hamiltonian given by equation (65) for an atom in the $F = 1$ ground state manifold affected by the RWA effective Zeeman field $\boldsymbol{\Omega} = (\mathrm{Re}\Omega_+, \mathrm{Im}\Omega_+, \delta)$. The latter $\boldsymbol{\Omega}$ is induced by the

Raman transitions and the real magnetic field. In this case the states $|1\rangle$, $|0\rangle$ and $|2\rangle$ corresponds to the magnetic sublevels with $m = -1$, $m = 0$ and $m = 1$, respectively. In the next subsection we shall analyze in detail the gauge potentials resulting from such a coupling between the magnetic sublevels.

If $\Omega_1 \neq \Omega_2^*$ the atom–light coupling operator (74) can no longer be represented as a Hamiltonian for the atomic spin (or quasispin) interacting with the effective magnetic field. Assuming exact resonance between the atomic levels 1 and 2 ($\delta = 0$), the interaction operator $\hat{M}(\boldsymbol{r})$ given by equation (74) has a single dressed eigenstate $|D\rangle$ known as the dark or uncoupled state:

$$|D\rangle = \frac{|1\rangle - \zeta|2\rangle}{1+\zeta^2}, \quad \zeta = \frac{\Omega_1}{\Omega_2} = |\zeta|\,\mathrm{e}^{\mathrm{i}S}, \tag{75}$$

where S is a relative phase between the two Rabi frequencies. The state $|D\rangle$ contains no contribution from the excited state $|0\rangle$ and is characterized by a zero eigenvalue $\varepsilon_D = 0$. Dark states are frequently encountered in quantum optics. They play an important role in applications such as the electromagnetically induced transparency (EIT) [155–158] and the stimulated Raman adiabatic passage (STIRAP) [159–161], relying on the fact that the excited level $|0\rangle$ is not populated for the dark state atoms and spontaneous decay is therefore suppressed.

As we have seen in section 3.1, if the atom is in a selected internal dressed state well separated from the remaining dressed states, an Abelian geometric vector potential emerges for the center of mass motion. For atoms in the internal dark state the adiabatic motion takes place if the total Rabi frequency $\sqrt{|\Omega_1|^2 + |\Omega_2|^2}$ exceeds the characteristic kinetic energy of the atomic motion. The corresponding vector potential $\boldsymbol{\mathcal{A}} = \mathrm{i}\hbar\langle D|\nabla|D\rangle$ and the associated magnetic field $\boldsymbol{\mathcal{B}} = \boldsymbol{\nabla}\times\boldsymbol{\mathcal{A}}$ are

$$\boldsymbol{\mathcal{A}} = -\hbar\frac{|\zeta|^2}{1+|\zeta|^2}\nabla S, \tag{76}$$

$$\boldsymbol{\mathcal{B}} = \hbar\frac{\nabla S\times\nabla|\zeta|^2}{(1+|\zeta|^2)^2}. \tag{77}$$

The geometric scalar potential for the dark state atoms is given by

$$W = \frac{\hbar^2}{2m}\frac{(\nabla|\zeta|)^2 + |\zeta|^2(\nabla S)^2}{(1+|\zeta|^2)^2}. \tag{78}$$

One easily recognizes that the vector gauge potential yields a non-vanishing artificial magnetic $\boldsymbol{\mathcal{B}}$ only if the gradients of the relative intensity and the relative phase are both non-zero and not parallel to each other. Therefore the synthetic magnetic field cannot be created for the dark state atoms of the Λ scheme using the plane-waves driving the transitions $|1\rangle \to |0\rangle$ and $|2\rangle \to |0\rangle$ [46, 47]. However, plane waves can indeed be used in more complex tripod [55, 162–167] or closed loop [168, 169] setups to generate non-Abelian gauge fields for a pair of degenerate internal dressed states, as we shall see in the section 6.

Equation (77) has a very intuitive interpretation [49]. The vector $\nabla[|\zeta|^2/(1+|\zeta|^2)]$ connects the 'center of mass' of the two light beams and ∇S is proportional to the vector of the relative momentum of the two light beams. Thus a nonvanishing $\boldsymbol{\mathcal{B}}$ requires a *relative orbital angular momentum* of the two light beams. This is the case for light beams carrying optical vortices [48, 120, 151–153] or if one uses two counterpropagating light beams of finite diameter with an axis offset [49, 123], as depicted in figure 8. A more detailed analysis of these schemes is available in the cited references and the previous reviews [80, 170].

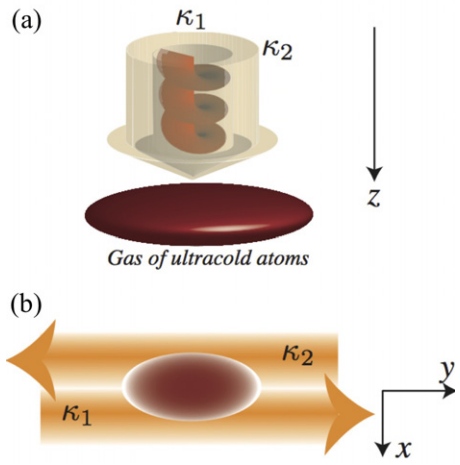

Figure 8. (*a*) The light beams carrying optical vortices [48, 120, 151–154] or (*b*) the counterpropagating beams with spatially shifted profiles [49, 50, 123, 171] provide a non-zero artificial magnetic field for the atoms in the laser-dressed states of the Λ scheme shown in figure 7.

5.2. Spins in effective Zeeman fields

5.2.1. General treatment. Let us now turn to a situation where the atom–light Hamiltonian can be represented as an interaction of a spin $\hat{\boldsymbol{F}}$ with an effective Zeeman field

$$\hat{M}(\boldsymbol{r}) = \boldsymbol{\Omega}\cdot\hat{\boldsymbol{F}} = \Omega\left(\cos\theta\,\hat{F}_z + \sin\theta\cos\phi\,\hat{F}_x + 2\sin\theta\sin\phi\,\hat{F}_y\right) \tag{79}$$

where we have parametrized the Zeeman vector $\boldsymbol{\Omega} = (\Omega_x, \Omega_y, \Omega_z)$ in terms of the spherical angles θ and ϕ shown in figure 9.

$$\tan\phi = \frac{\Omega_y}{\Omega_x} \quad \text{and} \quad \cos\theta = \frac{\Omega_z}{\Omega} \tag{80}$$

where Ω is the length of the Zeeman vector. Such a coupling can be produced using bichromatic laser beams considered in the previous section, leading to equation (65) which has the same form as equation (79). For the spin 1 case, the Hamiltonian (79) corresponds to the Λ (ladder) scheme described by the Hamiltonian (74) as long as $\Omega_1 = \Omega_2^*$ and $\Delta = 0$. Note that the operator $\hat{\boldsymbol{F}}$ does not necessarily represent the true atomic spin operator; it can be other atomic vector operators with Cartesian components obeying the angular momentum algebra (figure 9).

The coupling Hamiltonian $\hat{M}$ can be diagonalized via a unitary transformation

$$\hat{R} = \mathrm{e}^{-\mathrm{i}\hat{F}_z\phi/\hbar}\mathrm{e}^{-\mathrm{i}\hat{F}_y\theta/\hbar}\mathrm{e}^{\mathrm{i}\hat{F}_z\phi/\hbar}. \tag{81}$$

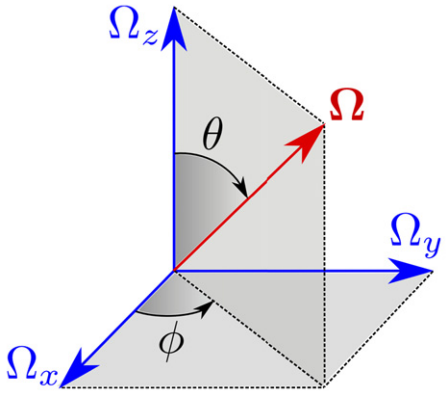

Figure 9. Representation of the coupling vector $\boldsymbol{\Omega} = (\Omega_x, \Omega_y, \Omega_z)$ in terms of the spherical angles θ and ϕ .

The first operator $\mathrm{e}^{-\mathrm{i}\hat{F}_z\phi/\hbar}$ rotates the spin around the z-axes by the angle ϕ eliminating the phase ϕ in $\hat{M}(\boldsymbol{r})$, equation (79). The subsequent transformation using the second operator $\mathrm{e}^{-\mathrm{i}\hat{F}_y\theta/\hbar}$ rotates the spin around the y-axes by the angle θ making the operator $\hat{M}(\boldsymbol{r})$ proportional to $\hat{F}_z$. Although the third operator $e^{i\hat{F}_z\phi/\hbar}$ no longer affects the transformed operator $\hat{M}(\boldsymbol{r})$, its inclusion ensures that the whole transformation $\hat{R}$ reduces to the unit operator for zero polar angle $\theta = 0$ and arbitrary azimuthal angle ϕ. Thus one has

$$\hat{R}^\dagger \hat{M}\, \hat{R} = \Omega \hat{F}_z. \tag{82}$$

The transformed Hamiltonian $\Omega\hat{F}_z$ has eigenstates $|f, m\rangle \equiv |m\rangle$ characterized by the total angular momentum f and its $\boldsymbol{e}_z$ projection m. In the following, we use both notations m and m_F to denote the projection of the total angular momentum. Therefore the eigenstates $|m, \boldsymbol{\Omega}\rangle \equiv |m, \theta, \phi\rangle$ of the original atom–light Hamiltonian $\hat{M}$ read

$$|m, \boldsymbol{\Omega}\rangle = \hat{R}\,|m\rangle = \mathrm{e}^{\mathrm{i}\left(m-\hat{F}_z/\hbar\right)\phi}\mathrm{e}^{-\mathrm{i}\hat{F}_y\theta/\hbar}\,|m\rangle\,, \tag{83}$$

the corresponding eigenenergies being

$$\varepsilon_m = \hbar m\Omega, \qquad m = -f, \ldots, f, \tag{84}$$

where both the eigenenergies $\varepsilon_m(\boldsymbol{r})$ and also the local eigenstates $|m, \boldsymbol{\Omega}(\boldsymbol{r})\rangle$ are position-dependent through the position dependence of the effective Zeeman vector $\boldsymbol{\Omega}(\boldsymbol{r})$. It is to be noted that similar kinds of eigenstates give rise to artificial gauge potentials describing the rotation of diatomic molecules [112, 172] and the physics of atomic collisions [113, 173].

If an atom is prepared in a dressed state $|m, \boldsymbol{\Omega}\rangle$ and if its characteristic kinetic energy is small compared to the energy difference between adjacent spin states $\Delta E = \hbar\Omega$, the internal state of the atom will adiabatically follow the dressed state $|m, \boldsymbol{\Omega}\rangle$ as the atom moves, and contributions due to other states with $m'_F \neq m_F$ can be neglected. Projecting the atomic dynamics onto the selected internal eigenstate $|m_F, \boldsymbol{\Omega}\rangle$ yields a reduced Schrödinger equation for the atomic center of mass motion affected by the geometric vector potential $\boldsymbol{\mathcal{A}} \equiv \boldsymbol{\mathcal{A}}_m(\boldsymbol{r}) = \mathrm{i}\hbar\,\langle m, \boldsymbol{\Omega}|\,\boldsymbol{\nabla}|m, \boldsymbol{\Omega}\rangle$ and the scalar potential $W \equiv W_n(\boldsymbol{r})$ which are generally defined by equation (19). In the current situation these potentials explicitly read [144]

$$\boldsymbol{\mathcal{A}}(\boldsymbol{r}) = \hbar m\,(\cos\theta - 1)\,\boldsymbol{\nabla}\phi \tag{85}$$

and

$$W_m(\boldsymbol{r}) = \frac{\hbar^2}{4m}\left[f(f+1) - m^2\right]\left[\sin^2\theta\,(\nabla\phi)^2 + (\nabla\theta)^2\right]. \tag{86}$$

The geometric vector potential $\boldsymbol{\mathcal{A}}(\boldsymbol{r})$ yields the artificial magnetic field

$$\boldsymbol{\mathcal{B}}(\boldsymbol{r}) = \boldsymbol{\nabla}\times\boldsymbol{\mathcal{A}}(\boldsymbol{r}) = \hbar m_F\,\boldsymbol{\nabla}\,(\cos\theta)\times\boldsymbol{\nabla}\phi, \tag{87}$$

which is non-zero if $\boldsymbol{\nabla}\phi$ and $\boldsymbol{\nabla}(\cos\theta)$ are not parallel to each other. Both $\boldsymbol{\mathcal{A}}(\boldsymbol{r})$ and $\boldsymbol{\mathcal{B}}(\boldsymbol{r})$ have the largest magnitude for maximum absolute values of the spin projection m and are zero for $m = 0$. On the other hand, the geometric scalar potential $W(\boldsymbol{r})$ is maximum for $m = 0$ and reduces with increasing $|m|$.

The atomic motion is affected by three distinct scalar potentials: (a) the state-independent potential $V(\boldsymbol{r})$ representing the 'scalar light shift' given by equation (64) for bichromatic fields, (b) the 'adiabatic scalar potential' $\varepsilon_m(\boldsymbol{r}) \equiv \varepsilon_m$ arising from spatial variations in the magnitude of the Zeeman vector $\boldsymbol{\Omega}(\boldsymbol{r})$, and (c) the 'geometric scalar potential' $W(\boldsymbol{r})$ described above. All three contribute to the potential energy of atoms in the dressed state basis.

5.2.2. A pair of Raman beams. For two counterpropagating Raman beams, the effective Zeeman field $\boldsymbol{\Omega}$, equation (71), defining the gauge fields, is characterized by the azimuthal angle $\phi = 2k_R x - \pi/2$ with the gradient

$$\boldsymbol{\nabla}\phi = 2\boldsymbol{k}_R, \qquad \boldsymbol{k}_R = k_R\boldsymbol{e}_x, \tag{88}$$

equal to the Raman recoil wave-vector $2\boldsymbol{k}_R$. On the other hand, the polar angle θ and the length of the Zeeman vector Ω are determined by the detuning δ and the Raman Rabi frequency Ω_R with

$$\cos\theta = \frac{\delta}{\Omega}, \quad \Omega = \sqrt{\delta^2 + \Omega_R^2}. \tag{89}$$

Typically experiments are performed in the lowest energy dressed state, where $m = -f$ assumes its maximum absolute value. Equations (85) and (88)–(89) illustrate two important points: (1) the magnitude of the vector potential $\boldsymbol{\mathcal{A}}_m(\boldsymbol{r})$ is defined by the recoil momentum of the lasers as well as the spin projection $\hbar m$, and (2) the vector potential is strictly bounded between $\pm 2\hbar k_R m_F$, where the maximum possible value is the recoil momentum $2\hbar k_R$ times the spin f.

We note that employing an extra spatially uniform radio-frequency magnetic field adds a constant term to the spatially oscillating x component of effective Zeeman field $\boldsymbol{\Omega}$, equation (71). In that case both the adiabatic energy ε_m and the geometric scalar potential $W_m(\boldsymbol{r})$ become spatially oscillating functions, thus creating a composite lattice potential in addition to the vector potential $\boldsymbol{\mathcal{A}}(\boldsymbol{r})$ [62]. We shall discuss this issue in more detail in the section 8.5.

Returning to equations (87)–(89), we see that in order to have a non-zero $\boldsymbol{\mathcal{B}}$, either the optical intensity or the detuning must depend on y or z, i.e. their gradient(s) should not be parallel to the wave-vector $\boldsymbol{k}_R$. The position-dependent

detuning can be generated by the vector light shift itself, which is absent for co-propagating light beams. This provides an additional term analogous to δ, but proportional to the Raman Rabi frequency. This is the case if the laser beams propagate at the angle $\alpha = \pi/2$, one of them being circularly polarized [52], as one can see in equation (73) of the previous section. Therefore, by simply making $\delta = 0$ and having the intensity-dependent detuning (which adds to δ) depend on position in equation (73), it is possible to create artificial gauge potentials which are truly geometric in nature, as the absolute light intensity then completely vanishes from the azimuthal angle θ.

The first experimental implementation of the synthetic magnetic field [22] was based on a different insight, namely that with constant Ω_R a gradient of the detuning δ due to a magnetic field gradient also generates a non-zero artificial magnetic field $\boldsymbol{\mathcal{B}}$ providing an artificial Lorentz force. The generated field $\boldsymbol{\mathcal{B}}$ is not purely geometric, and depends on the relative strength of δ and Ω_R in addition to their geometry.

It is noteworthy that the maximum magnetic flux produced by means of two counterpropagating laser beams amounts to $2fk_RL$ Dirac flux quanta and is thus proportional to the systems length L [150]. This is a drawback in creating very large magnetic fluxes necessary for reaching the fractional quantum Hall regimes. The use of the optical flux lattices considered in the following section overcomes this drawback making the induced flux proportional to the area rather than the length of the atomic cloud.

Note also that instead of counterpropagating laser fields one can employ co-propagating beams carrying optical vortices with opposite vorticity [154]. For the first-order Laguerre–Gaussian beams the azimuthal angle ϕ entering the vector and scalar potentials is then twice the real space azimuthal angle. On the other hand, the Raman Rabi frequency Ω_R, entering in equations (88)–(89) for the polar angle, linearly depends on the cylindrical radius in the vicinity of the vortex core. Non-zero artificial magnetic fields can therefore be generated without making the detuning position-dependent. Using vortex beams the number of Dirac flux quanta imparted onto the atomic cloud is determined by the vorticity of the beams [48, 151, 152, 154] and is thus normally much smaller than that induced by counter-propagating laser fields.

5.2.3. Optical flux lattices. Optical flux lattices were introduced by Cooper in [174]. This concept is based on the observation that singularities in the synthetic vector potential could be created and exploited so as to produce periodic structures with non-trivial magnetic fluxes [144, 174]. Such optical flux lattices could be created using a bichromatic laser field [144, 150], as considered in the previous section. Following the proposal by Cooper and Dalibard [150], we consider that the $f = 1/2$ ground state magnetic sublevels are coupled via Raman transitions (figure 10) involving laser fields with two frequencies. One frequency component $\boldsymbol{E}_{\omega_+}$ shown in green represents a circular σ_- polarized plane wave propagating along the z axis. Another frequency field $\boldsymbol{E}_{\omega_-}$ shown in red has all three circular polarizations. Dalibard and Cooper considered a situation where the field

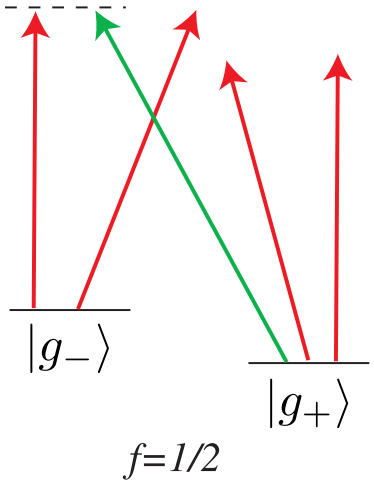

Figure 10. Raman transitions providing the optical flux lattice for $f = 1/2$.

$\boldsymbol{E}_{\omega_-}$ represents a superposition of three linearly polarized plane waves propagating in the $\boldsymbol{e}_x$–$\boldsymbol{e}_y$ plane and intersecting at 120°, with polarizations being tilted by some angle with respect to the propagation plane [150]. In that case one can produce triangular or hexagonal state-dependent lattices for the adiabatic motion of laser-dressed atoms affected by a non-staggered magnetic flux.

A square optical flux lattice is formed if the first frequency component $\boldsymbol{E}_{\omega_+}$ is again a circular σ_- polarized plane wave propagating along the z axis, yet the second frequency field $\boldsymbol{E}_{\omega_-}$ represents a sum of polarization-dependent standing waves with a $\pi/2$ time-phase difference between the standing waves oscillating in the $\boldsymbol{e}_x$ and $\boldsymbol{e}_y$ directions [144, 175][6]. In that case one arrives at an atom–light coupling described by the state-dependent Hamiltonian $\hat{M}(\boldsymbol{r}) = \boldsymbol{\Omega} \cdot \hat{\boldsymbol{F}}$ with a spatially periodic Zeeman field $\boldsymbol{\Omega}$:

$$\Omega_x = b\Omega_\parallel \cos(x\pi/a), \quad \Omega_y = b\Omega_\parallel \cos(y\pi/a),$$
$$\Omega_z = \Omega_\parallel \sin(x\pi/a)\sin(y\pi/a), \tag{90}$$

where a dimensionless ratio b is controlled by changing the polarizations of the standing waves [144, 175].

Atoms with a fixed spin projection m (along the Zeeman field $\boldsymbol{\Omega}$) then undergo an adiabatic motion in a square lattice potential $\varepsilon_m(\boldsymbol{r}) + W_n(\boldsymbol{r})$ with a periodicity in the $\boldsymbol{e}_x$ and $\boldsymbol{e}_y$ directions twice smaller than the periodicity $2a$ of the atom–light Hamiltonian $\hat{M}(\boldsymbol{r})$. The adiabatic motion is accompanied by a vector potential $\boldsymbol{\mathcal{A}}_m(\boldsymbol{r})$ containing two Aharonov–Bohm type singularities (per elementary cell) corresponding to the points where $\Omega_x = \Omega_y = 0$ and $\Omega_z < 0$. In the vicinity of each singular point, the vector potential $\boldsymbol{\mathcal{A}}_m$ has a Dirac-string piercing the $\boldsymbol{e}_x$–$\boldsymbol{e}_y$ plane and carrying $-2m$ Dirac flux quanta (with $-f \leqslant m \leqslant f$) [144]

$$\boldsymbol{\mathcal{A}}_m \to \boldsymbol{\mathcal{A}}_m^{AB} = -2\hbar m \nabla\phi. \tag{91}$$

Note that these singular fluxes are gauge-dependent and non-measurable. One can shift each singular points to another location via a gauge transformation [144], yet the singularities cannot be removed from the $\boldsymbol{e}_x$–$\boldsymbol{e}_y$ plane.

[6] The standing waves with time-phase difference were previously exploited in the context of the light forces [176, 177].

Due to the periodicity of the system, the total flux over the elementary cell is equal to zero

$$\frac{1}{\hbar}\oint_{\text{cell}} \boldsymbol{\mathcal{A}}_m \cdot \mathrm{d}\boldsymbol{r} = \frac{1}{\hbar}\int\!\!\int_{\text{cell}} \boldsymbol{\mathcal{B}}_{\text{m}}^{\text{tot}} \cdot \mathrm{d}\boldsymbol{S} = 0, \tag{92}$$

where $\boldsymbol{\mathcal{B}}_{\text{m}}^{\text{tot}} = \boldsymbol{\mathcal{B}}_m(\boldsymbol{r}) + \sum \boldsymbol{\mathcal{B}}_{\text{m}}^{AB}(\boldsymbol{r})$ is the total magnetic flux density composed of the continuous (background) magnetic flux density $\boldsymbol{\mathcal{B}}_m(\boldsymbol{r})$ and a set of above-mentioned gauge-dependent singular fluxes $\boldsymbol{\mathcal{B}}_{\text{m}}^{AB}(\boldsymbol{r})$ of the Aharonov–Bohm type corresponding to $\boldsymbol{\mathcal{A}}_m^{AB}$, equation (91).

Thus it is strictly speaking impossible to produce a non-zero effective magnetic flux over the elementary cell using the periodic atom–light coupling. Yet this does not preclude having a non-staggered continuous magnetic flux density $\boldsymbol{\mathcal{B}}(\boldsymbol{r})$ over the elementary cell, because of the existence of non-measurable Dirac strings. Deducting the latter, the continuous physical flux over the elementary cell is

$$\frac{1}{\hbar}\int\!\!\int_{\text{cell}} \boldsymbol{\mathcal{B}}_m \cdot \mathrm{d}\boldsymbol{S} = -\frac{1}{\hbar}\sum \oint_{\text{singul}} \boldsymbol{\mathcal{A}}_m \cdot \mathrm{d}\boldsymbol{r} = 4m, \tag{93}$$

where the summation is over the singular points of the vector potential (emerging at $\cos\theta \to -1$) around which the contour integration is carried out.

To summarize, the optical flux lattice contains a background non-staggered magnetic field $\boldsymbol{\mathcal{B}}$ plus an array of gauge-dependent Dirac-string fluxes of the opposite sign as compared to the background. The two types of fluxes compensate each other, so the total magnetic flux over an elementary cell is zero, as it is required from the periodicity of the Hamiltonian. However, the Dirac-string fluxes are non-measurable and hence must be excluded from any physical consideration. As a result, a non-staggered magnetic flux over the optical flux lattice appears, and topologically non-trivial bands with non-zero Chern numbers can be formed [144, 150]. By choosing the proper laser beams producing the optical flux lattice, one can produce a configuration where the lowest energy band is topologically non-trivial and nearly dispersionless, leading to a possible formation of fractional quantum Hall states [178]. Note also that unlike other lattice schemes involving laser-assisted-tunneling methods, such as proposed in [179, 180] (see section 8), the concept of optical flux lattices is based on the adiabatic motion of the atoms. Finally, it is also convenient to reinterpret optical flux lattices as tight-binding models defined in reciprocal space [181]. This complementary picture offers an efficient method to establish the atom–light coupling configurations leading to non-trivial topological bands: following [181], any tight-binding model exhibiting non-trivial Chern insulating phases, such as the Haldane model [182], could constitute the roots of an interesting optical flux lattice.

5.3. Dressed states: explicit picture

The preceding discussion followed our initial introduction to artificial gauge fields (section 3), where we first explicitly solved the state-dependent part of the Hamiltonian $\hat{M}(\boldsymbol{r})$, thereby introducing a vector potential $\boldsymbol{\mathcal{A}}$ for the adiabatic motion of atoms in the dressed-state manifold. This elegant description clearly illustrates the geometric origin of these gauge fields, but the projection process is an approximation, and in many cases, relevant information can be obtained by directly solving the total Hamiltonian (including the kinetic energy part and the atom–light coupling $\hat{M}$). This can be done explicitly if the atom–light coupling is induced by plane waves [51, 183], such as in the case of two counterpropagating laser beams considered above.

In order to establish a general framework that accommodates the effects of inter-particles collisions, we find convenient to use the second-quantized formalism, where the Hamiltonian for a particle in a uniform time-independent magnetic field normal to a 2D plane is

$$\int \mathrm{d}^2\boldsymbol{x}\frac{\hbar^2}{2m}\hat{\psi}^\dagger(\boldsymbol{x})\left\{\left[k_x - \frac{\mathcal{A}_x}{\hbar}\right]^2 + \left[k_y - \frac{\mathcal{A}_y}{\hbar}\right]^2\right\}\hat{\psi}(\boldsymbol{x}), \tag{94}$$

and $\psi^\dagger(\boldsymbol{x})$ is the field operator for the creation of a particle at position $\boldsymbol{x}$, with momentum represented by $\hbar k_{x,y} = -\mathrm{i}\hbar\partial_{x,y}$. We have in mind a situation which explicitly realizes equation (94) in a specific gauge. The actual gauge will depend on the details of the experimental setup, and will be in this case the Landau gauge with $\boldsymbol{\mathcal{A}} = -\mathcal{B}y\boldsymbol{e}_x$. The goal is to arrive at a Hamiltonian where the minimum of the energy-momentum dispersion relation $E(\boldsymbol{k})$ becomes asymmetric [183] and is displaced from zero momentum as a function of spatial position. The dressed single-particle states are spin and momentum superpositions whose state decomposition depends on the effective vector potential $\boldsymbol{\mathcal{A}}$. The canonical momentum associated with this vector potential can be observed by probing the internal state decomposition of the dressed states, as was done by Lin *et al* [21], see section 5.4.

This approach relies on a collection of atoms with two or more electronic ground states which interact with two counter-propagating Raman coupling lasers aligned along $\boldsymbol{e}_x$. If both Raman beams are far detuned from the ground to excited state transition there is negligible population in the excited state. The Raman beams then induce a coupling $\Omega_R \exp(\pm \mathrm{i}k_R x)$ between ground states which can lead to synthetic magnetic fields.

5.3.1. The two-level system. We will first consider a coupled two level system with internal states $|+\rangle$ and $|-\rangle$, where exact solutions can be obtained [183]. Physically, these two states might be two m_F levels in the ground state manifold of an alkali atom. For example, the $F = 1$ manifold of Rb^{87} at large enough field such that the quadratic Zeeman effect can resolve two out of the three Zeeman sublevels for the Raman or radio frequency transitions. In the frame rotating with angular frequency Δ_R/h, the Raman fields are detuned $\delta = g\mu_{\text{B}}\Delta B/\hbar$ from resonance. The atom–light coupling term in the RWA is then

$$\hat{H}' = \int \mathrm{d}y \int \frac{\mathrm{d}k_x}{2\pi}\left\{\frac{\hbar\Omega_R}{2}\left[\hat{\phi}_+^\dagger(k_x - 2k_R, y)\hat{\phi}_-(k_x, y) + \text{h.c.}\right]\right. \tag{95}$$

$$\left. + \frac{\hbar\delta}{2}\left[\hat{\phi}_+^\dagger(k_x, y)\hat{\phi}_+(k_x, y) - \hat{\phi}_-^\dagger(k_x, y)\phi_-(k_x, y)\right]\right\}. \tag{96}$$

The notation $\hat{\phi}^\dagger_\sigma(k_x, y)$ denotes the creation of a particle with wave vector k_x along $\boldsymbol{e}_x$ at position y, with $\sigma = \pm$. Here $\hat{H}'$ also includes the Raman detuning terms. In the following Ω_R and δ will be treated as spatially varying functions of y, but not x. This is the explicit expansion of the $\boldsymbol{\Omega} \cdot \hat{F}$ contribution to equation (63) with the effective magnetic field from equation (71) in terms of field operators for the two-level case.

With no coupling, the Hamiltonian is given by $\hat{\mathcal{H}} = \hat{H}_x + \hat{H}_y + \hat{U} + \hat{H}_{\rm int}$, which represent motion along $\boldsymbol{e}_x$, motion along $\boldsymbol{e}_y$, the external potential, and interparticle interactions respectively. When expressed in terms of the real space field operators $\hat{\psi}_\sigma(\boldsymbol{r})$we obtain

$$\hat{H}_x = \int \mathrm{d}^2\boldsymbol{r} \sum_\sigma \hat{\psi}^\dagger_\sigma(\boldsymbol{r}) \left(-\frac{\hbar^2\partial_x^2}{2m}\right) \hat{\psi}_\sigma(\boldsymbol{r}) \tag{97}$$

$$\hat{H}_y = \int \mathrm{d}^2\boldsymbol{r} \sum_\sigma \hat{\psi}^\dagger_\sigma(\boldsymbol{r}) \left(-\frac{\hbar^2\partial_y^2}{2m}\right) \hat{\psi}_\sigma(\boldsymbol{r}), \tag{98}$$

$$\hat{U} = \int \mathrm{d}^2\boldsymbol{r} \sum_\sigma \hat{\psi}^\dagger_\sigma(\boldsymbol{r}) U(\boldsymbol{r}) \hat{\psi}_\sigma(\boldsymbol{r}), \tag{99}$$

$$\hat{H}_{\rm int} = \frac{g_{2D}}{2} \int \mathrm{d}^2\boldsymbol{r} \sum_{\sigma,\sigma'} \hat{\psi}^\dagger_\sigma(\boldsymbol{r}) \hat{\psi}^\dagger_{\sigma'}(\boldsymbol{r}) \hat{\psi}_{\sigma'}(\boldsymbol{r}) \hat{\psi}_\sigma(\boldsymbol{r}). \tag{100}$$

The contact interaction for collisions between ultracold atoms in three dimensions is set by the three-dimensional (3D) s-wave scattering length a_s, here assumed to be state independent. Strong confinement in one direction results in an effective 2D coupling constant $g_{2D} = \sqrt{8\pi}\hbar^2 a_s/m l_{\rm HO}$ where $l_{\rm HO}$ is the harmonic oscillator length resulting from a strongly confining potential along $\boldsymbol{e}_z$. Finally, $U(\boldsymbol{r})$ is an external trapping potential, which we assume also to be state-independent.

This problem can be solved exactly when considering free motion along $\boldsymbol{e}_x$, i.e., treating only $\hat{H}_x$ and $\hat{H}'$, and going to the momentum representation for the atomic motion along the x-axis. The second quantized Hamiltonian for these two contributions can be compactly expressed in terms of the operators $\hat{\varphi}^\dagger_\pm(q_x, y) = \hat{\phi}^\dagger_\pm(q_x \mp k_R, y)$. Using this set, $\hat{H} \approx \hat{H}_x + \hat{H}'$ reduces to an integral over 2×2 blocks

$$\hat{H}(q_x, y) = \begin{pmatrix} \dfrac{\hbar^2(q_x - k_R)^2}{2m} + \dfrac{\hbar\delta}{2} & \dfrac{\hbar\Omega_R}{2} \\ \dfrac{\hbar\Omega_R}{2} & \dfrac{\hbar^2(q_x + k_R)^2}{2m} - \dfrac{\hbar\delta}{2} \end{pmatrix} \tag{101}$$

labeled by q_x and y. The expression in terms of $\hat{\varphi}$ operators instead of $\hat{\phi}$ is a gauge transformation which boosts the $|+\rangle$ and $|-\rangle$ states in opposite directions. The dependence of the two-photon coupling Ω_R and detuning δ on y has been suppressed for notational clarity. The resulting Hamiltonian density for motion along $\boldsymbol{e}_x$ at a fixed y is then

$$\hat{H}_x + \hat{H}' = \int \frac{\mathrm{d}q_x}{2\pi} \sum_{\sigma,\sigma'} \hat{\varphi}^\dagger_\sigma(q_x, y) \hat{H}_{\sigma,\sigma'}(q_x, y) \hat{\varphi}_{\sigma'}(q_x, y). \tag{102}$$

For each q_x, $\hat{H}(q_x, y)$ can be diagonalized by the unitary transformation $\hat{R}(q_x, y)\hat{H}(q_x, y)\hat{R}^\dagger(q_x, y)$. Unlike the approximate solutions discussed in the context of adiabatic gauge fields in sections 5.1–5.2, these represent the exact solution for motion along $\boldsymbol{e}_x$.

The resulting eigenvalues of $\hat{H}(q_x, y)$,

$$E_\pm(q_x, y) = E_R \left[\left(\frac{q_x}{k_R}\right)^2 + 1 \pm \frac{1}{2}\sqrt{\left(\frac{4q_x}{k_R} - \frac{\hbar\delta}{E_R}\right)^2 + \left(\frac{\hbar\Omega_R}{E_R}\right)^2} \right] \tag{103}$$

give the effective dispersion relations in the dressed basis, $\hat{\tilde{\varphi}}_\sigma(q) = \sum R_{\sigma,\sigma'}(q)\hat{\varphi}_{\sigma'}(q)$. For each q the eigenvectors of $H(q_x)$ form a family of states [184]. In terms of the associated real-space operators $\hat{\psi}'_\sigma(\boldsymbol{r})$ these diagonalized terms of the initial Hamiltonian are

$$\hat{H}_x + \hat{H}' = \int \mathrm{d}^2\boldsymbol{r} \sum_{\sigma=\pm} \hat{\psi}'^\dagger_\sigma(\boldsymbol{r}) E_\sigma\left(-\mathrm{i}\hbar\frac{\partial}{\partial x}, y\right) \hat{\psi}'_\sigma(\boldsymbol{r}). \tag{104}$$

In analogy with the term 'crystal-momentum' for particles in a lattice potential, we call the quantum number q_x the 'quasi-momentum'. Here $-\mathrm{i}\hbar\partial_x$ is the real-space representation of the quasi-momentum q_x. The symbol $E_\pm(-\mathrm{i}\hbar\partial_x, y)$ is a differential operator describing the dispersion of the dressed eigenstates, just as the operator $E_x(-\mathrm{i}\hbar\partial_x, y) = (-\mathrm{i}\hbar\partial_x + eBy)^2/2m$ describes quadratic dispersion along $\boldsymbol{e}_x$ of a charged particle moving in a magnetic field $B\boldsymbol{e}_z$ in the Landau gauge.

To lowest order in $E_R/\hbar\Omega_R$ and second order in q_x/k_R, $E_\pm(q_x, y)$ can be expanded as

$$E_\pm \approx \frac{E_R}{m^*}\left(\frac{q_x}{k_R} - \frac{\hbar\delta}{4E_R \pm \hbar\Omega_R}\right)^2 + \frac{2E_R \pm \hbar\Omega_R}{2} + \frac{\hbar^2\delta^2(4E_R \pm \hbar\Omega_R)}{4(4E_R + \hbar\Omega_R)^2}. \tag{105}$$

Atoms in the dressed potential are significantly changed in three ways: (1) The energies of the dressed state atoms are shifted by a scalar shift analogous to the sum of the adiabatic and geometric potentials $V(\boldsymbol{r})$ and $W(\boldsymbol{r})$. (2) Atoms acquire an effective mass $m^*/m = \hbar\Omega_R/(\hbar\Omega_R \pm 4E_R)$. This change is absent in the adiabatic picture. (3) The center of the dispersion relation is shifted to $\mathcal{A}_x/\hbar k_R = \hbar\delta/(\hbar\Omega_R \pm 4E_R)$. Just as with the adiabatic case considered in the previous subsections 5.1–5.2, $\mathcal{A}_x$ can depend on y by a spatial dependence on Ω_R, or, via $\delta(y)$ as described below. In either case, the effective Hamiltonian is that of a charged particle in a magnetic field expressed in the Landau gauge.

Figure 11 shows the dressed state dispersion relations in this model. Panels (*a*) and (*c*) show the undressed case ($\Omega_R = 0$) for detuning $\hbar\delta = 0$ and $5E_R$ respectively. Panels (*b*) and (*d*) depict the same detunings, for $\hbar\Omega_R = 16E_R$, where the exact results (solid line) are displayed along with the approximate dispersion (red dashed line). Figure 11(*b*) shows the strongly dressed states for large Ω_R, each of which is symmetric about $q = 0$. When detuned as in panel (*c*), the dispersion is displaced from $q = 0$. If space dependent this displacement leads to a non-trivial gauge potential. In the limit of very small Ω_R the dressed curve $E_-(q_x, y)$ forms a double-well potential as a function of k_x. In a related Raman-coupled system, Bose condensation in such double-well potentials were studied theoretically [165, 183, 185, 186], and has been explored in detail in the context of SOC [25–28].

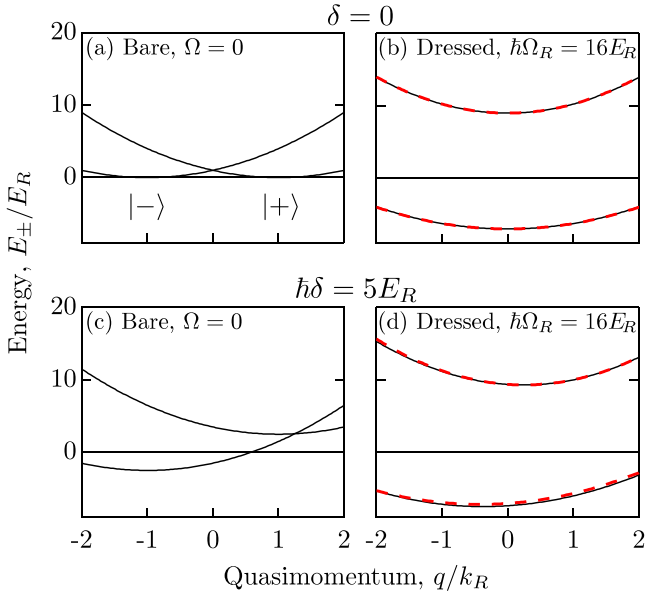

Figure 11. Each panel illustrates the dressed state dispersion relations for two level dressed state atoms. The horizontal axis is quasi-momentum q_x, and the vertical axis is the dressed state energy $E_\pm(q_x)$. The black lines are the exact eigenvalues of equation (101), and the red dashed lines are the analytic approximation. (*a*) Bare potentials with Raman beams on resonance ($\Omega_R = \delta = 0E_R$). (*b*) Dressed potentials with $\hbar\Omega_R = 16E_R, \hbar\delta = 0E_R$. (*c*) Bare potentials with Raman beams off resonance ($\Omega_R = 0$ and $\hbar\delta = 5E_R$). (*d*) Dressed potentials with Raman beams off resonance ($\hbar\Omega_R = 16E_R, \hbar\delta = 5E_R$).

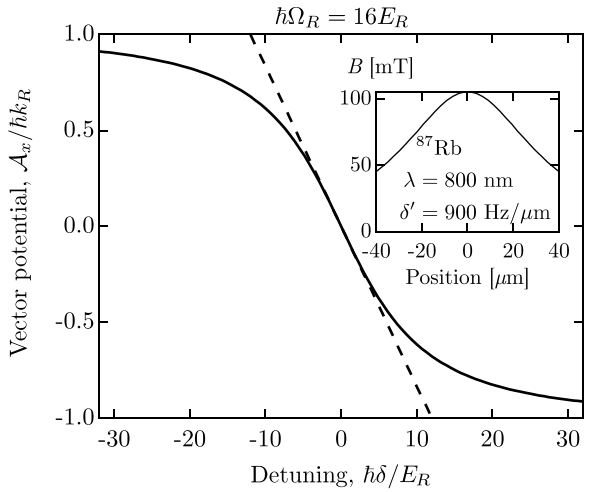

Figure 12. Effective vector potential $\mathcal{A}/\hbar k_R$ versus detuning $\hbar\delta/E_R$ for $\hbar\Omega_R = 16E_R$. The solid line is the exact result and the dashed line is the lowest order expansion in δ. The inset shows the synthetic magnetic field $|\mathcal{B}|$, indicating the predicted degree of field inhomogeneity predicted quantities relevant to experiment, computed for Rb^{87} with a detuning gradient $\hbar\delta'(y) = 900\,\mathrm{Hz}\,\mu\mathrm{m}^{-1}$, and $\lambda = 800$ nm Raman lasers.

5.3.2. Synthetic gauge fields. The Raman coupling leads to a dressed dispersion along $\boldsymbol{e}_x$, where motion along $\boldsymbol{e}_y$ is largely unaffected. When the detuning is made to vary linearly along $\boldsymbol{e}_y$, with $\delta(y) = \delta' y$, an effective single particle Hamiltonian contains a 2D effective vector potential $\boldsymbol{\mathcal{A}}/\hbar k_R \approx \hbar\delta' y/(4E_R \pm \hbar\Omega_R)\boldsymbol{e}_x$. The synthetic magnetic field is therefore $\mathcal{B}_z/\hbar k_R \approx -\hbar\delta'/(4E_R \pm \hbar\Omega_R)$. Figure 12 shows the vector potential as a function of detuning δ. As expected, the linear approximation discussed above (dashed line) is only valid for small δ. The synthetic field therefore decreases from its peak value as δ increases (top inset).

This technique also modifies the trapping potential along $\boldsymbol{e}_y$. In the adiabatic picture, this comprises the sum of the adiabatic and geometric potentials $V(\boldsymbol{r})$ and $W(\boldsymbol{r})$ which have no individual identity in this exact solution. When the initial potential $U(x, y)$ is harmonic with trapping frequencies ω_x and ω_y, the combined potential along $\boldsymbol{e}_y$ becomes $U_\pm(y) = m[\omega_y^2 + (\omega_\pm^*)^2]y^2/2$, where $m(\omega_\pm^*)^2/2 \approx \hbar^2\delta'^2(4E_R \pm \hbar\Omega_R)/4\hbar k_R(4E_R + \hbar\Omega_R)^2$.

This contribution to the overall trapping potential is not unlike the centripetal term which appears in a rotating frame of reference, where a synthetic magnetic field $\boldsymbol{\mathcal{B}}$ arises as well. In the case of a frame rotating with angular frequency Ω, the centripetal term gives rise to a repulsive harmonic term with frequency $\omega_{\mathrm{rot}}^2 = (\boldsymbol{\mathcal{B}}/2m)^2$. In the present case the scalar trapping frequency can be rewritten in a similar form $\omega_\pm^{*2} = (\mathcal{B}/2m)^2 \times |4E_R \pm \hbar\Omega_R|^3/\hbar k_R(4E_R + \hbar\Omega_R)^2$. The scalar potential may be attractive or repulsive, and it increases in relative importance with increasing Ω_R.

We have so far omitted motion along $\boldsymbol{e}_y$, interactions, and the effect of an external potential. The inclusion of these effects are discussed in detail in [51]. The outcome is that in the limit of large Ω_R these are unchanged by the transformation into the dressed basis. Together these allow the construction of the real space Hamiltonian in the basis of localized spin-superposition states $\hat{\psi}'(\boldsymbol{r})$. The density distribution of these localized states is not perfectly localized, but are some fraction of an optical wavelength λ in extent. For interactions, this is important because dressed state atoms separated by this distance will in fact interact. For particles starting in higher bands, transitions to lower bands are energetically allowed and a Fermi's Golden Rule argument thus gives rise to decay from all but the lowest energy dressed state [187].

5.3.3. Limitations. This technique is not without its limitations. Foremost among them is the range of possible $\mathcal{A}_x/\hbar k_R$ shown in figure 12 where $\hbar\Omega_R = 16E_R$. While the linear expansion (dashed) is unbounded, the exact vector potential is bounded by $\pm k_R$. For example, the hybridized combination of $|+, q - k_R\rangle$ and $|-, q + k_R\rangle$ cannot give rise to dressed states with minima more positive than $q = +k_R$ where the energy of the $|+\rangle$ states is minimized without dressing, figure 11(*c*). The minima can also not be more negative than $q = -k_R$.

This limitation does not affect the maximum attainable field, only the spatial range over which this field exists. Specifically, a linear gradient in $\delta(y)$ gives rise to the synthetic field $\mathcal{B}_z(y)$ which is subject to $\int_{-\infty}^{\infty}\mathcal{B}_z(y)\,\mathrm{d}y = 2\hbar k_R$. This simply states that the vector potential—bounded by $\pm\hbar k_R$—is the integral of the magnetic field. Note however, that along $\boldsymbol{e}_x$ the region of large $\mathcal{B}_z$ has no spatial bounds.

A second limitation of this technique is the assumption of strong Raman coupling between the Zeeman split states. As already pointed out at the end of the section 4.4.1, for

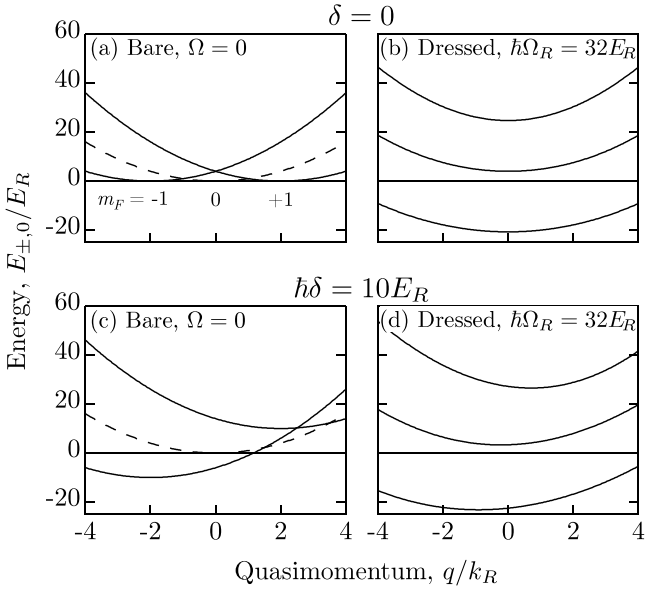

Figure 13. Each panel denotes the dressed state dispersion relations $E(q_x)$ for three level atoms dressed by counter-propagating Raman beams. The horizontal axis is quasi-momentum q_x, and the vertical axis is energy. (*a*) Bare potentials (undressed) with Raman beams on resonance. (*b*) Dressed potentials ($\hbar\Omega_R = 32E_R, \hbar\delta = 0E_R$). (*c*) Bare potentials (undressed) with Raman beams off resonance ($\hbar\delta = 5E_R$). (*d*) Dressed potentials with Raman beams off resonance ($\hbar\Omega_R = 32E_R, \hbar\delta = 10E_R$).

alkali atoms, when the detuning from atomic resonance Δ_e is large compared to the excited state fine structure $\Delta_{\rm FS}$, the two-photon Raman coupling for $\Delta m_F = \pm 1$ transitions drops as $\Omega_R \propto \Delta_{\rm FS}/\Delta_e^2$, not Δ_e^{-1} as for the AC Stark shift. As a result, the ratio between the Raman coupling Ω_R and off-resonant scattering cannot be increased by using larger detuning, and the only solution is to consider atoms with large fine structure splitting $\Delta_{\rm FS}$, such as rubidium (figure 13).

5.3.4. Three-level system. The range of possible effective vector potentials can be extended by coupling more states, for example the m_F states of an $f > 1/2$ manifold in the linear Zeeman regime. We can follow the two-level example above, except there are no compact closed-form solutions. In the adiabatic picture, equations (85) and (88)–(89), additional levels extended the range of the vector potential from $\pm 2\hbar k_R$ (the two level case) to $\pm 2\hbar f k_R$ for arbitrary f.

This can be illustrated by considering an optically trapped system of Rb^{87} atoms in the $f = 1$ manifold in a small magnetic field which splits the three m_F levels by $g\mu_{rmB}|\boldsymbol{B}|$. The 3×3 blocks $\hat{H}(q_x)$ describing the three internal states of the $f = 1$ manifold are

$$\hat{H}(q_x) = \begin{pmatrix} \frac{\hbar^2(q_x-2k_R)^2}{2m} + \hbar\delta & \frac{\hbar\Omega_R}{2} & 0 \\ \frac{\hbar\Omega_R}{2} & q_x^2 + \epsilon & \frac{\hbar\Omega_R}{2} \\ 0 & \frac{\hbar\Omega_R}{2} & \frac{\hbar^2(q_x+2k_R)^2}{2m} - \hbar\delta \end{pmatrix}. \tag{106}$$

In this expression, δ is the detuning of the two photon dressing transition from resonance, ϵ accounts for any quadratic Zeeman shift (not included in the section 5.2), Ω_R is the two-photon transition matrix element, and q_x, in units of the recoil momentum k_R, is the atomic momentum displaced by a state-dependent term $q_x = k - 2k_R$ for $m_F = -1$, $q_x = k$ for $m_F = 0$, and $q_x = k + 2k_R$ for $m_F = +1$. Here, the three eigenvalues are denoted by $E_\pm$ and E_0. As with the two-level case, the states associated with eigenvalues $E_\pm$ experience an effective vector potential which can be made position-dependent with a spatially varying detuning δ. The E_0 also experiences a synthetic field, but at higher order in Ω_R^{-1}. A magnetic field gradient along $\boldsymbol{e}_y$ gives $\delta \propto y$, and generates a uniform synthetic magnetic field normal to the plane spanned by the dressing lasers and real magnetic field $\boldsymbol{B}$.

5.4. Experimental implementation

The preceding sections described an overall procedure by which light-induced artificial gauge fields can be created. In this section, we look at three effects: the introduction of a spatially uniform vector potential $\boldsymbol{\mathcal{A}}$, the use of a temporal gradient to induce an electric field $\boldsymbol{\mathcal{E}} = -\partial\boldsymbol{\mathcal{A}}/\partial t$, and lastly the inclusion of a spatial gradient which gives rise to a magnetic field $\boldsymbol{\mathcal{B}} = \boldsymbol{\nabla} \times \boldsymbol{\mathcal{A}}$. For more technical details we refer the reader to the original publications [21–23].

5.4.1. The effective vector potential. Figure 14 shows the basic principle for creating artificial vector potentials. In these experiments an optically trapped ^{87}Rb BEC was adiabatically transferred from the initial $|f = -1, m_F = 1\rangle$ state into the $|q_x = 0, -\rangle$ dressed state, with quasimomentum $q = 0$, which corresponds to the lowest energy dressed band at $\delta = 0$, as identified by the black arrow in the top-left panel to figure 14(*a*). Once loaded into this state, the atoms were held for a brief equilibration time, at which point both the Raman lasers and the trapping lasers were suddenly turned off. After the turn off, the atoms were allowed to travel ballistically along $\boldsymbol{e}_x$, while a magnetic field gradient Stern–Gerlach separated the three m_F components along $\boldsymbol{e}_y$. This process allowed the direct detection of the spin-momentum superpositions which comprise the Raman dressed states. The top-right panel of figure 14(*a*) shows that for $\delta = 0$ the ground state BEC is located at $q = 0$, and that the dressed state is made up of three different m_F states each with momentum given by $k_{m_F} = q - 2m_F k_R$.

The lower two panels of figure 14(*a*) depict an experiment where the BEC is loaded as described above. The detuning is slowly ramped from 0 to $\hbar\delta = -2E_R$. During such a ramp, the BEC adiabatically remains at the minimum of $E_-(q)$. The magnitude of the resulting shift is consequently associated with the artificial vector potential. The results of many such experiments is shown in figure 14(*b*) which compares the measured vector potential. In this case the Raman lasers intersected at 90°. This has the effect of decreasing the effective recoil momentum to $k_L = k_R/\sqrt{2}$ and the recoil momentum to $E_L = E_R/2$. The prediction of the model is obtained by numerically solving equation (106) with no free parameters.

It is important to note that the BEC was always at rest in these experiments. The uniform and static vector potential would therefore normally not be experimentally detectable. In

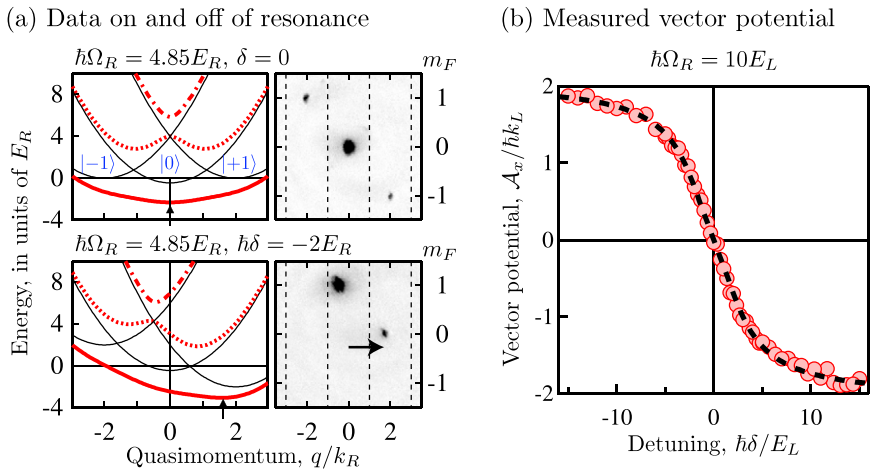

Figure 14. The artificial vector potential. (*a*) Left: computed dispersion relations, where the solid curves are the bare states and the dashed curves are the dressed states. The vertical arrow locates the minimum of the lowest energy dressed curve. Right: representative image of Raman-dressed atoms both on and off of resonance showing the three m_F components differing in momentum by $\pm\hbar k_R$, displaced from zero q when $\delta \neq 0$. The horizontal arrow depicts the displacement of the $m_F = 0$ cloud from zero corresponding to the non-zero vector potential. (*b*) Measured momentum of $m_F = 0$ component as a function of detuning δ. With the gauge choice $\boldsymbol{\mathcal{A}}(\delta = 0) = 0$, this constitutes a direct measurement of the artificial vector potential $\boldsymbol{\mathcal{A}}(\delta)$. The dashed curve is the predicted vector potential for the experimental parameters. Data first appeared in [21] and [23].

this case, however, the vector potential's difference from the $\delta = 0$ case is encoded into the spin-momentum superposition making up the dressed state, and can be accessed in experiment. See also [23] for more details of this effect.

5.4.2. Creating artificial electric fields. With access to an artificial vector potential it is natural to consider what kind of mechanical forces one can induce on the atoms with suitable gradients of this potential. Several possibilities are available. One can for instance change the vector potential from an initial $\boldsymbol{\mathcal{A}}_i$ to a final $\boldsymbol{\mathcal{A}}_f$ by suddenly changing δ. If $\boldsymbol{\mathcal{A}}$ behaves as a real vector potential, then this change should be associated with a force that accelerates the atoms, changing their *mechanical* momentum by an amount $\delta\boldsymbol{p}_{\rm mech} = (\boldsymbol{\mathcal{A}}_i - \boldsymbol{\mathcal{A}}_f)$.

There are currently two experiments by Lin *et al* [23] which illustrate the effect of an artificial electric field. The atoms were first prepared at an initial detuning δ producing a non-zero $\boldsymbol{\mathcal{A}}_i$, and then suddenly making $|\delta| \gg \Omega_R$. This results in $\boldsymbol{\mathcal{A}}_f = \pm 2\hbar k_L \boldsymbol{e}_x$ which depends on the sign of δ, see figure 14(*b*). Combined with free expansion of the cloud the final momentum can be measured, shown in figure 15(*a*).

Alternatively, $\boldsymbol{\mathcal{A}}$ can be changed only slightly, as illustrated in figure 15(*b*). By taking the average velocity of all three spin-momentum components the quasimomentum and also the group velocity can be monitored. The subsequent evolution in the harmonic confining potential is then monitored. Figure 15(*b*) depicts the mechanical momentum $p_{\rm mech}$, related to the group velocity, by multiplying the average velocity by the effective mass $m^* \approx 2.5\,$m. This quantity has the same amplitude as the canonical momentum oscillations, but is centered on zero.

5.4.3. Inclusion of a magnetic field. With a synthetic Abelian vector potential present, it is also natural to consider creating an artificial magnetic field $\boldsymbol{\mathcal{B}} = \boldsymbol{\nabla} \times \boldsymbol{\mathcal{A}}$. The key ingredient for obtaining a non-zero effective magnetic field is the dressed state, given by a detuning which varies linearly along $\boldsymbol{e}_y$, with $\delta(y) = \delta' y$. This gives $\boldsymbol{\mathcal{A}} \approx -2\hbar k_R \delta / \Omega_R \boldsymbol{e}_x$ when $\delta \ll \Omega_R$.

To create an artificial magnetic field such as in [22], the geometry shown in figure 6 can be used, with the three m_F states of ^{87}Rb's hyperfine ground state Zeeman split by a biasing magnetic field along $\boldsymbol{e}_y$. The states are coupled with a pair of Raman lasers giving a momentum exchange along $\boldsymbol{e}_x$. Using a pair of quadrupole coils in an anti-Helmholtz geometry aligned along $\boldsymbol{e}_z$, produces a magnetic field gradient of the form $\boldsymbol{B}_{\rm quad} \approx \beta'(x\boldsymbol{e}_x + y\boldsymbol{e}_y - 2z\boldsymbol{e}_z)$ which adds to the bias field $\boldsymbol{B}_0 = B_0\boldsymbol{e}_y$. The resulting Zeeman shift is proportional to $|\boldsymbol{B}_0 + \boldsymbol{B}_{\rm quad}| \approx B_0 + \beta' y$ giving the desired detuning gradient along $\boldsymbol{e}_y$, which in turn results in a synthetic magnetic field $\boldsymbol{\mathcal{B}} = \mathcal{B}\boldsymbol{e}_z$. Figure 16(*a*) depicts images of atoms after TOF, in which the appearance of an artificial magnetic field is marked in two ways.

Firstly, the initially symmetric cloud acquires a shear as $\mathcal{B}$ increases. With the gradient present, the vector potential depends on y as $\mathcal{A}_x \propto y$. When the Raman lasers are turned off at the beginning of the time of flight (TOF), $\mathcal{A}_x \to 0$. This process introduces an electric field along $\boldsymbol{e}_x$ proportional to y, and as a result the BEC undergoes a shearing motion during the expansion.

Above a critical gradient vortices spontaneously enter into the non-rotating BEC. In this regime, the BEC is described by a macroscopic wave function $\psi(\boldsymbol{r}) = |\psi(\boldsymbol{r})|e^{i\phi(\boldsymbol{r})}$, which obeys the Gross–Pitaevskii (GP) equation. The phase ϕ winds by 2π around each vortex, with amplitude $|\psi| = 0$ at the vortex center. The magnetic flux $\Phi_{\mathcal{B}}$ results in N_v vortices and for an infinite, zero temperature system, the vortices are arrayed in a lattice [188] with density $\mathcal{B}/h$. For finite systems vortices are energetically less favorable, and their areal density is below this asymptotic value, decreasing to zero at a critical field $\mathcal{B}_c$.

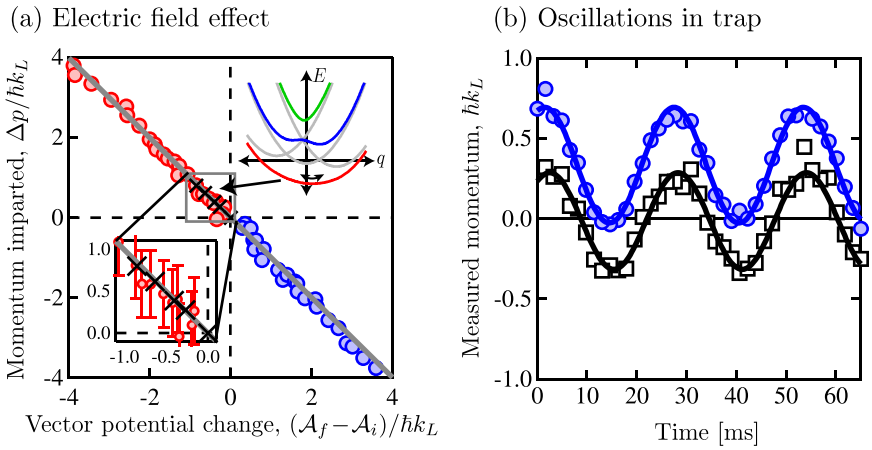

Figure 15. The artificial electric field. (*a*) Observed momentum kick resulting from a sudden change in $\boldsymbol{\mathcal{A}}$. The symbols indicate data in which the vector potential was changed from $\boldsymbol{\mathcal{A}}_i \propto \boldsymbol{e}_x$ to $\boldsymbol{\mathcal{A}}_f = \pm 2\hbar k_L \boldsymbol{e}_x$ ('+' for red and '−' for blue), at which point the BEC's momentum was measured. The black crosses (bottom inset) reflect data for which $\boldsymbol{\mathcal{A}}_f = 0$, where the BEC was allowed to oscillate in the harmonic trap. The amplitude in momentum of these oscillations is plotted. The gray line is the expected outcome, with slope −1. (*b*) The in trap oscillation data, fitted to a sinusoidal model. The blue circles depict data where $\mathcal{A}_f \neq 0$. As depicted by the top inset in (*a*), the measured canonical momentum oscillates around a non-zero value given by $\mathcal{A}_f$. The black squares depict the average velocity of the three components measured after TOF multiplied by the effective mass $m^* \approx 2.5\,\mathrm{m}$. Data first appeared in [23].

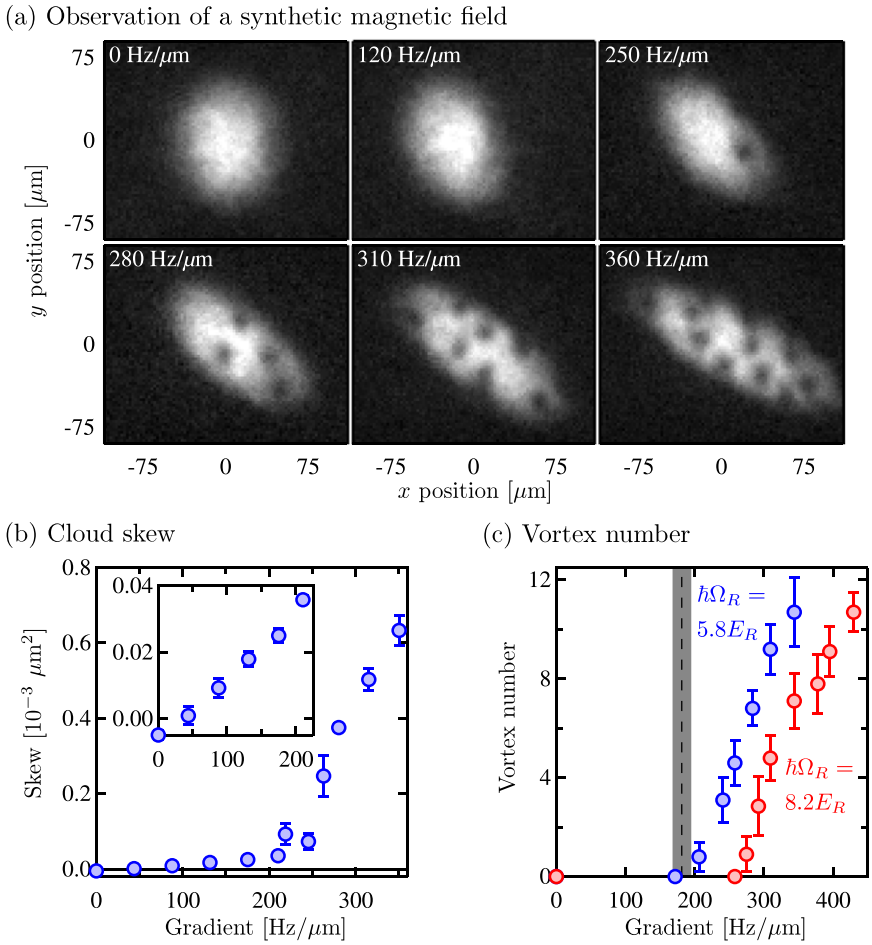

Figure 16. The artificial magnetic field. (*a*) A detuning gradient δ' along $\boldsymbol{e}_y$ from a magnetic field gradient creates an artificial magnetic field. This causes a shearing of the atomic cloud and allows the entry of vortices into the BEC. (*b*) With the gradient present, the vector potential depends on y as $\mathcal{A}_x \propto y$. When the Raman lasers are turned off, $\mathcal{A}_x \to 0$. This process introduces an electric field along $\boldsymbol{e}_x$ that depends on y, and as a result the BEC undergoes a shearing motion during TOF. (*c*) Above a critical gradient (gray band) it becomes energetically favorable for vortices to enter the BEC. Data in (*a*) and (*c*) first appeared in [22].

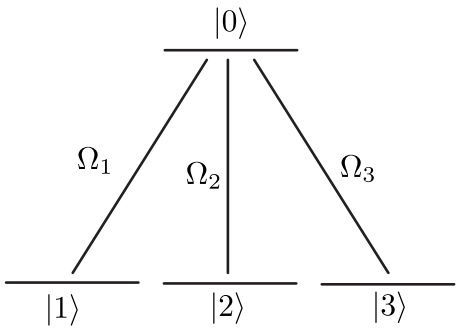

Figure 17. The tripod configuration of the atom–light coupling in which the atomic ground states $|j\rangle$ (with $j = 1, 2, 3$) are coupled to the excited state $|0\rangle$ via the Rabi frequencies Ω_j of the laser fields.

6. Non-Abelian gauge potentials and SOC

Let us now turn to the case of non-Abelian geometric gauge potentials. As already mentioned in section 3, they emerge when the center of mass motion of atoms takes place in a manifold of degenerate or quasi-degenerate internal dressed states. The non-Abelian gauge potentials provide a coupling between the center of mass motion and the internal (spin or quasi-spin) degrees of freedom, thus causing an effective 'spin–orbit' coupling. In this section, we shall overview several schemes for creating these gauge potentials in cold-atom setups.

6.1. The tripod scheme

Let us begin with a tripod setup (shown in figure 17) for the atom–light coupling, comprising three lower atomic levels coupled with an excited level via the laser fields with the Raman frequencies Ω_j. Compared to the Λ setup analyzed in the previous section, now there is an additional third laser driving the transitions between an extra ground state 3 and the excited state 0. The tripod scheme has two degenerate dark states representing the superpositions of the three ground states immune to the atom–light coupling.

The tripod scheme was initially considered by Olshanii and co-authors [189, 190] in the context of velocity selective coherent population trapping. In another development Klaas Bergmann and co-workers theoretically [54, 124, 191] and experimentally [192, 193] explored the adiabatic evolution of the dark-state atoms in the time-dependent laser fields (the tripod-STIRAP), governed by the matrix valued geometric phase [24]. Ruseckas *et al* considered the adiabatic motion of the dark-state atoms in the spatially varying laser fields [55] providing non-Abelian gauge potentials for the center of mass motion using the tripod scheme.

Assuming exact resonance for the atom–light coupling, the Hamiltonian of the tripod atom reads in the interaction representation

$$\hat{M} = \frac{\hbar}{2}\Big(\Omega_1|0\rangle\langle 1| + \Omega_2|0\rangle\langle 2| + \Omega_3|0\rangle\langle 3|\Big) + \text{H.c.}$$
$$= \frac{\hbar}{2}\Omega|0\rangle\langle B| + \text{H.c.}, \qquad (107)$$

where $\Omega = \sqrt{|\Omega_1|^2 + |\Omega_2|^2 + |\Omega_3|^2}$ is the total Rabi frequency and $|B\rangle = (\Omega_1^*|1\rangle + \Omega_2^*|2\rangle + \Omega_3^*|3\rangle)/\Omega$ is the atomic bright state, representing a superposition of the atomic ground states directly coupled to the excited state $|0\rangle$.

The Hamiltonian $\hat{M}$ has two eigenstates $|\chi_1(\boldsymbol{r})\rangle \equiv |D_1\rangle$ and $|\chi_2(\boldsymbol{r})\rangle \equiv |D_2\rangle$ known as the dark (or uncoupled) states which are orthogonal to the bright state $|B\rangle$, contain no excited state contribution and are characterized by zero eigenenergies ($\hat{M}|D_j\rangle = 0$). The bright state $|B\rangle \equiv |B(\boldsymbol{r})\rangle$ is position dependent due to the position dependence of the amplitude and the phase of the laser Rabi frequencies $\Omega_j \equiv \Omega_j(\boldsymbol{r})$. Thus the adiabatic elimination of the bright and excited states leads to the adiabatic center of mass motion of the dark state atoms affected by the vector potential $\hat{\boldsymbol{\mathcal{A}}}^{(q)}$ (with $q = 2$ since there are two dark states) to be labeled simply by $\hat{\boldsymbol{\mathcal{A}}}$. The explicit expressions for the vector potential $\hat{\boldsymbol{\mathcal{A}}}$ and the accompanying geometric scalar potential are available in the previous original [55] or review [80, 170] articles.

If two Rabi frequencies $\Omega_{1,2}$ represent co-propagating First-order Laguerre–Gaussian beams with opposite vorticity along the propagation axis z and the third Rabi frequency Ω_3 represent the first-order Hermite-Gaussian beam propagating in x direction, the induced vector potential $\hat{\boldsymbol{\mathcal{A}}}$ contains a contribution due to a magnetic monopole [55, 194] times a Pauli matrix. On the other hand, if all three beams co-propagate, two of them carrying opposite vortices, the third beams being without the vortex, a persistent current can be generated for ultracold atoms [195].

By properly choosing the laser fields, the Cartesian components of the vector potential $\hat{\boldsymbol{\mathcal{A}}}$ do not commute, leading to the non-Abelian gauge potentials. We note that this can happen even if the Rabi frequencies Ω_j of the tripod setup represent (non-collinear) plane waves [163, 164, 167, 196] or the properly chosen standing waves [162, 165, 166]. In that case, one can produce a uniform vector potential whose Cartesian components are proportional to the Pauli matrices, thus generating a SOC of the Rashba–Dresselhaus type for ultracold atoms. The rapidly progressing field of spin–orbit-coupled atomic gases will be further explored in the following.

6.2. SOC for ultracold atoms

SOC is pervasive in material systems. In some cases it leads to parasitic effects such as reduced spin coherence times [197], while in other contexts, like topological insulators, it is essential [74, 198]. Topological insulators—non-interacting fermionic systems—represent a first realization of time-reversal (TR) invariant systems with topological order [74]. In analogy with the progression from the TR-violating single-particle IQHE to the interaction driven fractional quantum Hall effects (FQHEs), the next important step is realizing strongly interacting cousins to the topological insulators, of which topological superconductors are a first example [199, 200]. Ultracold atoms are an ideal platform to study strongly interacting SOC systems, both with bosonic [165] and fermionic atoms [50]. Since ultracold atoms lack intrinsic SOC, numerous techniques (including the tripod setup considered above) have been suggested for generating SOC

(generally equivalent to non-Abelian gauge potentials [80]), with optical [50, 55, 56, 167, 201], rf [202] or pulsed magnetic [203, 204] fields. A first step towards this goal has been experimentally achieved with the recent implementation of an Abelian SOC (i.e. a SOC term generated along one spatial direction only) in several laboratories [25–32, 127], see section 6.3.

In section 3, we considered how non-trivial artificial gauge fields can appear for atoms adiabatically moving in a restricted set of 'target' states. Then in section 5, we studied an experimentally relevant case where the artificial gauge field $\boldsymbol{\mathcal{A}}$ was a vector of real numbers, i.e. a gauge potential related to an Abelian (U(1)) gauge structure. Here we will focus on the most simple extension where the vector potential is non-Abelian, but is spatially uniform, such as the one generated using the tripod setup mentioned above. Because of the $-\mathrm{i}\hat{\boldsymbol{\mathcal{A}}} \times \hat{\boldsymbol{\mathcal{A}}}/\hbar$ term appearing in the expression (25) for the non-Abelian magnetic field, a uniform non-Abelian vector potential can have measurable effects [42].

SOC can be a simple example of non-Abelian vector potentials: suppose $\hat{\boldsymbol{\mathcal{A}}}$ is a spatially uniform vector potential with non-commuting elements each described by 2×2 matrices acting on a pseudospin-degree of freedom. We can expand the general Hamiltonian

$$\hat{H} = \frac{\hbar^2}{2m}\left[\boldsymbol{k} - \frac{\hat{\boldsymbol{\mathcal{A}}}}{\hbar}\right]^2 + V(\hat{\boldsymbol{r}}) \tag{108}$$

$$= \frac{\hbar^2\boldsymbol{k}^2}{2m} - \frac{\hbar}{m}\left[\hat{\boldsymbol{\mathcal{A}}}_x k_x + \hat{\boldsymbol{\mathcal{A}}}_y k_y + \hat{\boldsymbol{\mathcal{A}}}_z k_z\right] + \frac{1}{2m}\hat{\boldsymbol{\mathcal{A}}}\cdot\hat{\boldsymbol{\mathcal{A}}} + V(\boldsymbol{r}), \tag{109}$$

where each of the terms $\hat{A}_j k_j$ couple the spin to the atom's linear motion. In general, because $[\hat{\boldsymbol{\mathcal{A}}}_i, \hat{\boldsymbol{\mathcal{A}}}_j] \neq 0$ for some i, j, this uniform vector potential cannot be eliminated by a gauge transformation.

As we argued in section 3, non-trivial gauge fields require that the atomic motion be restricted to a target subspace of the initial Hamiltonian. In the present case this implies that the full Hamiltonian be spanned by a minimum of three internal states. The tripod scheme—involving four laser-coupled levels—is the most commonly used theoretical model in which non-Abelian gauge fields appear. Here we will present a slightly simpler 'ring coupling' model containing only three sequentially coupled levels [168] which displays the same physics (Interestingly, the familiar tripod scheme [55, 80, 163–165, 167, 205] reduces to the three level ring model when the excited state is far from resonance and thus can be adiabatically eliminated.)

We consider 3 ground or metastable atomic 'spin' states $\{|1\rangle, |2\rangle, |3\rangle\}$ coupled together with complex valued matrix elements $\Omega_{j+1,j} = \frac{1}{2}\Omega\exp[\mathrm{i}(\boldsymbol{k}_j\cdot\boldsymbol{x})]$, linking each state to each other state. Here, Ω describes the optical coupling strength, $\hbar\boldsymbol{k}_j$ is the respective momentum acquired in the $j \to j+1$ atomic transition. Throughout this section, spin indices are taken mod(3), implying periodic boundary conditions $|4\rangle = |1\rangle$ for spin states.

Including the motional degrees of freedom, the momentum representation second-quantized Hamiltonian

$$\hat{\mathcal{H}} = \int \frac{\mathrm{d}^2\boldsymbol{k}}{(2\pi)^2}\sum_j \left\{\left(\frac{\hbar^2|\boldsymbol{k}|^2}{2m}\right)\hat{\phi}_j^\dagger(\boldsymbol{k})\hat{\phi}_j(\boldsymbol{k}) + \frac{\Omega}{2}\left[\hat{\phi}_{j+1}^\dagger(\boldsymbol{k}+\boldsymbol{k}_j)\hat{\phi}_j(\boldsymbol{k}) + \mathrm{h.c.}\right]\right\} \tag{110}$$

describes a system of 2D atoms in the momentum representation, where all summations over j range from 1 to 3. Here, $\{\phi_j^\dagger(\boldsymbol{k})\}$ is the spinor field operator describing the creation of a particle with momentum $\hbar\boldsymbol{k}$ in internal state $|j\rangle$. In what follows, we require that $\sum\boldsymbol{k}_i = 0$, so that no momentum is transferred to an atom upon completing a closed-loop transition $|1\rangle \to |2\rangle \to |3\rangle \to |1\rangle$. In this case, the momenta-exchange can be represented in terms of the differences $\boldsymbol{k}_j = \boldsymbol{K}_{j+1} - \boldsymbol{K}_j$, and we require $\boldsymbol{K}_j$ to have zero average. The displacement vectors $\boldsymbol{K}_j = \sum_l l\boldsymbol{k}_{l+j-1}/3$ define these transformations explicitly.

In the spirit of sections 5.3.1 and 5.3.4, we substitute $\hat{\varphi}_j^\dagger(\boldsymbol{q}) = \hat{\phi}_j^\dagger(\boldsymbol{q}+\boldsymbol{K}_j)$ into the Hamiltonian in equation (110) which separates into an integral $\int\sum_{j,j'}\hat{\varphi}_j^\dagger(\boldsymbol{q})\hat{H}_{j,j'}(\boldsymbol{q})\hat{\varphi}_{j'}(\boldsymbol{q})\mathrm{d}^2\boldsymbol{q}/(2\pi)^2$ over 3×3 blocks

$$H_{j,j'}(\boldsymbol{q}) = \frac{\hbar^2\left|\boldsymbol{q}+\boldsymbol{K}_j\right|^2}{2m}\delta_{j,j'} + \frac{\Omega}{2}\left(\delta_{j,j'+1} + \mathrm{h.c.}\right), \tag{111}$$

where each block is labeled by the quasi-momentum $\hbar\boldsymbol{q}$.

We can relate the coupling term in equation (111) to the situation of a 1D periodic tight binding Hamiltonian with a hopping matrix element $\Omega/2$, and where the three sites correspond to the three internal states of the atom. For Ω much larger than the kinetic energy the coupling term can be diagonalized using a basis conjugate to the spin-index j with field operators

$$\hat{\tilde{\varphi}}_\ell^\dagger(\boldsymbol{q}) = \frac{1}{3^{1/2}}\sum_{j=1}^{N}\mathrm{e}^{\mathrm{i}2\pi\ell j/N}\hat{\varphi}_j^\dagger(\boldsymbol{q}). \tag{112}$$

The corresponding eigenenergies are given by $E_\ell = \Omega\cos(2\pi\ell/3)$, where $\ell \in \{0, 1, 2\}$ is analogous to the usual crystal momentum.

The ground state is two-fold degenerate for $\Omega > 0$ for states at $\ell = 1$ and $\ell = 2$. If the displacement vectors $\boldsymbol{K}_j$ are chosen such that $\boldsymbol{K}_j = -k_L\sin(2\pi j/3)\boldsymbol{e}_x + k_L\cos(2\pi j/3)\boldsymbol{e}_y$, the full Hamiltonian matrix becomes

$$H_{\ell,\ell'}(\boldsymbol{q}) = \left(q^2 + 1 + E_\ell\right)\delta_{\ell,\ell'} + \left[\left(\mathrm{i}q_x + q_y\right)\delta_{\ell-1,\ell'} + \mathrm{h.c.}\right], \tag{113}$$

where momentum is expressed in units of k_L and energy in units of recoil energy $E_L = \hbar^2k_L^2/2m$. We will in the following consider the two nearly degenerate states with $\ell = 1$ and $\ell = 2$, yielding the pseudospins $|\downarrow\rangle$ and $|\uparrow\rangle$.

In the subspace spanned by the lowest energy pair of dressed states, we consequently get a zeroth order Hamiltonian of the Rashba form

$$\hat{H}^{(0)} = |\boldsymbol{q}|^2\,\hat{1} + \left(\hat{\sigma}_x q_y - \hat{\sigma}_y q_x\right), \tag{114}$$

where $\hat{\sigma}_{x,y,z}$ are the standard Pauli matrices. For finite coupling Ω it is instructive to adiabatically eliminate the excited states order-by-order in perturbation theory, which gives additional effective terms $\hat{H}^{(n)}$ [168].

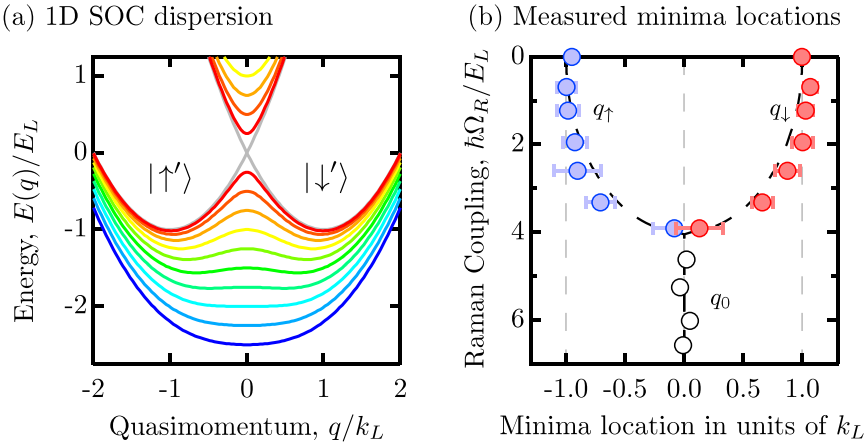

Figure 18. The spin–orbit coupled BEC. (*a*) The dispersion $E(q)$, where the transition between the double minimum and the single minima configurations are illustrated. (*b*) The quasi momentum obtained by adiabatically loading a spin mixture into a Raman dressed state with the desired Ω_R. Data first appeared in [25].

6.3. Experimental realization of SOC

The key to the experimental realization of SOC is in the fact that the laser geometry in equation (101) can also be used to obtain a coupling of the form,

$$\hat{H} = \frac{\hbar^2\hat{\boldsymbol{k}}^2}{2m} - \frac{\hbar^2 k_R}{m}\hat{\sigma}_y\hat{k}_x + \frac{\hbar\delta}{2}\hat{\sigma}_y + \frac{\hbar\Omega_R}{2}\hat{\sigma}_z + U(\hat{\boldsymbol{r}}) + \frac{\hbar^2 k_R^2}{2m}, \tag{115}$$

where $f = 1/2$ was chosen, together with a pseudo-spin rotation $\hat{\sigma}_z \to \hat{\sigma}_y \to \hat{\sigma}_x \to \sigma_z$. The Hamiltonian in equation (115) describes a spin–orbit coupled system consisting of an equal sum of Rashba and Dresselhaus terms. This corresponds to the Abelian gauge potential $\boldsymbol{\mathcal{A}} = \hbar k_R \boldsymbol{e}_x \sigma_y$ containing a single Cartesian component. The situation is non-trivial due to an additional Zeeman term $\frac{\hbar\Omega_R}{2}\hat{\sigma}_z$, and leads to a number of interesting single- and many-body effects recently studied both experimentally [25–32, 127] and theoretically [206–214].

In figure 18(*a*) it is shown how the SOC dispersion, as a function of the laser coupling strength, is dramatically different from that of a free particle. For small Ω_R, the lowest dressed band consists of a double-well in momentum space [186], with two distinct momenta where the group velocity is zero. The states near the two minima are the dressed spin states, $|\uparrow'\rangle$ and $|\downarrow'\rangle$. As Ω increases, the two dressed spin states merge. In this limit the picture corresponds to spinless bosons with a tunable dispersion relation [215].

In the experiment by Lin *et al* [25] the effective two-level system was created in ^{87}Rb's $f = 1$ manifold where the $|m_F = -1\rangle = |\downarrow\rangle$ and $|m_F = 0\rangle = |\uparrow\rangle$ states were isolated. This could be achieved by using sufficiently large magnetic field ($g_F\mu_B B_0 \approx 4.81$ MHz) such that the quadratic Zeeman shift detuned the $|m_F = H\rangle$ state appreciably from the Raman resonance. Figure 18(*a*) shows the quasimomentum measured by first preparing an equal mixture with $|\downarrow\rangle - |\uparrow\rangle$, and then slowly increasing Ω_R. In this process, each dressed spin state adiabatically follows its associated minima. The resulting momentum can be measured using TOF, which will reveal the presence of a non-trivial SOC in the system.

Up to now only a 1D SOC corresponding Abelian gauge potential has been generated [25–32, 127] in spite of numerous proposal for creating the 2D [55, 80, 119, 162–169, 203, 204, 216–219] and 3D [203, 220] Rashba type SOC in cold atomic gases. Implementation of the 2D or 3D Rashba SOC would allow for the study of rich ground state physics proposed in systems of many-body fermions [56, 218, 221–231] and bosons [130, 165, 219, 232–241], of which many properties have no solid-state physics analog. This will be considered in the next section.

7. The effects of collisions in the presence of SOC

Synthetic magnetic fields and SOCs result from engineering the single particle Hamiltonian, however, ultracold gases can be strongly influenced by collisions. Absent artificial gauge fields, these systems are a unique playground where the inter-particle interaction strength can be tuned virtually at will [33, 34]. In this section, we describe how interacting BECs and degenerate Fermi gases behave in the presence of an external gauge potential, focusing on the case where atoms are subjected to a synthetic SOC. The interplay between interactions and synthetic magnetic fields induced by rotation were described in the review by Cooper [60]; for a more complete overview on interacting spin–orbit-coupled atomic gases, consider the reviews by Zhai [216, 242] and Zhou *et al* [243], as well as other articles recently published in the special issue on non-Abelian gauge fields edited by Gerbier *et al* [244].

7.1. The weakly interacting Bose gas with SOC

In a weakly interacting Bose gas where $a^3\rho \ll 1$ (a is the s-wave scattering length and ρ is the atom density), only two-body scattering processes are relevant. The interaction between atoms can be described by the contact potential

$$V_{\rm int}(\boldsymbol{r} - \boldsymbol{r}') = \frac{4\pi\hbar^2 a}{m}\delta(\boldsymbol{r} - \boldsymbol{r}') = g\,\delta(\boldsymbol{r} - \boldsymbol{r}'). \tag{116}$$

In most cases, the dynamics is accurately described by the mean-field GP equation [34]

$$\mathrm{i}\hbar\frac{\partial}{\partial t}\Psi(\boldsymbol{r},t)=\left(-\frac{\hbar^2}{2m}\nabla^2+V(r)+g|\Psi(\boldsymbol{r},t)|^2\right)\Psi(\boldsymbol{r},t), \tag{117}$$

a nonlinear Schrödinger equation describing the condensate wavefunction $\Psi = \langle\hat{\Psi}\rangle$, with a potential $V(r)$ and a nonlinearity proportional to the density $\rho = |\Psi(\boldsymbol{r},t)|^2$. Interactions—captured by this nonlinearity—change the dynamics dramatically compared to the non-interacting gas, as evidenced by the elementary excitation spectra [245–247] and the nucleation of vortices [84].

In the context of artificial gauge potentials we ask: what effects are added for interacting gases with SOC? This scenario has been studied by a number of authors [165, 232, 248–259], showing that SOC dramatically alters the ground state properties. In such situations, the general second-quantized Hamiltonian is

$$\begin{aligned}\hat{H}&=\int \mathrm{d}\boldsymbol{r}\,\hat{\Psi}^\dagger\left[\frac{1}{2m}(\boldsymbol{p}-\hat{\boldsymbol{\mathcal{A}}})^2+V(r)+\hat{G}(\hat{\Psi},\hat{\Psi}^\dagger)\right]\hat{\Psi}\\&=\hat{H}_0+\hat{H}_{\mathrm{int}},\end{aligned} \tag{118}$$

where the SOC is described by the gauge potential $\hat{\boldsymbol{\mathcal{A}}}$, $\hat{\Psi}$ is a multicomponent field operator, and $V(r) = m\omega^2 r^2/2$ is the confining potential with frequency ω. The exact form of the interaction term $\Psi^\dagger\hat{G}(\hat{\Psi},\hat{\Psi}^\dagger)\Psi$ depends on the details of the physical setup [34, 232, 248]. Typically, the field operator $\hat{\Psi}$ associated with a dressed state—a superposition of the bare atomic levels—and the two-body scattering lengths entering $\hat{G}(\hat{\Psi},\hat{\Psi}^\dagger)$ depend on the different bare states. In this dressed-state picture, this can yield spin-dependent collision terms, e.g., $\hat{G}_{\mu\nu}(\hat{\Psi},\hat{\Psi}^\dagger) = g_{\mu\nu}\hat{\Psi}_\mu\hat{\Psi}_\nu^\dagger$ with $g_{\mu\nu}\neq$ const, independent of the gauge potential $\hat{\boldsymbol{\mathcal{A}}}$, see [232, 248]. Furthermore (and beyond the scope of the discussion here) the atomic contact interaction can acquire momentum dependence—a finite range—from the momentum dependence of the dressed states as expressed in the basis of bare atomic states [149].

Here, we review the ground-state properties of a quasi-spin-1/2 system with isotropic 2D Rashba SOC, where $\hat{\Psi} = (\hat{\Psi}_1,\hat{\Psi}_2)^T$, and where $\hat{\boldsymbol{\mathcal{A}}}$ is simply expressed in terms of the Pauli matrices as $\hat{\boldsymbol{\mathcal{A}}} = \hbar\kappa(\hat{\sigma}_x,\hat{\sigma}_y)$[7]. The synthetic gauge potentials giving rise to SOC are remarkably flexible in the sense that the precise shape of the gauge potential can often be controlled at will. The Rashba type coupling is one example, which is also often encountered in solid-state scenarios. Such SOCs can be achieved optically [55, 167, 261], but also using periodically driven cold-atom systems, such as those based on pulsed-magnetic fields [101, 203, 204], see also section 8.

In this configuration, the single-particle energy spectrum of the homogeneous ($V(r) = 0$) system has the two energy branches $E_\pm(\boldsymbol{k}) \propto (|\boldsymbol{k}| \pm \kappa)^2$ illustrated in figure 19. The main effect of the Rashba coupling $\hat{\boldsymbol{\mathcal{A}}}$ is to replace the unique condensation point $k_{\min}(\hat{\boldsymbol{\mathcal{A}}} = 0) = 0$ by a continuum of minima located on the ring $k_{\min}(\hat{\boldsymbol{\mathcal{A}}} \neq 0) = \kappa$, see figure 19.

[7] For the ground-state properties of interacting spin-1 and spin-2 SOC bosons, see [235, 237, 238, 240, 260].

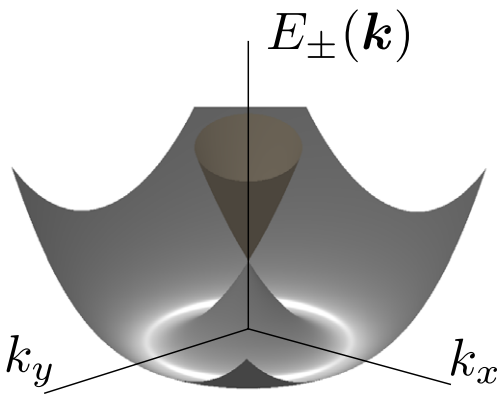

Figure 19. Dispersion for a homogeneous gas with Rashba SOC: $E_\pm(\boldsymbol{k})$. $\boldsymbol{k}$ denotes momentum in the $\boldsymbol{e}_x$-$\boldsymbol{e}_y$ plane. When $\hat{\boldsymbol{\mathcal{A}}} = \hbar\kappa(\hat{\sigma}_x,\hat{\sigma}_y)$, the lowest band is minimal on the ring $|\boldsymbol{k}| = \kappa$.

These degenerate single-particle ground states affect the many-body problem, where an interacting condensate's ground state will be chosen through a complex competition between the interactions and the parameters of the non-interacting model (e.g. the trap frequency ω and the Rashba coupling strength κ). Hence, in the presence of Rashba SOC, interactions play a major role even when they are weak [216, 242, 243].

7.1.1. The homogeneous interacting system with Rashba SOC. The mean-field phase diagram of the homogenous, $V(\boldsymbol{r}) = 0$, spin–orbit-coupled BEC is already altered by a simple interaction term of the form [248]

$$\hat{H}_{\mathrm{int}}=\int \mathrm{d}\boldsymbol{r}\,g\hat{n}_1^2+g\hat{n}_2^2+g_{12}\hat{n}_1\hat{n}_2, \tag{119}$$

where the two scattering parameters g and g_{12} account for spin-dependent collisions in a minimal manner, and where $\hat{n}_\mu = \hat{\Psi}_\mu^\dagger\hat{\Psi}_\mu$ denote the density operators. The mean-field phase diagram described below has been obtained by Wang *et al* [248], through a minimization of the GP free energy for the two-component order parameter $\Psi(\boldsymbol{r}) = \langle\hat{\Psi}(\boldsymbol{r})\rangle$, derived from the SOC Hamiltonian (118)–(119). When $g_{12} < 2g$, the densities associated with the two spin components $\rho_{1,2}(\boldsymbol{r}) = |\Psi_{1,2}|^2$ are uniform in space, but the phase of the condensate $\Psi(\boldsymbol{r}) = \langle\hat{\Psi}(\boldsymbol{r})\rangle$ varies periodically along one direction, spontaneously breaking rotational symmetry. This regime characterizes the 'plane wave phase', where the macroscopic wave function of the condensate takes the simple form [216, 248]

$$\Psi(\boldsymbol{r})=\sqrt{(\rho_1+\rho_2)/2}\,\mathrm{e}^{\mathrm{i}\kappa x}\,(1,1)^T. \tag{120}$$

Without loss of generality, we have taken the plane wave to be along $\boldsymbol{e}_x$, reflecting the spontaneous symmetry breaking. When $g_{12} > 2g$, the condensate $\Psi(\boldsymbol{r})$ is described by a superposition of two such plane waves,

$$\begin{aligned}\Psi(\boldsymbol{r})&=\frac{1}{2}\sqrt{\rho_1+\rho_2}\left[\mathrm{e}^{\mathrm{i}\kappa x}\begin{pmatrix}1\\1\end{pmatrix}+\mathrm{e}^{-\mathrm{i}\kappa x}\begin{pmatrix}1\\-1\end{pmatrix}\right]\\&=\sqrt{\rho_1+\rho_2}\begin{pmatrix}\cos(\kappa x)\\\mathrm{i}\sin(\kappa x)\end{pmatrix},\end{aligned} \tag{121}$$

yielding a periodic spatial modulation of the spin-density

$$\rho_s(\boldsymbol{r}) = |\Psi_1(\boldsymbol{r})|^2 - |\Psi_2(\boldsymbol{r})|^2 = (\rho_1 + \rho_2)\cos(2\kappa x).$$

This phase is known as the 'stripe superfluid' or 'standing wave phase' [248]. The mean-field phase diagram of the homogeneous system, obtained from the GP equation derived from equations (118)–(119) is robust against deformation of the SOC term $\hat{\boldsymbol{\mathcal{A}}}$ (without losing the cylindrical symmetry), and generally holds in the presence of additional fields, e.g. Zeeman terms [216].

7.1.2. The trapped interacting system with Rashba SOC. The phase diagram is enriched by the harmonic confinement $V(r) = m\omega^2 r^2/2$ generally present in cold-atom experiments [34]. Remarkably, novel phases emerge in trapped systems [232], even under the strong (and generally unphysical) assumption that all the interaction processes are described by a single scattering parameter, i.e. when the interaction term reduces to the spin-independent form $\Psi^\dagger \hat{G}\Psi = g_{\rm eff}(\rho_1(r) + \rho_2(r))^2$, where $g_{\rm eff}$ is an effective scattering length describing all collisions [232]. This strong simplification aims to isolate the main effects introduced by the trap in spin–orbit coupled gases[8]. The external trap introduces an additional energy scale $\hbar\omega$ into the homogenous problem discussed above, hence it is natural to describe the resulting phase diagram in terms of the dimensionless parameters $\mathfrak{K} = \kappa l_0$ and $\mathfrak{g} = g_{\rm eff} m/\hbar^2$, where $l_0 = \sqrt{\hbar/m\omega}$.

In the non-interacting regime where SOC dominates ($\mathfrak{g} = 0$, $\mathfrak{K} \gg 1$), the upper branch $E_+(\boldsymbol{k})$ can be neglected, and, going to the momentum representation, one obtains the single particle wavefunction $\Psi(\boldsymbol{k}) = \psi(\boldsymbol{k})\,\boldsymbol{u}_-(\boldsymbol{k})$, where

$$\boldsymbol{u}_-(\boldsymbol{k}) = \frac{1}{\sqrt{2}}\begin{pmatrix} 1 \\ \frac{k_x + \mathrm{i}k_y}{k} \end{pmatrix} = \frac{1}{\sqrt{2}}\begin{pmatrix} 1 \\ \mathrm{e}^{\mathrm{i}\varphi} \end{pmatrix} \qquad (122)$$

is an eigenstate of the homogeneous system in the lowest branch $E_-(\boldsymbol{k})$; and φ denotes the polar angle of $\boldsymbol{k}$. Adding the confining potential to the single-particle Hamiltonian, $H(\boldsymbol{k}) \propto (\hbar\boldsymbol{k} - \hat{\boldsymbol{\mathcal{A}}})^2 - \nabla_k^2$, and solving the corresponding Schrödinger equation using the ansatz $\psi(\boldsymbol{k}) = \sum_l k^{-1/2} f_l(\boldsymbol{k})\mathrm{e}^{\mathrm{i}l\varphi}$, yields the eigenenergies [232, 259]

$$E_{nl} = \frac{(l + \frac{1}{2})^2}{2\mathfrak{K}^2} + n + \frac{1}{2}, \qquad (123)$$

where n labels the radial excitations around the minima of the Mexican-hat potential $k \approx \kappa$ (see figure 19) and $l \in \mathbb{Z}$. The degenerate ground states

$$\Psi_{l=\{0,-1\}}(k) \propto \mathrm{e}^{-(k-\kappa)^2 l_0^2/2 + \mathrm{i}l\varphi}\boldsymbol{u}_-(\varphi) \qquad (124)$$

have quantum numbers $n = 0$ and $l = \{0, -1\}$. In real space, and using polar coordinates (r, θ), the two degenerate ground states become

$$\Psi_0(r,\theta) \propto \begin{pmatrix} J_0(\mathfrak{K}r) \\ \mathrm{e}^{\mathrm{i}\theta} J_1(\mathfrak{K}r) \end{pmatrix},$$
$$\text{and} \quad \Psi_{-1}(r,\theta) \propto \begin{pmatrix} \mathrm{e}^{-\mathrm{i}\theta} J_1(\mathfrak{K}r) \\ J_0(\mathfrak{K}r) \end{pmatrix}. \qquad (125)$$

These half-vortex states [165, 216, 232, 242, 248, 262] appear in various contexts, including topological quantum computing [263], superfluid ^{3}He [264] and triplet superconductors. The degenerate states in equation (125) and any linear combination thereof, yield the rotationally symmetric density distribution illustrated in figure 20(*a*). As pointed out in [232], this half-vortex regime (HV 1/2) survives for finite interaction strength $\mathfrak{g} < \mathfrak{g}_1$, where $\mathfrak{g}_1 \sim \mathfrak{K}^{-2}$ is related to the energy difference between the ground ($|l + 1/2| = 1/2$) and higher energy ($|l + 1/2| = 3/2$) states. Indeed, for large SOC strength $\mathfrak{K}^2 \gg 1$, the energy difference between successive angular excitations (equation (123)) is small compared to radial excitations. Thus, the population of higher angular momentum states ($l \geqslant 1$) should be favored at greater, but still reasonably small, interaction strength $\mathfrak{g} \geqslant \mathfrak{g}_1$ [232]. A condensate formed with higher angular momentum states satisfying $|l+1/2| = 3/2$, called the (HV 3/2)–phase, occurs in a certain range of the interaction strength $\mathfrak{g}_1 < \mathfrak{g} < \mathfrak{g}_2$, and has the ring-shaped density distribution depicted in figure 20(*b*).

For larger interaction strength, $\mathfrak{g} > \mathfrak{g}_2$, the gas enters a 'lattice phase', where its density is modulated in the form of a hexagonal lattice, see figure 20(*c*). Interestingly, rotational symmetry is broken and the lattice period is independent of the interaction strength $\mathfrak{g}$. In fact, the distance between the lattice minima is solely dictated by the SOC strength $\mathfrak{K}$. Consequently, the resulting momentum distribution has a robust ring-like structure with six peaks, see figure 20(*d*).

The three phases discussed above all have in common that their densities satisfy (continuous or discrete) rotational symmetry. This is no longer the case for large interaction strength ($\mathfrak{g} \gg \mathfrak{g}_2$). In this 'highly' interacting regime, the spin–orbit coupled cloud enters a 'striped phase', where the density is sinusoidally modulated in a specific direction, see figures 20(*e*)–(*f*). This anisotropic state shares similarities with the 'stripe phase' in the homogeneous system with spin-dependent interactions $g_{12} > g$ (see equation (121) and section 7.1.1). Mapping out the full phase diagram for the trapped spin–orbit coupled gas, by scanning the dimensionless parameters $\mathfrak{g}$ and $\mathfrak{K}$, reveals a surprisingly intricate picture, see figure 21. For readers further interested in the effects of finite temperature, anisotropic Rashba coupling $\hat{\boldsymbol{\mathcal{A}}} = \hbar(\kappa_x\hat{\sigma}_x, \kappa_y\hat{\sigma}_y)$ and beyond-mean-field descriptions, we refer to [216, 242], and references therein. Finally, the interplay between SOC and dipolar interactions, leading to diverse spin and crystalline structures, have been explored in [265, 266], and the effects due to the position-dependent SOC have been studied in [241].

7.2. Interacting Fermi gases with SOC

Degenerate atomic Fermi gases are a remarkably rich platform for studying strongly correlated phases common in condensed-matter systems [34, 37]. Today, the atomic systems are

[8] The interplay between spin-dependent collisions and the effects of the trap could be investigated by introducing additional scattering parameters $g_{\mu\nu} \neq g_{\rm eff}$ into the problem, in the spirit of equation (119), which could lead to even more involved phase diagrams than the one presented here.

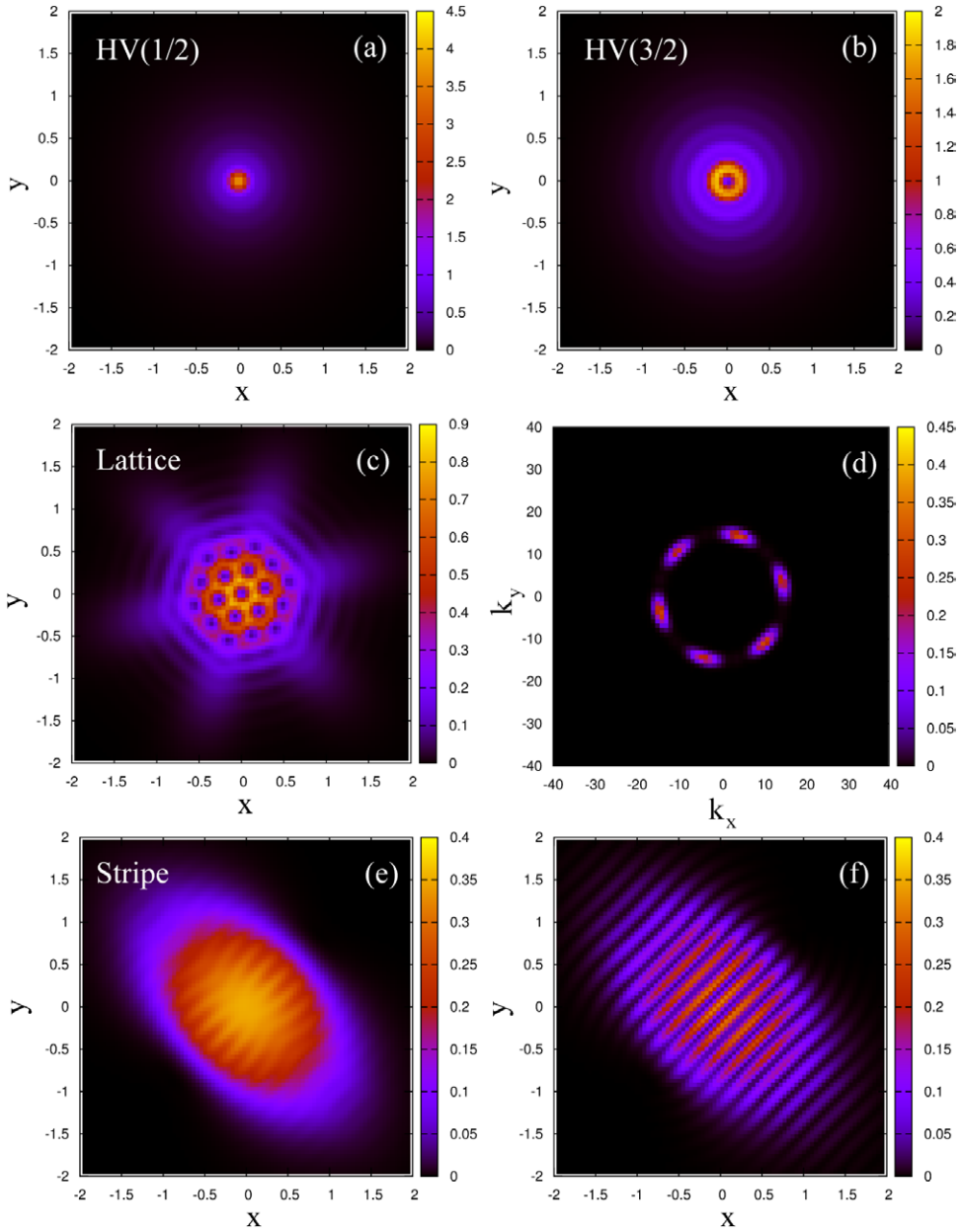

Figure 20. Trapped spin–orbit coupled gas. (*a*)–(*c*), (*e*): the ground state density $\rho = |\Psi_1(\boldsymbol{r})|^2 + |\Psi_2(\boldsymbol{r})|^2$, for increasing interaction strengths $\mathfrak{g} = 0.05, 0.1, 0.85, 2$. The dimensionless SOC strength is $\mathfrak{K} = 15$. (*d*) The momentum distribution for $\mathfrak{g} = 0.85$. (*f*) Density $\rho_1 = |\Psi_1(\boldsymbol{r})|^2$ of a single component for $\mathfrak{g} = 2$. Reproduced with permission from [232].

widely investigated, both theoretically and experimentally, to deepen our understanding of (high-T_c) superconductivity and topological phases (see also section 9). Degenerate Fermi gases offer unique advantages compared to their solid-state brethren. The interactions between fermions can be tuned at will through Feshbach resonances [34, 37], leading to various phase diagrams that describe the evolution from strongly repulsive to strongly attractive Fermi systems. For two-component (spin-1/2) fermions interacting through *s*-wave collisions, the system evolves from a BCS phase of Cooper pairs (a fermionic superfluid) when the scattering length is small and negative $a_s < 0$, to a BEC of tightly bound molecules (a bosonic superfluid) when $a_s > 0$. The crossover between the BCS and the BEC phases [9, 267, 268] takes place as $1/a_s$ travels through zero (i.e. the unitary limit $a_s = \infty$), the threshold for the formation of bound molecular states in the two-body problem [34, 37]. Here we discuss how these phase transitions are modified by the inclusion of synthetic SOC. This problem was already considered in solid-state physics, where it was shown that Rashba SOC significantly alters the physical properties of superconductors displaying strong electric fields near their surface [269]. For non-zero SOC, the Cooper-pair wavefunction is a mixture of singlet and triplet components, which results in a non-trivial and anisotropic spin susceptibility tensor that reflects the response of the system to an external magnetic field.

Vyasanakere and Shenoy [221] first demonstrated that the inclusion of a SOC term drastically modifies the properties of

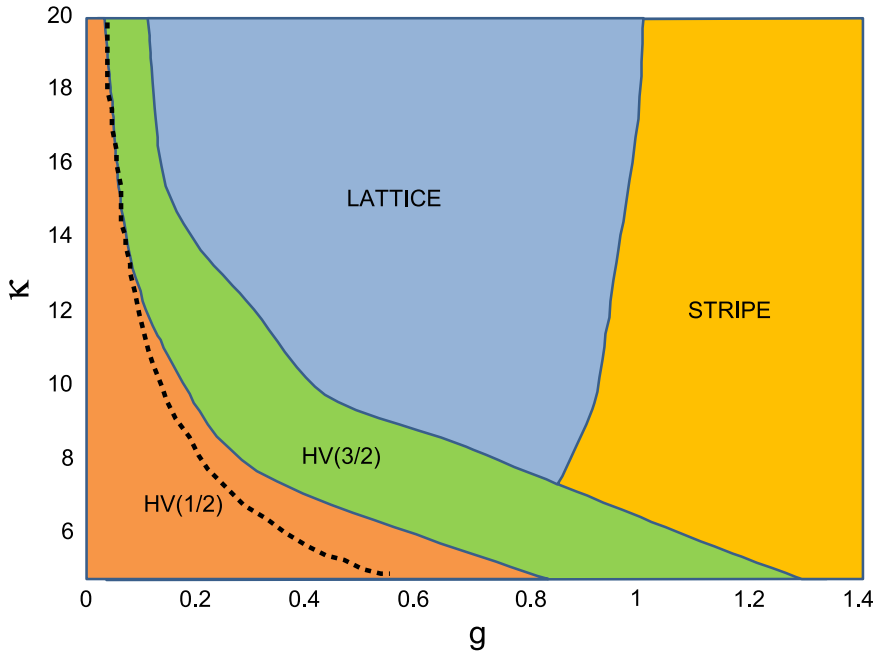

Figure 21. Ground state phase diagram of the harmonically trapped spin–orbit coupled Bose gas. Reproduced with permission from [232].

the interacting Fermi gas, especially on the BCS side of the resonance (where the scattering length is negative, $a_s < 0$). In the presence of a non-Abelian gauge potential, two-body bound states are present *even in the BCS side* $a_s < 0$ of the resonance. In other words, the SOC shifts the threshold for the formation of bound states towards finite negative values $a_s < 0$. Moreover, for certain configurations of the gauge potential (e.g. sufficiently large SOC strength), bound states are formed for *any* value of the scattering length. These SOC-induced bound states, referred to as 'rashbons', are described by a two-body wavefunction featuring singlet and triplet components, similarly to the Cooper-pair wave function in the presence of SOC [269, 270]. The rashbons lead to superfluids with nematic spin structures at low temperature, similar to superfluid ^{3}He [221]. Since bound states are allowed within the BCS regime and the binding energy E_b strongly depends on the gauge potential's strength, a subsequent work by Vyasanakere *et al* [222] showed that a BCS–BEC crossover could be induced by varying the Rashba spin–orbit strength while keeping the scattering length $a_s < 0$ *fixed* within the BCS regime. This Rashba-induced transition, from the BCS state to the molecular BEC formed by rashbons, is accompanied by a topological modification of the Fermi surface [222]. The general structure of the two-body wavefunction, with singlet and triplet components, is maintained during the transition: as the Rashba coupling is increased, the Cooper-pair wave function converges towards the rashbon wave function, suggesting that the crossover nature of the transition is preserved [222, 270]. The crossover has been further established, by confirming that the ground state is indeed protected by a gap throughout the transition [270]. A complete description of the Rashba-induced BCS–BEC crossover, in terms of various gauge potential configurations, is presented in [222] (see also [271]).

Surprisingly, at zero temperature, the condensed ρ_c/ρ and superfluid ρ_s/ρ fractions behave oppositely as the Rashba coupling strength κ is increased, see [227, 228, 272]. The condensate fraction increases monotonically with κ, eventually reaching $\rho_c/\rho \to 1$. This enhanced condensate formation, even present for $a_s < 0$ (BCS side), is compatible with the formation of the rashbons discussed above. In contrast, the superfluid fraction ρ_s/ρ is generally *reduced* by Rashba SOC. Depending on the value of the scattering length a_s, the fraction $(\rho_s/\rho)(\kappa)$ decreases monotonically or non-monotonically with increasing Rashba SOC. Superfluidity is never totally suppressed by Rashba SOC [272], furthermore, on the BCS side of resonance, the superfluid transition temperature T_c as well as the pairing gap Δ increase as a function of the Rashba coupling strength [270]. These two quantities respectively converge towards the significantly higher molecular-BEC superfluid temperature $T_c(\kappa) \to T_c^{\mathrm{BEC}} \gg T_c^{\mathrm{BCS}}(\kappa = 0)$ and the two-body binding energy $\Delta(\kappa) \to E_b \gg \Delta(\kappa = 0)$. He and Huang [227] investigated the Rashba-induced BCS–BEC crossover in two dimensions, where the Berezinskii–Kosterlitz–Thouless transition temperature is also enhanced by the Rashba coupling. Similar properties have been studied for Fermi gases trapped in optical lattices, where the interplay between interactions and the pseudo-relativistic (Dirac) spectrum generated by the Rashba coupling leads to interesting behavior [273]. Taken together, these results highlight the major deviations from standard superconductivity, which is offered by the large and tunable Rashba coupling possible in atomic systems. Methods for probing the unusual properties of atomic BCS superfluids in the presence of Rashba coupling and rashbon condensates (i.e. molecular BEC induced by Rashba coupling in the BCS limit $a_s < 0$) have been proposed in [224], based on Bragg spectroscopy and density profiles. Other effects related to the presence of Rashba (or equal Rashba–Dresselhaus) SOC during the BCS–BEC crossover could also

be measured through the isothermal compressibility and the spin susceptibility [208].

In most studies, the scattering length a_s was chosen to be independent of the synthetic SOC, and thus, it is treated as a constant along the Rashba-induced BCS–BEC crossover. [274–276] describe how interactions are modified in the presence of strong Rashba coupling, offering a relation between physical scattering lengths and mean-field interactions.

Another important topic concerns the realization of topologically ordered superfluids using Fermi gases subjected to Rashba SOC [209, 210, 225, 277–281]. This line of research is motivated by the possibility to create and control non-Abelian excitations such as Majorana fermions in a versatile setup, with possible application to topological computation (see [263] and section 9). To achieve this goal in a Fermi gas, the following basic ingredients are required: (a) a Rashba SOC $\hat{\boldsymbol{\mathcal{A}}} \sim \kappa\,\hat{\sigma}_\mu \boldsymbol{e}_\mu$ (or in 1D, any form of SOC), (b) a Zeeman term $\hat{H}_Z = h_Z\hat{\sigma}_z$ and (c) s-wave interactions with scattering length a_s [200, 278]. Based on this minimal and realistic system, several authors have investigated the rich interplay between the Rashba-induced BCS–BEC crossover, the population imbalance produced by the Zeeman term, and the emergence of topological order, which could be observed by varying the control parameters (h_z, κ, a_s) [209, 280–282]. These simple systems present a new path for exploring the FFLO finite-momentum paired states [283–287]. Finally, we note that finite-momentum ground-states can be generated in Rashba-coupled Fermi gases also in the *absence* of a Zeeman splitting term, provided that the collisional interaction is strong enough [231].

8. Gauge potentials in optical lattices: Engineering the Peierls phases

In the previous sections, we have considered the creation of artificial gauge fields for ultracold atoms moving in continuous space (i.e. typically, atoms in a harmonic trap). Here, we discuss the emergence of lattice gauge structures (e.g. artificial magnetic fluxes), which can be realized by taking advantage of the discrete motion of atoms in optical lattices. We begin with a brief overview of lattice gauge structures and lattice models, and we then describe their experimental implementation with optical lattices.

8.1. Introduction: optical lattices

In theoretical physics, lattice models are generally developed for two different reasons. The first motivation for discretizing configuration space is to apply analytical or numerical tools that are unavailable for continuum systems. The results obtained from these lattice descriptions are relevant for large systems with vanishingly small lattice periods. A prime example of this approach are lattice gauge theories, which deepen our understanding of quantum electrodynamics (QED) and QCD [288–291].

In contrast, many systems have crystalline order and are therefore quite naturally described by lattice models. This situation frequently arises in condensed-matter systems, where electrons move about in the periodic potential formed by an orderly array of ions [292] which together comprise a crystalline material. Here, the lattice is physical: the lattice spacing is finite and the hopping parameters are determined by the material under scrutiny. When electrons at the Fermi-energy are tightly bound to the ionic potential, the system is well described by the Fermi–Hubbard Hamiltonian

$$\hat{H} = -J \sum_{\langle j,k\rangle,\sigma} \left(\hat{c}^\dagger_{j,\sigma}\hat{c}_{k,\sigma} + \text{h.c.}\right) + \frac{U}{2}\sum_j \hat{c}^\dagger_{j,\uparrow}\hat{c}^\dagger_{j,\downarrow}\hat{c}_{j,\downarrow}\hat{c}_{j,\uparrow}, \tag{126}$$

a single-band tight-binding model, in which $\langle j, k\rangle$ indicates that the summation is over neighboring lattice sites. Here, J and U describe the tunneling amplitude and on-site interactions, respectively; and $\hat{c}^\dagger_{j,\sigma}$ describes the creation of a fermion at lattice site j with spin $\sigma = (\uparrow, \downarrow)$. The Hubbard model, and its generalizations, have shed light on numerous physical phenomena such as metal–insulator transitions [293], high-T_c superconductivity [294], transport properties in graphene [295], and recently topological insulating phases [73, 74, 296]. The emulation of lattice models, using quantum analog simulators [38], makes possible the exploration of effects common in condensed-matter and high-energy systems.

Ultracold atoms trapped in optical lattices can nearly perfectly realize the Hubbard model [7, 297] in the laboratory [8, 298]. Spinless bosonic or fermionic atoms are described by the general Hamiltonian

$$H = \int \mathrm{d}\boldsymbol{x}\, \hat{\psi}^\dagger(\boldsymbol{r})\left[\frac{\boldsymbol{p}^2}{2m} + V_{\text{opt}}(\boldsymbol{r}) + V_{\text{conf}}(\boldsymbol{r})\right]\hat{\psi}(\boldsymbol{r}) + g\int \mathrm{d}\boldsymbol{x}\, \hat{\psi}^\dagger(\boldsymbol{r})\hat{\psi}^\dagger(\boldsymbol{r})\hat{\psi}(\boldsymbol{r})\hat{\psi}(\boldsymbol{r}), \tag{127}$$

where $\psi^\dagger(\boldsymbol{r})$ describes the creation of an atom at position $\boldsymbol{x}$, $V_{\text{opt}}(\boldsymbol{r})$ is a periodic optical potential, $V_{\text{conf}}(\boldsymbol{r})$ is an external confining potential, and g characterizes the interatomic interaction. As a consequence of $V_{\text{opt}}(\boldsymbol{r})$'s lattice structure, it is convenient to express the field operator $\hat{\psi}^\dagger(\boldsymbol{r})$ in terms a sum over Wannier orbitals $w_\lambda(\boldsymbol{r} - \boldsymbol{r}_j)$ at site $\boldsymbol{r}_j$ and band λ, which together constitute a set of orthogonal functions [7, 292, 297, 299, 300]. For a sufficiently deep lattice potential, this expansion can be restricted to the lowest band, namely $\hat{\psi}^\dagger(\boldsymbol{r}) \approx \sum_j \hat{c}^\dagger_j w^*(\boldsymbol{r} - \boldsymbol{r}_j)$, in which case the general Hamiltonian (127) reduces to the tight-binding Hamiltonian

$$\hat{H} = \sum_j \epsilon_j \hat{c}^\dagger_j\hat{c}_j - J\sum_{\langle j,k\rangle}\left(\hat{c}^\dagger_j\hat{c}_k + \text{h.c.}\right) + \frac{U}{2}\sum_j \hat{c}^\dagger_j\hat{c}^\dagger_j\hat{c}_j\hat{c}_j, \tag{128}$$

a spinless bosonic Hubbard Hamiltonian (126), where $U \propto g$ is the on-site interaction strength and $\epsilon_j \approx V_{\text{conf}}(\boldsymbol{r}_j)$ is the energy offset [7]. The atomic Hubbard Hamiltonian (128) features the tunneling amplitudes $J_{jk} = -\int \mathrm{d}\boldsymbol{x}\, w^*(\boldsymbol{r}_j)[\boldsymbol{p}^2/2m + V_{\text{opt}}(\boldsymbol{r})]w(\boldsymbol{r}_k)$ between the nearest-neighboring sites $J_{jk} \equiv J$, which are typically much larger than the tunneling matrix elements between more distant sites [292]. Spinful Hubbard models can be implemented using fermionic or bosonic atoms with two or more internal states [301]. Experimental

realization of Hubbard type systems with ultracold atoms in optical lattices has produced important insight, starting with the experimental observation of quantum phase transitions: superfluid to Mott insulator for bosons [8] and Fermi liquid to Mott insulator for fermions [298]. In addition, different lattice topologies give rise to pseudo-relativistic Dirac fermions [302], and systems far from equilibrium can be realized [303].

Today, significant experimental effort is being devoted to realizing strong synthetic magnetic fields and to creating new kinds of SOCs in optical lattices [61, 64, 65]. Such systems are well suited for studying quantum Hall states, topological insulators and superconductors (see section 9). Optical lattices penetrated by staggered magnetic fluxes have also been realized with a view to studying frustrated magnetism [95, 97, 304]. In this section, we focus on different experimental methods for creating synthetic gauge fields in optical lattices. First, we recall how general gauge structures are defined in the lattice framework, mainly discussing the case of a uniform magnetic field (i.e. the Hofstadter model [305]). We then comment on generalizations of this concept to other families of lattice gauge structures, such as non-Abelian gauge fields. Finally, we present methods for implementing the Hofstadter model and its generalization in the lab.

8.2. Gauge structures on the lattice

Here, we review the physics of quantum particles constrained to evolve on a lattice and subjected to classical (static) gauge fields, firstly, focusing on Abelian gauge potentials, i.e. magnetic fields, in 2D lattices, and then moving to non-Abelian gauge fields.

8.2.1. The Abelian case. Consider a particle subject to a gauge potential $\boldsymbol{\mathcal{A}} \equiv q\boldsymbol{A}$ (where the coupling constant q would be the electric charge in conventional electromagnetism) confined to the $\boldsymbol{e}_x - \boldsymbol{e}_y$ plane $\mathbb{R}^2$, described by the single-particle Hamiltonian

$$H = \frac{1}{2m}\left[\boldsymbol{p} - \boldsymbol{\mathcal{A}}(\boldsymbol{r})\right]^2. \tag{129}$$

When the particle follows a path from a reference point j to a point k, whose coordinates are denoted $\boldsymbol{r}_j$ and $\boldsymbol{r}_k$, respectively, it acquires a 'magnetic phase factor' [40, 41, 306, 307]

$$\psi(\boldsymbol{r}_k) = \exp\left(\frac{\mathrm{i}}{\hbar}\int_j^k \boldsymbol{\mathcal{A}}\cdot \mathrm{d}\boldsymbol{l}\right)\psi_0(\boldsymbol{r}_k) = U_{jk}\psi_0(\boldsymbol{r}_k), \tag{130}$$

where $\psi_0(\boldsymbol{r}_k)$ denotes the wavefunction in the absence of the gauge potential, as in figure 22(*a*). Here, we introduced the *link variable* [288]

$$U_{jk} = \exp\left(\frac{\mathrm{i}}{\hbar}\int_j^k \boldsymbol{\mathcal{A}}\cdot \mathrm{d}\boldsymbol{l}\right) = \mathrm{e}^{\mathrm{i}\phi_{jk}} = \left(U_{kj}\right)^* \in \mathrm{U}(1), \tag{131}$$

embodying the effect of the gauge potential on the fictitious link connecting the points j and k. From the perspective of fiber-bundle theory, the link variables define the parallel transport on a principle fiber bundle $P(\mathrm{U}(1), \mathbb{R}^2)$, where the connection $\mathbb{A} = \mathrm{i}\mathcal{A}_\mu\,\mathrm{d}x^\mu$ is determined by the gauge potential $\mathcal{A}$ (see [76]). The link variables $U_{jk} = \exp(\mathrm{i}\phi_{jk})$ are generally called 'Peierls phases' in condensed-matter physics (see section 8.3), where they naturally appear in the description of solids subjected to magnetic fields [305, 308]. Under gauge transformations, the link variables (131) change according to

$$\boldsymbol{\mathcal{A}} \to \boldsymbol{\mathcal{A}}' = \boldsymbol{\mathcal{A}} + \boldsymbol{\nabla}\chi \tag{132}$$

$$U_{jk} \to U'_{jk} = U_{jk}\exp\left[\mathrm{i}\frac{\chi(\boldsymbol{r}_k) - \chi(\boldsymbol{r}_j)}{\hbar}\right]. \tag{133}$$

To develop lattice models, we introduce the notion of a *plaquette*, a closed region in space delimited by a set of points $\{\boldsymbol{r}_1, \boldsymbol{r}_2, \boldsymbol{r}_3, \ldots, \boldsymbol{r}_L\}$, connected by links. When the particle performs a loop $\square$ around such a plaquette, it acquires an Aharonov–Bohm phase [41, 307]

$$\psi(\boldsymbol{r}_1) \xrightarrow{\square} \exp\left(\frac{\mathrm{i}}{\hbar}\oint_\square \boldsymbol{\mathcal{A}}\cdot \mathrm{d}\boldsymbol{l}\right)\psi(\boldsymbol{r}_1) = \exp\left(2\pi\mathrm{i}\Phi_\square\right)\psi(\boldsymbol{r}_1), \tag{134}$$

where $\Phi_\square = h^{-1}\int \boldsymbol{\mathcal{B}}\cdot \mathrm{d}\boldsymbol{S}$ is the number of magnetic flux quanta $\Phi_0 = h$ penetrating the plaquette $\square$ and $\boldsymbol{\mathcal{B}} = \boldsymbol{\nabla}\times\boldsymbol{\mathcal{A}}$ is the magnetic field associated with the gauge potential $\boldsymbol{\mathcal{A}}$, see figure 22(*bc*). This is the well-known Aharonov–Bohm effect [307, 309], which can also be expressed in terms of the link variables $U_{jk} = \exp(\mathrm{i}\phi_{jk})$ defined in equation (131) as

$$\begin{aligned}\mathrm{e}^{\mathrm{i}2\pi\Phi_\square} &= U_{12}\,U_{23}\,U_{34}\ldots U_{L-1\,L}\,U_{L1} = \prod_\square U_{jk}\\ &= \exp\left(\mathrm{i}\sum_\square \phi_{jk}\right).\end{aligned} \tag{135}$$

Using equation (133), we see that the magnetic flux obtained through the 'loop' product (135) is a gauge-invariant quantity associated with the link variables

$$\begin{aligned}\mathrm{e}^{\mathrm{i}2\pi\Phi'_\square} &= \prod_\square U'_{jk} = \underbrace{\exp\left\{\frac{\mathrm{i}}{\hbar}\sum_\square\left[\chi(\boldsymbol{r}_k) - \chi(\boldsymbol{r}_j)\right]\right\}}_{=1}\prod_\square U_{jk}\\ &= \mathrm{e}^{\mathrm{i}2\pi\Phi_\square}.\end{aligned} \tag{136}$$

Here, $\tilde{\Phi} = \Phi + N$ is physically equivalent to Φ for $N \in \mathbb{Z}$, since $\exp(\mathrm{i}2\pi\tilde{\Phi}) = \exp(\mathrm{i}2\pi\Phi)$.

These general considerations suggest that the lattice description of a quantum system subject to a gauge potential $\boldsymbol{\mathcal{A}}$ should include

(a) a set of lattice sites $\{\boldsymbol{r}_j\}$,
(b) a set of links $\{j - k\}$ connecting the sites and defining plaquettes $\square$,
(c) a set of link variables $\{U_{jk}\}$ associated with the links $\{j - k\}$, see figure 22(*c*).

Here, the information in $\boldsymbol{\mathcal{A}}(\boldsymbol{r})$ is fully contained in the link variables $\{U_{jk}\}$. The physical gauge-invariant quantity is the magnetic flux penetrating each plaquette $\Phi_\square$, which can be derived from the link variables (see equation (135), and figure 22(*c*)). The gauge-invariance relation (136) is interesting from a quantum-simulation point of view, as it defines the simplest set of link variables $\{U_{jk}\}$ for any magnetic

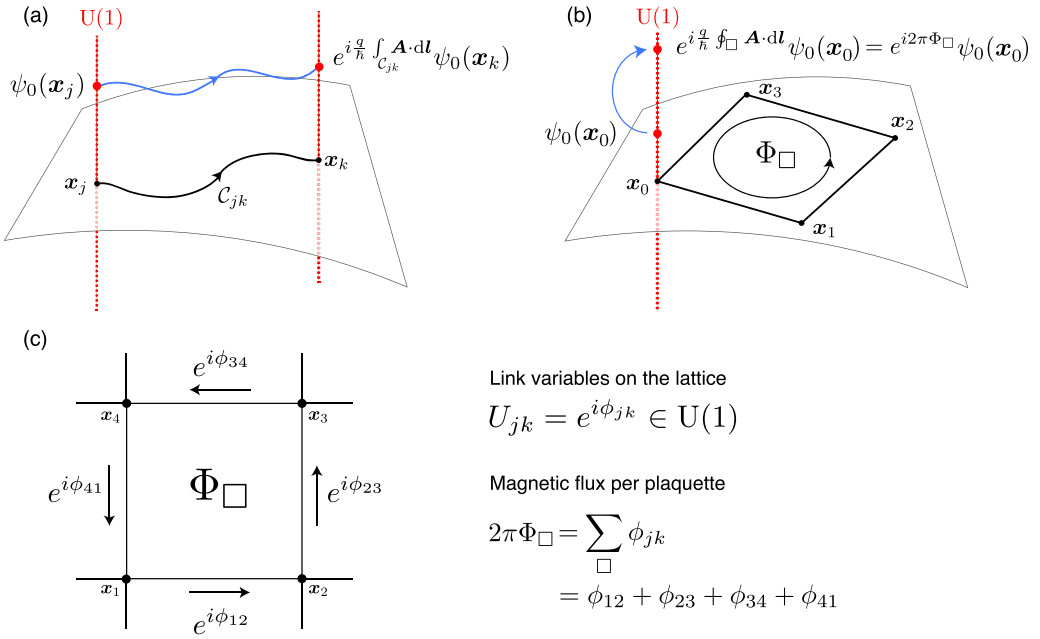

Figure 22. Quantum particle in a magnetic field $\boldsymbol{\mathcal{B}}=\boldsymbol{\nabla}\times\boldsymbol{\mathcal{A}}$. (*a*) When a particle follows a path $\mathcal{C}_{jk}$, from a reference point $\boldsymbol{x}_j$ to a point $\boldsymbol{x}_k$, it acquires a 'magnetic phase factor' $U_{jk}=\exp(\mathrm{i}\phi_{jk})\in\mathrm{U}(1)$ determined by the gauge potential $\boldsymbol{\mathcal{A}}$. (*b*) When a particle performs a loop $\square$, it realizes the Aharonov–Bohm effect. The wave function acquires a Berry phase proportional to the number of magnetic flux quanta $\Phi_{\square}$ penetrating the region enclosed by the loop. The loop $\square$ defines a U(1) transformation, called holonomy [76]. (*c*) Gauge structures on the lattice: the links $j-k$ are all associated with link variables $U_{jk}=\exp(\mathrm{i}\phi_{jk})\in\mathrm{U}(1)$, which are directly related to the magnetic flux $\Phi_{\square}$ penetrating the plaquettes, see equation (135).

flux configuration. The generalization of these concepts to higher dimensions is straightforward.

$B\sim 50\,\mathrm{T}$ is the largest magnetic field that can routinely be applied to materials. Because the typical lattice spacing is $a\approx 10^{-10}\,\mathrm{m}$, the flux per elementary plaquette $\Phi_{\square}\sim 10^{-4}$ is tiny. At higher fields, with $\Phi\sim 0.1$–1 (requiring a fantastically large magnetic field $B\sim 10^4\,\mathrm{T}$), the interplay between magnetic and lattice structures is captured by the Hofstadter model discussed in section 8.3.1. In contrast, synthetic magnetic fields for cold atoms trapped in optical lattices (section 8.4) can be engineered in the high-flux regime $\Phi\sim 0.1$–1.

8.2.2. The non-Abelian case. The proceeding discussion focused on Abelian gauge potentials and magnetic fields, where the link variables $U_{jk}\in\mathrm{U}(1)$ are phase factors that do not couple to internal degrees of freedom. These concepts can be generalized to a wide family of multi-component systems with electronic spin, color, flavor or atomic spin degrees of freedom. In the following, we will generically refer to these as 'spin' degrees of freedom. In this context, gauge potentials and link variables may act differently on the different spin states, and they are therefore matrix-valued objects (see [42, 288]). The link variables belong to a Lie group, e.g. $\hat{U}_{jk}\in\mathrm{U(N)}$ or $\hat{U}_{jk}\in\mathrm{SU(N)}$, while the non-Abelian gauge potential is an element of the corresponding Lie algebra, e.g. $\hat{\mathcal{A}}_{\mu}\in\mathfrak{u}(N)$ or $\hat{\mathcal{A}}_{\mu}\in\mathfrak{su}(N)$. A formal generalization of equation (131) defines the link variable

$$\hat{U}_{jk}=\mathcal{P}\left\{\exp\left[\frac{\mathrm{i}}{\hbar}\int_{j}^{k}\hat{\boldsymbol{\mathcal{A}}}(\boldsymbol{r})\cdot\mathrm{d}\boldsymbol{l}\right]\right\}, \tag{137}$$

in terms of the non-Abelian gauge potential $\hat{\boldsymbol{\mathcal{A}}}(\boldsymbol{r})$ (the coupling constant is again subsumed into the definition of $\hat{\boldsymbol{\mathcal{A}}}$). The path-ordered integral $\mathcal{P}(\cdot)$ is required because the matrices $\hat{\mathcal{A}}_{x,y}(\boldsymbol{r})$ at different points of the path do not necessarily commute [288, 290, 291]. The link variable $\hat{U}_{jk}$ and the non-Abelian gauge structures are clearly connected in the continuum limit, where the sites $\boldsymbol{r}_{j,k}$ are sufficiently close to each other, $\boldsymbol{r}_j=\boldsymbol{r}$ and $\boldsymbol{r}_k=\boldsymbol{r}+\epsilon\boldsymbol{e}_{\mu}$, where $\epsilon\ll 1$, $\boldsymbol{e}_{\mu}$ is the unit vector along the μ direction and $\mu=x,y$. In this case, the link variables are [288–291]

$$\begin{aligned}\hat{U}_{\boldsymbol{r},\boldsymbol{r}+\epsilon\boldsymbol{e}_{\mu}}&=\hat{U}_{\mu}(\boldsymbol{r})=\exp\left[\mathrm{i}\frac{\epsilon}{\hbar}\hat{\mathcal{A}}_{\mu}(\boldsymbol{r})\right],\\ \hat{U}_{\boldsymbol{r}+\epsilon\boldsymbol{e}_{\mu},\boldsymbol{r}}&=\hat{U}_{-\mu}(\boldsymbol{r}+\boldsymbol{e}_{\mu})=\exp\left[-\mathrm{i}\frac{\epsilon}{\hbar}\hat{\mathcal{A}}_{\mu}(\boldsymbol{r})\right],\end{aligned} \tag{138}$$

which lead to the 'loop' product around a unit square plaquette,

$$\begin{aligned}&\hat{U}_x(\boldsymbol{r})\hat{U}_y(\boldsymbol{r}+\epsilon\boldsymbol{e}_x)\hat{U}_{-x}(\boldsymbol{r}+\epsilon(\boldsymbol{e}_x+\boldsymbol{e}_y))\hat{U}_{-y}(\boldsymbol{r}+\boldsymbol{e}_y)\\ &\quad=\prod_{\square}\hat{U}_{jk}=\exp\left[\frac{\mathrm{i}\epsilon^2}{\hbar}\hat{\mathcal{F}}_{xy}(\boldsymbol{r})\right].\end{aligned} \tag{139}$$

Equations (138)–(139) define the Yang–Mills field strength [310] (analogous to the antisymmetric tensor $\hat{\mathcal{F}}_{kl}$ defined by equation (23) for the geometric gauge potentials)

$$\hat{\mathcal{F}}_{\mu\nu}(\boldsymbol{r})=\partial_{\mu}\hat{\mathcal{A}}_{\nu}(\boldsymbol{r})-\partial_{\nu}\hat{\mathcal{A}}_{\mu}(\boldsymbol{r})+\frac{\mathrm{i}}{\hbar}[\hat{\mathcal{A}}_{\mu}(\boldsymbol{r}),\hat{\mathcal{A}}_{\nu}(\boldsymbol{r})], \tag{140}$$

to leading order in ϵ (see [288] and [291] for derivations). In general, the commutator, $[\hat{\mathcal{A}}_x,\hat{\mathcal{A}}_y]\neq 0$, which is the hallmark of non-Abelian gauge theories [288]. The loop product (139) thus generalizes equation (135) to the non-Abelian case. This result connects the link variables, defined in the lattice context,

and the field strength which plays a fundamental role in continuum theories.

As for the Abelian case, a lattice system with a non-Abelian gauge structure can be entirely described by (a) the lattice topology: the sites coordinates, and the links, delimiting the unit plaquettes, and (b) the link variables $\{\hat{U}_{jk}\}$ associated with the links. Under local gauge transformations, the link variables $\hat{U}_{jk} \in U(N)$ transform according to [288, 291]

$$\hat{U}_{jk} \longrightarrow \hat{U}'_{jk} = \hat{T}_j \hat{U}_{jk} \hat{T}_k^{\dagger}, \tag{141}$$

where $\hat{T}_k \in U(N)$ is a local transformation (a rotation in spin space at the lattice site $\boldsymbol{r}_k$). Therefore, the loop product around a unit plaquette, delimited by the lattice sites $\{\boldsymbol{r}_1, \ldots, \boldsymbol{r}_L\}$,

$$\hat{U}_{\square} = \prod_{\square} \hat{U}_{jk} = \hat{U}_{12}\, \hat{U}_{23}\, \hat{U}_{34} \ldots \hat{U}_{L-1\,L}\, \hat{U}_{L1}, \tag{142}$$

is not in general gauge invariant [42, 288], since

$$\hat{U}_{\square} \longrightarrow \hat{U}'_{\square} = \hat{T}_1 \hat{U}_{\square} \hat{T}_1^{\dagger}. \tag{143}$$

This is related to the fact that the field strength $\hat{\mathcal{F}}_{\mu\nu}$, or curvature [76], of the continuum theory is not gauge-invariant. We therefore introduce the Wilson loop [288, 289, 311], a gauge-invariant quantity associated to each plaquette $\square$,

$$W(\square) = \mathrm{Tr}\big(\hat{U}_{\square}\big), \tag{144}$$

where $\mathrm{Tr}(\cdot)$ indicates the trace of the $N \times N$ matrix. The gauge invariant Wilson loop (144) generalizes the notion of flux per plaquette $\Phi_{\square}$ to non-Abelian gauge fields.

8.2.3. Genuine non-Abelian structures and the Wilson loop. Genuine non-Abelian properties result from the non-commutativity of the gauge structure. When a particle performs two successive loops γ_1 and γ_2, that both start and end at the same point $\boldsymbol{r}_0$, it will acquire a geometric phase factor $U \in U(N)$. If, for every pair of loops $\gamma_{1,2}$, this geometric phase factor does not depend on the order of the operations $U = U_{12} = U_{21}$ (where U_{12} (respectively, U_{21}) corresponds to the situation where the loop γ_1 (respectively, γ_2) has been performed first), then the system is *Abelian* in nature. The observable effects related to these phase factors are those of a *commutative* gauge theory. On the other hand, if the phase factors differ $U_{12} \neq U_{21}$ for some loops γ_1 and γ_2, then the gauge theory is genuinely *non-Abelian*. The manifestations of the underlying non-Abelian gauge structure do not have any Abelian counterpart [42, 126, 288–291].

In continuum gauge theories, the non-Abelian property $U_{12} \neq U_{21}$ can be traced back to the non-commutativity of the field strength, $[\hat{\mathcal{F}}_{\mu\nu}(\boldsymbol{r}), \hat{\mathcal{F}}_{\mu'\nu'}(\boldsymbol{r}')] \neq 0$, which naturally stems from the non-commutativity of the gauge potential's components $[\hat{\mathcal{A}}_{\mu}, \hat{\mathcal{A}}_{\nu}] \neq 0$, see [42].

As already pointed out in section 3.3, the criterion $[\hat{\mathcal{A}}_{\mu}, \hat{\mathcal{A}}_{\nu}] \neq 0$ is generally used in the literature to specify 'non-Abelian gauge potentials', but it is not sufficient to attest that the system hosts genuine non-Abelian properties, which are captured by the field strength $\hat{\mathcal{F}}_{\mu\nu}$ or the loop operators U, as described above [42, 126]. To avoid any ambiguity, we stress that the term *non-Abelian gauge fields* should be entirely based on the non-commutativity of the field strength or loop operators (see also equation (145) below), as described in this section.

An analogous criterion can be introduced in the lattice framework, in terms of the loop operator $\hat{U}_{\square}$ defined in equation (142). The lattice gauge structure associated with the link variables $\{\hat{U}_{jk}\}$ is said to be *genuinely non-Abelian* if there exists a pair of loops $\hat{U}_{\square_1}$ and $\hat{U}_{\square_2}$, both starting and ending at some site $j = 1$, such that

$$\hat{U}_{\square_1} \hat{U}_{\square_2} \neq \hat{U}_{\square_2} \hat{U}_{\square_1}. \tag{145}$$

Note that the non-Abelian criterion, based on the non-commutativity property (145), is gauge invariant, as can be verified using equation (143). Therefore, the link variables $\{\hat{U}_{jk}\}$ which lead to non-commutating loop operators, provide genuine non-Abelian effects [42, 126, 261] on the lattice.

Besides, one can introduce a simple criterion to detect lattice configurations in which all the loop matrices $\hat{U}_{\square}$ can be simultaneously gauge-transformed into a simple phase factor

$$\hat{U}_{\square} = \exp(\mathrm{i}2\pi\,\Phi)\,\hat{1}_{N\times N}, \quad \forall\, \text{loops}\, \square. \tag{146}$$

If such a reduction (146) was possible over the whole lattice, then the multi-component system would behave as a collection of uncoupled Abelian subsystems subjected to the same flux Φ [311]. On the square lattice, denoting $\hat{U}_{x,y}$ the link variables along $\boldsymbol{e}_x$ and $\boldsymbol{e}_y$, the condition $[\hat{U}_x, \hat{U}_y] \neq 0$ would constitute a natural, but incomplete criterion to detect non-Abelian structures. For example, the link variables $\hat{U}_{x,y} = \exp(\mathrm{i}\pi\hat{\sigma}_{x,y}/2)$ have $[\hat{U}_x, \hat{U}_y] = -2\mathrm{i}\hat{\sigma}_z \neq 0$, while the loop matrix around a unit cell is $\hat{U}_{\square} = \exp(\mathrm{i}\pi)\hat{1}_{2\times 2}$: this configuration therefore corresponds to a two-component lattice subjected to a uniform (Abelian) flux per plaquette $\Phi = 1/2$[9]. As shown in [311], the Wilson loop (144) provides an unambiguous criterion to determine whether the set $\{\hat{U}_{jk}\}$ leads to uncoupled Abelian subsystems captured by equation (146). Indeed, the loop operator $\hat{U}_{\square} \in U(N)$ reduces to a simple phase factor $\hat{U}_{\square} = \exp(\mathrm{i}2\pi\,\Phi)\hat{1}_{N\times N}$ if and only if the Wilson loop satisfies $|W(\square)| = N$.

The criterion based on non-trivial Wilson loops $|W(\square)| \neq N$ is a necessary condition for attesting that the link variables $\{\hat{U}_{jk}\}$ produce a non-Abelian gauge field (equation (145)). However, we stress that this condition is not *sufficient*. For instance, a spin-1/2 lattice satisfying $\hat{U}_{\square} = \exp(\mathrm{i}2\pi\,\Phi\hat{\sigma}_z)$ in all its plaquettes is clearly Abelian in the sense of equation (145), while it is generally associated with a non-trivial Wilson loop $|W(\square)| \neq 2$, since the different spin components feel an opposite magnetic flux $\Phi\hat{\sigma}_z$, i.e. the trivialization (146) is not satisfied in this case. We note that in the context of the non-Abelian Aharonov–Bohm effect [313], such a gauge field, although *Abelian*, is loosely referred to as a 'non-Abelian flux'. Again, to avoid any ambiguity, we stress that *non-Abelian gauge fields* defined on a lattice are those that satisfy the strict criterion based on non-commutating loop operations (equation (145)).

[9] Note that the mapping from N uncoupled lattices penetrated by the same magnetic flux Φ to a SU(N) tight-binding model with constant hopping operators $\hat{U}_{x,y} \in$ SU(N) has been explored in [312].

8.3. The lattice Hamiltonians: a few models

The non-relativistic Abelian and non-Abelian lattice gauge structures discussed above derive from applied gauge potentials (or equivalently, link variables). These are classical and non-dynamical and are captured by the non-relativistic tight-binding Hamiltonian

$$\hat{H} = -J \sum_{j,k} \sum_{\sigma,\sigma'} \hat{c}^{\dagger}_{j,\sigma} \left(U_{jk}\right)_{\sigma\sigma'} \hat{c}_{k,\sigma'} + \text{h.c.} \tag{147}$$

In this general expression, the operator $\hat{c}^{\dagger}_{j,\sigma}$ describes the creation of a particle at the lattice site $\boldsymbol{r}_j$, in the spin state $\sigma = 1, \ldots, N$, and the link variables $U_{jk} \in U(N)$ contribute to the hopping between connected sites (j, k). The tunneling's strength is characterized by the hopping rate matrix element J. For simplicity, we take J to be uniform; and since we are focusing on non-interacting particles, we omitted the interaction term in equation (147). In the next paragraphs, we review a few relevant lattice models corresponding to specific configurations of the lattice and link variables.

8.3.1. A uniform magnetic flux through the lattice: the Hofstadter model. A square lattice with a uniform magnetic field $\boldsymbol{\mathcal{B}} = \boldsymbol{\nabla} \times \boldsymbol{\mathcal{A}} = B\boldsymbol{e}_z$ is an iconic model—called the Hofstadter model [305]—of a two-dimensional electron gas (2DEG) in a strong magnetic field, and is the most simple case of a non-trivial gauge field in a lattice. Here, particles undergo the traditional (i.e. Abelian) Aharonov–Bohm effect when they circulate around the unit square plaquettes, $\psi(\boldsymbol{r}) \to \psi(\boldsymbol{r}) \exp(\mathrm{i}2\pi\Phi)$. This model is described by equation (147), with the specific form

$$\hat{H} = -J \sum_{m,n} \mathrm{e}^{\mathrm{i}\phi_x(m,n)} \hat{c}^{\dagger}_{m+1,n} \hat{c}_{m,n} + \mathrm{e}^{\mathrm{i}\phi_y(m,n)} \hat{c}^{\dagger}_{m,n+1} \hat{c}_{m,n} + \text{h.c.}, \tag{148}$$

where the lattice sites are located at $(x, y) = (ma, na)$, $m, n \in \mathbb{Z}$, and a is the lattice period. Here, the link variables $U_{jk} = \exp\left[\mathrm{i}\phi_{x,y}(m,n)\right] \in \mathrm{U}(1)$, commonly known as 'Peierls phases', satisfy (135),

$$\prod_{\square} U_{jk} = \mathrm{e}^{\mathrm{i}\left[(\phi_x(m,n)+\phi_y(m+1,n)-\phi_x(m+1,n+1)-\phi_y(m,n+1)\right]}, \\ = \mathrm{e}^{\mathrm{i}2\pi\Phi}. \tag{149}$$

In a tight-binding treatment [292, 305, 308], equation (148) can be obtained through the *Peierls substitution* $E_0(\hbar\boldsymbol{k} \to \hat{\boldsymbol{p}} - \boldsymbol{\mathcal{A}})$, where $E_0(\boldsymbol{k})$ is the tight-binding model's field-free dispersion relation[10]. The Hofstadter Hamiltonian (148) can also be obtained from the continuum Hamiltonian (129), by discretizing the spatial coordinates and the derivative operators [314]. This continuum approach is only rigorously valid in the limit $a \to 0$, namely for small flux $\Phi = Ba^2/\Phi_0$, where the energy structure only slightly deviates from the Landau levels. Away from this continuum limit, $\Phi \sim 1$, the tight-binding Hamiltonian (148) displays new features originating from the underlying lattice structure. The hopping phases in the Landau gauge are

$$\phi_x = 0, \phi_y(m) = 2\pi\Phi m, \text{ see figure 23 (a).} \tag{150}$$

For rational flux $\Phi = p/q$, with $p, q \in \mathbb{Z}$, the Hamiltonian commutes with the magnetic translation operators $T^q_x \psi(m,n) = \psi(m+q,n)$ and $T_y \psi(m,n) = \psi(m,n+1)$. In this gauge, the system is described by $q \times 1$ magnetic unit cells (gauge dependent) and its energy spectrum splits into q (gauge independent) subbands, see figure 23(b). The spectrum has a fractal self-similar pattern set of eigenenergies, called the Hofstadter butterfly [305], see figure 23(c), and it has quantum Hall phases with topological order, to be discussed in section 9 (see also figure 23(b)). At the special 'π-flux' case $\Phi = 1/2$, the Hofstadter lattice reduces to a two-band model displaying conical intersections at zero energy [315–317], similar to graphene's pseudo-relativistic spectrum [295, 318]. In this singular case, the system satisfies time-reversal symmetry (TRS) $H(\Phi = 1/2) \equiv H(-\Phi)$. The Hofstadter model can easily be extended to other 2D lattices [319–323], and in particular to the honeycomb lattice [316, 324], making it an efficient tool to investigate the electronic properties of graphene or other exotic materials in strong magnetic fields [325]. Finally, the effects of interactions in the Hofstadter model have been analyzed in [326–329].

8.3.2. Local magnetic flux: the Haldane model. In the early 1980s, the quantum Hall effect was discovered in 2D electronic systems at modest magnetic fields [77], and until a seminal work by Haldane [182], it was believed that the presence of a uniform magnetic field was necessary to produce this effect. In [182], Haldane introduced a lattice model demonstrating that the essential ingredient was not the magnetic field, but rather the associated breaking of TRS. In Haldane's model, while TRS is broken *locally*, the magnetic flux per unit cell is zero. Figure 23(d) shows this model's honeycomb lattice topology, featuring both nearest-neighbor (NN) and next-nearest-neighbor (NNN) hopping. While the NN hopping is trivial (positive and real valued), the NNN hopping terms are accompanied by non-trivial Peierls phases, indicating the presence of a TRS-breaking gauge potential. The corresponding Hamiltonian (147) is

$$\hat{H} = -J \sum_{\langle k,l \rangle} \hat{c}^{\dagger}_k \hat{c}_l + \mathrm{i}\lambda \sum_{\langle\langle k,l \rangle\rangle} \nu_{k,l} \hat{c}^{\dagger}_k \hat{c}_l, \tag{151}$$

where $\langle k,l \rangle$ and $\langle\langle k,l \rangle\rangle$ denotes the NN and NNN sites respectively of a honeycomb lattice, and $\nu_{k,l} = \pm 1$ depending on the orientation of the path connecting the NNN sites $\langle\langle k,l \rangle\rangle$. The Peierls phases $U_{kl} = \exp(\mathrm{i}\pi\nu_{k,l}/2)$ are complex for NNN sites, leading to non-zero *local* magnetic flux Φ_α within triangular 'subplaquettes' α, even though the total flux $\Phi = \sum_\alpha \Phi_\alpha = 0$ inside each honeycomb unit cell. For $\lambda \neq 0$, an energy gap opens in the spectrum, see figure 23(e), leading to non-trivial topological orders and quantum 'anomalous' Hall phases (see also section 9). The Haldane model played a surprising role in the prediction of the quantum spin Hall effect, an early precursor to TR preserving topological insulators (see

[10] In the case of a square lattice, the field-free dispersion relation is $E_0(\boldsymbol{k}) = -2J(\cos(k_x a) + \cos(k_y a))$, where a is the lattice spacing. Performing the Peierls substitution, $\hbar\boldsymbol{k} \to \hat{\boldsymbol{p}} - \boldsymbol{A}$ yields the effective single-particle Hamiltonian $\hat{h} = -J[\mathrm{e}^{\mathrm{i}\phi_x(r)}\hat{T}^x_a + \mathrm{e}^{\mathrm{i}\phi_y(r)}\hat{T}^y_a + \text{h.c.}]$, where $\phi_{x,y}(\boldsymbol{r}) = (a/\hbar)A_{x,y}(\boldsymbol{r})$ and where $\hat{T}^{x,y}_a$ are translation operators on the lattice, $\hat{T}^{\mu}_a \psi(\boldsymbol{r}) = \psi(\boldsymbol{r} - a\boldsymbol{1}_\mu)$ [305, 308].

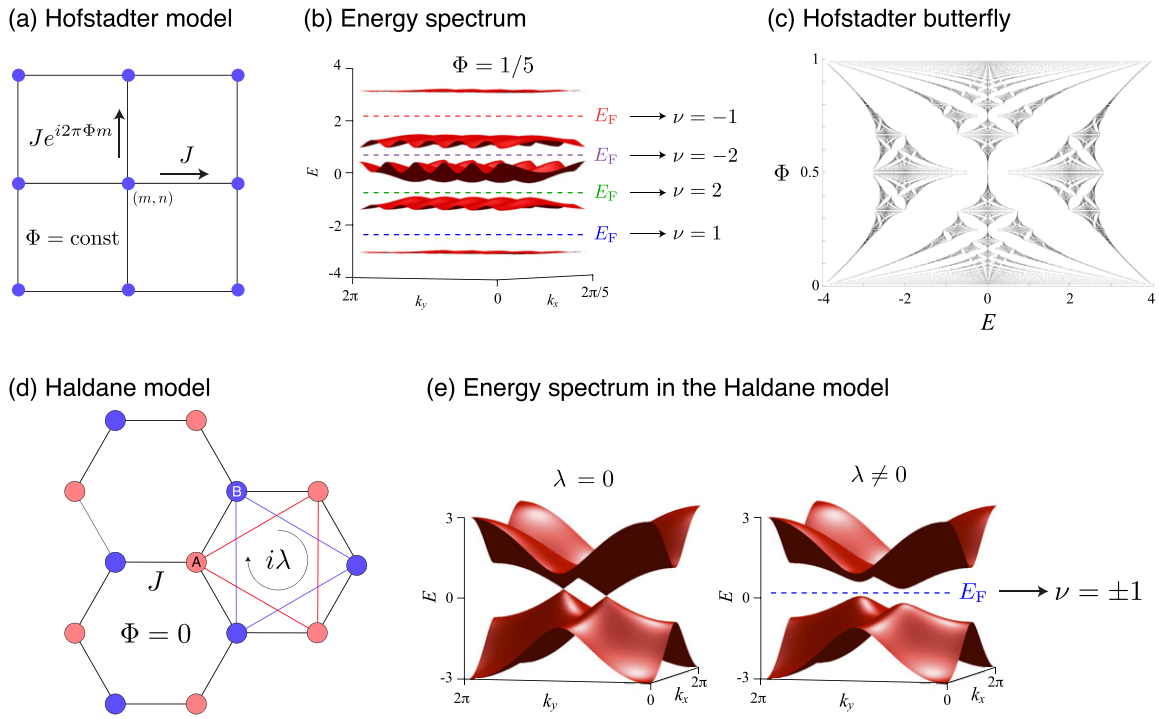

Figure 23. (*a*) The Hofstadter model on the square lattice. (*b*) Bulk energy spectrum of the Hofstadter model for $\Phi = 1/5$. The quantized Hall conductivity $\sigma_H = (e^2/h)\,\nu$ is shown for Fermi energies located within the bulk gaps. (*c*) The Hofstadter butterfly and its energy spectrum as a function of the magnetic flux Φ. (*d*) The Haldane model on the honeycomb lattice. (*e*) Energy spectrum of the Haldane model. In the absence of NNN hopping ($\lambda = 0$), the spectrum has two Dirac cones. In the presence of complex NNN hopping ($\lambda \neq 0$), a bulk gap opens, leading to an anomalous quantum Hall phase with Chern number $\nu = \pm 1$. Note that the lowest bands of the Haldane and Hofstadter models presented in (*b*) and (*e*) are topologically equivalent. However, in contrast with the Haldane model, the lowest band of the Hofstadter spectrum shown in (*b*) exhibits an almost completely flat dispersion; these topological-flat-band configurations are good candidates for realizing fractional Chern insulators [491].

below). It has recently been implemented with cold atoms using time-modulated optical lattices [490].

8.3.3. SOC on the lattice: the Kane–Mele and the spin-dependent Hofstadter models. The Kane–Mele model was introduced as a tight binding framework to explore the effects of SOCs in graphene [330, 331]. Based on this model, Kane and Mele predicted a quantum spin Hall effect, leading to the current interest in TR-invariant topological insulators (see also [73, 74, 332] and [296]). Interestingly, the intrinsic SOC term can be modeled by a NNN Haldane hopping term, acting oppositely on the two spin components $\sigma = \uparrow, \downarrow$. In the presence of SOC, each spin component feels a local 'magnetic' flux, yet TRS is preserved because the fluxes are opposite for $\uparrow$ and $\downarrow$. The corresponding link variables can be represented as 2×2 matrices, with $\hat{U}^{\rm SO}_{kl} = \mathrm{i}\nu_{k,l}\hat{\sigma}_z$. In solids, the Rashba SOC produced by an external electric field [333, 334], is modeled by a NN hopping term that mixes the spin components non-uniformly. It involves SU(2) link variables such as $\hat{U}^{\rm R}_{kl} = (\hat{\boldsymbol{\sigma}} \times \hat{\boldsymbol{d}}_{kl})_z \propto \hat{\sigma}_{x,y}$, where $\hat{\boldsymbol{d}}_{kl}$ denotes the unit vector along the link connecting the NN sites k, l. The total Kane–Mele Hamiltonian is

$$\hat{H} = -J\sum_{\langle k,l\rangle}\hat{c}^\dagger_k\hat{c}_l + \mathrm{i}\lambda_{\rm SO}\sum_{\langle\langle k,l\rangle\rangle}\nu_{k,l}\hat{c}^\dagger_k\hat{\sigma}_z\hat{c}_l + \mathrm{i}\lambda_{\rm R}\sum_{\langle k,l\rangle}\hat{c}^\dagger_k(\hat{\boldsymbol{\sigma}}\times\hat{\boldsymbol{d}}_{kl})_z\hat{c}_l, \quad (152)$$

where the three terms correspond to: direct hopping between NN sites, intrinsic SOC, and Rashba SOC [330, 331]. The Kane–Mele model for graphene can therefore be viewed as the direct SU(2) analog of the Haldane model (151) with an extra Rashba term characterized by the strength $\lambda_{\rm R}$ featured in equation (152). Just as the Haldane model produces quantum Hall states, the Kane–Mele model produces quantum *spin* Hall states, which can be viewed as two superimposed, and opposite, spin-filtered QH phases. A 3D generalization of the Kane–Mele model (152), where the link variables $\hat{U}^{\rm SO}_{kl}$ are defined along the links of a diamond lattice [335] reveals the exciting physics of 3D topological insulators [73, 74, 296].

In the same spirit, Goldman *et al* [336] introduced a spinful SU(2) analog of the Hofstadter model on a square lattice. In this model, particles with spin $\sigma = \uparrow, \downarrow$ experience a uniform magnetic flux per plaquette $\Phi_\uparrow = -\Phi_\downarrow$ opposite in sign for the two spin components. The corresponding Hamiltonian is

$$\mathcal{H} = -J\sum_{m,n}\hat{c}^\dagger_{m+1,n}\mathrm{e}^{\mathrm{i}2\pi\gamma\hat{\sigma}_x}\hat{c}_{m,n} + \hat{c}^\dagger_{m,n+1}\mathrm{e}^{\mathrm{i}2\pi m\Phi\hat{\sigma}_z}\hat{c}_{m,n} + \mathrm{h.c.}, \quad (153)$$

where the SU(2) link variables $\hat{U}_x, \hat{U}_y(m)$ act on the two-component field operator $\hat{c}_{m,n}$, defined at lattice site $(x, y) = (ma, na)$. For $\gamma = 0$, this models corresponds to two decoupled copies of the spinless Hofstadter model (148)–(150). The effect of the link variable $\hat{U}_y(m) \propto \hat{\sigma}_z$ is therefore analogous to the intrinsic SOC in equation (152). For $\gamma \neq 0$,

the two spin components are mixed as they tunnel from one site to its NN. The link variable $\hat{U}_x \propto \sin(2\pi\gamma)\hat{\sigma}_x$ plays a role similar to the Rashba coupling in equation (152). This model therefore captures the essential effects of the Kane–Mele TRS-invariant model in a multi-band framework, but offers the practical advantage of only involving NN hopping on a square lattice. The optical-lattice implementation of this model has been reported by Aidelsburger *et al* [64] and investigated by Miyake *et al* [65]. The effects of interactions in the SU(2) Hofstadter model have been analyzed by Cocks, Orth and co-workers in [338, 339].

8.3.4. The square lattice subjected to a non-Abelian gauge potential. The interplay between Abelian and non-Abelian gauge fields can be studied in a simple two-component model defined on a square lattice [311, 340], where the link variables along $\boldsymbol{e}_x$ and $\boldsymbol{e}_y$ are

$$\hat{U}_x = \mathrm{e}^{\mathrm{i}\alpha\hat{\sigma}_y}, \quad \text{and} \quad \hat{U}_y(m) = \mathrm{e}^{\mathrm{i}\beta\hat{\sigma}_x}\mathrm{e}^{\mathrm{i}2\pi\Phi m}. \tag{154}$$

The Abelian part of the gauge structure given by the U(1) phase $\phi_y(m) = \exp(\mathrm{i}2\pi\Phi m)$ in $\hat{U}_y$, corresponds to a uniform magnetic flux per plaquette Φ (see section 8.3.1). The SU(2) part is controlled by the parameters α and β. In two limiting cases this system is purely Abelian, i.e. $|W(\square)| = 2$, when $\alpha =$ integer $\times\,\pi$ or $\beta =$ integer $\times\,\pi$, and when $\alpha =$ integer $\times\,\pi/2$ and $\beta =$ integer $\times\,\pi/2$. In both cases, the system reduces to two uncoupled (Abelian) models. For arbitrary values of α, β the system features non-Abelian fluxes (see section 8.2.3) where the Wilson loop is uniform and non-trivial $|W(\square)| \neq 2$. This model was investigated in the contexts of quantum Hall physics [340–345], transition to the Mott-insulating phase [346] and non-Abelian anyonic excitations [129]. Alternative non-Abelian lattice models have been proposed and studied [261, 347–353], showing the rich properties stemming from non-Abelian structures in non-relativistic quantum systems.

8.4. Experimental realizations using optical lattices

Let us now consider the schemes enabling to create lattice gauge structures for ultracold atoms moving in optical lattices. In this context, the main ingredient for generating Peierls phases along the links of the lattice is the so-called *laser-assisted-tunneling method*, initially introduced by Ruostekoski-Dunne–Javanainen [354, 355], and Jaksch–Zoller [179].

8.4.1. Laser-assisted-tuneling using different internal states. This method is based on the possibility to couple atoms living on neighboring sites of an optical lattice, hence controlling their tunneling over the lattice, as illustrated in figure 24(*a*). Peierls phases are then engineered by controlling the phase of the coupling, which allows to simulate lattice (tight-binding) Hamiltonians with non-trivial link variables U_{jk}, for example leading to the Hofstadter Hamiltonian (148) in 2D. This method was further developed by several authors, such as Mueller [356], Gerbier–Dalibard [180], Anisimovas *et al* [362], Goldman *et al* [336, 363] and Mazza *et al* [20, 365]. The method, which can be extended to non-Abelian structures [261, 363, 365] and more exotic lattice geometries [366], can be summarized as follows:

(a) Gauge fixing: what link variables U_{jk} should be generated?
(b) Prevent spontaneous hopping along the links for which $U_{jk} \neq 1$.
(c) Atom–light coupling: induce the hopping externally and engineer the desired link variables U_{jk} by tuning the coupling lasers, see figure 24(*a*).

Any physical scheme accomplishing the crucial steps (b)–(c), relies on the specific properties of the atoms used in the experiment. For instance, Gerbier and Dalibard proposed an elegant method exploiting the unique properties of alkaline-earth or ytterbium atoms [180] (see also Anisimovas *et al* [362]). In their proposal, the induced-hopping (c) involves a coupling between the ground state and a long-lived metastable excited electronic state. For these atomic species, metastable states have remarkably long lifetimes, and thus, the single-photon transitions to the excited state have greatly reduced spontaneous emission rates (as compared, e.g., to schemes based on two-photon transitions). For the more common alkali atoms, e.g. Li, K, Rb, alternative schemes based on Raman couplings, i.e. two-photon transitions, are required [61, 64, 65, 179, 364].

8.4.2. Laser-assisted-tuneling using shaking methods. We point out that the concept of laser-induced tunneling, which is based on the coupling of atoms living on neighboring lattice sites (figure 24(*a*)), is intimately related to methods exploiting time-periodic modulations ('shaking') of the optical lattice [59, 63, 96, 304, 357, 367]. This analogy is illustrated in figure 24(*b*). Here, atoms are trapped in an optical superlattice potential, where neighboring sites are shifted in energy by the offset Δ so as to inhibit the natural hopping. A resonant modulation of the lattice then allows to re-establish the hopping in a controllable manner. In this framework, and in contrast with the standard laser-assisted method described in section 8.4.1, the atoms can be prepared in a single internal state. Designing a modulation that also transfers momentum to the atoms, e.g. using two Raman beams, also allows to generate Peierls phases in the effective hopping matrix elements (see section 8.4.3 and works by Kolovsky [357], Creffield and Sols [358, 359], Bermudez *et al* [360, 361], Lim *et al* [412] and Baur–Schleier–Smith–Cooper [103]). This 'shaking' scheme was considered in the Munich [61, 64, 364] and MIT [65] experiments to imprint space-dependent Peierls phase in a 2D optical lattice, with a view to creating the Hofstadter model (148) with cold atoms. We point out that off-resonant potential modulations can also be considered to engineer Peierls phases in optical lattices, as recently demonstrated in Hamburg [95, 97] (see section 8.5 for a more detailed discussion on periodically driven cold-atom systems).

Below, we present the main ingredients for engineering Abelian gauge structures in optical lattices, based on the experiment performed in Munich in 2011 [61, 364]. The generalization to non-Abelian (matrix-valued) link variables $\hat{U}_{jk} \in \mathrm{U}(N)$ is briefly discussed in section 8.4.6. Other interesting schemes are further discussed in section 8.5.

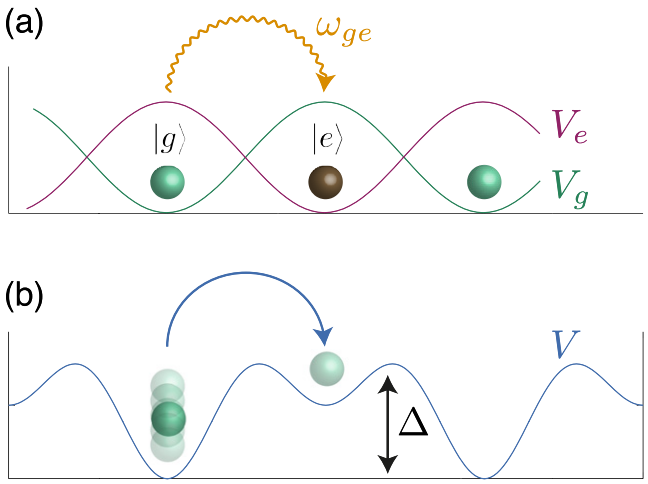

Figure 24. (*a*) Laser-assisted tunneling. Two internal states of an atom, denoted $|g\rangle$ and $|e\rangle$, are trapped in state-dependent optical lattices $V_{g,e}$. A resonant laser with frequency ω_{ge} couples the two states and induces effective tunneling matrix elements [179, 180]. The configuration where $V_g = -V_e$ can be simply implemented for Yb atoms, by using lasers at the 'anti-magic' wavelength [180, 362, 363]. (*b*) Shaking an optical superlattice. Atoms are trapped in a superlattice potential V, displaying an energy offset Δ between neighboring lattice sites and chosen so as to inhibit the hopping (i.e. $\Delta \gg J$, where J is the natural hopping amplitude). A resonant modulation of the lattice potential, with frequency $\omega \approx \Delta/\hbar$, re-activates the hopping in a controlled manner [103, 357–361]. The lattice modulation can be created by two (far-detuned) running-wave beams with frequencies $\omega_{1,2}$, such that $\omega_2 - \omega_1 = \Delta/\hbar$. The effective tunneling matrix element can be decorated with non-zero Peierls phases, when the modulation further transfers momentum $\delta\boldsymbol{k}$ to the atoms, which can be realized using Raman lasers with wave vectors $\boldsymbol{k}_{1,2}$, such that $\delta\boldsymbol{k} = \boldsymbol{k}_2 - \boldsymbol{k}_1$ (see section 8.4.3). An extension of this scheme was recently implemented in the Munich [61, 64, 364] and MIT [65] experiments. See also figure 25.

8.4.3. Laser-assisted tunneling methods: the main ingredients.

Choosing the gauge. The first step consists in selecting the gauge, thus dictating the explicit form of the link variables U_{jk}. For the Hofstadter model, we typically choose the Landau gauge (150), in which the link variables $U_{jk} = \exp\left[\mathrm{i}\phi_{x,y}(m,n)\right]$ are non-trivial along $\boldsymbol{e}_y$ only (i.e. $\phi_x = 0$ and thus the hopping along $\boldsymbol{e}_x$ can be the lattice's native tunneling). It is convenient to create non-trivial link variables U_{jk} along the links connecting the NN sites of the lattice [179, 180, 368, 369], so as to maximize the overlap between the Wannier functions (see equation (156) below).

Preventing natural hopping. In this case, the native hopping along the links for which $U_{jk} \neq 1$ must be eliminated. For example, in the Landau gauge (150), this would be the natural hopping along $\boldsymbol{e}_y$ of a square lattice. This simple, but important, task allows the subsequent external induction and control of hopping. In the Munich experiment of 2011 [61], spontaneous hopping is prohibited using a superlattice along $\boldsymbol{e}_y$, namely, by applying an energy offset Δ much larger than the natural hopping amplitude J between alternating sites, see figure 25(*a*). Schemes involving state-dependent lattices are also envisaged [179, 180], where atoms located in neighboring sites experience distinct optical potentials. State-dependent lattices are convenient for Ytterbium atoms [180], and for bosonic alkali atoms. However, for fermionic alkali atoms, they generally lead to large spontaneous rates, and thus alternative schemes are required [336].

Atom–light coupling. The tunneling between neighboring sites $j \to k$ must be induced and controlled externally, leading to an effective hopping matrix element $J^{\mathrm{eff}}_{j\to k}$. In this section, we consider the superlattice configuration used in the Munich experiment [61, 364], which is similar to the tilted lattice configuration implemented in the subsequent Munich and MIT experiments [64, 65]. We refer the reader to Refs. [80, 179, 180, 362, 363] for a description of the laser-induced tunneling methods using different internal states together with state-dependent lattices and inter-species coupling. In the superlattice illustrated in figure 25(*a*), atoms in neighboring sites occupy Wannier functions $w_l(\boldsymbol{r} - \boldsymbol{r}_j)$ and $w_h(\boldsymbol{r} - \boldsymbol{r}_k)$, respectively (here the indices l and h refer to the low energy and high energy sites in the superlattice). For a given energy offset Δ, tunneling can be induced by an external time-dependent perturbation

$$V_{\mathrm{coupl}}(\boldsymbol{r}, t) = \hbar\Omega\cos(\boldsymbol{q}\cdot\boldsymbol{r} - \omega_L t), \tag{155}$$

from a pair of Raman lasers with wave vectors $\boldsymbol{k}_{1,2}$ and frequencies $\omega_{1,2}$. The $\hbar\omega_L = \hbar(\omega_1 - \omega_2) \approx \Delta$ energy difference allows resonant coupling between the staggered lattice sites, see figure 25(*b*). Here, Ω denotes the Rabi frequency characterizing the strength of the atom–light coupling. The key ingredient of the scheme is that the momentum transfer $\hbar\boldsymbol{q} = \hbar(\boldsymbol{k}_2 - \boldsymbol{k}_1)$ can be adjusted by tuning the angle between the Raman beams. The resulting hopping amplitude, from a *low* energy site $\boldsymbol{r}_j$ to a *high* energy site $\boldsymbol{r}_k$, is then given by the integral [61, 64, 65] (see also [179, 180])

$$\begin{aligned} J^{\mathrm{eff}}_{j\to k} &= \frac{\hbar\Omega}{2}\int w_h^*(\boldsymbol{r} - \boldsymbol{r}_k) w_l(\boldsymbol{r} - \boldsymbol{r}_j)\mathrm{e}^{\mathrm{i}\boldsymbol{q}\cdot\boldsymbol{r}}\mathrm{d}\boldsymbol{r}, \\ &= J_0^{\mathrm{eff}}\mathrm{e}^{\mathrm{i}\boldsymbol{q}\cdot\boldsymbol{r}_j} = J_0^{\mathrm{eff}}\, U_{jk}, \end{aligned} \tag{156}$$

where $\boldsymbol{\delta}_{kl} = \boldsymbol{r}_k - \boldsymbol{r}_j = \boldsymbol{a}$ is the vector connecting neighboring sites j and k. The effective hopping is therefore characterized by the amplitude J_0^{eff}, along with a complex Peierls phase factor determined by the momentum transfer $\hbar\boldsymbol{q}$, see figure 25(*b*). In other words, the time-dependent perturbation (155) generates a link variable given by $U_{jk} = \exp\left[\mathrm{i}\phi(\boldsymbol{r}_j)\right]$, where $\phi(\boldsymbol{r}_j) = (\boldsymbol{k}_2 - \boldsymbol{k}_1)\cdot\boldsymbol{r}_j$. The effective hopping in equation (156) can also be written in the 'symmetric' notation

$$\begin{aligned} J^{\mathrm{eff}}_{j\to k}(\boldsymbol{r}_j, \boldsymbol{r}_k) &= \frac{\hbar\Omega}{2}\mathrm{e}^{\mathrm{i}\boldsymbol{q}\cdot(\boldsymbol{r}_j+\boldsymbol{r}_k)/2} \\ &\quad\times\int w_h^*(\boldsymbol{r} - \boldsymbol{\delta}_{kl}/2) w_l(\boldsymbol{r} + \boldsymbol{\delta}_{kl}/2)\mathrm{e}^{\mathrm{i}\boldsymbol{q}\cdot\boldsymbol{r}}\mathrm{d}\boldsymbol{r} \\ &= \tilde{J}_0^{\mathrm{eff}}\mathrm{e}^{\mathrm{i}\boldsymbol{q}\cdot(\boldsymbol{r}_j+\boldsymbol{r}_k)/2}, \end{aligned} \tag{157}$$

which is appropriate for certain geometries, especially for the non-square lattices [363, 368–370]. Importantly, the effective hopping from a *high* energy site $\boldsymbol{r}_k$ to a *low* energy site $\boldsymbol{r}_j$

$$\begin{aligned} J^{\mathrm{eff}}_{k\to j}(\boldsymbol{r}_k) &= \left(J^{\mathrm{eff}}_{j\to k}(\boldsymbol{r}_j)\right)^* \\ &= J_0^{\mathrm{eff}}\mathrm{e}^{-\mathrm{i}\boldsymbol{q}\cdot\boldsymbol{r}_j} = \tilde{J}_0^{\mathrm{eff}}\mathrm{e}^{-\mathrm{i}\boldsymbol{q}\cdot(\boldsymbol{r}_j+\boldsymbol{r}_k)/2}, \end{aligned} \tag{158}$$

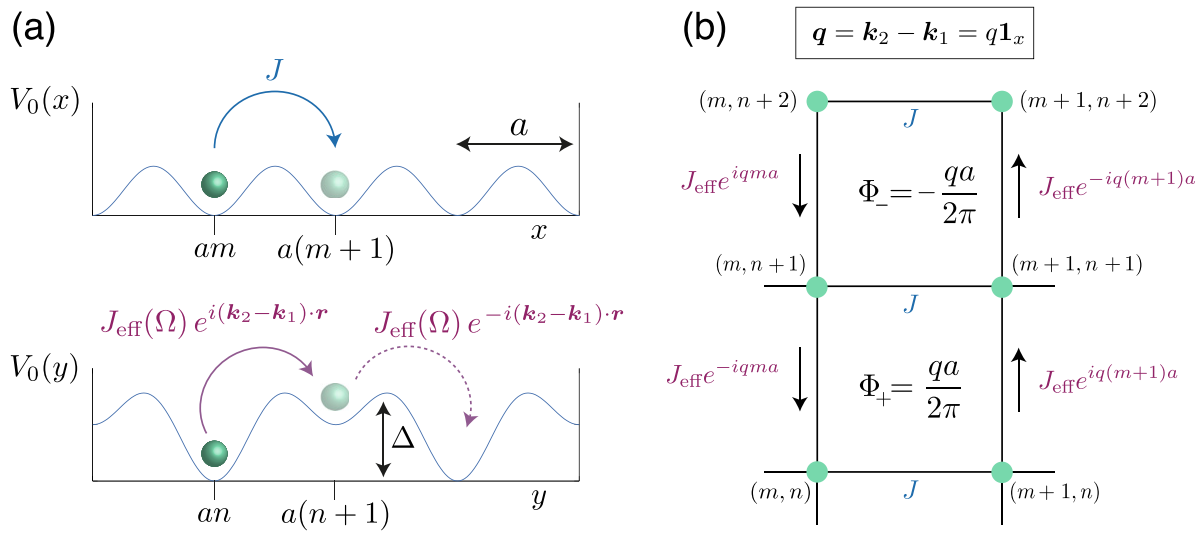

Figure 25. The laser-assisted tunneling method for creating Peierls phases in optical lattices. (*a*) The natural tunneling with amplitude J is permitted along $\boldsymbol{e}_x$, and is inhibited along $\boldsymbol{e}_y$ by a superlattice potential (with offset Δ). A pair of Raman lasers, with wave vectors $\boldsymbol{k}_{1,2}$ and frequencies $\omega_{1,2}$, induce hopping along $\boldsymbol{e}_y$ when $\omega_1-\omega_2\approx\Delta/\hbar$. The hopping matrix elements $J_{\rm eff}\exp[i\phi(\boldsymbol{r})]$ along $\boldsymbol{e}_y$ realize the Peierls substitution. (*b*) When $\boldsymbol{k}_2-\boldsymbol{k}_1=q\mathbf{1}_x$, this generates synthetic magnetic fluxes $\Phi=\pm qa/2\pi$ in the plaquettes (in units of the flux quantum). In this configuration, the flux per plaquette Φ is staggered—alternating sign along $\boldsymbol{e}_y$. A 'flux rectification' leading to a uniform magnetic flux over the lattice necessitates a slightly alternative setup (see the experiments in [65, 364] and proposals in [80, 179, 180]).

results from a momentum transfer $-\hbar\boldsymbol{q}$ reversed in sign as compared to the *low*-to-*high* case[11]. Finally, we point out that the effective tunneling amplitude can be expressed in terms of a Bessel function of the first kind $J_0^{\rm eff}=J\mathcal{J}(\kappa)$, with $\kappa\propto\Omega/\Delta$, as expected for shaken lattice systems (see [64, 65, 357, 364], and also section 8.5.1 where off-resonant driving is discussed in a related context).

8.4.4. Flux configurations on the square lattice.

Staggered flux configuration. Equations (156)–(158) and figure 25 show that the induced tunneling is necessarily accompanied with alternating Peierls phases: $\phi_y(m,n)=-\phi_y(m,n+1)=\phi_y(m,n+2)=\ldots$. Generating such Peierls phases on a square lattice,

$$\phi_x=0,\phi_y(m,n)=(-1)^n\,2\pi\Phi m, \tag{159}$$

leads to a staggered flux configuration, where successive plaquettes along $\boldsymbol{e}_y$ are penetrated by fluxes $\pm\Phi$. Here, the synthetic magnetic flux Φ is governed by the Raman coupling lasers $\Phi\sim a|\boldsymbol{q}|=a|\boldsymbol{k}_2-\boldsymbol{k}_1|$, and it can thus be set in the high-flux regime $\Phi\sim 0.1-1$, equivalent to the effects of a gigantic magnetic field $B\sim 10^4$ T for electrons in a crystalline lattice. However, this staggered configuration does not break TRS, and is only equivalent to the Hofstadter model (150) in the 'π-flux' limit $\Phi\to 1/2$. The experimental realization of the staggered flux model in 2011 [61] constituted a first important step towards the realization of the Hofstadter model (i.e. uniform magnetic flux over the whole lattice). Staggered magnetic fluxes have also been realized in off-resonant shaken triangular optical lattices in 2013 [97].

[11] Here, we assumed that the overlap integrals $J_0^{\rm eff}$ and $\tilde{J}_0^{\rm eff}$ are real [61, 179, 180, 363].

The uniform flux configuration. This alternating field must somehow be rectified to produce a uniform field. This rectification requires individually addressing successive hoppings $J^{\rm eff}_{j\to k}(\boldsymbol{r}_j)$ and $J^{\rm eff}_{k\to j'}(\boldsymbol{r}_k)$, for example using more elaborate superlattice structures and additional coupling lasers [180, 337, 365]. In such superlattices, the energy offsets Δ_1 and Δ_2 between successive NN sites are different and the induced hoppings are produced independently. This 'flux rectification', which is necessary to break TRS and produce quantum Hall states on the square lattice, has been realized in 2013 by the groups of I Bloch [64] and W Ketterle [65], using a potential gradient to individually address adjacent tunneling processes (as originally suggested in the Jaksch–Zoller proposal [179]). The uniform flux configuration has also been realized with an all-optical setup, which has been used to extract the Chern number of Hofstadter bands [492].

8.4.5. Flux configurations on the hexagonal lattice.

Additional coupling lasers (see above) are needed for special lattice geometries, such as the honeycomb lattice. As was shown in [368, 369] and [362], it is possible to generate local Haldane-like fluxes using two intertwined triangular sublattices, denoted A and B, coupled together by a single Raman coupling $A\leftrightarrow B$. In this setup, the natural hopping between the NNN sites of the honeycomb lattice (i.e. the NN sites of the triangular sublattices A and B) remains, while the laser-induced hopping with Peierls phases acts between NN sites. For arbitrary values of the Raman wave vectors $\boldsymbol{k}_1-\boldsymbol{k}_2=\boldsymbol{q}$, this configuration has non-trivial fluxes inside the subplaquettes of the unit hexagonal cells, and therefore reproduces the Haldane model's quantum Hall phases. A complete description of the phase diagrams and flux configurations stemming from this cold-atom setup can be found in [369]. This scheme could also be easily implemented

with Yb atoms, in which case it is convenient to set the lattice potential at a so-called 'anti-magic' wave-length [180]. In this case, the two internal states are automatically trapped in two intertwined triangular and honeycomb lattices, and the coupling can be directly addressed with a single-photon transition, see Anisimovas *et al* [362].

This honeycomb system could be also extended to the spinful Kane–Mele model for Z_2 topological insulators [330]. In this case, each sublattice must trap atoms in two internal atomic states (see section 8.4.6) coupled independently by lasers such that the tunneling operators (2×2 matrices acting between NN sites j and k) are $\hat{U}(j,k) = \exp(\mathrm{i}\hat{\sigma}_z \delta \boldsymbol{p} \cdot (\boldsymbol{r}_j + \boldsymbol{r}_k)/2)$. In this spinful honeycomb lattice configuration, non-trivial Z_2 topological phases, featuring helical edge states exist [369]. This system can include TR breaking perturbations, testing the robustness of the Z_2 topological phases and exploring phase transitions between helical and chiral edge textures [348, 352].

8.4.6. Matrix link variables: non-Abelian gauge potentials. The general atom-coupling method presented in section 8.4.3 for creating Peierls phases $U_{jk} = \exp\big(\mathrm{i}\phi(\boldsymbol{r})\big)$ can be extended to produce matrix-valued link variables (e.g. $\hat{U}_{jk} \in \mathrm{U}(N)$). For this, each lattice site must host N nearly degenerate spin states with index $\tau = 1, \ldots, N$. Using external (real) magnetic fields to lift any degeneracies, each state τ can then be individually trapped and coupled to other sublevel states $\tau \neq \tau'$. In particular, the effective tunneling of an atom in a specific internal state τ, from site j to k, could then be induced and controlled individually by external couplings [261, 311, 340, 363]. In principle, the coupling can be chosen to flip the atomic spin $\tau \to \tau' \neq \tau$ during the hopping process, resulting in a non-diagonal hopping matrix $\hat{J}^{\tau\tau'}_{j\to k} \propto \hat{1}_{N\times N}$. Considering the simplest case $N = 2$, this scheme can produce synthetic SOC terms with $\hat{U}_{jk} \sim \hat{\sigma}_\mu$. Such non-Abelian gauge potentials, based on spin-dependent hopping, lead to the spin-1/2 models presented in section 8.3.3, making possible topological insulators in 2D and 3D optical lattices [20, 64, 336, 337, 365]. Non-trivial hopping operators along both spatial directions, using laser-induced tunneling techniques, generally require checkerboard lattices [363].

8.5. Other relevant schemes

While our list of ingredients for inducing non-trivial link operators U_{jk} in optical lattices was based on laser-induced tunneling methods, alternative methods have been proposed and some of them have been experimentally realized. This section reviews these schemes.

8.5.1. Shaking the lattice. A quite different strategy consists in using off-resonant periodically driven optical lattices [96, 98]. One can generate artificial magnetic flux in such lattices by combining lattices and time-dependent quadrupolar potentials [101, 371], by modulating the lattice depth (i.e. the tunneling amplitude) in a directional manner [105] or by shaking optical lattices [59, 63, 96, 304, 357, 367]. Similarly, SOCs could be generated by subjecting an optical lattice to time-dependent magnetic fields [101, 203, 204]. A general formalism describing periodically driven quantum systems and effective gauge structures can be found in [101, 105].

Motivated by the recent experiments in Hamburg [63, 95, 97], let us consider a scheme based on shaken optical lattices, as already outlined in section 2.2. The method relies on off-resonant modulations of the lattice potential $V_{\mathrm{OL}}(\boldsymbol{r}')$, where $\boldsymbol{r}' \equiv \boldsymbol{r}'(t) = \boldsymbol{r} - \boldsymbol{r}_0(t)$ is the position vector in the oscillating frame of reference (see equation (4)). The displacement vector $\boldsymbol{r}_0(t) = \boldsymbol{r}_0(t+T)$ is time-periodic, with period $T = 2\pi/\omega$, and is given by equation (5) for linear or circular harmonic shaking. As presented in section 2.2, the transformation to a non-inertial frame of reference modifies the Hamiltonian by adding a spatially homogeneous vector potential $\boldsymbol{\mathcal{A}}(t)$ to the momentum, see equation (7):

$$H' = \frac{(\boldsymbol{p} - \boldsymbol{\mathcal{A}}(t))^2}{2m} + V_{\mathrm{OL}}(\boldsymbol{r}), \quad \text{with} \quad \boldsymbol{\mathcal{A}} = m\dot{\boldsymbol{r}}_0(t). \tag{160}$$

The full Hamiltonian H' shares the same spatial periodicity as the lattice potential $V_{\mathrm{OL}}(\boldsymbol{r})$, hence, the quasimomenta are still good quantum numbers for the instantaneous eigenstates and eigenenergies of the Hamiltonian H'. Since the Hamiltonian is also time-periodic, it is appropriate to deal with the quasi-energies and the corresponding eigenstates of the effective (Floquet) Hamiltonian $\hat{H}_{\mathrm{F}}$ (defined below in equation (162)) when analyzing the topological properties and effective gauge structures induced by the driving [101, 105, 106].

Let us consider a situation where the potential $V_{\mathrm{OL}}(\boldsymbol{r})$ traps atoms in a deep 1D optical lattice, directed along x, which is subjected to a harmonic modulation $x_0(t) = \kappa \sin(\omega t)$. Using the tight-binding approximation, the second-quantized lattice Hamiltonian reads

$$\hat{H}(t) = -J\left(\hat{T}\mathrm{e}^{\mathrm{i}\mathcal{A}(t)a/\hbar} + \hat{T}^\dagger \mathrm{e}^{-\mathrm{i}\mathcal{A}(t)a/\hbar}\right), \quad \hat{T} = \sum_j \hat{a}^\dagger_{j+1}\hat{a}_j, \tag{161}$$

with $\mathcal{A}(t) = m\dot{x}_0(t) = m\kappa\omega\cos(\omega t)$, where the operator $\hat{a}^\dagger_j$ creates a particle at lattice site $x = ja$, a is the lattice spacing and J is the tunneling matrix element between the neighboring sites. The time-dependent phase factors $\exp(\pm\mathrm{i}\mathcal{A}(t)a/\hbar)$ accompanying the hopping terms appear by simple application of the Peierls substitution [305, 372]. It is to be emphasized that these 'time-dependent Peierls phases' oscillate fast in time, and in particular, they should not be mistaken with the standard Peierls phases associated with (synthetic) magnetic flux discussed in section 8.3.1.

The effective (Floquet) Hamiltonian $\hat{H}_{\mathrm{F}}$ ruling the time-averaged dynamics can be defined through the evolution operator over a cycle [101, 105, 106]

$$\hat{U}(T) = \mathcal{T}\exp\left(-\mathrm{i}\int_0^T \hat{H}(\tau)\mathrm{d}\tau\right) = \exp\left(-\mathrm{i}T\hat{H}_{\mathrm{F}}\right), \tag{162}$$

where $\mathcal{T}$ denotes time ordering. In the absence of additional confining trap (e.g. a harmonic trap $V_{\mathrm{conf}} \sim x^2$), and imposing the periodic boundary conditions, one verifies that the 1D tight-binding Hamiltonian in equation (161) commutes with itself at different times. In this case, the time ordering can be omitted

in equation (162), and the effective Hamiltonian $\hat{H}_{\rm F}$ is then simply obtained through the time average

$$\hat{H}_{\rm F} = (1/T)\int_0^T \hat{H}(\tau)\,{\rm d}\tau, \tag{163}$$

$$= -J\mathcal{J}_0(\xi_0)\left[\sum_j \hat{a}^\dagger_{j+1}\hat{a}_j + a^\dagger_{j-1}\hat{a}_j\right], \quad \xi_0 = m\kappa a\omega/\hbar, \tag{164}$$

where $\mathcal{J}_0(\xi_0)$ denotes the Bessel function of the first kind [59, 101, 357].

Thus, modulating an optical lattice enables one to control the sign and amplitude of the tunneling between the neighboring sites: $J^{\rm eff}_{j\to k} = -J\mathcal{J}_0(\xi_0)$. This can have non-trivial consequences for triangular optical lattices, where a change of sign $\mathcal{J}_0(\xi_0) < 0$ leads to staggered synthetic magnetic fluxes and frustrated magnetism [95]. The effects of additional potentials, which would require time-ordering in equation (162), can be evaluated by considering a perturbative treatment in $(1/\omega)$ [101, 104, 373, 374]. In particular, we note that the cycle-averaged effective Hamiltonian in equation (163) corresponds to the lowest-order term of the Magnus expansion [373], which is generally relevant for sufficiently short periods T.

To induce complex effective Peierls phase factors, $J^{\rm eff}_{j\to k} \to J^{\rm eff}_{j\to k}{\rm e}^{{\rm i}\theta_{jk}}$, non-sinusoidal driving is necessarily required, so that certain temporal symmetries should be broken by the forcing [63]. The specific protocol implemented by Struck *et al* [63], consists in a sinusoidal forcing over a period T_1 interrupted by a short periods of rest T_2, so the lattice perturbation has a total period of $\tau = T_1 + T_2$ and a zero mean value. Under such conditions, the effective tunneling operator is [63]

$$\frac{J^{\rm eff}_{j\to k}(\xi_0,\omega)}{J} = \frac{T_2}{\tau}{\rm e}^{{\rm i}K(T_1/\tau)} + \mathcal{J}_0(\xi_0)\frac{T_1}{\tau}{\rm e}^{-{\rm i}K(T_2/\tau)}, \tag{165}$$

leading to a constant but complex valued effective Peierls phase. This scheme was realized experimentally in Hamburg, for bosons in a 1D optical lattice, where the phase θ affected the lowest Bloch band dispersion through $E(k) = -2|J^{\rm eff}_{j\to k}(\xi_0,\omega)|\cos(ka-\theta)$. In this setup, the effective Peierls phase θ can therefore be evaluated by measuring the quasimomentum distribution of the BEC, whose superfluid ground state is reached at a finite value dictated by θ [63].

The extension of this method to generate synthetic (staggered) magnetic fluxes in 2D optical lattices has been implemented for a triangular optical lattice [95, 97]. The Haldane model has been realized experimentally using such time-modulated honeycomb optical lattices [490] as already mentioned in section 8.4.2. Similar schemes can be envisaged to produce synthetic SOCs, uniform magnetic fields and topological insulating states with shaken optical lattices [100]. Recently, and in direct analogy with solid-state-physics Floquet topological states [104, 105, 107, 109, 375], it has been suggested that (circularly) shaken hexagonal optical lattices could reproduce the physics of graphene subjected to circularly polarized light (see section 2.2 and [102, 103]), with a view to realizing the Haldane model [182] and topological bands with cold atoms.

In general, the great versatility of periodically driven systems can be exploited to generate a wide family of gauge structures in cold-matter systems. Let us illustrate this fact by considering a general static Hamiltonian $\hat{H}_0$ subjected to a single-harmonic modulation $\hat{V}(t) = \hat{A}\cos(\omega t) + \hat{B}\sin(\omega t)$, where $\hat{A}$ and $\hat{B}$ are arbitrary operators. Following [101], the effective Hamiltonian reads

$$\hat{H}_{\rm eff} = \hat{H}_0 + \frac{\rm i}{2\omega}[\hat{A},\hat{B}] + \frac{1}{4\omega^2}\left([[\hat{A},\hat{H}_0],\hat{A}] + [[\hat{B},\hat{H}_0],\hat{B}]\right) + \mathcal{O}(1/\omega^3). \tag{166}$$

Hence, convenient choices for the static Hamiltonian $\hat{H}_0$ and 'pulsed' operators $\hat{A}$ and $\hat{B}$ can generate a large variety of gauge structures, such as SOC (e.g. $[\hat{A},\hat{B}] \sim p_x\sigma_x + p_y\sigma_y$) and orbital magnetism (e.g. $[\hat{A},\hat{B}] \sim xp_y - yp_x$).

The main advantage of the shaking method is that it can be applied to different lattice geometries and various atomic species. In this sense, it is particularly interesting when considering the physics of fermionic species, where state-dependent lattices and Raman coupling (see section 8.5.3) are generally associated with higher spontaneous emission rates. However, periodically driven systems might also suffer from heating issues, which could naturally emanate from the external forcing. For instance, inter-particle collisions due to the micro-motion—which is inherent to the fast modulations captured by the time-dependent Hamiltonian, e.g. equation (161)—or transitions to higher energy bands could potentially lead to uncontrollable heating processes. Moreover, the manner by which a driven quantum system absorbs energy strongly depends on its characteristics (e.g. energy spectrum), which indicates that this question should generally be addressed on a case-by-case basis. The thermodynamics of periodically driven systems is an important subject, which has been recently studied in [376–379].

8.5.2. Using RF fields. Recently, Jimenez-Garcia *et al* proposed and implemented an original setup producing periodic potential for cold atoms [62], with naturally complex tunneling operators $J^{\rm eff}_{j\to k}{\rm e}^{{\rm i}\theta}$. In other words, this scheme produces the lattice and the Peierls phases θ *simultaneously*. In this method, ^{87}Rb atoms in the $f = 1$ ground level are concurrently subjected to a radio-frequency (RF) magnetic field and to two counter-propagating Raman laser beams with wave number $k_{\rm R}$. The Raman and RF fields resonantly coupled the three spin states $|m_F = 0, \pm 1\rangle$, yielding the coupling Hamiltonian, see sections 4.4.1 and 5.2.2,

$$\hat{H}_{\rm RF+R}(\boldsymbol{r}) = \boldsymbol{\Omega}(\boldsymbol{r})\cdot\hat{\boldsymbol{F}} + \text{constant}, \tag{167}$$

where $\hat{\boldsymbol{F}}$ is the angular momentum operator and

$$\boldsymbol{\Omega}(\boldsymbol{r}) \equiv \boldsymbol{\Omega}(x) = \frac{1}{\sqrt{2}}(\Omega_{\rm RF} + \Omega_{\rm R}\cos(2k_{\rm R}x), -\Omega_{\rm R}\sin(2k_{\rm R}x), \sqrt{2}\delta).$$

Here $\Omega_{\rm RF}$ and $\Omega_{\rm R}$ are the coupling strength, or Rabi frequencies, associated with the RF and Raman fields, and δ is

the detuning from Raman resonance [62]. The two non-trivial eigenvalues obtained of (167) are

$$\Omega(x) = \pm\sqrt{\Omega_{\rm RF}\Omega_{\rm R}\cos(2k_{\rm R}x) + \text{constant}}, \qquad (168)$$

producing a periodic potential along $\boldsymbol{e}_x$ when $\Omega_{\rm RF}, \Omega_{\rm R} \neq 0$. Importantly, equation (167) describes a spin-1 particle subjected to an effective space-dependent magnetic field $\boldsymbol{B}_{\rm eff}(\boldsymbol{r}) = \hbar\boldsymbol{\Omega}(\boldsymbol{r})/g_F\mu_{\rm B}$, where g_F and $\mu_{\rm B}$ are the Landé factor and Bohr magneton, respectively. Now, according to Berry [41], an eigenstate of Hamiltonian (167) acquires a geometric (Berry) phase θ when a loop γ is performed in the parameter space spanned by the 'magnetic' field $\boldsymbol{B}_{\rm eff}(\boldsymbol{r})$. Here, $\boldsymbol{B}_{\rm eff}(\boldsymbol{r})$ is space-dependent, and therefore, the spin will precess and make a loop each time an atom hops from one lattice site to its neighboring sites (the lattice structure being dictated by equation (168)). The hopping process is therefore naturally accompanied with a non-trivial 'Peierls' phase θ, proportional to the solid angle subtended $B_{\rm eff}(\boldsymbol{r})$. This strategy relies on the fine tuning of both the Raman and RF fields, and simultaneously produces a periodic structure intrinsically featuring Peierls phases, as demonstrated experimentally at NIST [62].

Extensions of this setup could realize non-trivial magnetic flux configurations in 2D lattices, through space-dependent Peierls phases. Again, this requires more complicated but realistic arrangements, for example, combining a state-independent optical lattice along one direction with a state-dependent 'vector' lattice along the other [62]. Alternatively, one could make use of the optical flux lattices [144, 150, 174, 175, 178, 181] considered in section 5.2.3.

8.5.3. On a chip. Most proposals based on laser-coupling methods for the alkali atoms, involve two-photon Raman transitions coupling different internal atomic states. In this context, a crucial experimental issue concerns the minimization of undesired heating stemming from spontaneous emission, which cannot be reduced even using large detuning of the Raman lasers, as pointed out at the end of the section 4.4.1. This drawback is particularly severe for alkali fermions, e.g. ^{40}K and ^{6}Li, where the possible detunings are so small that they necessarily imply large spontaneous emission rates. Therefore alternative methods are required to investigate the physics of fermionic atoms subjected to synthetic gauge potentials. Several solutions have already been invoked above, such as exploiting the coupling to long-lived electronically excited states (e.g. using Ytterbium) or engineering the gauge potential through lattice-shaking methods.

Another solution consists in trapping and coupling different hyperfine levels using the magnetic (Zeeman) potentials produced by an array of current-carrying wires, therefore avoiding the use of optical state-dependent lattices and Raman coupling [336]. Here we describe how such a setup could be implemented to reproduce the Abelian gauge structure (150) of the Hofstadter model (a generalization of this atom-chip method has been described in [336] to produce the SU(2) Hamiltonian (153)). First, consider two atomic states $|g\rangle = |f = 1/2, m_F = 1/2\rangle$, $|e\rangle = |3/2, 1/2\rangle$ of ^{6}Li, trapped in a primary (state-independent) optical lattice potential $V_1(x) = V_x \sin^2(kx)$ along $\boldsymbol{e}_x$. Importantly, the corresponding pair of laser beams are incident on an atom chip's reflective surface, trapping the atoms about 5 μm above the device. The atom chip consists of an array of conducting wires, with alternating currents $\pm I$ [380], which traps the atoms in a deep 1D Zeeman lattice along $\boldsymbol{e}_y$. Since the chosen states $|e, g\rangle$ have opposite magnetic moments, the Zeeman shifts produce a state-dependent lattice along this direction. Then, additional *moving* Zeeman lattices [380], with space-dependent currents $I_m = I\sin(2\pi\Phi m - \omega t)$, act as a time-dependent (RF) perturbation directly coupling the internal states (in direct analogy with (155)), and thereby producing the desired space-dependent Peierls $\phi_y(m) = 2\pi\Phi m$. Such an elegant and versatile method, suitable both for bosonic and fermionic species, is currently in development at NIST, Gaithersburg.

8.5.4. Immersion into a rotating BEC. Jaksch and Klein proposed immersing the optical lattice and the atoms of interest (A-atoms) into a BEC formed by B-atoms [381]. Then, the interaction between the A and B atoms result in phonon excitations, which in turn induce effective interactions between A-atoms located at NN sites [381]. When B-BEC is made to rotate, the resulting effective interactions imprint space-dependent Peierls phases to the tunneling matrix elements of the A-atoms. Such a system could potentially lead to the realization of a synthetic magnetic field in the dynamics of the A-system.

8.5.5. Quasi-2D gauge structures using 1D optical lattices. Finally, interesting properties of 2D systems can be captured by 1D systems, through the concept of dimensional reduction [296]. This fact, which is particularly relevant for topological systems, offers an interesting route for the exploration of topological order using 1D optical lattices [382, 383]. Also, this strategy suggests an alternative way to reproduce the effects of magnetic fields in a simple optical-lattice environment.

Let us illustrate this concept for 2D topological systems, namely, systems exhibiting robust edge states at their 1D boundaries with energies $E_{\rm edge}$ located within bulk gaps [73]. First, suppose that the system is defined on a 2D square lattice and described by a general Hamiltonian

$$\hat{H} = \sum_{j,k} \hat{c}_j^\dagger\, h_{jk}\, \hat{c}_k, \qquad (169)$$

where $c_j^\dagger$ creates a particle at lattice site $\boldsymbol{r}_j = (m, n)$ and $m, n = 1, \ldots, L$. In this open 2D geometry, topological edge states are localized along the single 1D boundary delimiting the large square $L \times L$ [296]. Now, consider the cylindrical geometry obtained by identifying the opposite edges at $n = 1$ and $n = L$, namely, by imposing periodic boundary conditions along the y direction only. In this geometry, and considering Bloch's theorem, the system is well described by the spatial coordinate $m = 1, \ldots, L$ and the quasi-momentum

$k_y = (2\pi/L)l$, where $l = 1, \ldots, L$. In particular, the system Hamiltonian (169) can be decomposed as a sum

$$\hat{H} = \sum_{m=1}^{L} \sum_{k_y} \hat{H}(m; k_y) = \sum_{k_y} \hat{H}_{1D}(k_y), \tag{170}$$

which indicates that the 2D system can be partitioned into independent 1D chains [296]. The edge states are now located at the two opposite edges of the cylinder, defined at $m = 1$ and $m = L$, and their dispersion relations are expressed as $E_{\text{edge}} = E_{\text{edge}}(k_y)$. The general dimensional-reduction strategy can be formulated as follows: the energy spectrum and edge-state structures emanating from the 2D Hamiltonian (169)–(170) could be captured by a family of 1D models with Hamiltonians $\hat{H}_{1D}(\theta)$, where the controllable parameter $\theta \in [0, 2\pi]$ should be identified with the quasi-momentum k_y. In other words, engineering a 1D system with tunable Hamiltonian $\hat{H}_{1D}(\theta)$ would provide useful informations related to the full 2D system of interest (169).

To be specific, let us consider the Hofstadter model introduced in section 8.3.1 and described by the Hamiltonian (148)–(150). Using the Landau gauge, the single-particle wave function can be written as $\psi(m, n) = \exp(ik_y n)u(m)$, where the function $u(m)$ satisfies a 1D Schrödinger equation and where k_y is the quasi-momentum along $\boldsymbol{e}_y$. The Schrödinger equation associated with this 'Hofstadter cylinder' takes the form of the Harper–Aubry–André equation [78, 305, 384]

$$E\psi(m) = -J\big[\psi(m+1) + \psi(m-1) + 2\cos(2\pi\Phi m - k_y)\psi(m)\big], \tag{171}$$

where $m = 1, \ldots, L$. Solving this equation yields the projected bulk bands of the Hofstadter model $E(k_x, k_y) \to E(k_y)$, which display $q - 1$ bulk gaps for $\Phi = p/q \in \mathbb{Q}$. Moreover, since the cylinder is a partially opened geometry (with edges), new states with energies $E_{\text{edge}}(k_y)$ are located within the bulk gaps. These states are topological edge states, which play an important role in the quantum Hall effect [78]. A typical spectrum, showing the bulk and edge states dispersions, is shown in figure 26. Originally, the Aubry–André model (171) was studied as a simple model for Anderson localization [384]. In this 1D model, k_y is an adjustable parameter (not related to quasi-momentum), and it is therefore treated on the same level as the parameter Φ. Recently, this model has been realized with cold atoms [385], in a quasi-periodic 1D lattice created by interfering two optical lattices with incommensurate wave numbers $k_{1,2}$. In this context, the parameters in equation (171), $\Phi = k_2/k_1$ and k_y, are tuned by the lasers creating the two lattices [385]. This reproduces the dimensional reduction of the Hofstadter optical lattice, where the synthetic magnetic flux Φ can be easily adjusted and where the 'quasi-momentum' k_y is fixed by the laser phases. Considering fermionic atoms in such a 1D setup, and setting the Fermi energy inside a bulk gap, it is possible to populate topological edge states for a certain range of the tunable phase k_y [382, 386].

Extending this scheme to two-component 1D optical lattices, and considering well-designed state-dependent bichromatic optical lattices [383], Mei *et al* obtained the dimensional reduction of the Z_2 topological insulator in equation (153). By sweeping the tunable phase k_y, one is then able to transfer topological (helical [330]) edge states with opposite spin, from one edge to the other [383]. The interacting bosonic version of the 1D bichromatic optical lattice described above has been explored by Deng and Santos [387], where the topological phase diagram has been obtained in terms of the interaction strength, the atomic filling factor and the strength of the auxiliary lattice.

The dimensional reduction strategy therefore allows to access gauge structures and topologically ordered phases in a rather simple manner. These methods could be extended to access unobserved phenomena, such as the 4D quantum Hall effect [388].

Finally, 2D atomic lattice systems could be realized through the concept of *synthetic dimensions* [389], where the dimensionality of the physical optical lattice D_{phys} is augmented by a synthetic dimension spanned by the internal states of the atoms. For instance, a 2D (semi-)synthetic lattice could be obtained from a $D_{\text{phys}} = 1$ optical lattice with L lattice sites (with spatial coordinates $x = ma$, where a is the physical lattice spacing and $m = 1, 2, \ldots, L$), and filled with a N-component atomic gas: in such a configuration, the 2D synthetic lattice is characterized by $L \times N$ lattice sites located at the coordinates $\boldsymbol{r}_{\text{site}} = (m, n)$, where $m = 1, \ldots, L$ and $n = 1, \ldots, N$. In synthetic lattices, the hopping is natural along the physical direction x, while it is assisted along the synthetic (spin) direction through atom–light coupling (e.g. Raman transitions). The realization of synthetic magnetic fluxes in synthetic lattices has been described by Celi *et al* in [390], where it was shown that such setups could be exploited to observe the Hofstadter butterfly spectrum and the evolution of chiral (topological) edge states, using atoms with $N > 2$ internal states. The propagation of chiral edge states in ladder systems ($N = 2$) penetrated by synthetic magnetic fields has been studied by Hügel and Paredes [391]. An experimental implementation of such a ladder scheme (without involvement of the synthetic dimension) has been recently reported by Atala *et al* [392].

9. Probing the effects of synthetic gauge potentials: a quantum simulation perspective

The addition of synthetic gauge potentials can modify the properties of the atomic system significantly. By appropriately tuning this gauge field, single- and many-body configurations can be obtained, leading to a plethora of interesting quantum phases. Numerous cold-atom systems can realize quantum Hall physics, where Landau-like levels emerge from a synthetic magnetic field, e.g. through rotation [60] or laser-induced methods [80]. Similarly, optical-lattice setups subjected to synthetic magnetic fluxes lead to band structures characterized by non-zero Chern numbers or Wilson loops, offering an alternative route to reach quantum Hall (Chern insulating) phases. Cold-atom simulators of quantum Hall states are motivated by the fact that these controllable systems could offer an instructive insight on the physics of QH liquids, such as those featuring non-Abelian excitations [60, 129, 178, 393].

We note that QH photonics systems offer an alternative route towards this goal [394–401].

The full set of non-interacting topological phases of matter have now been classified [73, 74]. This 'Periodic Table' includes the Z_2 topological insulators, which have been experimentally observed in 2D and 3D materials [402–404], but also includes topological insulating and superconducting phases that are not known to exist in materials [73, 74]. Cold-atom setups subjected to gauge potentials might be tailored to access these phases, including those exhibiting Majorana zero modes [225, 278] (see also the proposals to realize topological Kitaev-like chains using atomic quantum wires [405–408]).

Gauge structures have been experimentally realized in several laboratories (see previous sections), and a first observation of the Zak (geometric) phase [116] has been reported for a 1D optical lattice reproducing the Rice–Mele model [409]. However, going beyond this first step, the detection of quantized topological invariants in atomic setups remains an important issue.

In this section, we review methods for identifying topological matter using probes that are available in existing cold-atom laboratories. While we focus on detecting topological order, synthetic gauge potentials can also lead to other interesting effects, such as pseudo-relativistic band structures (see the review [410] and the laboratory measurement of Zitterbewegung [32]) and vortex physics (see the review [60] and also [351, 411, 414]). Finally, the quantum simulation of quantum field theories, such as encountered in high-energy physics, is discussed in section 10.

9.1. Probing quantum Hall physics in synthetic magnetic fields: from atomic Landau levels to strongly correlated states

In 2D electronics systems, the Lorentz force from a perpendicular magnetic field deflects electrons perpendicular to a driving electric field, resulting in a non-zero transverse Hall conductivity [292]. Thus the associated transverse current is a natural signature of synthetic magnetic fields in cold-atom systems. However, transport measurements are relatively complicated to perform in cold-atom experiments, as it requires the challenge of first connecting reservoirs to the system and then detect currents [415]. Recently, an analogue of a transport experiment in a flattened BEC subjected to a synthetic magnetic field was performed in the AC limit—analogous to capacitively contacting an electronic system. In this scheme [147], currents are induced by modulating the external confining potential, allowing the full reconstruction of the resistivity tensor (including the Hall response).

The quantum mechanical problem of a particle in a magnetic field has the well-known Landau levels as its eigenenergies, which lie at the root of the quantum Hall effect [77]. For non-interacting fermions in a synthetic magnetic field, the 'LLL-regime' (where only the LLL is occupied) could be detected in TOF experiments, by simply observing that the LLL states expand much faster than the states in higher Landau levels [416]. In the weakly interacting regime of cold bosonic gases in a synthetic magnetic field, the mean field ground state is characterized by a macroscopic occupation of the LLL, giving rise to a triangular vortex lattice in the particle density (see section 5.4.3 and [60]). As the number of vortices increases, the atomic analog of the QH filling factor decreases and the system enters the strongly correlated regime where a family of FQH-like liquids have been predicted [60, 178, 326, 393, 417, 418]. A thoughtful description of the atomic Landau problem is given in [60], where observable signatures are discussed both for the weakly and strongly interacting regimes. The stabilization of FQH atomic states in realistic conditions, e.g. by significantly increasing the incompressibility gap with respect to typical experimental temperatures, still constitutes a fundamental issue [60, 178, 417, 419, 420]. Once realized in laboratories, the FQH liquids could be distinguished in experiments owing to their incompressible nature, manifested as plateaus in the atomic density distribution [421]. Additional signatures of these strongly correlated states are present in transport measurements with fractional transverse (Hall-like) conductivities [326, 422], through density–density correlation functions [423], or by the response of the atomic cloud to quasihole excitations induced by an external laser beam [424]. Finally, the topological order associated with these FQH states could be evaluated by directly detecting the topological edge states (see [79] and section 9.2.1 below).

9.2. Identifying topological order

Diverse theoretical proposals to simulate topological phases with cold atoms exist. These proposals describe techniques for creating Chern insulators [150, 174, 178, 179, 181, 350, 368, 369, 425–429], Z_2 topological insulators in 2D [336, 365, 383, 430] and 3D lattices [20], (interaction-induced) topological Mott insulators [431, 432], Z (class AIII) topological insulators in 1D [433], and topological superconductors [225, 406–408, 434]. Recently, the 1D Rice–Mele model was realized in a 1D optical lattice [409], where its non-trivial topological phase has been identified through the experimental determination of the Zak phase.

In general, detecting topological properties is subtle. Topological phases are all specified by two 'holographic' characteristics [73, 74]: (1) in a topologically ordered bulk, there exists a non-zero topological invariant associated with the bulk states [435], and (2) topological edge states are spatially localized on the periphery of the system with energies within the bulk gaps [78]. Both properties are robust and simultaneously survive as long as the bulk gaps remain open and temperatures are small compared to the gaps. In the following, we consider non-interacting fermionic systems with the Fermi energy tuned inside such a topological gap.

Before reviewing proposals for measuring topological properties in atomic systems, let us briefly summarize the state-of-the-art in solid-state systems. Topological invariants have been revealed through transport measurements, e.g., by measuring the Hall conductivity in the integer QH regime [435, 436], or in the quantum spin Hall (QSH) regime of topological insulators [73, 74]. Besides, edge states have been identified through spectroscopy [73, 74] and interference methods [437, 438]. Very recently, QSH helical edge states

have been directly imaged using a cryogenic microwave impedance microscope [439].

Performing transport measurements in atomic systems is not as straightforward as in condensed-matter setups. However, cold-atoms setups offer complementary techniques that can be exploited to measure topological invariants and identify topological edge states. In the following sections, we sketch several methods allowing to identify the Chern number ν, which classifies Chern (QH) insulating phases [435, 436]. Generalizations of these methods to detect other topological classes are also discussed.

9.2.1. Atomic Chern insulators: measuring the Chern number and topological edge states.

Density plateaus in the Hofstadter optical lattice, the Streda formula and signatures in TOF experiments. The Hofstadter butterfly is the spectrum of a particle on a 2D lattice subjected to a uniform magnetic field [305]. When the magnetic flux per plaquette is rational, $\Phi = p/q \in \mathbb{Q}$, this spectrum splits into q sub-bands $E_\lambda(\boldsymbol{k})$, where $\lambda = 1, \ldots, q$ and where $\boldsymbol{k} = (k_x, k_y)$ is the quasi-momentum, see figure 23(*b*). Each bulk band $E_\lambda(\boldsymbol{k})$ is associated with a Chern number N_λ, a topological index which remains constant under external perturbations as long as the bulk gaps do not close [435]. The Chern number ν_λ is an integer given by the integral

$$\begin{aligned}\nu_\lambda &= \frac{1}{2\pi}\int_{BZ} \mathcal{F}_\lambda(\boldsymbol{k})\mathrm{d}\boldsymbol{k} \\ &= \frac{\mathrm{i}}{2\pi}\int_{\mathbb{T}^2} \langle\partial_{k_x} u_\lambda(\boldsymbol{k})|\partial_{k_y} u_\lambda(\boldsymbol{k})\rangle - (\partial_{k_x} \leftrightarrow \partial_{k_y})\mathrm{d}^2\boldsymbol{k}, \end{aligned} \tag{172}$$

over the first Brillouin zone (BZ) of the Berry's curvature $\mathcal{F}_\lambda$ associated with the band $E_\lambda(\boldsymbol{k})$. Here, $|u_\lambda(\boldsymbol{k})\rangle$ is the single-particle state in the E_λ band with crystal momentum $\boldsymbol{k}$. This topological order strikingly manifest itself when the Fermi energy E_F resides in a bulk energy gap. The transverse (Hall) conductivity is then quantized as

$$\sigma_H = \sigma_0\,\nu = \sigma_0 \sum_{\lambda<E_F} \nu_\lambda, \tag{173}$$

where the sum includes the contribution of all occupied bulk bands, and σ_0 is the conductivity quantum, see figure 23(*b*). Interestingly, this quantized quantity is related to the particle density $n(\boldsymbol{x})$, making its detection with cold atoms particularly practical [440]. The connection to density is based on the Streda formula [315, 441], which re-expresses the quantized Hall conductivity as the derivative $\sigma_H \propto \partial N/\partial B$, where N is the number of states lying below the Fermi energy and B is the magnetic field. For optical lattice experiments with a smooth confining potential $V_c(r)$, the spatial density profile $n(r)$ in the local-density approximation is [180]

$$n(r) = \int \mathrm{d}E\; D(E)\,\Theta[E_F - V_c(r) - E], \tag{174}$$

where $D(E)$ is the homogeneous-system density of states. Thus, the density $n(r)$ counts the number of states below the 'local chemical potential' $\mu(r) = E_F - V_c(r)$. In the presence of a uniform synthetic magnetic flux $\Phi \approx p/q$, the bulk energy spectrum $E(\boldsymbol{k})$ associated with the homogeneous system is split into q bulk bands. According to equation (174), this splitting will produce $q-1$ plateaus in the density profile $n(r)$ [180]. One can thus associate each density plateau with one of the $q-1$ bulk gaps characterizing the homogeneous-system spectrum $E(\boldsymbol{k})$. Then, by comparing the density plateaus $n_{1,2}$ obtained from two different configurations of the magnetic flux $\Phi_{1,2}$ but corresponding to the opening of the same bulk gap in the bulk spectrum $E(\boldsymbol{k})$, one obtains the analogue of the Streda formula for the Hofstadter optical lattice [440]. Identifying the plateaus $n_{1,2}$ corresponding to the same rth bulk gap, one obtains the integer

$$\nu = \frac{\Delta n}{\Delta\Phi} = \frac{n_2 - n_1}{\Phi_2 - \Phi_1} = \sum_{\lambda=1}^{r} \nu_\lambda, \tag{175}$$

analogous to the quantized Hall conductivity of an electronic system with the Fermi energy set within the rth gap [440]. This method allows access to the sum of Chern numbers $\sum_{\lambda=1}^{r}\nu_\lambda$, by comparing two measurements of atom density at different values of synthetic magnetic flux, and offers a simple method to identify topological order [440] and phase transitions [442].

Moreover, it was shown in [443] that the topological quantity ν could also be revealed in the momentum density $\rho(\boldsymbol{k})$ of the same Hofstadter optical-lattice. Indeed, under specific conditions, i.e. in the limit of large hopping anisotropy or for small synthetic flux per plaquette Φ, the images obtained from TOF experiments should display oscillations whose periodicity can be related to the value of ν [443].

Measuring the winding number of a Haldane–Chern insulator. The Haldane model [182] and its cold-atom generalizations [368–370, 425–429] are all described by two-band Hamiltonians of the form

$$H(\boldsymbol{k}) = \epsilon(\boldsymbol{k})\hat{1} + \boldsymbol{d}(\boldsymbol{k})\cdot\hat{\boldsymbol{\sigma}}, \tag{176}$$

where $\hat{\boldsymbol{\sigma}} = \hat{\sigma}_{x,y,z}$ is the vector of Pauli matrices. The Berry's curvature $\mathcal{F}$ associated with the lowest energy band $E_-(\boldsymbol{k})$, and the related Chern number ν in equation (172), can be expressed in terms of the normalized vector $\boldsymbol{n}(\boldsymbol{k}) = \boldsymbol{d}(\boldsymbol{k})/|\boldsymbol{d}(\boldsymbol{k})|$ [296],

$$\mathcal{F}(\boldsymbol{k}) = \frac{1}{2}\boldsymbol{n}\cdot(\partial_{k_x}\boldsymbol{n}\times\partial_{k_y}\boldsymbol{n}), \tag{177}$$

$$\nu = \frac{1}{4\pi}\int_{\mathbb{T}^2} \boldsymbol{n}\cdot(\partial_{k_x}\boldsymbol{n}\times\partial_{k_y}\boldsymbol{n})\,\mathrm{d}\boldsymbol{k}. \tag{178}$$

From this, we notice that the Chern number ν measures the number of times the vector field $\boldsymbol{n}(\boldsymbol{k})$ covers the unit sphere as $\boldsymbol{k}$ is varied over the entire BZ $\mathbb{T}^2$. Therefore, for a system prepared in a phase $\nu \neq 0$, an experimental measurement of $\boldsymbol{n}(\boldsymbol{k})$ would depict a Skyrmion pattern on a 'pixelated' BZ, leading to an approximate measure of the Chern number [368–370]. For the specific Haldane-like model introduced by Alba *et al* and discussed in section 8.4.5, the vector field $\boldsymbol{n}(\boldsymbol{k})$ can be reconstructed from spin-resolved momentum densities $\rho_{A,B}(\boldsymbol{k})$ associated with the two atomic species present in the lattice [368–370]. This model therefore offers a simple platform to measure the Skyrmion patterns and topological index ν from spin-resolved TOF images.

Semiclassical dynamics, the Berry's curvature and the Chern number. The equations of motion of a wave packet evolving on a lattice, centered at position $\boldsymbol{r}$ with crystal-momentum $\boldsymbol{k}$, and driven by an external force $\boldsymbol{F}$, are given by [116]

$$\dot{\boldsymbol{r}} = \frac{1}{\hbar}\frac{\partial E(\boldsymbol{k})}{\partial \boldsymbol{k}} - \left[\dot{\boldsymbol{k}} \times \mathbf{1}_z\right]\mathcal{F}(\boldsymbol{k}) \tag{179}$$

$$\hbar\dot{\boldsymbol{k}} = \boldsymbol{F}, \tag{180}$$

where $\mathcal{F}(\boldsymbol{k})$ is the Berry's curvature introduced in equation (172), and where $E(\boldsymbol{k})$ is the band structure characterizing the lattice system. In [444], Price and Cooper showed that cold atoms undergoing Bloch oscillations [445] can follow trajectories (180) where the band structure's contribution to the velocity $\propto \partial E(\boldsymbol{k})/\partial \boldsymbol{k}$ vanishes. Following this protocol, a measure of the mean velocity for many trajectories gives the Berry's curvature $\mathcal{F}(\boldsymbol{k})$ over a 'pixelated' BZ [444]. By properly adjusting the path undergone by the wave packet, the Chern number (172) can be evaluated. In principle, this method could be applied to any lattice system.

A similar scheme was recently proposed by Abanin *et al* [446], where Bloch oscillations are combined with interferometry techniques to determine the Berry's curvature and the Chern number of 2D optical lattice systems. This method is based on the measure of the Zak phase [116], which has already been experimentally implemented in a 1D system [409]. In [447], Liu *et al* introduced a method to measure the Chern number based on spin-resolved Bloch oscillations, observing that the topological index can be obtained by measuring the spin polarization of the atomic gas at specific (highly symmetric) points within the BZ.

Finally, it was shown by Dauphin and Goldman that the Chern number (or equivalently the Hall conductivity) could be measured by imaging the center-of-mass displacement of a Fermi gas subjected to a constant force $\boldsymbol{F} = F\mathbf{1}_y$. Setting the Fermi energy within a topological bulk gap, the contribution from the group velocity naturally vanishes and the displacement along the transverse direction x is then directly proportional to the force multiplied by the Chern number [448]. This simple and direct scheme is robust against perturbations and it could be implemented in any cold-atom setup hosting Chern insulating phases to detect non-trivial topological order. We stress that this method requires high-resolution microscopes to measure the (integral) Chern number with high precision, i.e. $\nu_{\text{measured}} = \nu \pm 0.01$, the mean displacement being of the order of a few tens of lattice sites after reasonable experimental times [448].

The hybrid TOF measurement. Wang *et al* [449] showed that the Chern number could be read out from hybrid TOF images, by detecting atom density after suddenly releasing the external confining potential $V_{trap}(x, y)$ along one direction only, for example along $\boldsymbol{e}_y$. By combining *in situ* imaging along $\boldsymbol{e}_x$ and TOF imaging along the release direction $\boldsymbol{e}_y$, such an experiment would give access to the hybrid particle density $\rho(x, k_y)$, where k_y is the crystal momentum along $\boldsymbol{e}_y$. The relation between the hybrid density and the Chern number are related through dimensional reduction (section 8.5.5). In this picture, the 2D Hofstadter model is viewed as a 1D Harper–Aubry–André lattice directed along $\boldsymbol{e}_x$ and described by a Hamiltonian $\hat{H}(\Phi, k_y)$, where Φ (the flux) and k_y (crystal momentum) are both interpreted as parameters (see equation (171)). The proposal of [449] exploits a relation between the electric polarization of electronic systems to their quantized Chern number [116, 450]. The Chern number measures the charge transported from one boundary of the 1D lattice to the other under the variation of the parameter $k_y = 0 \to 2\pi$, i.e. after a full cycle in the BZ. In the cold-atom framework, the measured hybrid density $\rho(x, k_y)$ permits a numerical reconstruction of this transport property, thereby providing an efficient way to directly evaluate the Chern number of topologically ordered optical lattices [449].

Detecting topological edge states in atomic Chern insulators. Topological edge states are populated when the Fermi energy is located within a topological bulk gap [73, 74]. In Chern insulators, as described by the Hofstadter [305] or Haldane [182] models, for example, this happens when the sum of Chern numbers associated with the bulk bands lying below the gap is non-zero

$$\nu = \sum_{\lambda < E_F} \nu_\lambda \neq 0. \tag{181}$$

According to the bulk-edge correspondence, the topological index ν corresponds to the number of edge modes present within the bulk gap (these modes are responsible for the quantized Hall conductivity in equation (173), see [78]). The bulk-edge correspondence is illustrated in figure 26(*a*). In general, the number of occupied edge modes within a bulk gap N_{edge} and below E_F contains a very small fraction of the total number of particles in the system N_{tot}. In a circular atomic Chern insulator, produced by an external confining potential $V_c(r)$, the ratio of edge to total states is $N_{\text{edge}}/N_{\text{tot}} \sim a/R_F$, where R_F is the Fermi radius of the system and a is the lattice spacing [451]. For typical systems with $R_F \sim 100a$ and $N \sim 10^4$ particles, only a few tens of atoms will occupy edge modes. This simple observation indicates that the direct detection of topological edge states is a subtle and challenging task.

Identifying bulk topological order using the system's edges requires measuring characteristics of topological edge states distinct from those of the many bulk states. In Chern insulators, all the edge states present within a bulk gap propagate in the same direction—they are chiral—and their dispersion relation is approximately linear. Therefore, with the Fermi energy in a bulk gap, the dispersion relations of low-energy excitations give a clear signature for the presence (or absence) of topological edge states [428, 429, 453, 454]. In principle, Bragg spectroscopy [455]—a technique based on momentum-sensitive light scattering which, for example, found application in measuring BEC's collective modes—could offer such a probe [428, 429]. Unfortunately, the number of particles $\sim N_{\text{edge}}$ excited by a Bragg probe focused on the cloud's edge (e.g. using high-order Laguerre-Gaussian beams [454]) would be extremely small compared to the total number of particles N_{tot}, making the Bragg signal undetectable [451, 454]. To overcome this drawback, a 'shelving method' was proposed in [451, 454]. In this scheme, the Bragg

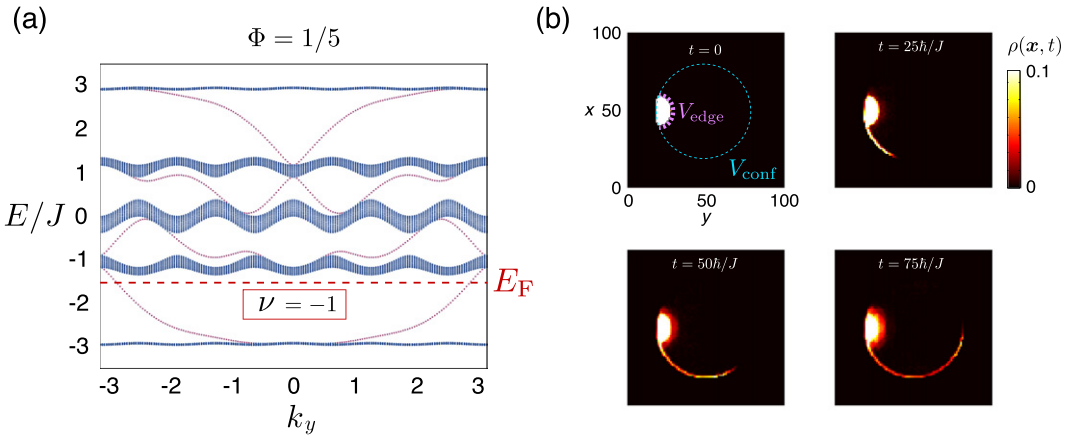

Figure 26. (*a*) The Hofstadter model's energy spectrum with open boundary conditions along e_x (from $x = 0$ to $x = L$), and with periodic boundary conditions along e_y. The spectrum $E(k_y)$ is shown as a function of the quasi-momentum k_y for $\Phi = 1/5$. The projected bulk bands $E(k_x, k_y) \rightarrow E(k_y)$, shown in figure 23(*b*) are plotted in blue. The red dispersion branches within the bulk gaps correspond to propagating edge modes near $x = 0$ and $x = L$. When the Fermi energy is within the first bulk gap, edge modes up to the Fermi energy are populated, one each on the system's top and bottom. The number of edge-state modes within each gap is in agreement with the Chern numbers presented in figure 23(*b*). (*b*) An atomic Fermi gas with E_F as in (*a*), was initially confined by a potential wall V_{edge} in a small region located in the vicinity of the circular edge. After releasing the wall V_{edge}, the edge states propagate along the circular edge created by the potential $V_{conf}(r)$, making them directly observable in *in situ* images of the spatial density $\rho(\boldsymbol{x}, \boldsymbol{t})$ [452].

probe transfers energy and angular momentum to atoms located in the vicinity of the Fermi radius and simultaneously changes their internal states. This completely removes the edge states from the cloud—allowing imaging on a dark background unpolluted by the untransferred atoms—enabling the detecting of the edge-mode's dispersion relation from the Bragg signal [451, 454].

Another method forces the edge states to propagate in a region that is unoccupied by the bulk states, allowing for a direct imaging of these topological states. Such a method was proposed in [452], where the atomic cloud is initially shaped by large repulsive walls and prepared in a Chern insulating phase. After suddenly removing the walls, the chiral edge states propagate in a chiral manner along the circular edge of the cloud, while the bulk states tend to fill the initially vacant regions. This method is particularly efficient starting from a topological flat band, in which case the bulk states remain immobile for long times, allowing for the clear imaging of the propagating edge states, see figure 26(*b*). Schemes for isolating the edge state signal in the case of dispersive bulk states were also proposed in [452], based on their chiral nature. Other methods to launch the edge state currents, by quenching the parameters of the microscopic Hamiltonian, were proposed in [456].

Topological edge states generally survive in smooth confining potentials [426, 429, 451, 452, 454, 457]. However, their angular velocity dramatically decreases and their localization length increases as the potential is smoothened. The use of sharp boundaries is therefore preferable to detect this edge-states physics in experiments [451, 452, 454]. The detection of atomic topological edge states has been further studied in [355, 390, 391, 458–460].

Finally, we stress that extending the schemes to probe topological invariants and edge states in static systems to the case of periodically driven systems, should be handled with care. Indeed, any potential $\hat{V}_{probe}$ associated with a probing protocol, e.g. a static force to measure the Chern number, or a walking potential to probe edge-state dispersion relations, will potentially alter the effective Hamiltonian, and hence, the quasi-energy band structure [101]. In other words, measuring the topological order associated with an effective Hamiltonian may destroy it.

9.2.2. Simulating Z_2 topological insulators and axion electrodynamics. Adding synthetic SOCs to 2D and 3D optical lattices opens the possibility to simulate and detect the unusual properties of Z_2 topological insulators [20, 336, 365, 430]. The methods for detecting the chiral edge states of Chern atomic insulators discussed above can be directly applied to the case of Z_2 insulators exhibiting helical edge states[12]. For instance, spin-resolved density measurements [461] could be used to identify the propagation of the different spin species. Using cold atoms subjected to both synthetic SOCs and magnetic fields, one could then identify the transition between QH and QSH phases, by studying the nature of the propagating edge states [348, 352]. While the Bragg spectroscopy scheme of [451, 454] could be generalized to identify the edge states of any 2D topological phase, the 'wall-removal' strategy of [452] could be applied to any topological phase exhibiting propagating states (in 2D, but also 3D systems). Moreover, the methods to directly measure the Chern number could be extended to detect the topologically invariant spin-Chern number of Z_2 insulators [336]. Finally, 3D optical lattices emulating Z_2 topological insulators provide a versatile platform for detecting emerging axion electrodynamics; the unusual modifications of Maxwell's equations due to the topological axion term [73, 74]. A protocol to detect the fractional magnetic capacitor [462]—a signature of axion electrodynamics—was described in [20].

[12] Helical edge states are counter-propagating edge states with opposite spins, which lead to the QSH effect [330].

9.2.3. Majorana fermions in atomic topological superconductors. The beautiful universality of topological band insulators motivated theorists to seek for similar structures in different physical systems. For example, the Bogoliubov–de Gennes Hamiltonian, describing the excitations of superconductors, can also describe topological phases and topological superconductors. Some topological superconductors—those that break TRS—host topologically protected zero modes which are Majorana fermions with non-Abelian exchange statistics [73] (akin to the quasiparticle excitations of the $\nu = 5/2$ quantum Hall state [263]). Several platforms have been envisaged in the quest for these properties, such as (a) the interface between a 3D topological insulator and a conventional s-wave superconductor [463], and (b) semiconductors with Rashba SOC, s-wave pairing and a TR-breaking perturbation (e.g. a Zeeman coupling) [200, 464, 465]. This second route has been envisaged for 1D spin–orbit coupled semiconducting wires that map onto Kitaev's superconducting chain [465], but also for 2D spin–orbit coupled semiconductors [200, 464].

Neutral atoms with synthetic SOC therefore gives a natural and experimentally complementary platform for realizing TR-breaking topological superconductors, where s-wave pairing and TR breaking terms can be easily controlled. In addition, Raman coupling and laser-assisted tunneling methods can also give 2D topological superconductors [225, 277, 278] and Kitaev's superconducting chain with cold atoms trapped in 1D optical lattices [405–408].

These proposals are all motivated by the desire to clearly detect and manipulate the properties of atomic Majorana zero modes, with an eye for methods that are not experimentally practical in solid-state systems [225, 406, 408, 466, 467]. A first signature might be the anomalous density of an atomic topological superfluid. A Majorana mode located inside a vortex core, should contribute to the total density in a detectable manner [225], and TOF images would reveal the Majorana mode's non-local correlations. By considering a topological atomic chain, Kraus *et al* [406] discussed how the Majorana mode's long-range correlations give modulations in the TOF images, and also, that this signal is related to the number of topological modes present in the system. As stressed above when discussing the detection of Chern insulators, it is crucial to reduce the large background stemming from the many bulk states to emphasize the Majorana signal, which could be realized by local addressing [406]. Spectroscopic measurements, similar to the Bragg probe discussed above, both gives access to the energy of the Majorana states and provides a proof of their localization [406, 408]. Finally, the Chern number measurement introduced by Alba *et al* [368] could also be generalized to demonstrate the existence of Majorana modes in optical lattices [468].

Braiding operations, which reveal the anyonic nature of the Majorana modes, have been proposed for 2D topological superfluids [466], where braiding is realized by externally moving the vortices hosting the zero modes. More recently, a braiding protocol was proposed for atomic Kitaev wires [467], where the braiding operations are realized through local addressing by locally switching on/off potentials, hopping and pairing terms.

10. Interacting gauge theories and dynamical gauge fields

So far we have considered the effects of gauge fields—or strictly speaking gauge *potentials*—that are classical and static (in the sense that any time dependence of the field is experimentally specified). These gauge potentials are externally controlled, and thus, they typically depend on atom–light coupling parameters, on rotation frequency or on other types of external driving features. As we have seen, effective magnetic and electric fields arise and give rise to observable effects, however, these *applied* fields do not reproduce a complete field-theory picture; they are not dynamical degrees of freedom. In contrast to 'real' fields, the synthetic fields considered in the previous sections are not influenced by the matter fields (i.e. the atoms). To be concrete, the synthetic electric and magnetic fields produced in laser-coupled atomic gases (section 4) need not obey Maxwell's equations. This aspect of synthetic gauge potentials emphasizes their artificial origin, and in fact, it could be exploited constructively to simulate exotic situations where electromagnetism is no longer ruled by Maxwell's equations.

Generating *interacting gauge theories* with cold atoms, where matter fields and synthetic gauge structures are dynamically related, importantly connects simple experiments with intractable problems in QED and QCD [18, 69, 71, 469, 470]. Such quantum simulators are a novel tool for gaining physical insight in issues encountered in high-energy physics, such as the fundamental problem of *confinement*, which precludes the observation of free quarks in Nature [469, 471]. A first step towards realizing dynamical gauge fields is introducing back-action where atoms affect a synthetic gauge potential $\boldsymbol{A}(\boldsymbol{r}, t)$ locally and dynamically. One possibility is to create a gauge potential that explicitly depends on the atomic density $\boldsymbol{A}(\boldsymbol{r}, t) \sim \rho(\boldsymbol{r}, t)$, as was proposed in [19, 472]. These density-dependent gauge structures, (described in section 10.1), do not fully reproduce a conventional gauge field theory in the sense that the emerging fields do not exist in the absence of matter (i.e. when $\rho = 0$). However, they give rise to interesting properties, such as anyonic structures and chiral solitons, suggesting novel perspectives in quantum simulation. Schemes that fully realize quantum field theories [18, 69, 71, 469–471, 473, 474] require (a) quantum matter (fermionic) fields $\hat{\psi}$ *and* gauge (bosonic) fields $\hat{a}$ represented by different atomic species interacting with each other, and (b) gauge-invariance conditions usually synthesized by imposing some constraints. These proposals highlight the birth of a very new and exciting field of research possibly connecting cold-atom and high-energy physicists, and are discussed in section 10.2. A recent review on the quantum simulation of lattice gauge theories has been recently written by Wiese [68]. Finally, we mention the possibility to realize dynamical gauge fields of condensed matter models, such as spin-ice materials, using polar molecules [475] or Rydberg atoms [476].

10.1. Density-dependent gauge potentials

We first consider a non-interacting two component Bose gas evolving in space-dependent coupling fields described by the

single-particle Hamiltonian

$$\hat{H} = \frac{\boldsymbol{p}^2}{2m}\hat{1} + \hat{U} = \frac{\boldsymbol{p}^2}{2m}\hat{1} + \frac{\hbar\Omega}{2}\begin{pmatrix} 0 & \mathrm{e}^{-\mathrm{i}\phi} \\ \mathrm{e}^{\mathrm{i}\phi} & 0 \end{pmatrix}, \tag{182}$$

where Ω is the Raman Rabi frequency, ϕ is the coupling laser's phase, and for simplicity the detuning δ from the two-photon Raman resonance is set to zero. According to section 4, a non-trivial gauge structure is generated through the atom–light coupling, when the gradient of the detuning is non-zero $\boldsymbol{\nabla}\delta \neq 0$. The general idea behind the concept of density-dependent synthetic gauge potentials, is that collisions between the atoms can induce an effective *density-dependent detuning* at the mean-field level. Reference [19] considered the mean-field Hamiltonian

$$\hat{H} = \frac{\boldsymbol{p}^2}{2m}\hat{1} + \hat{U} + \hat{V}_{MF} = \frac{\boldsymbol{p}^2}{2m}\hat{1} + \begin{pmatrix} g_{11}|\Psi_1|^2 + g_{12}|\Psi_2|^2 & \frac{\hbar\Omega}{2}\mathrm{e}^{-\mathrm{i}\phi} \\ \frac{\hbar\Omega}{2}\mathrm{e}^{\mathrm{i}\phi} & g_{22}|\Psi_2|^2 + g_{12}|\Psi_1|^2 \end{pmatrix}, \tag{183}$$

for an interacting two-level atomic system, where $\rho_{1,2} = |\Psi_{1,2}|^2$ are the densities associated with the two atomic species, and $g_{\mu\nu}$ are the species-dependent contact-interaction parameters. When the atom–light coupling energy $\hbar\Omega$ is much larger than the mean field terms $g_{\mu\nu}\rho_\mu \ll \hbar\Omega$, the corresponding gauge potential and dressed states

$$|\chi_\pm\rangle = |\chi_\pm^{(0)}\rangle \pm \frac{g_{11} - g_{22}}{8\hbar\Omega}\rho_\pm|\chi_\mp^{(0)}\rangle, \tag{184}$$

$$\boldsymbol{A}_\pm = \boldsymbol{A}^{(0)} \pm \boldsymbol{a}_1\rho_\pm(\boldsymbol{r}) = -\frac{\hbar}{2}\boldsymbol{\nabla}\phi \pm \frac{g_{11} - g_{22}}{8\Omega}(\boldsymbol{\nabla}\phi)\rho_\pm(\boldsymbol{r}), \tag{185}$$

can be obtained perturbatively. $|\chi_\pm^{(0)}\rangle$ are the standard unperturbed dressed states for $\hat{V} = 0$, and $\rho_\pm = |\Psi_\pm|^2$ denote the dressed state densities. Equation (185) highlights the main result: species-dependent collisions, with $g_{11} \neq g_{22}$, can produce a density-dependent gauge potential $\boldsymbol{A} \sim \rho(\boldsymbol{r})$. This interaction-induced detuning is the simplest scheme realizing a pseudo-dynamical gauge theory with back action between the matter field $\Psi(\boldsymbol{r})$ and the gauge potential $\boldsymbol{A}(\boldsymbol{r})$. The key point is that the parameters in the resulting density-dependent gauge potential $\boldsymbol{A}$ are governed by the Rabi frequency Ω, the gradient of the phase $\boldsymbol{\nabla}\phi$ and the scattering length difference $a_{11} - a_{22} \propto g_{11} - g_{22}$. All these parameters are largely adjustable by tuning the coupling lasers and the scattering lengths, which can be achieved using Feshbach resonances [34].

The properties of this unusual Bose gas can be studied through a generalized GP equation, which takes into account the presence of the density-dependent gauge potential [19]

$$\mathrm{i}\hbar\partial_t\Psi = \left[\frac{(\boldsymbol{p} - \boldsymbol{A})^2}{2m} + \boldsymbol{a}_1 \cdot \boldsymbol{j}(\Psi, \Psi^*) + W + g\rho\right]\Psi, \tag{186}$$

where $\boldsymbol{A} = \boldsymbol{A}_+$ is given by equation (185), $g = (g_{11} + g_{22} + 2g_{12})/4$, $W = |\boldsymbol{A}^{(0)}|^2/2m$ and a single dressed-state branch has been isolated in the dynamics (i.e. $\Psi = \Psi_+$, $\rho = \rho_+$). Here, the nonlinearity of the GP equation manifests itself both through the standard term $\sim g\rho$, and also through the current

$$\boldsymbol{j}(\Psi, \Psi^*) = \frac{\hbar}{2m\mathrm{i}}\left[\Psi\left(\nabla + \frac{\mathrm{i}}{\hbar}\boldsymbol{A}\right)\Psi^* - \Psi^*\left(\nabla - \frac{\mathrm{i}}{\hbar}\boldsymbol{A}\right)\Psi\right]. \tag{187}$$

Thus, this gives rise to rich nonlinear dynamics. The modified GP equation (186)–(187) already leads to exotic properties in 1D, including chiral soliton solutions, as was already pointed out in the context of 1D anyons [477]. Supposing a coupling laser phase in the form $\phi = kx$ and setting $\Psi(x, t) = \varphi(x, t)\mathrm{e}^{-\mathrm{i}kx/2}$, the dynamics of the 1D atomic system is described by

$$\mathrm{i}\hbar\partial_t\varphi = \left[\frac{(p - a_1\rho)^2}{2m} + a_1 j + W_1 + g\rho\right]\varphi, \tag{188}$$

where $a_1 \propto k(g_{11} - g_{22})$ is the k-dependent nonlinearity strength and $W_1 = \hbar^2k^2/8m$. This equation supports bright or dark chiral solitons, depending on the sign of $\mathfrak{g} = g - 2a_1u$, where u is the speed of the soliton. At the critical value $\mathfrak{g} = 0$, the chiral soliton is destroyed. Hence, in contrast to a conventional soliton, the chiral solitons are strongly altered when reflected from a hard wall [19]. Other non-trivial effects stemming from the unusual nonlinear equation (188) have been reported in [19], including an asymmetric free expansion of the cloud accompanied with a drift of the center of mass, and the existence of critical particle numbers for the onset of persistent currents in a ring geometry [19].

A density-dependent gauge structure can also be created in optical lattices. In the lattice framework (see section 8), gauge potentials manifest themselves through the Peierls-modified hopping matrix element $J\mathrm{e}^{\mathrm{i}\phi_{jk}}$, describing hopping between lattice sites j and k. Hence, the key idea is to engineer Peierls phases ϕ_{ij} that depend on the occupation number n_j at each lattice site j, e.g. $\phi_{ij} = \theta n_j$. Such a scenario was proposed by Keilmann *et al* [472], giving the generalized Bose–Hubbard model

$$H = -J\sum_j\left(\hat{b}_j^\dagger\hat{b}_{j+1}\mathrm{e}^{\mathrm{i}\theta\hat{n}_j} + \mathrm{h.c.}\right) + \frac{U}{2}\sum_j\hat{n}_j(\hat{n}_j - 1). \tag{189}$$

This is the lattice version of the Hamiltonian leading to equation (186), contains the density operator $\hat{n}_j = \hat{b}_j^\dagger\hat{b}_j$ at site j, the onsite interaction strength U, and the $\hat{n}_j$-dependent tunneling rate $J\mathrm{e}^{\mathrm{i}\theta\hat{n}_j}$. This unusual Peierls substitution can be realized using a generalization of the laser-assisted tunneling method presented in section 8.4, as illustrated in figure 27 for the case $n_j \leqslant 2$. In this picture, the two neighboring sites at j and $j + 1$ can either host $n = 1$ or $n = 2$ atoms (omitting the trivial case $n = 0$), resulting in a four-dimensional ground state manifold $\{|g_1\rangle, \ldots, |g_4\rangle\}$. Coupling this subsystem to an excited state $|e\rangle$, with four different coupling fields, allows to individually address each hopping process, thanks to the energy offsets produced by the onsite interaction U and by an additional lattice tilt Δ, see figure 27. Finally, tuning the phases associated with each laser-induced tunneling process (see section 8.4) results in the required n_j-dependent tunneling matrix elements between lattice sites j and $j + 1$ [472].

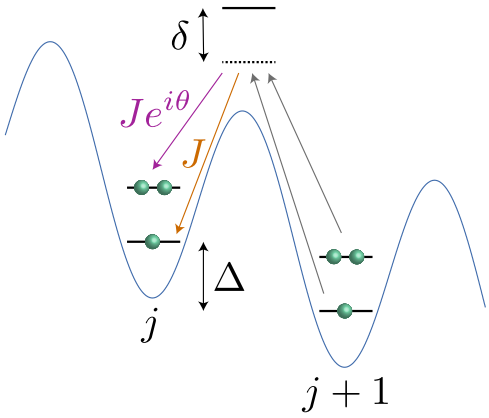

Figure 27. A schematic view of the proposal by Keilmann *et al* for creating density dependent tunneling matrix elements $J\mathrm{e}^{\phi_{jk}} = J\mathrm{e}^{\mathrm{i}\theta n_j}$, for the case $n_j \leqslant 2$. Laser assisted tunneling using four detuned (δ) lasers in combination with a tilted lattice given by the off-set Δ induces a phase which depends on the occupation number of the target site.

The Hamiltonian (189) maps onto a theory of anyons in 1D lattice. The mapping between bosonic ($\hat{b}_j$) and anyonic ($\hat{a}_j$) operators, $\hat{a}_j = \hat{b}_j \exp[\mathrm{i}\theta \sum_j \hat{n}_j]$, gives rise to the Anyon–Hubbard Hamiltonian

$$H = -J \sum_j \left(\hat{a}_j^\dagger \hat{a}_{j+1} + \text{h.c.}\right) + \frac{U}{2} \sum_j \hat{n}_j(\hat{n}_j - 1), \quad (190)$$

where the commutation relation for $\hat{a}_j^{(\dagger)}$ is anyonic:

$$\hat{a}_j \hat{a}_k^\dagger - \mathrm{e}^{-\mathrm{i}\theta\, \mathrm{sign}(j-k)} \hat{a}_k^\dagger \hat{a}_j = \delta_{jk}. \quad (191)$$

Since $\mathrm{sign}(j-k) = 0$ when $j = k$, particles behave as bosons on-site, and as anyons off-site with statistical angle θ. Thus, the anyonic nature of equation (189) stems from the density-dependent Peierls phases $\mathrm{e}^{\mathrm{i}\theta\hat{n}_j}$.

The Hamiltonian in equation (189) is a lattice version of the continuum Hamiltonian leading to the mean-field GP equation in equation (186). As such it shows unconventional tunneling dynamics due to its nonlinearities (see equations (186)–(187)), which will affect any Josephson type dynamics in the lattice [478]. Reference [472] showed that density-dependent tunneling gives rise to phase transitions between the standard superfluid phase and exotic Mott states, where the particle distributions show plateaus at fractional densities, due to the anionic statistics.

10.2. Simulating quantum gauge theories

The simulation of Dirac fermions with atoms in optical lattices [20, 100, 302, 322, 340, 353, 365, 410, 412, 442, 479, 480], together with the possibility of generating background Abelian and non-Abelian gauge fields [100, 261, 340, 363], suggest that cold atoms could be exploited to deepen our understanding of QED and QCD; a powerful alternative to numerical lattice-gauge theory (LGT). For instance, cold atoms in optical lattices of various spatial dimensions ($D = 1, 2, 3$ [34] and beyond $D > 3$ [389]) may reveal the mechanisms by which confined phases emerge in various configurations in Abelian and non-Abelian gauge theories, or in $D + 1 = 3$ and $D + 1 = 4$ space–time dimensions. These mechanisms could be investigated in a setup where different atomic species encode the matter and the gauge degrees of freedom, and exploit the fact that the interactions between the particles can be tuned (e.g. by Feshbach resonances). Such cold-atom quantum simulators are a physical platform where the coupling strength of the gauge theory is externally controllable, and where phase transitions between confined and unconfined phases might be externally driven [469, 471].

This quantum-simulation scenario requires that both the matter and the gauge fields be dynamical, and also, that the simulated theory be gauge invariant. For instance, realizing QED with cold atoms requires that the Gauss's law be imposed by a constraint, which generally requires a precise control over the simulated Hamiltonian [18, 69, 71, 469–471]. The versatility of cold-atom systems also allows for the simulation of simple toy models, such as the Gross–Neveu model, which played a major role in the exploration of QCD-like effects [473, 481].

The quantum simulation of the Gross–Neveu model [473] already captures the general strategy and the main ingredients needed to simulate more elaborate field theories, such as QED and QCD. The Gross-Neveu model describes the interaction between a massless Dirac fermion $\hat{\Psi}$ and a massive quantized scalar field $\hat{\Phi}$ in $D = 1$ spatial dimension, with the Hamiltonian

$$\hat{H} = \hbar \int \mathrm{d}x \left[c\, \hat{\Psi}^\dagger \gamma_1 \hat{p} \hat{\Psi} + gm\, \hat{\Phi} \hat{\Psi}^\dagger \hat{\Psi} + \frac{m^2}{2} \hat{\Phi}^2 \right], \quad (192)$$

where c is a velocity, g is the coupling strength, m is the mass of the scalar field and γ_1 is a Dirac matrix (the color quantum numbers $\sigma = 1, \ldots, N$ of the Dirac field $\hat{\Psi}_\sigma$ are implicit in equation (192)). In this simple field theory the scalar field $\hat{\Phi}$ has no kinetic term, and the coupling between the Dirac $\hat{\Psi}$ and the scalar field $\hat{\Phi}$ can be formally traced back to the original Gross–Neveu model (which describes Dirac fermions interacting through the term $\sim g^2(\hat{\Psi}^\dagger\hat{\Psi})^2$ in the absence of the scalar field) [473]. This interacting field theory could be implemented with a N-component Fermi gas in an optical lattice featuring spatially modulated tunneling amplitudes $J = J_{1,2}$, see figure 28, and along with an independent BEC loaded into a separate optical lattice with double spacing, as represented in figure 28. The resulting Bose–Hubbard Hamiltonian is

$$\hat{H} = -\sum_j \left[J_1\, \hat{f}_{j,A}^\dagger \hat{f}_{j,B} + J_2\, \hat{f}_{j,B}^\dagger \hat{f}_{j+1,A} + \delta\, \hat{b}_j^\dagger \hat{b}_j \hat{f}_{j,A}^\dagger \hat{f}_{j,B} + \text{h.c.} \right] - U\, (\hat{b}_j^\dagger)^2 (\hat{b}_j)^2 - \mu\, \hat{b}_j^\dagger \hat{b}_j, \quad (193)$$

where $\hat{f}_{j,A}^\dagger$ (respectively, $\hat{f}_{j,B}^\dagger$) creates a fermion at lattice site (j, A) (resp. (j, B)); $\hat{b}_j^\dagger$ creates a boson at lattice site j, U is the onsite interaction strength for bosons, μ is the chemical potential, and δ denotes the strength of the fermion–boson 'on-site' interaction, see figure 28. According to [473], when the Fermi energy is at half-filling, the low-energy excitations exactly reproduce the dynamics dictated by (192) for specific

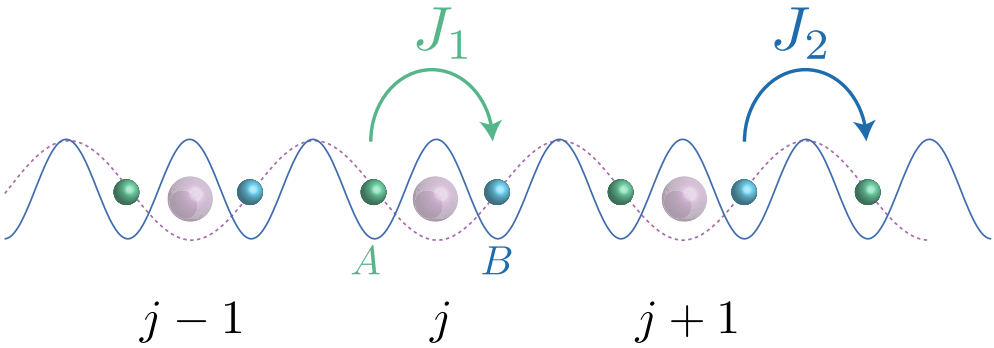

Figure 28. Optical-lattice implementation of equation (193). A primary optical lattice (blue) traps fermions in the two inequivalent sites A and B, which are distinguished by the alternating tunneling rates $J_{1,2}$. A superimposed optical lattice (purple) traps a BEC between the A and B sites of each unit cell, labeled by the index j. The interaction between fermions and bosons within each unit cell j results in a boson-mediated tunneling process for the fermions, giving rise to an effective quantum field theory at low energy [473].

values of the optical-lattice parameters. Since the matter-gauge field coupling strength g of the simulated field theory results from a boson-mediated tunneling process of fermions that is proportional to the inter-species interaction strength $g \sim \delta/\sqrt{U}$ [473], the coupling constant g is tunable.

Realizing more involved field theories, such as lattice QED or non-Abelian Yang–Mills lattice gauge theories, requires additional ingredients and control over inter-species interactions to retain gauge invariance [18, 69–71, 469–471, 482, 483]. These more complex proposals are still based on the strategy outlined above: different atomic species, fermions and bosons, are trapped in interpenetrating optical lattices, forming a many-body lattice system, whose effective (low-energy) description is that of an interacting quantum field theory. These elaborate cold-atom schemes are largely based on available technologies—taken to the extreme—suggesting that experimental realizations of lattice gauge theories are within reach. Very recently, a scheme has been proposed where the Gauss's law and gauge invariance emerge naturally (i.e. they are not imposed by an external constraint that modifies the effective low-energy description), based on the fundamental symmetries of the atomic system [474]. Optical-lattice implementations of lattice gauge theories offer unique measurement tools. Experimenters might observe the mass dynamically acquired by fermions in the Gross-Neveu model [473], the 'electric flux tube' at the origin of confinement in 3 + 1 Abelian LGT [471], the Wilson-loop area law [71], cosmological inflation processes [483] and the nonperturbative string breaking effect present in quantum link models and QCD [69].

11. Conclusions

Artificial gauge potentials in cold gases are a new laboratory tool that allow access to new physical phenomena. A handful of techniques for inducing the gauge potentials have been proven in the lab. These range from optically addressing the internal level structure of the atoms in combination with orbital motion, to mechanical shaking of optical lattices. In particular, synthetic uniform magnetic fields were realized leading to quantized vortices in BEC [22], and non-trivial lattice gauge structures have been produced in optical lattices, leading to staggered [61, 364, 490] and uniform [64, 65, 492] magnetic flux configurations. The staggered synthetic magnetic flux has been produced for a shaken triangular optical lattice [95, 97], and the Haldane model has been implemented by circularly shaking a hexagonal optical lattice [490]. Mapping the Berry curvature and Chern numbers of Bloch bonds has also been carried out [492, 494]. Additionally, the (one-dimensional) spin–orbit coupling has now been created and its manifestations have been explored for atomic bosons and fermions [25–32, 127, 501]. Examples of recent theoretical developments in the area of artificial guage potentials include thermometry of cold atoms in optical lattices [493], Efimov states with SOC [495, 496] and gauge potentials in Rydberg gases [497–500].

Artificial electromagnetism has begun to mature. It can be applied with or without an optical lattice present, leading to a broad spectrum of applications. At the single particle level, a surge of theoretical work using optical lattices propose to emulate exotic condensed matter systems. Prominent examples include topological insulators, quasi-relativistic systems, integer quantum Hall physics, and non-trivial spin dynamics from spin–orbit coupling. Including collisional interactions enables a whole new field of research. Interacting bosonic and fermionic gases show intriguing new effects when gauge fields are present. In the Abelian case, fractional quantum Hall (FQH) physics could be realized. To generate and stabilize such FQH liquids, it is crucial to develop schemes leading to topological flat bands [103, 178, 375], namely, dispersionless bands characterized by non-zero Chern numbers, which are well separated with respect to higher energy bands (see figure 26 for such a configuration offered by the Hofstadter model at flux $\Phi = 1/5$). Moreover, the rich set of spin–orbit coupled systems enable a range of novel effects such as unconventional superfluid properties in BCS-BEC crossover regimes, and finite momentum ground states for Fermi gases. Interacting spin–orbit coupled gases also offer an interesting route towards interacting topological phases in 3D, namely, the high-dimensional cousins of fractional quantum Hall states.

The prospect of creating non-trivial topological states of matter also opens up the possibility to address fundamental questions in quantum information. The availability of orbital

magnetism provides a novel tool for atomtronics situations, i.e., the atomic version of spintronics. The non-trivial topological states together with the concept of non-Abelian dynamics may also provide the route towards the mercurial and highly anticipated topological quantum computer [263], which promises to be the holy grail of fault tolerant quantum computing.

Quantum simulators would in general benefit from artificial orbital magnetism. The gauge fields might enable the simulation of more exotic gauge theories that are computationally intractable. A prominent example—linked to the ability to create dynamical gauge fields—is the quantum chromodynamics description of the strong force between elementary particles. While dynamical gauge fields are still in their infancy and unrealized in the lab, recent advances and theoretical proposals using optical lattices show that it is in principle possible to engineer fully dynamical gauge fields.

It is intriguing to speculate on the future direction for artificial gauge fields. First of all there are challenges both theoretically and experimentally which need to be addressed. From a theoretical point of view perhaps the most pressing question is to what extent the gauge fields can be combined with strong collisional interactions and whether there are any fundamental or practical limitations for doing so and still retain the dynamics governed by the effective magnetic fields. An interesting and promising direction in this respect is the inclusion of cavity QED where also strong interaction between the light and matter can be achieved which may provide a mechanism for creating a back-action between the matter field and the effective gauge fields [484–488], and by doing so also address the question of creating dynamical gauge fields but now possibly in the quantum regime.

Experimentally the challenges are also many. The level of controllability of key parameters such as stable laser frequencies, collisional properties, maintaining ultralow temperatures, avoiding numerous sources of heating and decay of the prepared quantum superpositions, are certainly taxing, and will require a constant development and refining of experimental techniques and technologies. This will have implications for reaching strongly correlated regimes in experiments. All techniques for creating artificial magnetic fields to date could in principle reach the strongly correlated regime such as quantum Hall liquids. Each one of them have however their own experimental drawbacks. For instance the Raman based proposals including also flux lattices, will have problems with spontaneous emission which will cause heating. The mechanical shaking of a lattice will also induce heating eventually. Finally the rotational techniques have the disadvantage that there one would have to work with a very small number of particles. These limitations are all of a technical character, and we are likely to see a development of all them in parallel in the future.

On a more speculative note artificial electromagnetism may provide a route to completely new physical scenarios which cannot be found in conventional solid-state systems. Emulating solid-state phenomena with the hope to shed some light on new and not so well understood phenomena, is the most natural application of the artificial gauge fields. It is however not inconceivable to envisage a situation where the effective gauge field allows for the preparation of highly exotic quantum states which captures not only the solid-state and condensed matter phenomena, but also addresses fundamental question regarding the fabric of space–time. For instance, gauge fields in the presence of analog gravity in Bose–Einstein condensates [489] could address important questions, such as the role of quantum entanglement and unitarity near black holes. The inclusion of gauge fields, and in particular dynamical gauge fields, into the picture of analog gravity, is largely uncharted territory and may provide some insight into the interplay between the quantum world and gravity.

Acknowledgments

We acknowledge helpful discussions with M Aidelsburger, B Anderson, E Anisimovas, L Aycock, M A Baranov, R Barnett, G Barnich, A Bermudez, J Beugnon, I Bloch, N R Cooper, J Dalibard, M Dalmonte, A Dauphin, A Eckardt, M Edmonds, T Esslinger, V Galitski, P Gaspard, F Gerbier, P Hauke, W Ketterle, C V Kraus, Z Lan, J Larson, M Lewenstein, D Maldonado-Mundo, S Nascimbene, M Rechtsman, J Ruostekoski, J Ruseckas, L Santos, M Valiente, H Zhai and P Zoller.

N G thanks the FRS-FNRS and the ULB for financial support. G J acknowledges the financial support by the Lithuanian Research Council Project No MIP-082/2012. P Ö acknowledges support from the UK EPSRC grant no. EP/J001392/1 and the Carnegie Trust for the Universities of Scotland. I B S acknowledges the financial support by the NSF through the Physics Frontier Center at JQI, and the ARO with funds from both the Atomtronics MURI and DARPA's OLE Program.

References

[1] Anderson M H, Ensher J R, Matthews M R, Wieman C E and Cornell E A 1995 *Science* **269** 198
[2] Davis K B, Mewes M O, Andrews M R, van Druten N J, Durfee D S, Kurn D M and Ketterle W 1995 *Phys. Rev. Lett.* **75** 3969–73
[3] DeMarco B and Jin D S 1999 *Science* **285** 1703–6
[4] Ketterle W and Miesner H J 1996 *Phys. Rev.* A **56** 3291
[5] Jeltes T *et al* 2007 *Nature* **445** 402–5
[6] Fisher M P A, Weichman P B, Grinstein G and Fisher D S 1989 *Phys. Rev.* B **40** 546–70
[7] Jaksch, Bruder C, Cirac J, Gardiner C and Zoller P 1998 *Phys. Rev. Lett.* **81** 3108
[8] Greiner M, Mandel O, Esslinger T, Hänsch T and Bloch I 2002 *Nature* **415** 39–44
[9] Greiner M, Regal C A and Jin D S 2003 *Nature* **426** 537–40
[10] Bourdel T, Khaykovich L, Cubizolles J, Zhang J, Chevy F, Teichmann M, Tarruell L, Kokkelmans S and Salomon C 2004 *Phys. Rev. Lett.* **93** 050401
[11] Bartenstein M, Altmeyer A, Riedl S, Jochim S, Chin C, Denschlag J and Grimm R 2004 *Phys. Rev. Lett.* **92** 120401
[12] Zwierlein M, Stan C, Schunck C, Raupach S, Kerman A and Ketterle W 2004 *Phys. Rev. Lett.* **92** 120403
[13] Kinast J, Hemmer S, Gehm M, Turlapov A and Thomas J 2004 *Phys. Rev. Lett.* **92** 150402
[14] Bissbort U, Götze S, Li Y, Heinze J, Krauser J S, Weinberg M, Becker C, Sengstock K and Hofstetter W 2011 *Phys. Rev. Lett.* **106** 205303

[15] Endres M, Fukuhara T, Pekker D, Cheneau M, Schau P, Gross C, Demler E, Kuhr S and Bloch I 2012 *Nature* **487** 454–8
[16] Williams J, Hazlett E, Huckans J, Stites R, Zhang Y and O'Hara K 2009 *Phys. Rev. Lett.* **103** 130404
[17] Kapit E and Mueller E 2011 *Phys. Rev.* A **83** 033625
[18] Banerjee D, Bögli M, Dalmonte M, Rico E, Stebler P, Wiese U J and Zoller P 2013 *Phys. Rev. Lett.* **110** 125303
[19] Edmonds M J, Valiente M, Juzeliūnas G, Santos L and Öhberg P 2013 *Phys. Rev. Lett.* **110** 085301
[20] Bermudez A, Mazza L, Rizzi M, Goldman N, Lewenstein M and Martin-Delgado M 2010 *Phys. Rev. Lett.* **105** 190404
[21] Lin Y J, Compton R L, Perry A R, Phillips W D, Porto J V and Spielman I B 2009 *Phys. Rev. Lett.* **102** 130401
[22] Lin Y J, Compton R L, Jimenez-Garcia K, Porto J V and Spielman I B 2009 *Nature* **462** 628–32
[23] Lin Y J, Compton R L, Jimenez-Garcia K, Phillips W D, Porto J V and Spielman I B 2011 *Nature Phys.* **7** 531–4
[24] Wilczek F and Zee A 1984 *Phys. Rev. Lett.* **52** 2111–4
[25] Lin Y J, Jiménez-García K and Spielman I B 2011 *Nature* **471** 83–6
[26] Wang P, Yu Z Q, Fu Z, Miao J, Huang L, Chai S, Zhai H and Zhang J 2012 *Phys. Rev.. Lett.* **109** 095301
[27] Cheuk L W, Sommer A T, Hadzibabic Z, Yefsah T, Bakr W S and Zwierlein M W 2012 *Phys. Rev. Lett* **109** 095302
[28] Zhang J Y *et al* 2012 *Phys. Rev. Lett.* **109** 115301
[29] Fu Z, Huang L, Meng Z, Wang P, Zhang L, Zhang S, Zhai H, Zhang P and Zhang J 2014 *Nature Phys.* **10** 110
[30] Zhang L, Zhang J Y, Ji S C, Du Z D, Zhai H, Deng Y, Chen S, Zhang P and Pan J W 2013 *Phys. Rev.* A **87** 011601(R)
[31] Qu C, Hamner C, Gong M, Zhang C and Engels P 2013 *Phys. Rev.* A **88** 021604
[32] LeBlanc L J, Beeler M C, Jimenez-Garcia K, Perry A R, Sugawa S, Williams R A and Spielman I B 2013 *New J. Phys.* **15** 073011
[33] Lewenstein M, Sanpera A, Ahufinger V, Damski B, De A S and Sen U 2007 *Adv. Phys.* **56** 243–379
[34] Bloch I, Dalibard J and Zwerger W 2008 *Rev. Mod. Phys.* **80** 885
[35] Lewenstein M, Sanpera A and Ahufinger V 2012 *Ultracold Atoms in Optical Lattices: Simulating Quantum Many-Body Systems* (Oxford: Oxford University Press)
[36] Görlitz A et al 2001 *Phys. Rev. Lett.* **87** 130402
[37] Chin C, Grimm R, Julienne P and Tiesinga E 2010 *Rev. Mod. Phys.* **82** 1225
[38] Feynman R P 1982 *Int. J. Theor. Phys.* **21** 467
[39] Mead C A and Truhlar D G 1979 *J. Chem. Phys.* **70** 2284–96
[40] Berry M V 1980 *Eur. J. Phys.* **1** 240
[41] Berry M 1984 *Proc. R. Soc. Lond.* A **392** 45
[42] Mead C 1992 *Rev. Mod. Phys.* **64** 51
[43] Shapere A and Wilczek F (ed) 1989 *Geometric Phases in Physics* (Singapore: World Scientific)
[44] Bohm A, Mostafazadeh A, Koizumi H, Niu Q and Zwanziger J 2003 *Geometric Phases in Quantum Systems* (Berlin: Springer)
[45] Taichenachev A V, Tumaikin A M and Yudin V I 1992 *Laser Phys.* **2** 575
[46] Dum R and Olshanii M 1996 *Phys. Rev. Lett.* **76** 1788–91
[47] Visser P M and Nienhuis G 1998 *Phys. Rev.* A **57** 4581–91
[48] Juzeliūnas G and Öhberg P 2004 *Phys. Rev. Lett.* **93** 033602
[49] Juzeliūnas G, Ruseckas J, Öhberg P and Fleischhauer M 2006 *Phys. Rev.* A **73** 025602
[50] Zhu S L, Fu H, Wu C J, Zhang S C and Duan L M 2006 *Phys. Rev. Lett.* **97** 240401
[51] Spielman I B 2009 *Phys. Rev.* A **79** 063613
[52] Günter K J, Cheneau M, Yefsah T, Rath S P and Dalibard J 2009 *Phys. Rev.* A **79** 011604
[53] Dutta S K, Teo B K and Raithel G 1999 *Phys. Rev. Lett.* **83** 1934–7
[54] Unanyan R G, Shore B W and Bergmann K 1999 *Phys. Rev.* A **59** 2910
[55] Ruseckas J, Juzeliūnas G, Öhberg P and Fleischhauer M 2005 *Phys. Rev. Lett.* **95** 010404
[56] Liu X J, Borunda M F, Liu X and Sinova J 2009 *Phys. Rev. Lett.* **102** 046402
[57] Liu X J, Liu X, Kwek L C and Oh C H 2007 *Phys. Rev. Lett.* **98** 026602
[58] Beeler M C, Williams R A, Jimenez-Garcia K, LeBlanc L J, Perry A R and Spielman I B 2013 *Nature* **498** 201–4
[59] Eckardt A, Weiss C and Holthaus M 2005 *Phys. Rev. Lett.* **95** 260404
[60] Cooper N R 2008 *Adv. Phys.* **57** 539–616
[61] Aidelsburger M, Atala M, Nascimbène S, Trotzky S, Chen Y A and Bloch I 2011 *Phys. Rev. Lett.* **107** 255301
[62] Jiménez-García K, LeBlanc L, Williams R, Beeler M, Perry A and Spielman I B 2012 *Phys. Rev. Lett.* **108** 225303
[63] Struck J, Ölschläger C, Weinberg M, Hauke P, Simonet J, Eckardt A, Lewenstein M, Sengstock K and Windpassinger P 2012 *Phys. Rev. Lett.* **108** 225304
[64] Aidelsburger M, Atala M, Lohse M, Barreiro J T, Paredes B and Bloch I 2013 *Phys. Rev. Lett.* **111** 185301
[65] Miyake H, Siviloglou G A, Kennedy C J, Burton W C and Ketterle W 2013 *Phys. Rev. Lett.* **111** 185302
[66] Cheng T P and Li L F 1991 *Gauge Theory of Elementary Particle Physics* (Oxford: Oxford University Press)
[67] Levin M and Wen X G 2005 *Rev. Mod. Phys.* **77** 871–9
[68] Wiese U J 2013 *Ann. Phys.* **525** 777
[69] Banerjee D, Dalmonte M, Müller M, Rico E, Stebler P, Wiese U J and Zoller P 2012 *Phys. Rev. Lett.* **109** 175302
[70] Tagliacozzo L, Celi A, Orland P, Mitchell M W and Lewenstein M 2013 *Nature Commun.* **4** 2615
[71] Zohar E, Cirac J I and Reznik B 2013 *Phys. Rev. Lett.* **110** 125304
[72] Tagliacozzo L, Celi A, Zamora A and Lewenstein M 2013 *Ann. Phys.* **330** 160–91
[73] Qi X L and Zhang S C 2011 *Rev. Mod. Phys.* **83** 1057–110
[74] Hasan M and Kane C 2010 *Rev. Mod. Phys.* **82** 3045–67
[75] Nayak C, Simon S H, Stern A, Freedman M and Das Sarma S 2008 *Rev. Mod. Phys.* **80** 1083
[76] Nakahara M 2003 *Geometry, Topology, and Physics* (*Graduate Student Series in Physics*) (Bristol: Institute of Physics Publishing) ISBN 9780750306065
[77] von Klitzing K 1986 *Rev. Mod. Phys.* **58** 519–31
[78] Hatsugai Y 1993 *Phys. Rev. Lett.* **71** 3697–700
[79] Wen X G 1995 *Adv. Phys.* **44** 405
[80] Dalibard J, Gerbier F, Juzeliūnas G and Öhberg P 2011 *Rev. Mod. Phys.* **83** 1523–43
[81] Fetter A L 2009 *Rev. Mod. Phys.* **81** 647
[82] Landau L D and Lifshitz E M 1987 *Quantum Mechanics* (New York: Pergamon)
[83] Matthews M R, Anderson B P, Haljan P C, Hall D S, Wieman C E and Cornell E A 1999 *Phys. Rev. Lett.* **83** 2498–501
[84] Madison K W, Chevy F, Wohlleben W and Dalibard J 2000 *Phys. Rev. Lett.* **84** 806–9
[85] Abo-Shaeer J R, Raman C, Vogels J M and Ketterle W 2001 *Science* **292** 476–9
[86] Tung S, Schweikhard V and Cornell E A 2006 *Phys. Rev. Lett.* **97** 240402
[87] Williams R A, Al-Assam S and Foot C J 2010 *Phys. Rev. Lett.* **104** 050404
[88] Wright K C, Blakestad R B, Lobb C J, Phillips W D and Campbell G K 2012 *Phys. Rev. Lett.* **110** 025302
[89] Engels P, Coddington I, Haljan P, Schweikhard V and Cornell E 2003 *Phys. Rev. Lett.* **90** 170405

[90] Schweikhard V, Coddington I, Engels P, Mogendorff V P and Cornell E A 2004 *Phys. Rev. Lett.* **92** 040404
[91] Chevy F, Madison K W and Dalibard J 2000 *Phys. Rev. Lett.* **85** 2223–7
[92] Haljan P C, Anderson B P, Coddington I and Cornell E A 2001 *Phys. Rev. Lett.* **86** 2922–5
[93] Gemelke N, Sarajlic E and Chu S 2010 arXiv:1007.2677
[94] Madison K W, Fischer M C, Diener R B, Niu Q and Raizen M G 1998 *Phys. Lett. Lett.* **81** 5093
[95] Struck J, Ölschläger C, Targat R L, Soltan-Panahi P, Eckardt A, Lewenstein M, Windpassinger P and Sengstock K 2011 *Science* **333** 996
[96] Arimondo E, Ciampinia D, Eckardt A, Holthaus M and Morsch O 2012 *Adv. At. Mol. Opt. Phys.* **61** 515
[97] Struck J *et al* 2013 *Nature Phys.* **9** 738–43
[98] Windpassinger P and Sengstock K 2013 *Rep. Prog. Phys.* **76** 086401
[99] Dalibard J 2013 *Cours du Collège de France* (www.phys.ens.fr/∼dalibard/CdF/2013/Cours_2013.pdf)
[100] Hauke P *et al* 2012 *Phys. Rev. Lett.* **109** 145301
[101] Goldman N and Dalibard J 2014 *Phys. Rev.* X **4** 031027
[102] Zheng W and Zhai H 2014 *Phys. Rev.* A **89** 061603
[103] Baur S K, Schleier-Smith M H and Cooper N R 2014 *Phys. Rev.* A **89** 051605
[104] Anisimovas E, Anderson B, Juzeliūnas G and Eckardt A 2014 in preparation
[105] Kitagawa T, Berg E, Rudner M and Demler E 2010 *Phys. Rev.* B **82** 235114
[106] Lindner N H, Refael G and Galitski V 2011 *Nature Phys.* **7** 490
[107] Cayssol J, Dóra B, Simon F and Moessner R 2013 *Phys. Status Solidi* (RRL) **7** 101–8
[108] Levy N, Burke S A, Meaker K L, Panlasigui M, Zettl A, Guinea F, Castro Neto A H and Crommie M F 2010 *Science* **329** 544
[109] Oka T and Aoki H 2009 *Phys. Rev.* B **79** 081406(R)
[110] Cohen-Tannoudji C, Dupont-Roc J and Grynberg G 1989 *Photons and Atoms: Introduction to Quantum Electrodynamics* (New York: Wiley)
[111] Jackson J D 1998 *Classical Electrodynamics* (New York: Wiley)
[112] Moody J, Shapere A and Wilczek F 1986 *Phys. Rev. Lett.* **56** 893
[113] Zygelman B 1987 *Phys. Lett.* A **125** 476
[114] Zee A 1988 *Phys. Rev.* A **38** 1
[115] Jackiw R 1988 *Comments At. Mol. Phys.* **21** 71
[116] Xiao D, Chang M C and Niu Q 2010 *Rev. Mod. Phys.* **82** 1959
[117] Zygelman B 2012 *Phys. Rev.* A **86** 042704
[118] Grynberg G and Robilliard C 2001 *Phys. Rep.* **355** 335
[119] Dudarev A M, Diener R B, Carusotto I and Niu Q 2004 *Phys. Rev. Lett.* **92** 153005
[120] Zhang P, Li Y and Sun C P 2005 *Eur. Phys. J.* D **36** 229
[121] Liu X J, Liu X, Kwek L C and Oh C H 2008 *Front. Phys. China* **3** 113–25
[122] Aharonov Y and Stern A 1992 *Phys. Rev. Lett.* **69** 3593–7
[123] Cheneau M, Rath S P, Yefsah T, Gunter K J, Juzeliūnas G and Dalibard J 2008 *Europhys. Lett.* **83** 60001
[124] Unanyan R G, Fleischhauer M, Shore B W and Bergmann K 1998 *Opt. Commun.* **155** 144
[125] Juzeliūnas G, Ruseckas J, Öhberg P and Fleischhauer M 2007 *Lithuanian J. Phys.* **47** 351–60
[126] Zhang X D, Wang Z D, Hu L B, Zhang Z M and Zhu S L 2008 *New J. Phys.* **10** 043031
[127] Fu Z, Huang L, Meng Z, Wang P, Liu X J, Pu H, Hu H and Zhang J 2013 *Phys. Rev.* A **87** 053619
[128] Lu L H and Li Y Q 2007 *Phys. Rev.* A **76** 023410
[129] Burrello M and Trombettoni A 2010 *Phys. Rev. Lett.* **105** 125304
[130] Radic J, Sedrakyan T A, Spielman I B and Galitski V 2011 *Phys. Rev.* A **84** 063604
[131] Zhou X F, Zhou J and Wu C 2011 *Phys. Rev.* A **84** 063624
[132] Xu X Q and Han J H 2011 *Phys. Rev. Lett.* **107** 200401
[133] Liu C F and Liu W M 2012 *Phys. Rev.* A **86** 033602
[134] Zhang X F, Gao R S, Wang X, Dong R F, Liu T and Zhang S G 2013 *Phys. Lett.* A **377** 1109
[135] Huckans J H, Spielman I B, Tolra B L, Phillips W D and Porto J V 2009 *Phys. Rev.* A **80** 043609
[136] Happer W and Mathur B 1967 *Phys. Rev.* **163** 12
[137] Cohen-Tannoudji C and Dupont-Roc J 1972 *Phys. Rev.* A **5** 968–84
[138] Deutsch I H and Jessen P S 1998 *Phys. Rev.* A **57** 1972–86
[139] Grimm R, Weidemüller M and Ovchinnikov Y B 2000 *Adv. At. Mol. Opt. Phys.* **42** 95–170
[140] Cui X, Biao L, Ho T L, Lev B L and Zhai H 2013 *Phys. Rev.* A **88** 011601(R)
[141] Cohen-Tannoudji C, Dupont-Roc J and Grynberg G 1998 *Atom–Photon Interactions* (Weinheim: Wiley-VCH)
[142] Loudon R 2000 *The Quantum Theory of Light* 3rd edn (Oxford: Oxford University Press)
[143] Sebby-Strabley J, Anderlini M, Jessen P S and Porto J V 2006 *Phys. Rev.* A **73** 033605
[144] Juzeliūnas G and Spielman I B 2012 *New J. Phys.* **14** 123022
[145] Breit G and Rabi I I 1931 *Phys. Rev.* **38** 2082–3
[146] Budker D, Kimball D and DeMille D 2004 *Atomic Physics: An Exploration through Problems and Solutions* (Oxford: Oxford University Press)
[147] LeBlanc L J, Jiménez-García K, Williams R A, Beeler M C, Perry A R, Phillips W D and Spielman I B 2012 *Proc. Natl Acad. Sci. USA* **109** 10811
[148] McKay D and DeMarco B 2010 *New J. Phys.* **12** 055013
[149] Williams R A, LeBlanc L J, Jiménez-García K, Beeler M C, Perry A R, Phillips W D and Spielman I B 2012 *Science* **335** 314–7
[150] Cooper N R and Dalibard J 2011 *Europhys. Lett* **95** 66004
[151] Juzeliūnas G, Öhberg P, Ruseckas J and Klein A 2005 *Phys. Rev.* A **71** 053614
[152] Juzeliūnas G, Ruseckas J and Öhberg P 2005 *J. Phys. B: At. Mol. Opt. Phys.* **38** 4171
[153] Song J J, Foreman B A, Liu X J and Oh C H 2008 *Europhys. Lett.* **84** 20012
[154] Cooper N R and Hadzibabic Z 2010 *Phys. Rev. Lett.* **104** 030401
[155] Arimondo E 1996 *Progress in Optics* vol 35 ed E Wolf (Amsterdam: Elsevier) p 259
[156] Harris S E 1997 *Phys. Today* **50** 36
[157] Lukin M D 2003 *Rev. Mod. Phys.* **75** 457–72
[158] Fleischhauer M, Imamoglu A and Marangos J P 2005 *Rev. Mod. Phys.* **77** 633
[159] Bergmann K, Theuer H and Shore B W 1998 *Rev. Mod. Phys.* **70** 1003–25
[160] Vitanov N V, Fleischhauer M, Shore B W and Bergmann K 2001 *Adv. At. Mol. Opt. Phys.* **46** 55
[161] Král P, Thanopulos I and Shapiro M 2007 *Rev. Mod. Phys.* **79** 53
[162] Stanescu T D and Galitski V 2007 *Phys. Rev.* B **75** 125307
[163] Jacob A, Öhberg P, Juzeliūnas G and Santos L 2007 *Appl. Phys.* B **89** 439
[164] Juzeliūnas G, Ruseckas J, Lindberg M, Santos L and Öhberg P 2008 *Phys. Rev.* A **77** 011802(R)
[165] Stanescu T D, Anderson B and Galitski V 2008 *Phys. Rev.* A **78** 023616
[166] Vaishnav J Y and Clark C W 2008 *Phys. Rev. Lett.* **100** 153002
[167] Juzeliūnas G, Ruseckas J and Dalibard J 2010 *Phys. Rev.* A **81** 053403
[168] Campbell D L, Juzeliūnas G and Spielman I B 2011 *Phys. Rev.* A **84** 025602

[169] Galitski V and Spielman I B 2013 *Nature* **494** 49–54
[170] Juzeliūnas G and Öhberg P 2008 *Structured Light and its Applications: An Introduction to Phase-Structured Beams and Nanoscale Optical Forces* ed D L Andrews (Amsterdam: Elsevier) pp 295–333
[171] Li Y, Bruder C and Sun C P 2007 *Phys. Rev. Lett.* **99** 130403
[172] Bohm A, Kendrick B, Loewe M and Boya L 1992 *J. Math. Phys.* **33** 977
[173] Zygelman B 1990 *Phys. Rev. Lett.* **64** 256
[174] Cooper N 2011 *Phys. Rev. Lett.* **106** 175301
[175] Juzeliūnas G and Spielman I B 2012 *Proc. SPIE* **8274** 882740H
[176] Hemmerich A, Donald Schropp J and Hänsch T W 1991 *Phys. Rev.* A **44** 1910
[177] Hemmerich A, Schropp D, Esslinger T and Hansch T W 1992 *Europhys. Lett.* **18** 391
[178] Cooper N R and Dalibard J 2013 *Phys. Rev. Lett.* **110** 185301
[179] Jaksch D and Zoller P 2003 *New J. Phys.* **5** 56
[180] Gerbier F and Dalibard J 2010 *New J. Phys.* **12** 033007
[181] Cooper N R and Moessner R 2012 *Phys. Rev. Lett.* **109** 215302
[182] Haldane F D M 1988 *Phys. Rev. Lett.* **61** 2015
[183] Higbie J and Stamper-Kurn D M 2002 *Phys. Rev. Lett.* **88** 090401
[184] Papoff F, Mauri F and Arimondo E 1992 *J. Opt. Soc. Am.* B **9** 321–31
[185] Montina A and Arecchi F T 2003 *Phys. Rev.* A **67** 023616
[186] Higbie J and Stamper-Kurn D M 2004 *Phys. Rev.* A **69** 053605
[187] Spielman I B, Johnson P R, Huckans J H, Fertig C D, Rolston S L, Phillips W D and Porto J V 2006 *Phys. Rev.* A **73** 020702(R)
[188] Yarmchuk E J, Gordon M J V and Packard R E 1979 *Phys. Rev. Lett.* **43** 214–7
[189] Ol'shanii M A and Minogin V G 1991 *Quantum Opt.* **3** 317
[190] Kulin S, Castin Y, Ol'shanii M, Peik E, Saubaméa B, Leduc M and Cohen-Tannoudji C 1999 *Eur. Phys. J.* D **7** 279
[191] Unanyan R G and Fleischhauer M 2004 *Phys. Rev.* A **69** 050302(R)
[192] Theuer H, Unanyan R, Habscheid C, Klein K and Bergmann K 1999 *Opt. Express* **4** 77
[193] Vewinger F, Heinz M, Fernandez R G, Vitanov N V and Bergmann K 2003 *Phys. Rev. Lett.* **91** 213001
[194] Pietilä V and Möttönen M 2009 *Phys. Rev. Lett.* **102** 080403
[195] Song J J and Foreman B A 2009 *Phys. Rev.* A **80** 033602
[196] Juzeliūnas G, Ruseckas J, Jacob A, Santos L and Öhberg P 2008 *Phys. Rev. Lett.* **100** 200405
[197] Koralek J D, Weber C P, Orenstein J, Bernevig B A, Zhang S C, Mack S and Awschalom D D 2009 *Nature* **458** 610–3
[198] Kane C L and Mele E J 2005 *Phys. Rev. Lett.* **95** 146802
[199] Schnyder A P, Ryu S, Furusaki A and Ludwig A W W 2008 *Phys. Rev.* B **78** 195125
[200] Sau J D, Tewari S, Lutchyn R M, Stanescu T D and Das Sarma S 2010 *Phys. Rev.* B **82** 214509
[201] Osterloh K, Baig M, Santos L, Zoller P and Lewenstein M 2005 *Phys. Rev. Lett.* **95** 010403
[202] Goldman N, Satija I, Nikolic P, Bermudez A, Martin-Delgado M A, Lewenstein M and Spielman I B 2010 *Phys. Rev. Lett.* **105** 255302
[203] Anderson B M, Spielman I B and Juzeliūnas G 2013 *Phys. Rev. Lett.* **111** 125301
[204] Xu Z F, You L and Ueda M 2013 *Phys. Rev.* A **87** 063634
[205] Stanescu T D, Zhang C and Galitski V 2007 *Phys. Rev. Lett.* **99** 110403
[206] Ho T L and Zhang S 2012 *Phys. Rev. Lett.* **107** 150403
[207] Li Y, Pitaevskii L P and Stringari S 2012 *Phys. Rev. Lett.* **108** 225301
[208] Han L and Sá de Melo C A R 2012 *Phys. Rev.* A **85** 011606
[209] Seo K, Han L and Sá de Melo C A R 2012 *Phys. Rev.* A **85** 033601
[210] Seo K, Han L and Sá de Melo C A R 2012 *Phys. Rev. Lett.* **109** 105303
[211] Li Y, Martone G I and Stringari S 2012 *Europhys. Lett.* **99** 56008
[212] Martone G I, Li Y, Pitaevskii L P and Stringari S 2012 *Phys. Rev.* A **86** 063621
[213] Ozawa T, Pitaevskii L P and Stringari S 2013 *Phys. Rev.* A **87** 063610
[214] Li Y, Martone G I, Pitaevskii L P and Stringari S 2013 *Phys. Rev. Lett.* **110** 235302
[215] Lin Y J, Perry A R, Compton R L, Spielman I B and Porto J V 2009 *Phys. Rev.* A **79** 063631
[216] Zhai H 2012 *Int. J. Mod. Phys.* B **26** 1230001
[217] Xu Z F and You L 2012 *Phys. Rev.* A **85** 043605
[218] Liu X J, Law K T and Ng T K 2014 *Phys. Rev. Lett.* **112** 086401
[219] Sun Q, Wen L, Liu W M, Juzeliūnas G and Ji A C 2014 arXiv:1403.4338
[220] Anderson B M, Juzeliūnas G, Galitski V M and Spielman I B 2012 *Phys. Rev. Lett.* **108** 235301
[221] Vyasanakere J P and Shenoy V B 2011 *Phys. Rev.* B **83** 94515
[222] Vyasanakere J P, Zhang S and Shenoy V B 2011 *Phys. Rev.* B **84** 14512
[223] Jiang L, Liu X J, Hu H and Pu H 2011 *Phys. Rev.* A **84** 063618
[224] Hu H, Jiang L, Liu X J and Pu H 2011 *Phys. Rev. Lett.* **107** 195304
[225] Liu X J, Jiang L, Pu H and Hu H 2012 *Phys. Rev.* A **85** 21603
[226] Chen G, Gong M and Zhang C 2012 *Phys. Rev.* A **85** 013601
[227] He L and Huang X G 2012 *Phys. Rev. Lett.* **108** 145302
[228] He L and Huang X G 2012 *Phys. Rev.* B **86** 014511
[229] Cui J X, Liu X J, Long G L and Hu H 2012 *Phys. Rev.* A **86** 053628
[230] Zheng Z, Gong M, Zou X, Zhang C and Guo G 2013 *Phys. Rev.* A **87** 031602
[231] Maldonado-Mundo D, He L, Öhberg P and Valiente M 2013 *Phys. Rev.* A **88** 053609
[232] Sinha S, Nath R and Santos L 2011 *Phys. Rev. Lett.* **107** 270401
[233] C Wu I, Mondragon-Shem and Zhou X F 2011 *Chin. Phys. Lett.* **28** 097102
[234] Hu H, Ramachandhran B, Pu H and Liu X J 2012 *Phys. Rev. Lett.* **108** 010402
[235] Su S W, Liu I K, Tsai Y C, Liu W M and Gou S C 2012 *Phys. Rev.* A **86** 023601
[236] Kawakami T, Mizushima T, Nitta M and Machida K 2012 *Phys. Rev. Lett.* **109** 015301
[237] Ruokokoski E, Huhtamäki J A M and Möttönen M 2012 *Phys. Rev.* A **86** 051607
[238] Xu Z F, Kawaguchi Y, You L and Ueda M 2012 *Phys. Rev.* A **86** 033628
[239] Sedrakyan T A, Kamenev A and Glazman L I 2012 *Phys. Rev.* A **86** 063639
[240] Song S W, Zhang Y C, Wen L, Wang H, Sun Q, Ji A C and Liu W M 2013 *J. Phys. B: At. Mol. Opt. Phys.* **46** 145304
[241] Su S W, Gou S C, Spielman I B, Santos L, Acus A, Ruseckas J and Juzeliūnas G 2014 in preparation
[242] Zhai H 2014 arXiv:1403.8021
[243] Zhou X, Li Y, Cai Z and Wu C 2013 *J. Phys. B: At. Mol. Opt. Phys.* **46** 134001
[244] Gerbier F, Goldman N, Lewenstein M and Sengstock K 2013 *J. Phys. B: At. Mol. Opt. Phys.* **46** 130201
[245] Stringari S 1996 *Phys. Rev. Lett.* **77** 2360–3
[246] Öhberg P, Surkov E L, Tittonen I, Stenholm S, Wilkens M and Shlyapnikov G V 1997 *Phys. Rev.* A **56** R3346–9

[247] Fliesser M, Csordás A, Szépfalusy P and Graham R 1997 *Phys. Rev.* A **56** R2533–6
[248] Wang C, Gao C, Jian C M and Zhai H 2010 *Phys. Rev. Lett.* **105** 160403
[249] Barnett R, Powell S, Grass T, Lewenstein M and Das Sarma S 2012 *Phys. Rev.* A **85** 023615
[250] Zhang Y, Mao L and Zhang C 2012 *Phys. Rev. Lett.* **108** 035302
[251] Ozawa T and Baym G 2012 *Phys. Rev.* A **85** 013612
[252] Ozawa T and Baym G 2012 *Phys. Rev.* A **85** 063623
[253] Zhou X F, Zhou J and Wu C 2011 *Phys. Rev.* A **84** 63624
[254] Cui X and Zhou Q 2013 *Phys. Rev.* A **87** 31604
[255] He P S, Liao R and Liu W M 2012 *Phys. Rev.* A **86** 43632
[256] Liao R, Huang Z G, Lin X M and Liu W M 2013 *Phys. Rev.* A **87** 043605
[257] Han W, Juzeliūnas G, Zhang W and Liu W M 2014 arXiv:1407.2972
[258] Zhou Q and Cui X 2013 *Phys. Rev. Lett.* **110** 140407
[259] Chen X, Rabinovich M, Anderson B M and Santos L 2014 arXiv:1406.4938
[260] Lan Z and Öhberg P 2014 *Phys. Rev.* A **89** 023630
[261] Osterloh K, Baig M, Santos L, Zoller P and Lewenstein M 2005 *Phys. Rev. Lett.* **95** 010403
[262] Cong-Jun W, Mondragon-Shem I and Xiang-Fa Z 2011 *Chin. Phys. Lett.* **28** 097102
[263] Nayak C, Simon S H, Stern A, Freedman M and Das Sarma S 2008 *Rev. Mod. Phys.* **80** 1083
[264] Salomaa M M and Volovik G E 1985 *Phys. Rev. Lett.* **55** 1184
[265] Gopalakrishnan S, Martin I and Demler E A 2013 *Phys. Rev. Lett.* **111** 185304
[266] Wilson R M, Anderson B M and Clark C W 2013 *Phys. Rev. Lett.* **111** 185303
[267] Jochim S, Bartenstein M, Altmeyer A, Hendl G, Riedl S, Chin C, Denschlag J H and Grimm R 2003 *Science* **302** 2101
[268] Zwierlein M W, Abo-Shaeer J R, Schirotzek A, Schunck C H and Ketterle W 2003 *Nature* **435** 1047
[269] Gor'kov L P and Rashba E I 2001 *Phys. Rev. Lett.* **87** 37004
[270] Yu Z Q and Zhai H 2011 *Phys. Rev. Lett.* **107** 195305
[271] Shenoy V B and Vyasanakere J P 2013 *J. Phys. B: At. Mol. Opt. Phys.* **46** 134009
[272] Zhou K and Zhang Z 2012 *Phys. Rev. Lett.* **108** 025301
[273] Sun Q, Zhu G B, Liu W M and Ji A C 2013 *Phys. Rev.* A **88** 063637
[274] Gopalakrishnan S, Lamacraft A and Goldbart P M 2011 *Phys. Rev.* A **84** 061604
[275] Ozawa T and Baym G 2011 *Phys. Rev.* A **84** 043622
[276] Maldonado-Mundo D, Öhberg P and Valiente M 2013 *J. Phys. B: At. Mol. Opt. Phys.* **46** 134002
[277] Sato M, Takahashi Y and Fujimoto S 2009 *Phys. Rev. Lett.* **103** 020401
[278] Sau J, Sensarma R, Powell S, Spielman I and Das Sarma S 2011 *Phys. Rev.* B **83** 140510
[279] Zhang C, Tewari S, Lutchyn R M and Das Sarma S 2008 *Phys. Rev. Lett.* **101** 160401
[280] Gong M, Tewari S and Zhang C 2011 *Phys. Rev. Lett.* **107** 195303
[281] Iskin M and Subaş ı A L 2011 *Phys. Rev. Lett.* **107** 050402
[282] Liao R, Yi-Xiang Y and Liu W M 2012 *Phys. Rev. Lett.* **108** 80406
[283] Zheng Z, Gong M, Zou X, Zhang C and Guo G 2013 *Phys. Rev.* A **87** 031602
[284] Zheng Z, Gong M, Zhang Y, Zou X, Zhang C and Guo G 2012 arXiv:1212.6826
[285] Dong L, Jiang L, Hu H and Pu H 2013 *Phys. Rev.* A **87** 043616
[286] Shenoy V 2013 *Phys. Rev.* A **88** 033609
[287] Liu X J and Hu H 2012 *Phys. Rev.* A **85** 033622
[288] Zinn-Justin J 2002 *Quantum Field Theory and Critical Phenomena* (*International Series of Monographs on Physics*) 4th edn (Oxford: Clarendon)
[289] Wilson K G 1974 *Phys. Rev.* D **10** 2445
[290] Gupta R 1998 arXiv:hep-lat/9807028
[291] Kogut J B 1983 *Rev. Mod. Phys.* **55** 775
[292] Ashcroft N W and Mermin D N 1976 *Solid State Physics* 1st edn (Toronto: Thomson Learning)
[293] Mott N 1968 *Rev. Mod. Phys.* **40** 677
[294] Lee P, Nagaosa N and Wen X 2006 *Rev. Mod. Phys.* **78** 17
[295] Neto A H C, Guinea F, Peres N M R, Novoselov K S and Geim A K 2009 *Rev. Mod. Phys.* **81** 109
[296] Qi X L, Hughes T L and Zhang S C 2008 *Phys. Rev.* B **78** 195424
[297] Jaksch D and Zoller P 2005 *Ann. Phys.* **315** 52–79
[298] Jördens R, Strohmaier N, Günter K, Moritz H and Esslinger T 2008 *Nature* **455** 204–7
[299] Wannier G 1937 *Phys. Rev.* **52** 191
[300] Kohn W 1959 *Phys. Rev.* **115** 1460
[301] Altman E, Hofstetter W, Demler E and Lukin M D 2003 *New J. Phys.* **5** 113
[302] Tarruell L, Greif D, Uehlinger T, Jotzu G and Esslinger T 2012 *Nature* **483** 302
[303] Schneider U, Hackermüller L, Ronzheimer J P, Will S, Braun S, Best T, Bloch I, Demler E, Mandt S, Rasch D and Rosch A 2012 *Nature Phys.* **8** 213
[304] Eckardt A, Hauke P, Soltan-Panahi P, Becker C, Sengstock K and Lewenstein M 2010 *Europhys. Lett.* **89** 10010
[305] Hofstadter D 1976 *Phys. Rev.* B **14** 2239
[306] Dirac P 1931 *Proc. R. Soc. Lond.* A **133** 60
[307] Aharonov Y and Bohm D 1959 *Phys. Rev.* **115** 485
[308] Luttinger J 1951 *Phys. Rev.* **84** 814
[309] Gerry C C and Singh V A 1979 *Phys. Rev.* D **20** 2550
[310] Yang C N and Mills R L 1954 *Phys. Rev.* **96** 191
[311] Goldman N, Kubasiak A, Gaspard P and Lewenstein M 2009 *Phys. Rev.* A **79** 11
[312] Barnett R, Boyd G R and Galitski V 2012 *Phys. Rev. Lett.* **109** 235308
[313] Horváthy P 1986 *Phys. Rev.* D **33** 407
[314] Gagel F and Maschke K 1995 *Phys. Rev.* B **52** 2013
[315] Kohmoto M 1989 *Phys. Rev.* B **39** 11943–9
[316] Hatsugai Y, Fukui T and Aoki H 2006 *Phys. Rev.* B **74** 16
[317] Lim L K, Hemmerich A and Morais Smith C 2010 *Phys. Rev.* A **81** 023404
[318] Wallace P R 1947 *Phys. Rev.* **71** 622
[319] Kimura T, Tamura H, Shiraishi K and Takayanagi H 2002 *Phys. Rev.* B **65** 81307
[320] Aoki H, Ando M and Matsumura H 1996 *Phys. Rev.* B **54** 1517930
[321] Vidal J, Mosseri R and Douçot B 1998 *Phys. Rev. Lett.* **81** 5888
[322] Goldman N, Urban D F and Bercioux D 2011 *Phys. Rev.* A **83** 63601
[323] Bercioux D, Goldman N and Urban D 2011 *Phys. Rev.* A **83** 023609
[324] Rammal R 1985 *J. Phys. France* **46** 1345–54
[325] Goerbig M 2011 *Rev. Mod. Phys.* **83** 1193–243
[326] Palmer R, Klein A and Jaksch D 2008 *Phys. Rev.* A **78** 13
[327] Powell S, Barnett R, Sensarma R and Das Sarma S 2010 *Phys. Rev. Lett.* **104** 255303
[328] Powell S, Barnett R, Sensarma R and Das Sarma S 2011 *Phys. Rev.* A **83** 13612
[329] Harper F, Simon S H and Roy R 2014 *Phys. Rev.* B **90** 075104
[330] Kane C L and Mele E J 2005 *Phys. Rev. Lett.* **95** 226801
[331] Kane C L and Mele E J 2005 *Phys. Rev. Lett.* **95** 146802
[332] Bernevig B A and Zhang S C 2006 *Phys. Rev. Lett.* **96** 106802
[333] Bychkov Y A and Rashba E I 1984 *J. Phys. C: Solid State Phys.* **17** 6039

[334] Winkler R 2003 *Spin–Orbit Coupling Effects in Two-Dimensional Electron and Hole Systems* (Berlin: Springer)
[335] Fu L, Kane C L and Mele E J 2007 *Phys. Rev. Lett.* **98** 106803
[336] Goldman N, Satija I, Nikolic P, Bermudez A, Martin-Delgado M, Lewenstein M and Spielman I B 2010 *Phys. Rev. Lett.* **105** 255302
[337] Kennedy C J, Siviloglou G A, Miyake H, Burton W C and Ketterle W 2013 *Phys. Rev. Lett.* **111** 225301
[338] Cocks D, Orth P P, Rachel S, Buchhold M, Hur K L and Hofstetter W 2012 *Phys. Rev. Lett.* **109** 205303
[339] Orth P P, Cocks D, Rachel S, Buchhold M, Hur K L and Hofstetter W 2013 *J. Phys. B: At. Mol. Opt. Phys.* **46** 134004
[340] Goldman N, Kubasiak A, Bermudez A, Gaspard P, Lewenstein M and Martin-Delgado M A 2009 *Phys. Rev. Lett.* **103** 35301
[341] Zamora A, Szirmai G and Lewenstein M 2011 *Phys. Rev.* A **84** 53620
[342] Palmer R N and Pachos J K 2011 *New J. Phys.* **13** 5002
[343] Mei F, Zhu S L, Feng X L, Zhang Z M and Oh C 2011 *Phys. Rev.* A **84** 023622
[344] Graß T, Baranov M A and Lewenstein M 2011 *Phys. Rev.* A **84** 43605
[345] Komineas S and Cooper N R 2012 *Phys. Rev.* A **85** 053623
[346] Graß T, Saha K, Sengupta K and Lewenstein M 2011 *Phys. Rev.* A **84** 53632
[347] Vozmediano M A H, Katsnelson M I and Guinea F 2010 *Phys. Rep.* **496** 109
[348] Goldman N, Beugeling W and Morais Smith C 2012 *Europhys. Lett.* **97** 23003
[349] Satija I, Dakin D, Vaishnav J and Clark C 2008 *Phys. Rev.* A **77** 043410
[350] Goldman N and Gaspard P 2007 *Europhys. Lett.* **78** 60001
[351] Goldman N 2007 *Europhys. Lett.* **80** 20001
[352] Beugeling W, Goldman N and Morais Smith C 2012 *Phys. Rev.* B **86** 075118
[353] Maraner P and Pachos J K 2009 *Phys. Lett.* A **373** 2542
[354] Ruostekoski J, Dunne G V and Javanainen J 2002 *Phys. Rev. Lett.* **88** 180401
[355] Ruostekoski J, Javanainen J and Dunne G 2008 *Phys. Rev.* A **77** 013603
[356] Mueller E J 2004 *Phys. Rev.* A **70** 041603
[357] Kolovsky A R 2011 *Europhys. Lett.* **93** 20003
[358] Creffield C E and Sols F 2013 *Europhys. Lett.* **101** 40001
[359] Creffield C E and Sols F 2014 *Phys. Rev.* A **90** 023636
[360] Bermudez A, Schaetz T and Porras D 2011 *Phys. Rev. Lett.* **107** 150501
[361] Bermudez A, Schaetz T and Porras D 2012 *New J. Phys.* **14** 05304
[362] Anisimovas E, Gerbier F, Andrijauskas T and Goldman N 2014 *Phys. Rev.* A **89** 013632
[363] Goldman N, Gerbier F and Lewenstein M 2013 *J. Phys. B: At. Mol. Opt. Phys.* **46** 134010
[364] Aidelsburger M, Atala M, Nascimbène S, Trotzky S, Chen Y A and Bloch I 2013 *Appl. Phys.* B (doi:10.1007/s00340-013-5418-1)
[365] Mazza L, Bermudez A, Goldman N, Rizzi M, Martin-Delgado M A and Lewenstein M 2012 *New J. Phys.* **14** 015007
[366] Górecka A, Grémaud B and Miniatura C 2011 *Phys. Rev.* A **84** 23604
[367] Hemmerich A 2010 *Phys. Rev.* A **81** 063626
[368] Alba E, Fernandez-Gonzalvo X, Mur-Petit J, Pachos J and Garcia-Ripoll J 2011 *Phys. Rev. Lett.* **107** 235301
[369] Goldman N, Anisimovas E, Gerbier F, Öhberg P, Spielman I B and Juzeliūnas G 2013 *New J. Phys.* **15** 3025
[370] Juzeliūnas G and Spielman I B 2011 *Physics* **4** 99
[371] Sørensen A S, Demler E and Lukin M D 2005 *Phys. Rev. Lett.* **94** 086803
[372] Luttinger J M 1951 *Phys. Rev.* **84** 814–7
[373] Maricq M M 1982 *Phys. Rev.* B **25** 6622–32
[374] Rahav S, Gilary I and Fishman S 2003 *Phys. Rev.* A **68** 013820
[375] Grushin A G, Gomez-Leon A and Neupert T 2014 *Phys. Rev. Lett.* **112** 156801
[376] D'Alessio L and Polkovnikov A 2013 *Ann. Phys.* **333** 19–33
[377] Lazarides A, Das A and Moessner R 2014 *Phys. Rev. Lett.* **112** 150401
[378] Vorberg D, Wustmann W, Ketzmerick R and Eckardt A 2013 *Phys. Rev. Lett.* **111** 240405
[379] Langemeyer M and Holthaus M 2014 *Phys. Rev.* E **89** 012101
[380] Folman R, Kruger P, Schmiedmayer J, Denschlag J and Henkel C 2002 *Adv. At. Mol. Opt. Phys.* **48** 263
[381] Klein A and Jaksch D 2009 *Europhys. Lett.* **85** 13001
[382] Lang L J, Cai X and Chen S 2012 *Phys. Rev. Lett.* **108** 220401
[383] Mei F, Zhu S L, Zhang Z M, Oh C H and Goldman N 2012 *Phys. Rev.* A **85** 13638
[384] Aubry S and André G 1980 *Ann. Israel Phys. Soc.* **3** 133
[385] Roati G, D'Errico C, Fallani L, Fattori M, Fort C, Zaccanti M, Modugno G, Modugno M and Inguscio M 2008 *Nature* **453** 895
[386] Kraus Y E, Lahini Y, Ringel Z, Verbin M and Zilberberg O 2012 *Phys. Rev. Lett.* **109** 106402
[387] Deng X and Santos L 2014 *Phys. Rev.* A **89** 033632
[388] Kraus Y E, Ringel Z and Zilberberg O 2013 *Phys. Rev. Lett.* **111** 226401
[389] Boada O, Celi A, Latorre J I and Lewenstein M 2012 *Phys. Rev. Lett.* **108** 133001
[390] Celi A, Massignan P, Ruseckas J, Goldman N, Spielman I B, Juzeliūnas G and Lewenstein M 2014 *Phys. Rev. Lett.* **112** 043001
[391] Hügel D and Paredes B 2014 *Phys. Rev.* A **89** 023619
[392] Atala M, Aidelsburger M, Lohse M, Barreiro J T, Paredes B and Bloch I 2013 *Nature Phys.* **10** 588
[393] Juliá-Díaz B, Grass T, Barberán N and Lewenstein M 2012 *New J. Phys.* **14** 055003
[394] Carusotto I and Ciuti C 2013 *Rev. Mod. Phys.* **85** 299
[395] Hafezi M, Demler E A, Lukin M D and Taylor J M 2011 *Nature Phys.* **7** 907
[396] Rechtsman M C, Zeuner J M, Plotnik Y, Lumer Y, Podolsky D, Dreisow F, Nolte S, Segev M and Szameit A 2013 *Nature* **496** 196–200
[397] Ozawa T and Carusotto I 2014 *Phys. Rev. Lett.* **112** 133902
[398] Hafezi M, Lukin M D and Taylor J M 2013 *New J. Phys.* **15** 063001
[399] Umucalilar R O and Carusotto I 2012 *Phys. Rev. Lett.* **108** 206809
[400] Umucalilar R O and Carusotto I 2013 *Phys. Lett.* A **377** 2074
[401] Haldane F and Raghu S 2008 *Phys. Rev. Lett.* **100** 013904
[402] Konig M, Wiedmann S, Brune C, Roth A, Buhmann H, Molenkamp L W, Qi X L and Zhang S C 2007 *Science* **318** 766–70
[403] Hsieh D, Qian D, Wray L, Xia Y, Hor Y S, Cava R J and Hasan M Z 2008 *Nature* **452** 970–4
[404] Chen Y L *et al* 2009 *Science* **325** 178
[405] Jiang L, Kitagawa T, Alicea J, Akhmerov A, Pekker D, Refael G, Cirac J, Demler E, Lukin M and Zoller P 2011 *Phys. Rev. Lett.* **106** 220402
[406] Kraus C V, Diehl S, Zoller P and Baranov M A 2012 *New J. Phys.* **14** 3036
[407] Kraus C V, Dalmonte M, Baranov M A, Läuchli A M and Zoller P 2013 *Phys. Rev. Lett.* **111** 173004
[408] Nascimbène S 2013 *J. Phys. B: At. Mol. Opt. Phys.* **46** 134005
[409] Atala M, Aidelsburger M, Barreiro J T, Abanin D, Kitagawa T, Demler E and Bloch I 2013 *Nature Phys.* **9** 795

[410] Zhang D w, Wang Z d and Zhu S l 2012 *Front. Phys.* **7** 31–53
[411] Bhat R, Peden B M, Seaman B T, Kramer M, Carr L D and Holland M J 2006 *Phys. Rev.* A **74** 063606
[412] Lim L K, Smith C M and Hemmerich A 2008 *Phys. Rev. Lett.* **100** 130402
[413] Goldbaum D S and Mueller E J 2009 *Phys. Rev.* A **79** 21602
[414] Zhai H, Umucallar R O and Oktel M Ö 2010 *Phys. Rev. Lett.* **104** 145301
[415] Brantut J P, Meineke J, Stadler D, Krinner S and Esslinger T 2012 *Science* **337** 1069
[416] Öhberg P, Juzeliūnas G, Ruseckas J and Fleischhauer M 2005 *Phys. Rev.* A **72** 053632
[417] Hafezi M, Sorensen A S, Demler E and Lukin M D 2007 *Phys. Rev.* A **76** 023613
[418] Juliá-Díaz B, Dagnino D, Günter K J, Grass T, Barberán N, Lewenstein M and Dalibard J 2011 *Phys. Rev.* A **84** 053605
[419] Juliá-Díaz B, Grass T, Dutta O, Chang D E and Lewenstein M 2013 *Nature Commun.* **4** 2046
[420] Roncaglia M, Rizzi M and Dalibard J 2011 *Sci. Rep.* **1** 43
[421] Cooper N R, van Lankvelt F J M, Reijnders J W and Schoutens K 2005 *Phys. Rev.* A **72** 63622
[422] Bhat R, Kraemer M, Cooper J and Holland M J 2007 *Phys. Rev.* A **76** 043601
[423] Read N and Cooper N R 2003 *Phys. Rev.* A **68** 35601
[424] Graß T, Juliá-Díaz B and Lewenstein M 2012 *Phys. Rev.* A **86** 053629
[425] Shao L B, Zhu S L, Sheng L, Xing D Y and Wang Z D 2008 *Phys. Rev. Lett.* **101** 246810
[426] Stanescu T D, Galitski V, Vaishnav J Y, Clark C W and Das Sarma S 2009 *Phys. Rev.* A **79** 53639
[427] Li F, Sheng L and Xing D Y 2009 *Europhys. Lett.* **84** 60004
[428] Liu X J, Liu X, Wu C and Sinova J 2010 *Phys. Rev.* A **81** 033622
[429] Stanescu T D, Galitski V and Das Sarma S 2010 *Phys. Rev.* A **82** 013608
[430] Béri B and Cooper N 2011 *Phys. Rev. Lett.* **107** 145301
[431] Dauphin A, Müller M and Martin-Delgado M 2012 *Phys. Rev.* A **86** 053618
[432] Sun K, Liu W V, Hemmerich A and Das Sarma S 2012 *Nature Phys.* **8** 67
[433] Liu X J, Liu Z X and Cheng M 2013 *Phys. Rev. Lett.* **110** 076401
[434] Liu X J and Drummond P D 2012 *Phys. Rev.* A **86** 035602
[435] Kohmoto M 1985 *Ann. Phys.* **160** 343
[436] Thouless D J, Kohmoto M, Nightingale M P and den Nijs M 1982 *Phys. Rev. Lett.* **49** 405–8
[437] Ji Y, Chung Y, Sprinzak D, Heiblum M, Mahalu D and Shtrikman H 2003 *Nature* **422** 415
[438] Karmakar B *et al* 2011 *Phys. Rev. Lett.* **107** 236804
[439] Kundhikanjana W *et al* 2012 arXiv:1212.6441
[440] Umucalilar R O, Zhai H and Oktel M Ö 2008 *Phys. Rev. Lett.* **100** 70402
[441] Streda P 1982 *J. Phys. C: Solid State Phys.* **15** L717
[442] Bermudez A, Goldman N, Kubasiak A, Lewenstein M and Martin-Delgado M A 2010 *New J. Phys.* **12** 033041
[443] Zhao E, Bray-Ali N, Williams C, Spielman I B and Satija I 2011 *Phys. Rev.* A **84** 063629
[444] Price H and Cooper N 2012 *Phys. Rev.* A **85** 033620
[445] Dahan M B, Peik E, Reichel J, Castin Y and Salomon C 1996 *Phys. Rev. Lett.* **76** 4508
[446] Abanin D A, Kitagawa T, Bloch I and Demler E 2013 *Phys. Rev. Lett.* **110** 165304
[447] Liu X J, Law K T, Ng T K and Lee P A 2013 *Phys. Rev. Lett.* **111** 120402
[448] Dauphin A and Goldman N 2013 *Phys. Rev. Lett.* **111** 135302
[449] Wang L, Soluyanov A A and Troyer M 2013 *Phys. Rev. Lett.* **110** 166802
[450] King-Smith R D and Vanderbilt D 1993 *Phys. Rev.* B **47** 1651
[451] Goldman N, Beugnon J and Gerbier F 2013 *Eur. Phys. J.* **217** 135
[452] Goldman N, Dalibard J, Dauphin A, Gerbier F, Lewenstein M, Zoller P and Spielman I B 2013 *Proc. Natl Acad. Sci. USA* **110** 1–11
[453] Scarola V W and Das Sarma S 2007 *Phys. Rev. Lett.* **98** 4
[454] Goldman N, Beugnon J and Gerbier F 2012 *Phys. Rev. Lett.* **108** 255303
[455] Stenger J, Inouye S, Chikkatur A P, Stamper-Kurn D M, Pritchard D E and Ketterle W 1999 *Phys. Rev. Lett.* **82** 4569
[456] Killi M and Paramekanti A 2012 *Phys. Rev.* A **85** 061606
[457] Buchhold M, Cocks D and Hofstetter W 2012 *Phys. Rev.* A **85** 63614
[458] Javanainen J and Ruostekoski J 2003 *Phys. Rev. Lett.* **91** 150404
[459] Barnett R 2013 *Phys. Rev.* A **88** 063631
[460] Reichl M and Mueller E 2014 *Phys. Rev.* A **89** 063628
[461] Weitenberg C, Endres M, Sherson J F, Cheneau M, Schauß P, Fukuhara T, Bloch I and Kuhr S 2011 *Nature* **471** 319–24
[462] Wilczek F 1987 *Phys. Rev. Lett.* **58** 1799
[463] Fu L and Kane C L 2008 *Phys. Rev. Lett.* **100** 96407
[464] Alicea J 2010 *Phys. Rev.* B **81** 125318
[465] Alicea J, Oreg Y, Refael G, Oppen F V and Fisher M P A 2011 *Nature Phys.* **7** 412
[466] Zhu S L, Shao L B, Wang Z D and Duan L M 2011 *Phys. Rev. Lett.* **106** 100404
[467] Kraus C V, Zoller P and Baranov M A 2013 *Phys. Rev. Lett.* **111** 203001
[468] Pachos J K, Alba E, Lahtinen V and Garcia-Ripoll J J 2013 *Phys. Rev.* A **88** 013622
[469] Zohar E, Cirac J I and Reznik B 2012 *Phys. Rev. Lett.* **109** 125302
[470] Zohar E, Cirac J I and Reznik B 2013 *Phys. Rev. Lett.* **110** 55302
[471] Zohar E and Reznik B 2011 *Phys. Rev. Lett.* **107** 275301
[472] Keilmann T, Lanzmich S, McCulloch I and Roncaglia M 2011 *Nature Commun.* **2** 361
[473] Cirac J, Maraner P and Pachos J 2010 *Phys. Rev. Lett.* **105** 190403
[474] Zohar E, Cirac J I and Reznik B 2013 *Phys. Rev.* A **88** 023617
[475] Tewari S, Scarola V W, Senthil T and Das Sarma S 2006 *Phys. Rev. Lett.* **97** 200401
[476] Glaetzle A W, Dalmonte M, Nath R, Rousochatzakis I, Moessner R and Zoller P 2014 arXiv:1404.5326
[477] Aglietti U, Griguolo L, Jackiw R, Pi S Y and Seminara D 1996 *Phys. Rev. Lett.* **77** 4406–9
[478] Edmonds M, Valiente M and Öhberg P 2013 *J. Phys. B: At. Mol. Opt. Phys.* **46** 134013
[479] Lee K L, Grémaud B, Han R, Englert B G and Miniatura C 2009 *Phys. Rev.* A **80** 043411
[480] Hou J M, Yang W X and Liu X J 2009 *Phys. Rev.* A **79** 043621
[481] Merkl M, Jacob A, Zimmer F E, Öhberg P and Santos L 2010 *Phys. Rev. Lett.* **104** 073603
[482] Kapit E and Mueller E 2011 *Phys. Rev.* A **83** 33625
[483] Kasamatsu K, Ichinose I and Matsui T 2013 *Phys. Rev. Lett.* **111** 115303
[484] Larson J and Levin S 2009 *Phys. Rev. Lett.* **103** 013602
[485] Larson J 2010 *Phys. Rev.* A **81** 051803
[486] Mivehvar F and Feder D L 2014 *Phys. Rev.* A **89** 013803

[487] Dong L, Zhou L, Wu B, Ramachandhran B and Pu H 2014 *Phys. Rev.* A **89** 011602
[488] Deng Y, Cheng J, Jing H and Yi S 2014 *Phys. Rev. Lett.* **112** 143007
[489] Boada O, Celi A, Latorre J I and Lewenstein M 2011 *New J. Phys.* **13** 5002
[490] Jotzu G, Messer M, Desbuquois R, Lebrat M, Uehlinger T, Greif D and Esslinger T 2014 arXiv:1406.7874
[491] Parameswaran S A, Roy R and Sondhi S L 2003 *C. R. Phys.* **14** 816
[492] Aidelsburger M, Lohse M, Schweizer C, Atala M, Barreiro T, Nascimbene S, Cooper N R, Bloch I and Goldman N arXiv:1407.4205
[493] Roscilde T 2014 *Phys. Rev. Lett.* **112** 110403
[494] Duca L, Li T, Reitter M, Bloch I, Schleier-Smith M and Schneider U 2014 arXiv:1407.5635
[495] Xiaoling Cui and Wei Yi 2014 *Phys. Rev.* X **4** 031026
[496] Zhe-Yu Shi, Xiaoling Cui and Hui Zhai 2014 *Phys. Rev. Lett.* **112** 013201
[497] Zygelman B 2013 *J. Phys.* B **46** 134011
[498] Kiffner M, Li W and Jaksch D 2013 *Phys. Rev. Lett.* **110** 170402
[499] Grusdt F and Fleischhauer M 2013 *Phys. Rev.* A **87** 043628
[500] Cesa A and Martin J 2013 *Phys. Rev.* A **88** 062703
[501] Olson A J, Wang S J, Niffenegger R J, Li C H, Greene C H and Chen Y P 2014 *Phys. Rev.* A **90** 013616